DISSERTATION

Thermodynamics of strong-interaction matter

On the phase structure and thermodynamics of quantum chromodynamics with Dyson–Schwinger equations

Philipp Isserstedt

Genehmigt vom Fachbereich für
Mathematik und Informatik, Physik, Geographie
der Justus-Liebig-Universität Gießen

zur Erlangung des Grades eines
Doktors der Naturwissenschaften
(Dr. rer. nat.)

November 2021

Thermodynamics of strong-interaction matter
Genehmigte Dissertation von Philipp Isserstedt, M.Sc.

1. Gutachten:	Prof. Dr. Christian S. Fischer
2. Gutachten:	Priv.-Doz. Dr. Michael Buballa
Einreichung:	06.09.2021
Disputation:	26.11.2021

Justus-Liebig-Universität Gießen
Fachbereich für Mathematik und Informatik, Physik, Geographie
Institut für Theoretische Physik
Heinrich-Buff-Ring 16
35392 Gießen

"All it takes is a little faith,
and a lot of heart."

— The Weepies
(*Stars*, Say I am You, Nettwerk Records, 2006)

Zusammenfassung

In dieser in thematisch vier Teile gegliederten Arbeit wird die Phasenstruktur und Thermodynamik von Materie untersucht, die der starken Wechselwirkung unterliegt. Wir verwenden dafür eine Kombination von Ergebnissen reiner Yang–Mills-Theorie aus Gitterrechnungen mit einem System von trunkierten Dyson–Schwinger-Gleichungen für die Quark- und Gluon-Propagatoren der Quantenchromodynamik mit $2 + 1$ Quark-Flavor in Landau-Eichung.

Zu Beginn lösen wir das gekoppelte System der Dyson–Schwinger-Gleichungen für die nicht-störungstheoretischen Quark- und Gluon-Propagatoren, wobei die Rückkopplung der Quarks auf das Gluon explizit miteinbezogen wird. Dieses System stimmt bei verschwindendem chemischen Potential bezüglich der Temperaturabhängigkeit des Ordnungsparameters für chirale Symmetriebrechung quantitativ mit Ergebnissen der Gitter-Quantenchromodynamik überein. Bei nicht-verschwindendem chemischen Potential, bei dem Gitterrechnungen aufgrund des Vorzeichenproblems nicht verlässlich sind, finden wir einen kritischen Endpunkt bei moderaten Temperaturen und hohem chemischen Potential. Alle gefundenen Ergebnisse stimmen mit denen aus früheren Arbeiten überein. Weiterhin vergleichen wir unsere Resultate mit anderen kürzlich erschienenen Ergebnissen für das Phasendiagramm der Quantenchromodynamik.

Im Anschluss präsentieren wir Ergebnisse für Fluktuationen der Quark- und Baryonenzahl bei nicht-verschwindender Temperatur und chemischen Potential. Wir diskutieren, wie sich die Fluktuationen und deren Verhältnisse bis zur vierten Ordnung bei verschiedenen Temperaturen und chemischen Potentialen bis zum kritischen Endpunkt verhalten. Im Vergleich mit aktuellen experimentellen Daten für die Schiefe- und Kurtosis-Verhältnisse sind unsere Ergebnisse kompatibel mit dem Szenario eines kritischen Endpunktes bei hohem chemischen Potential und einem gewissen Abstand zur Freeze-Out-Linie.

Darauffolgend diskutieren wir eine trunkierungsunabhängige Methode zur Berechnung von thermodynamischen Größen mittels des Dyson–Schwinger-Zugangs. Der Machbarkeitsbeweis wird mit Hilfe eines Nambu–Jona-Lasinio-Modells erbracht und anschließend wenden wir die Methode auf das in dieser Arbeit verwendete Dyson–Schwinger-Framework an. Dadurch erhalten wir den Druck, die Entropiedichte, die Energiedichte und das Wechselwirkungsmaß. Sowohl im Bereich der chiralen Übergangstemperatur als auch darunter

stimmen die Ergebnisse zufriedenstellend mit Gitterresultaten überein. Ebenfalls diskutieren wir, wo die Methode ihre Grenzen findet.

Zuletzt untersuchen wir den Einfluss eines homogenen, endlichen, dreidimensionalen Volumens auf die Phasenstruktur der Quantenchromodynamik. Wir bestimmen die Abhängigkeit der Position des kritischen Endpunktes von der Wahl der Randbedingungen sowie der Größe eines kubischen Volumens mit Seitenlänge L. Während signifikante Volumeneffekte erst für $L \lesssim 5\,\mathrm{fm}$ auftreten, sind Volumina der Größe $L^3 \gtrsim (8\,\mathrm{fm})^3$ sehr nahe am unendlichen Volumen. Weiterhin zeigen wir, dass eine ordnungsgemäße Behandlung von Finite-Size-Artefakten essentiell für verlässliche Aussagen über Volumeneffekte ist.

Abstract

In this work, which is topically divided into four parts, we study the phase structure and thermodynamics of strong-interaction matter. To this end, we employ a sophisticated, well-studied combination of results for pure Yang–Mills theory from lattice calculations and a truncated set of Dyson–Schwinger equations for the quark and gluon propagators of $(2 + 1)$-flavor quantum chromodynamics in Landau gauge.

First, we solve this coupled set of Dyson–Schwinger equations for the fully nonperturbative quark and gluon propagators, where the backcoupling of quarks onto the gluon is explicitly taken into account. This system agrees at vanishing chemical potential quantitatively with results from lattice-regularized quantum chromodynamics regarding the temperature dependence of the order parameter for chiral symmetry breaking. Furthermore, at nonzero chemical potential, where lattice calculations are not reliable due to the sign problem, we find a critical endpoint at moderate temperatures and large chemical potential. All obtained results are in agreement with previous works. In addition, we compare our results with other recent phase-diagram calculations.

Then, we present results for quark and baryon number fluctuations at nonzero temperature and chemical potential that are extracted from the quark propagator. We discuss the changes of these fluctuations and ratios thereof up to fourth order for several temperatures and chemical potentials up to the critical endpoint. In view of recent experimental data for the skewness and kurtosis ratios, our results are compatible with the scenario of a critical endpoint at large chemical potential and with a certain offset from the freeze-out line.

Next, we discuss a method to compute thermodynamic quantities within the Dyson–Schwinger approach that is independent of the employed truncation. As a proof of principle, we first apply it to Nambu–Jona-Lasinio model and subsequently to our Dyson–Schwinger framework. As a result, we obtain the pressure, entropy density, energy density, and interaction measure across the phase diagram of quantum chromodynamics. Below and around the chiral transition temperature, we find a satisfactorily agreement with lattice results. The limitation of the method is discussed, too.

Finally, the impact of a uniform, finite, three-dimensional volume on the phase structure of quantum chromodynamics is investigated. In particular, we determine the dependence

of the location of the critical endpoint on the boundary conditions and the volume of a three-dimensional cube with edge length L. We find that noticeable volume effects appear for $L \lesssim 5\,\mathrm{fm}$, and volumes as large as $L^3 \gtrsim (8\,\mathrm{fm})^3$ are very close to infinite volume. Furthermore, we demonstrate that a proper treatment of finite-size artifacts is crucial for reliable statements about finite-volume effects.

Contents

List of abbreviations

Even though defined in the text when first introduced, here we collect the abbreviations that are used throughout this work.

ABC	antiperiodic boundary conditions
BRST	Becchi–Rouet–Stora–Tyutin
DCSB	dynamical chiral symmetry breaking
CEP	critical endpoint
DSE	Dyson–Schwinger equation
EoS	equation of state
FAIR	Facility for Antiproton and Ion Research
FRG	functional renormalization group
NICA	Nuclotron-based Ion Collider Facility
NJL	Nambu–Jona-Lasinio
nPI	n-particle irreducible
O(n)	orthogonal group of degree n
PBC	periodic boundary conditions
QCD	quantum chromodynamics
RHIC	Relativistic Heavy-Ion Collider
STAR	Solenoidal Tracker at RHIC
STI	Slavnov–Taylor identity
SU(n)	special unitary group of degree n
U(n)	unitary group of degree n
YM	Yang–Mills

1 Prologue

In the 1960s, due to the commissioning of more and more powerful particle accelerators, the physics community faced a vast abundance of particles which are subject to the strong interaction, one of the fundamental forces of nature. These particles, called hadrons, come in two types: mesons and baryons. The former carry integer spin, while the latter are particles with half-integer spin. It was realized that the whole hadron spectrum can be neatly explained if one assumes that hadrons are composite objects made of pointlike particles called quarks [1–3]. In particular, baryons are made out of three quarks and mesons consist of one quark and an antiquark. Therefore, quarks carry fractional elementary electric charge (minus one-third or two-thirds) and are spin-$\frac{1}{2}$ particles. That quarks are more than a mere classification scheme for hadrons and not fictitious particles was confirmed by high-energy electron-proton scattering experiments. It was found that the proton is indeed composite and consists of pointlike particles off which the electrons scatter [4, 5]. Originally, quarks came in three different species referred to as flavors (up, down, and strange). However, more flavors were theoretically postulated [6–9] and the existence of three additional ones (charm, bottom, and top) is experimentally confirmed [10–15].

It was soon realized that quarks need to have another quantum number [16, 17] in order to remedy the deficiencies of the quark picture as described above. For example, the Δ^{++} baryon, which is a spin-$\frac{3}{2}$ particle, would require the three quarks to be spin-aligned with vanishing angular momentum, thus violating the Pauli exclusion principle. This new quantum number, called color, can be interpreted as an additional charge akin to the electric one, and quarks occur in three different colors (red, green, and blue).[1] Finally, the quantum field theory of the strong interaction—quantum chromodynamics (QCD)—was formulated and presented as we know it today [19–24]: a non-Abelian gauge theory with quarks and gluons as fundamental fields. The latter are the massless spin-1 gauge bosons that couple to the color charge of the quarks, thereby mediating the strong force, and interact among themselves, too. QCD exhibits the remarkable feature of asymptotic freedom [25–28], i.e., the coupling strength tends to zero at asymptotically small distances. More precisely, the strong coupling constant decreases logarithmically at large momentum scales. This makes

[1] "The idiot physicists, unable to come up with any wonderful Greek words anymore, call this type of polarization by the unfortunate name of 'color,' which has nothing to do with color in the normal sense." — R. P. Feynman [18]

QCD perfectly suited for a perturbative treatment at these scales, and QCD is therefore extremely well and systematically understood in the regime where perturbation theory can be applied. Combined with key experiments that confirmed theoretical predictions, see, e.g., Refs. [29–32] and references therein, QCD became the established theory describing the strong interaction within the Standard Model of particle physics.

As the momentum scale decreases, the interaction strength becomes stronger and stronger which inevitably renders perturbation theory invalid at some point, and phenomena beyond the reach of perturbation theory emerge. Probably the most prominent ones are confinement and the dynamical breaking of chiral symmetry. Regarding confinement, one usually differentiates between color and quark confinement. The former describes the fact that all asymptotic particle states observed in nature are color singlets, i.e., color-neutral objects, while the latter is associated with the notion of a linear rising potential between a quark-antiquark pair. Explaining (and deriving) confinement thoroughly from the basic principles of QCD is an intricate task with many facets and still an open, unsettled question. However, confinement is not the focus of the investigations presented here, and we refer the reader, e.g., to Refs. [33–36] and references therein. On the other hand, the dynamical breaking of chiral symmetry, one of the global symmetries of QCD, is a common theme of this work. It accounts for the vast majority of the hadron masses because quarks acquire a large amount of dynamical mass due to the strong quark-gluon interaction in the low-momentum region—colloquially known as "mass from nothing." This solves the riddle of a proton mass of around one GeV even though the masses of its constituents, two up quarks and one down quark, are only a few MeV.

Soon after the emergence of QCD, its properties and phase structure at nonzero temperature and density gained significant attention, see, e.g., Ref. [37] and references therein, and are still subject of tremendous theoretical and experimental efforts [38, 39]. It was realized that QCD predicts a novel state of matter [40, 41]. At sufficiently high temperatures and/or densities, hadrons "dissolve," i.e., quarks and gluons are deconfined and form the so-called quark-gluon plasma. Convincing experimental evidence that the quark-gluon plasma indeed exists and is created in heavy-ion collisions has been put forward [42–44]. Its existence is by now widely accepted. The experimental exploration of the QCD phase diagram is subject of several large-scale heavy-ion collision facilities. In particular, the already operating Beam Energy Scan program [45–47] at the Relativistic Heavy-Ion Collider (RHIC) at Brookhaven National Laboratory, USA, as well as the future Compressed Baryonic Matter experiment [48] at the Facility for Antiproton and Ion Research (FAIR), Germany, and the future Nuclotron-based Ion Collider Facility (NICA) [49] at the Joint Institute for Nuclear Research, Russia, are tailored to probe QCD's phase structure. In a typical heavy-ion collision experiment, heavy nuclei, e.g., gold or lead, are accelerated close to the speed of light, collide head-on, and in course of that penetrate,

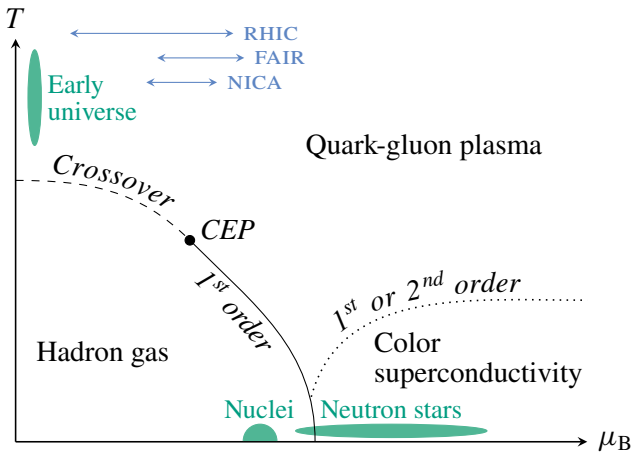

Figure 1.1 Contemporary, theoretically conjectured sketch of the QCD phase diagram in terms of baryon chemical potential μ_B and temperature T. Environments where the corresponding phases are expected to be realized are shown as green areas. Furthermore, we indicate the approximate chemical-potential regions that are/will be covered by RHIC, FAIR, and NICA (blue arrows).

compress, and heat each other. As a result, a short-living fireball of extremely hot and dense matter—the aforementioned quark-gluon plasma—is created for a very short time. As the fireball expands, it cools down and hadronizes. At some point after the hadronization, the chemical freeze-out takes place, i.e., the abundancies of the created hadrons do not change anymore (no more inelastic scattering). Finally, the kinetic freeze-out happens that is characterized by frozen momentum distributions of the reaction products; in other words, no more elastic scattering and the mean free path of the reaction products is large. Such a collision is a very transient event. From the initial lump of the quark-gluon plasma to kinetic freeze-out, only around 10^{-21} seconds pass. In the end, the produced hadrons and emitted dileptons as well as photons are experimentally measured. The former carry mostly information about the later stages of the collision event, while the latter are colloquially known as "messengers" of the early stages of a heavy-ion collision since they escape the initial fireball almost without any interaction. The experimental techniques and analyses to cope with a heavy-ion collision are highly nontrivial and by no means simple. For more details, we refer the reader, e.g., to Refs. [48, 50] and references therein.

On the theoretical side, the structure of the QCD phase diagram is mostly conjectured. In Fig. 1.1, we show a contemporary sketch of the phase diagram of strong-interaction matter in the μ_B-T plane, where μ_B and T denote baryon chemical potential and temperature, respectively. At vanishing chemical potential, ab-initio lattice QCD [51] provides firm, overwhelming evidence for the following and by now well-established picture: the confined hadronic low-temperature phase characterized by dynamical chiral symmetry breaking is

connected through an analytic crossover to the deconfined high-temperature phase of the quark-gluon plasma with (partially) restored chiral symmetry [52–56]. At nonvanishing chemical potential, however, lattice QCD is plagued by the notorious sign problem [57, 58]. It describes, loosely speaking, that the statistical probability interpretation of the integrand of the path integral breaks down at nonvanishing (real) chemical potential, making the standard lattice algorithms based on Monte Carlo importance sampling void. Therefore, other methods are needed to complement the lattice calculations in order to gain qualitative (and, in the long term, quantitative) information about the phase structure of QCD at nonzero temperature and chemical potential.

There are many effective models of QCD that have the same symmetries and describe some of its aspects. Prominent examples are the hugely successful Nambu–Jona-Lasinio (NJL) model [59–63] and its bosonized version, the quark-meson model [64–69]. A priori, these low-energy effective models of QCD do not contain any gluon dynamics. To remedy that (at least to some extent), enhanced versions of the NJL and quark-meson model rely on the Polyakov loop potential [70–75]. The latter couples aspects of confinement to the chiral dynamics, however without backcoupling of the fermionic matter sector onto the gluonic sector. Thus, gluons are no active degrees of freedom, and their reaction to the medium and the chiral dynamics of the quarks can neither be studied nor directly taken into account. A different approach is possible within the functional frameworks of Dyson–Schwinger equations (DSEs) [76–79] and the functional renormalization group (FRG) [80–83]. They are fully nonperturbative and obtained directly, without any approximation from the generating functional of the theory they are applied to. Thus, the DSE and FRG approaches to QCD are well-suited to obtain reliable information about the phase structure. Notably, they do not suffer from the sign problem and calculations at nonzero chemical potential are straightforward. In their untruncated form, both methods constitute an infinite set of coupled equations that describe QCD exactly, i.e., from first principles. However, truncations are necessary to obtain finite and hence numerically feasible sets of equations. In this work, we use DSEs to explore the phase diagram of QCD, which are, in short, the equations of motions for the correlation functions.[2] Particularly, we employ a truncation scheme that combines lattice results for quenched QCD with DSEs for the quark and unquenched gluon propagators. This scheme has been studied extensively in the past, see Ref. [79] for a comprehensive review, but some of its aspects are not mapped out yet: on the one hand thermodynamics and on the other hand the impact of finite volume—these two topics are subject of this thesis.

Coming back to Fig. 1.1, if we turn to nonzero chemical potential, DSE and FRG studies as well as model calculations find that the continuous crossover becomes steeper with

[2] Moreover, they are a versatile tool for the investigation of bound states [84–89], aspects of the purely gluonic sector of QCD [89–91], and contributions to the anomalous magnetic moment of the muon [92–94].

increasing chemical potential and eventually terminates in a second-order critical endpoint (CEP) followed by a first-order phase transition at large chemical potential. Proving the very existence of and hence subsequently locating the conjectured, putative CEP is one of the main goals of the experimental endeavors at RHIC, FAIR, and NICA. At low temperatures and very large chemical potential, it is expected that color-superconducting phases emerge. The transition to the quark-gluon plasma is either of first or second order, which depends on the details of how color superconductivity is realized. In course of the investigations presented here, we do not cover the whole phase diagram but are mostly interested in the crossover region up to the CEP and hence focus on that region.

As already mentioned, in this work we use a well-studied truncation scheme for the quark and gluon propagator DSEs to explore $(2 + 1)$-flavor QCD at nonzero temperature and chemical potential. While the phase structure was already studied in several previous works using that truncation scheme, thermodynamic aspects were not discussed, though they are crucial in order to make contact with experiment. Prime candidates for that are ratios of baryon number fluctuations, which can be measured in heavy-ion collision experiments; recent results from the STAR (Solenoidal Tracker at RHIC) collaboration are already available [95, 96]. These ratios are interesting because they are expected to deliver distinct signals as soon as the CEP—if existing—is approached [47, 97]. Thus, the first aim of this work is the computation of fluctuations with an emphasis on ratios and the question under which circumstances these are in qualitative agreement with experiment.

Fluctuations are defined as derivatives of the pressure, which is nothing but the negative thermodynamic potential. For a comprehensive thermodynamical understanding, however, it is highly desirable to get hold of the pressure itself because other quantities such as the entropy density or the energy density follow directly from the pressure. Unfortunately, computing the latter from DSEs is a difficult task, and results are scarce and obtained so far only within simple truncations. The reason for that is a technical obstacle rooted deep within the DSE framework. Generally speaking, the starting point for the derivation of every DSE is a first derivative of the thermodynamical potential. Alas, an integration is only possible for certain (simple) truncations. Therefore, it is highly desirable to be able to compute thermodynamic quantities using DSEs in a truncation-invariant manner. This is the second aim of this work. We explore a novel truncation-independent method that allows us to compute thermodynamic quantities from DSEs, demonstrate its effectiveness, and subsequently compute the pressure and associated quantities.

The previous two topics this work is concerned with are carried out within a DSE setup that is formulated in an infinite three-dimensional volume. However, it is apparent that a heavy-ion collision takes place in a finite volume: the initial fireball is of finite extent with typical scales of several femtometers in each direction. Volume effects on important

observables such as fluctuations may be considerable and need to be taken into account, particularly in view of the experimental search for the (putative) CEP. Moreover, the whole phase structure as sketched in Fig. 1.1 inevitably becomes volume dependent for small enough volumes. Thus, the third aim of this thesis is the investigation of finite-volume effects on the phase structure of QCD.

To summarize, this thesis is organized as follows. In the next chapter, we recapitulate selected aspects of QCD that are relevant for this work and discuss the functional framework of DSEs, which we use for our investigations. After introducing our truncation scheme for the coupled system of quark and gluon propagator DSEs and discussing our result for the phase diagram of $(2 + 1)$-flavor QCD in Chapter 3, we continue with the calculation of quark and baryon number fluctuations across the QCD phase diagram in Chapter 4. Then, in Chapter 5, we present a truncation-independent method to obtain thermodynamic quantities from DSEs and subsequently compute the pressure and associated quantities. In Chapter 6, we investigate the impact of a finite volume on the phase structure of QCD. Finally, we conclude with a summary and give an outlook in Chapter 7. At this point, we encourage the reader to have a glance at Appendix A where our notations and conventions are detailed.

Parts of this work are already published. Chapter 4 and parts of Chapter 3 are based on Ref. [98] while Chapter 5 is derived from Ref. [99]. The topics covered in Chapter 6 are subject of Ref. [100]. Furthermore, this work is partially connected to the topics discussed in Ref. [101], which are presented in detail elsewhere [102].

2 Setting the scene: QCD in a nutshell

In the following, we try to give an overview of the theoretical framework and concepts relevant for this work. Since a comprehensive treatment is beyond the scope of this chapter and details can be found in many textbooks on quantum field theory, we refer the reader to Refs. [37, 103–108] on which the following is based.

2.1 The generating functional

Being a quantum field theory, QCD's defining quantity is its Lagrangian. Working in four-dimensional Euclidean space-time[3], it is constrained by locality, Euclidean invariance[4], local $\mathrm{SU}(N_\mathrm{c})_\mathrm{color}$ gauge invariance, and renormalizability. The Lagrangian is given by

$$\mathscr{L}_\mathrm{QCD} = \bar{\psi}_\alpha (\not{D} + \hat{m})_{\alpha\beta} \psi_\beta + \frac{1}{4} F^a_{\nu\sigma} F^a_{\nu\sigma} \,, \tag{2.1}$$

and its first term describes the dynamics of the quark fields ψ and $\bar{\psi} = \psi^\dagger \gamma_4$. They are N_f-dimensional vectors in flavor space; each entry being a N_c-dimensional vector in color space, $N_\mathrm{c} = 3$, with Dirac spinors as components. These degrees of freedom are summarized by the collective indices α and β. The covariant derivative

$$D_\nu = \partial_\nu + \mathrm{i}\, g A^a_\nu \tau^a \tag{2.2}$$

contains the coupling of the quarks to the gluon fields A^a_ν, $a = 1, \ldots, N_\mathrm{c}^2 - 1$, with coupling constant g. Furthermore, $\hat{m}$ is the current-quark mass matrix and τ^a are the generators of the gauge group $\mathrm{SU}(N_\mathrm{c})_\mathrm{color}$. They span the corresponding Lie algebra and obey $[\tau^a, \tau^b] = \mathrm{i}\, f^{abc} \tau^c$ with totally antisymmetric structure constants f^{abc}. Quarks transform by construction according to the fundamental representation of $\mathrm{SU}(N_\mathrm{c})_\mathrm{color}$, while gluons transform with respect to the adjoint representation. The second term in Eq. (2.1) is the Yang–Mills (YM) Lagrangian [109] and governs the dynamics of the gluon

[3] See Appendix A for our notations and conventions.

[4] That is, invariance under translations, rotations, boosts, and reflections in $\mathbb{R}^4$. This corresponds to the usual Poincaré invariance in Minkowski space.

fields. It is expressed in terms of the field strength tensor

$$F^a_{\nu\sigma} = \partial_\nu A^a_\sigma - \partial_\sigma A^a_\nu - g f^{abc} A^b_\nu A^c_\sigma \,. \tag{2.3}$$

Its last term reflects the non-Abelian nature of QCD and gives rise to gluon self-interactions. Besides the usual kinetic term, the YM part of the Lagrangian contains terms cubic and quartic in the gluon fields. This feature makes QCD distinct from quantum electrodynamics with gauge group U(1). The latter is Abelian, thus, all structure constants vanish and no self-interactions between photons arise. From the QCD Lagrangian, we obtain the action

$$I_{\mathrm{QCD}} = \int_x \mathcal{L}_{\mathrm{QCD}} \tag{2.4}$$

and immediately the partition function[5]

$$\mathcal{Z} = \int \mathcal{D}[\psi\bar{\psi}A]\, \mathrm{e}^{-I_{\mathrm{QCD}}} \,. \tag{2.5}$$

Unfortunately, the partition function as naively written down above is plagued by deficiencies. These can be traced back to the local gauge invariance of QCD. The Lagrangian as well as the action are by construction invariant under local gauge transformations

$$\begin{aligned} \psi \to \psi^U &= U\psi \,, \qquad \bar{\psi} \to \bar{\psi}^U = \bar{\psi} U^{-1} \,, \\ A_\nu \to A^U_\nu &= U A_\nu U^{-1} + \frac{\mathrm{i}}{g} (\partial_\nu U) U^{-1} \,, \end{aligned} \tag{2.6}$$

where $U \in \mathrm{SU}(N_\mathrm{c})_{\mathrm{color}}$ is space-time dependent, $U = U(x)$, and $A_\nu = A^a_\nu \tau^a$. It follows that the integration in Eq. (2.5) includes field configurations that are related by a gauge transformation. They are physically equivalent, i.e., they yield the same action, and therefore generate an infinite factor, the volume of the gauge group, that has to be properly factorized and absorbed into the normalization of the path integral. In principle, this poses no problem if one considers only gauge-invariant quantities as usually done in lattice gauge theory. Functional methods like DSEs, however, rely on gauge-dependent quantities and we have to fix the degeneracy in the partition function caused by the gauge invariance of the theory. Furthermore, the differential operator $-\delta_{\nu\sigma}\partial^2 + \partial_\nu\partial_\sigma$ corresponding to the kinetic term of the gluons has vanishing eigenvalues. Thus, it cannot be inverted and the equation for the perturbative gluon propagator is ill-defined. The gauge must be fixed in order to overcome these problems.

[5] $\mathcal{D}[\psi\bar{\psi}A] = \mathcal{D}\psi\,\mathcal{D}\bar{\psi}\prod_{\nu,a}\mathcal{D}A^a_\nu$, and the normalization of the path integral is implicit.

However, even with a well-defined gluon propagator, e.g., from adding a gauge-fixing term to $\mathcal{L}_{\mathrm{QCD}}$ akin to quantum electrodynamics, it turns out that the scattering matrix of QCD lost the crucial property of being unitary. Unphysical longitudinal and scalar gluon polarizations remain in the spectrum. Historically, it was found that contributions from loops of scalar particles with the odd property obeying Fermi–Dirac statistics are missing to cancel these polarizations—eventually restoring the unitarity of the scattering matrix. This was observed and elaborated in the context of quantum gravity [110–112].[6] A more intuitive picture within the path-integral approach, where these odd particles naturally arise, was put forward in Refs. [116, 117] and is summarized in the following.

In order to overcome the above mentioned problems, we aim to restrict the integration in Eq. (2.5) to gluons obeying the condition

$$\mathcal{F}[A_\nu] = 0\,, \tag{2.7}$$

where $\mathcal{F}$ is a local functional that fixes the gauge. For a given field configuration and all physically equivalent ones related via a gauge transformation, the gauge-fixing functional is supposed to single out exactly one representative. To embed this into the path integral, we consider the quantity

$$\Delta_{\mathcal{F}}^{-1}[A_\nu] = \int \mathcal{D}U\, \delta\big(\mathcal{F}\big[A_\nu^U\big]\big) \tag{2.8}$$

known as the (inverse) Faddeev–Popov determinant. It is gauge invariant and the integration covers all possible gauge transformations.[7] From Eq. (2.8), it follows that

$$1 = \Delta_{\mathcal{F}}[A_\nu] \int \mathcal{D}U\, \delta\big(\mathcal{F}\big[A_\nu^U\big]\big)\,, \tag{2.9}$$

which resembles a completeness relation in the space of all gauge fields. After inserting this expression for the identity under the path integral in Eq. (2.5), a change of variables $A_\nu \to A_\nu^{U^{-1}}$ is performed. This allows for the desired factorization of the group integration because the measure, action, and $\Delta_{\mathcal{F}}$ are invariant. The (infinite) factor stemming from the group integration is absorbed into the normalization of the path integral and we arrive at the gauge-fixed partition function

$$\mathcal{Z} = \int \mathcal{D}[\psi\bar{\psi}A]\, \Delta_{\mathcal{F}}[A_\nu]\, \delta(\mathcal{F}[A_\nu])\, \mathrm{e}^{-I_{\mathrm{QCD}}}\,. \tag{2.10}$$

[6] The same is found in the path-dependent approach of Mandelstam [113–115].

[7] More mathematically, $\int \mathcal{D}U$ is the path-integral version of the integration with respect to the Haar measure $\mathrm{d}U$ on the gauge group $G = \mathrm{SU}(N_\mathrm{c})_\mathrm{color}$ [118, 119]: $\int \mathcal{D}U = \int_G \prod_x \mathrm{d}U(x)$. Since $\mathrm{SU}(N_\mathrm{c})_\mathrm{color}$ is a compact Lie group, the Haar measure is left and right invariant, i.e., $\int_G \mathrm{d}U = \int_G \mathrm{d}(U'U) = \int_G \mathrm{d}(UU')$. It is thus straightforward to show that $\Delta_{\mathcal{F}}^{-1}[A_\nu]$ is gauge invariant.

Now, it is left to bring Eq. (2.10) into a form more suitable for practical calculations since it looks still rather formal. First, we have to choose a gauge. We employ the generalized linear covariant condition

$$\mathcal{F}[A_\nu] = \partial_\nu A_\nu - w \tag{2.11}$$

with an arbitrary function w independent of A_ν. Because observables are insensitive to gauge-fixing details, Eq. (2.10) is further multiplied by a Gaussian $\mathrm{e}^{-\int w^2/(2\xi)}/\sqrt{2\pi}\xi$ followed by a functional integration with respect to w [120]. Again, this affects only the overall normalization of the partition function and is thus physically unimportant. The width ξ of the Gaussian is arbitrary and reflects the freedom of choosing a gauge. Second, we need an explicit expression for the Faddeev–Popov determinant. From its definition (2.8), we find

$$\begin{aligned} \Delta_{\mathcal{F}}[A_\nu] &= \det \frac{\delta \mathcal{F}[A_\nu^U]}{\delta U}\bigg|_{U=\mathbb{1}} \\ &= \det\left[-\frac{1}{g}\,\partial_\nu D_\nu^{ab}\,\delta^{(4)}(x-y)\right], \end{aligned} \tag{2.12}$$

where $D_\nu^{ab} = \delta^{ab}\,\partial_\nu + g f^{abc} A_\nu^c$ is the covariant derivative in the adjoint representation. The last step is to write $\Delta_{\mathcal{F}}$ as an exponential of some action such that Eq. (2.10) is of the form "$\int \mathcal{D}[\text{fields}]\,\mathrm{e}^{-\text{action}}$" again. This is accomplished by expressing the determinant as an integral over Grassmann variables [116, 121], viz.,[8]

$$\Delta_{\mathcal{F}}[A_\nu] = \int \mathcal{D}[c\bar{c}]\exp\left(-\int_x \bar{c}^a\,\partial_\nu D_\nu^{ab} c^b\right) \tag{2.13}$$

with Grassmann-valued, complex scalar fields c^a and $\bar{c}^a$. They are anticommuting like fermions, but the corresponding propagator is bosonic. Violating the spin-statistics theorem [122, 123], these fields are absent in the physical spectrum. Due to these rather odd properties, they are called ghosts. For an Abelian theory, $f^{abc} = 0$ and the Faddeev–Popov determinant is independent of the gauge field. Ghosts still appear but decouple and their contribution is absorbed into the normalization of the path integral. This is similarly true for some noncovariant gauge conditions, e.g., the class of axial gauges [124] or the flow gauges of Ref. [125].[9]

Putting all things together and introducing sources $J = (\bar{\eta}_\alpha, \eta_\alpha, j_\nu^a, \bar{\sigma}^a, \sigma^a)$ for the fields, we finally arrive at the generating functional

$$\mathcal{Z}[J] = \int \mathcal{D}[\psi\bar{\psi}Ac\bar{c}]\,\mathrm{e}^{-I_{\mathrm{QCD}}^{\mathrm{gf}}+I_J} \tag{2.14}$$

[8] The factor $1/g$ is conveniently absorbed into the normalization of c^a and $\bar{c}^a$.

with the gauge-fixed action

$$I_{\mathrm{QCD}}^{\mathrm{gf}} = \int_x \left(\bar{\psi}_\alpha (\not{D} + \hat{m})_{\alpha\beta} \psi_\beta + \frac{1}{4} F^a_{\nu\sigma} F^a_{\nu\sigma} + \frac{1}{2\xi} \left(\partial_\nu A^a_\nu\right)^2 + \mathrm{i} \tilde{c}^a \partial_\nu D^{ab}_\nu c^b \right) \tag{2.15}$$

and the source term

$$I_J = \int_x \left(\bar{\eta}_\alpha \psi_\alpha + \bar{\psi}_\alpha \eta_\alpha + j^a_\nu A^a_\nu + \tilde{\sigma}^a c^a + \tilde{c}^a \sigma^a \right). \tag{2.16}$$

The latter is an auxiliary quantity that allows for the derivation of correlations functions in terms of functional derivatives of $\mathcal{Z}[J]$ with respect to the sources. Note that an additional factor of i appears in front of the ghost term in Eq. (2.15) because we choose the ghosts to be real. More details about the choice of real versus complex (and anti-Hermitian) ghost fields can be found, e.g., in Refs. [78, 126]. Furthermore, Landau gauge is used throughout this work. This corresponds to the limit $\xi \to 0$ of the gauge parameter, and the gluons are thus strictly transverse, $\partial_\nu A^a_\nu = 0$.

In a series of works, it was shown that the theory given by the gauge-fixed action (2.15) is multiplicatively renormalizable [120, 128–131], see also Refs. [103, 132–135] and references therein. The unrenormalized Lagrangian is connected to the renormalized one containing counterterms via the multiplicative rescaling

$$\begin{gathered} \psi \to Z_2^{1/2} \psi \qquad \bar{\psi} \to Z_2^{1/2} \bar{\psi}\,, \qquad A^a_\nu \to Z_3^{1/2} A^a_\nu\,, \qquad c^a \to \tilde{Z}_3^{1/2} c^a \\ \tilde{c}^a \to \tilde{Z}_3^{1/2} \tilde{c}^a\,, \qquad g \to Z_g\, g\,, \qquad \hat{m} \to Z_m \hat{m} \end{gathered} \tag{2.17}$$

with renormalization constants Z_2, Z_3, $\tilde{Z}_3$, Z_g, and Z_m for quarks, gluons, ghosts, coupling constant, and mass, respectively. Though in principle necessary, a rescaling of the gauge parameter ($\xi \to Z_\xi\, \xi$) is omitted because Landau gauge is a fixed point of the renormalization group. The additional renormalization constants $Z_{1\mathrm{F}}$, Z_1, $\tilde{Z}_1$, and Z_4 for the quark-gluon, three-gluon, ghost-gluon, and four-gluon vertex, respectively, are not independent but related to the ones introduced in (2.17) via

$$\begin{aligned} Z_{1\mathrm{F}} &= Z_g\, Z_2\, Z_3^{1/2}\,, \qquad & Z_1 &= Z_g\, Z_3^{3/2}\,, \\ \tilde{Z}_1 &= Z_g\, \tilde{Z}_3\, Z_3^{1/2}\,, \qquad & Z_4 &= Z_g^2\, Z_3^2\,. \end{aligned} \tag{2.18}$$

These equations are consequences of the Slavnov–Taylor identities (STIs) [136, 137],

[9] Ghost-free YM theory in linear covariant gauges is discussed in Ref. [127]. However, the presented approach is limited to perturbation theory in Feynman gauge and at the expense of higher and higher multi-point gluon self-interactions depending on the order of the perturbative expansion.

which are extensive relations among QCD's correlation functions and the non-Abelian generalization of the Ward–Takahashi identities [138, 139]. Quantities on the left-hand sides of (2.17) are bare while the ones on the right-hand sides are renormalized. Generally, the renormalization constants depend on the regularization scheme, renormalization scheme, and renormalization point ζ. In our numerical calculations (see Appendix D) we employ a Pauli–Villars regulator [140] characterized by a regularization scale Λ_{reg}, resulting in the dependence $Z_i = Z_i(\zeta, \Lambda_{\mathrm{reg}})$ of the renormalization constants. We use a momentum-subtraction scheme to determine the Z_i's relevant for our calculations.

Finally, we would like to add the important remark that the Faddeev–Popov method does not fix the gauge completely, i.e., it is incomplete. In particular, we tacitly assumed that

(i) the gauge condition (2.7) has exactly one solution on the set

$$\mathfrak{E}(A_\nu) = \left\{ U A_\nu U^{-1} + \frac{\mathrm{i}}{g} (\partial_\nu U) U^{-1} \,:\, U \in \mathrm{SU}(N_\mathrm{c})_\mathrm{color} \right\} \tag{2.19}$$

of physically equivalent gauge-field configurations for a given A_ν;

(ii) the Faddeev–Popov determinant is positive, $\Delta_\mathcal{F}[A_\nu] > 0$.

Both assumptions are generally not true. The latter holds only in the vicinity of $A_\nu = 0$, and the multiple solutions of $\mathcal{F}|_{\mathfrak{E}(A_\nu)} = 0$ are known as Gribov copies [141–145].[10] The issue raised by the second assumption can be treated by restricting the integration in Eq. (2.14) to the subset of gauge fields obeying the gauge condition and for which the Faddeev-Popov operator $\delta\mathcal{F}[A_\nu^U]/\delta U\big|_{U=\mathbb{1}}$ is positive definite. More details can be found in Ref. [145] and references therein. Furthermore, the impact of Gribov copies was studied in detail on the lattice, see, e.g., Refs. [156–160], and found to affect the ghost propagator yet mildly influence the gluon propagator at (deep) infrared momenta—a scale much below the temperature and chemical potential range we are interested in. Thus, we can safely ignore the problem of Gribov copies in this work.

2.2 Symmetries

In the following, we summarize some of the symmetries of the gauge-fixed action (2.15) and Lagrangian, respectively. Even though we work in Landau gauge, what follows in this section is independent of the value of the gauge parameter ξ. Symmetries are an all-important concept in physics. For example, symmetry considerations lie at the heart

[10] There are, however, approaches that circumvent the Gribov problem, e.g., stochastic quantization [146–153] or topological gauge fixing [154, 155]. Their discussion lies beyond the scope of this work and we refer the reader to the cited literature.

of the immensely successful Standard Model of particle physics. Tightly connected to continuous symmetries is Noether's (first) theorem [161–163]: each unbroken, continuous symmetry that leaves the action invariant leads to a conserved current, and the integral of the current's time component over $\mathbb{R}^3$ defines the corresponding conserved charge. The breaking of a symmetry, which is characterized by the behavior of the action and the Noether current, can be

(i) explicit: the symmetry is in principle not a symmetry at all because the action is not invariant, and the corresponding Noether current is not conserved;

(ii) dynamical (or spontaneous): the action is invariant, and the Noether current is conserved. However, the ground state of the system does not share the symmetry. In other words, the corresponding charge operator does not annihilate the vacuum, and the latter is thus not invariant under the corresponding symmetry transformation. Intimately related to that is Goldstone's theorem [164, 165]: for each generator of a continuous global symmetry that does not annihilate the vacuum, there is a massless spin-zero boson in the particle spectrum. These particles are called Nambu–Goldstone bosons.[11] If the symmetry is in addition (weakly) explicitly broken, the emerging particles have a nonzero (though relatively small) mass. In this case, they are called pseudo-Nambu–Goldstone bosons. A pedagogical introduction to dynamical symmetry breaking can be found, e.g., in Ref. [167];

(iii) anomalous: the symmetry is broken during quantization, i.e., the classical action is invariant, and the classical Noether current is conserved, but the quantized theory is not invariant anymore. In general, the classical symmetry is violated during the (inevitable) process of regularization and renormalization. A prominent example is the anomalous nonconservation of the axial-vector current known as the Adler–Bell–Jackiw anomaly [168, 169].[12] More details on anomalous symmetry breaking can be found, e.g., in Refs. [173–175] and references therein.

With these different kinds of symmetry breaking in mind, we discuss the different symmetries of QCD in the following.

BRST symmetry

First, for the sake of completeness, we begin with a more technical symmetry. Since we gauge fixed our theory, the Lagrangian is not invariant under local $\mathrm{SU}(N_\mathrm{c})_\mathrm{color}$ transformations anymore. However, it was found by Becchi, Rouet, and Stora [176–178]

[11] The occurrence of a massless state due to dynamical symmetry breaking was first discovered by Nambu in the context of superconductivity [166].

[12] This issue already surfaced in the early days of quantum electrodynamics [170–172].

and independently by Tyutin [179, 180] that the gauge-fixed Lagrangian is invariant under a transformation that is, roughly speaking, a usual infinitesimal gauge transformation with the ghost field playing the role of the transformation parameter. This so-called BRST symmetry can be seen as a generalization of the $\mathrm{SU}(N_\mathrm{c})_\mathrm{color}$ symmetry. The corresponding BRST transform of a generic field ϕ is of the form $\phi \to \phi + \lambda \mathfrak{s}\phi$ with a constant Grassmann number λ, and $\mathfrak{s}$ denotes the BRST operator. Its action in linear covariant gauges on quarks, gluons, and ghosts is defined as follows:

$$\begin{aligned} \mathfrak{s}\psi &= -\mathrm{i}gc^a\tau^a\psi\,, & \mathfrak{s}A^a_\mu &= D^{ab}_\mu c^b\,, \\ \mathfrak{s}c^a &= -\frac{g}{2}f^{abd}c^b c^d\,, & \mathfrak{s}\tilde{c}^a &= \frac{1}{\xi}\partial_\mu A^a_\mu\,. \end{aligned} \tag{2.20}$$

The BRST operator has the important property of being nilpotent with index two on the ghost mass shell, i.e., $\mathfrak{s}^2\phi = 0$ for any field $\phi \in \{\psi, A^a_\mu, c^a, \tilde{c}^a\}$ provided the ghost equations of motion hold. An off-shell nilpotent formulation, which is more general and convenient in formal calculations, can be obtained by introducing the Nakanishi–Lautrup auxiliary field [181–184] that functions as a Lagrange multiplier for gauge fixing. The on-shell form (2.20) is then obtained by integrating out the auxiliary field. In general, the BRST transformation is a very powerful tool. For example, it can be used to proof the renormalizability of QCD and the gauge independence and unitarity of the scattering matrix; see, e.g., Refs. [185, 186]. Furthermore, it allows one to fix the gauge solely on the level of the Lagrangian, i.e, without referring to the path integral [187], and the STIs can be elegantly derived [78, 105]. Last, we would like to remark that the BRST symmetry generates a conserved charge, but it is still under debate if the BRST symmetry is broken by nonperturbative effects.[13] Since a more thorough discussion of the BRST framework is beyond the scope of this section, we refer the reader to the already cited literature and to Refs. [126, 188] as well as references therein.

Flavor symmetries

Next, we discuss the flavor symmetries of QCD. To this end, we decompose the quarks into left- and right-handed ones: $\psi = \psi_\mathrm{L} + \psi_\mathrm{R}$, where $\psi_\mathrm{L} = \frac{1}{2}(\mathbb{1} - \gamma_5)\psi$ and $\psi_\mathrm{R} = \frac{1}{2}(\mathbb{1} + \gamma_5)\psi$. In the chiral limit, $\widehat{m} = \mathbb{0}$, the classical QCD Lagrangian is thus invariant under global $\mathrm{U}(N_\mathrm{f})_\mathrm{L} \times \mathrm{U}(N_\mathrm{f})_\mathrm{R}$ transformations that transform left- and right-handed quarks independently. This invariance is known as chiral symmetry and is, together with its breaking, a central theme of this work. A pedagogical introduction can be found, e.g., in Ref. [189]. It is more convenient to express the chiral symmetry in terms of vector

[13] For example, the Kugo–Ojima confinement scenario [185] relies on an unbroken BRST charge.

(V) and axial-vector (A) transformations according to[14]

$$\mathrm{U}(N_\mathrm{f})_\mathrm{L} \times \mathrm{U}(N_\mathrm{f})_\mathrm{R} \simeq \mathrm{SU}(N_\mathrm{f})_\mathrm{V} \times \mathrm{U}(1)_\mathrm{V} \times \mathrm{SU}(N_\mathrm{f})_\mathrm{A} \times \mathrm{U}(1)_\mathrm{A}\,. \tag{2.21}$$

However, not all of these symmetries are (exactly) realized in the real world, partially due to the fact that the quarks are not massless. The $\mathrm{U}(1)_\mathrm{V}$ symmetry is the only exact symmetry of QCD and corresponds to the conservation of the baryon number in strong-interaction processes. The conserved Noether current reads $j_\nu = \bar{\psi}\gamma_\nu\psi$ with $\partial_\nu j_\nu = 0$.

Regarding $\mathrm{SU}(N_\mathrm{f})_\mathrm{V}$, from Noether's theorem we find the vector current $j^a_\nu = \bar{\psi}\gamma_\nu\tau^a\psi$. Its divergence is given by $\partial_\nu j^a_\nu = \bar{\psi}\,[\tau^a, \hat{m}]\,\psi$, and we see that the current is conserved as long as all quarks are mass degenerate, i.e., $\hat{m} \propto \mathbb{1}$. However, due to the very small mass difference between up and down quarks, $\mathrm{SU}(N_\mathrm{f})_\mathrm{V}$ is almost realized in the light $N_\mathrm{f} = 2$ sector of QCD and describes isospin symmetry. Even taking the heavier strange quark into account, $\mathrm{SU}(N_\mathrm{f} = 3)_\mathrm{V}$ can still be regarded as an approximate symmetry because the masses of up, down, and strange quarks are still smaller than the characteristic scale Λ_QCD of the strong interaction: $m_\mathrm{u} \approx m_\mathrm{d} \ll m_\mathrm{s} < \Lambda_\mathrm{QCD} = 200\text{–}300\,\mathrm{MeV}$. This is reflected, e.g., in pion and kaon masses that are in the same ballpark compared to the typical hadronic scale of one GeV. Furthermore, the low-lying hadron spectrum can be successfully deduced based on an $\mathrm{SU}(N_\mathrm{f} = 3)_\mathrm{V}$ symmetry [190, 191].

The $\mathrm{SU}(N_\mathrm{f})_\mathrm{A}$-related axial-vector current reads $j^a_{5,\nu} = \bar{\psi}\gamma_\nu\gamma_5\tau^a\psi$ with divergence $\partial_\nu j^a_{5,\nu} = \bar{\psi}\gamma_5\{\tau^a, \hat{m}\}\psi$. Thus, the current is explicitly broken as soon as $\hat{m} \neq \mathbb{0}$. Since the explicit breaking due to the quark masses is rather weak, at least in the two- and three-flavor sector, one would expect $\mathrm{SU}(N_\mathrm{f})_\mathrm{A}$ to be approximately realized. Therefore, one should find nearly-degenerate parity partners in the low-lying hadron spectrum. However, this is not observed in nature: the apparent isovector-vector and isovector-axial-vector partners ρ and a_1 differ in mass by about 460 MeV [192]. The solution of this puzzle is that QCD exhibits a feature called dynamical mass generation. In addition to their bare mass, quarks acquire a large dynamical mass of several hundred MeV—even in the chiral limit—due to the strong quark-gluon interaction. In other words, $\mathrm{SU}(N_\mathrm{f})_\mathrm{A}$ is dynamically broken, and we call this (in a slight abuse of notation) dynamical chiral symmetry breaking (DCSB). This also explains a proton mass of the order of one GeV even though the proton's constituents are only two up quarks and one down quark.[15] The pseudo-Nambu–Goldstone bosons in three-flavor QCD are the three pions, the four kaons, and the η meson. At this point, it is worth to emphasize that DCSB is an inherently nonperturbative phenomenon and appropriate tools are needed to explore it. One is the framework employed in this

[14] Rigorously, the isomorphism relation reads $\mathrm{U}(n) \simeq (\mathrm{SU}(n) \times \mathrm{U}(1))\,/\,\mathbb{Z}_n$, but we ignore this mathematical subtlety here.

[15] The large nucleon mass as a result of dynamical symmetry breaking was already proposed in the pre-QCD era by Nambu and Jona-Lasinio in the early 1960s [59, 60].

work, the DSEs. DCSB manifests in the nonvanishing vacuum expectation value of the composite operator $\bar{\psi}\psi$, the so-called quark condensate $\langle\bar{\psi}\psi\rangle = \langle\bar{\psi}_{\mathrm{L}}\psi_{\mathrm{R}} + \bar{\psi}_{\mathrm{R}}\psi_{\mathrm{L}}\rangle$. In general,

$$\langle\bar{\psi}\psi\rangle \begin{cases} = 0 & \text{if chiral symmetry is exactly realized}\,, \\ \neq 0 & \text{if chiral symmetry is broken}\,, \end{cases} \tag{2.22}$$

and the magnitude of the quark condensate is a measure for the extent of chiral symmetry breaking. For massless up and down quarks, $m_{\mathrm{u}}, m_{\mathrm{d}} \to 0$, the numerical value of the up- and down-quark condensates in vacuum is $\langle\bar{u}u\rangle = \langle\bar{d}d\rangle \approx -(250\,\mathrm{MeV})^3$ [193–195],[16] i.e., chiral symmetry is indeed dynamically broken. The quark condensate is a well-suited and widely employed order parameter for the breaking/restoration of chiral symmetry. In particular, monitoring its temperature and chemical-potential dependence allows one to draw the chiral phase diagram of QCD—the latter being the central object this work revolves around. Some more details on the calculation of $\langle\bar{\psi}\psi\rangle$ are given in Section 2.5.

Last, the $\mathrm{U}(1)_{\mathrm{A}}$ symmetry. It is anomalously broken because the path-integral measure is not invariant under $\mathrm{U}(1)_{\mathrm{A}}$ transformations [196, 197]. Tightly connected to that is the presence of instantons, regular solutions of the classical equations of motions minimizing the action [198], that induce additional effective $2N_{\mathrm{f}}$-quark interactions that break the $\mathrm{U}(1)_{\mathrm{A}}$ symmetry explicitly on the quantum level [199–201]. The relatively large η' mass of 958 MeV compared to the η with a mass of 548 MeV [192] indicates that the former is not a pseudo-Nambu–Goldstone boson, and $\mathrm{U}(1)_{\mathrm{A}}$ is thus not dynamically broken.

In order to summarize the flavor symmetries of QCD, the breaking patterns in the case of three quark flavors are graphically depicted in Fig. 2.1.

Discrete symmetries

Finally, the QCD action is invariant under charge conjugation (C), parity (P), and time reversal, which are discrete symmetries. In writing down the Lagrangian, we omitted the so-called θ term, which is given by

$$\mathcal{L}_\theta = \frac{N_{\mathrm{f}} g^2}{64\pi^2}\,\theta\,\varepsilon_{\nu\sigma\nu'\sigma'} F^a_{\nu\sigma} F^a_{\nu'\sigma'}\,. \tag{2.23}$$

It is CP violating but otherwise compatible with other symmetries and constraints. The θ parameter can be related to the electric dipole moment of the neutron, and from experimental results follows the upper bound $\theta \lesssim 10^{-9}$ [202, 203]. The question why θ

[16] The numerical value is to be understood within the modified minimal subtraction ($\overline{\mathrm{MS}}$) scheme at the customary renormalization scale of 2 GeV.

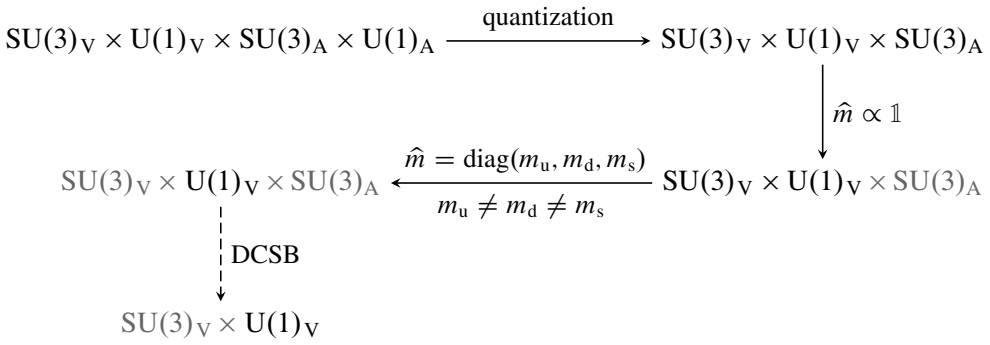

Figure 2.1 Global flavor symmetries and their successive breaking in three-flavor QCD starting from the classical theory in the chiral limit (upper left). A solid (dashed) arrow indicates that the breaking is explicit (dynamical). Symmetries shown grayed out are in principle broken but to an extent such that they can still be regarded as approximately fulfilled.

is so small is commonly known as the strong CP problem. The discussion of this issue lies outside the topic of this work, and we refer the reader, e.g., to Refs. [204–206] and references therein.

2.3 Functional relations and DSEs

Having collected and summarized aspects of QCD that are relevant for this work, we now focus on functional relations and further discuss the DSEs, which can be seen as the equations of motions for correlation functions. With the sources already collected in a tuple, $J = (\bar{\eta}_\alpha, \eta_\alpha, j_\nu^a, \tilde{\sigma}^a, \sigma^a)$, we do the same with the fields, viz., $\phi = (\psi_\alpha, \bar{\psi}_\alpha, A_\mu^a, c^a, \tilde{c}^a)$ for the sake of brevity. The most important objects of any field theory are correlation functions—normalized expectation values of an arbitrary number of fields. They are all encoded in the generating functional, Eq. (2.14), and obtained via functional differentiation with respect to the sources. Thus, a generic n-point correlation function, $n \geq 1$, in the presence of sources is given by

$$\begin{aligned} \langle \phi_{i_1}(x_{i_1}) \dots \phi_{i_n}(x_{i_n}) \rangle^{(J)} &= \frac{\int \mathcal{D}\phi \, \phi_{i_1}(x_{i_1}) \dots \phi_{i_n}(x_{i_n}) \, \mathrm{e}^{-I_{\mathrm{QCD}}^{\mathrm{gf}} + I_J}}{\int \mathcal{D}\phi \, \mathrm{e}^{-I_{\mathrm{QCD}}^{\mathrm{gf}} + I_J}} \\ &= \frac{1}{\mathcal{Z}[J]} \frac{\delta^n \mathcal{Z}[J]}{\delta J_{i_1}(x_{i_1}) \dots \delta J_{i_n}(x_{i_n})} , \end{aligned} \tag{2.24}$$

and the physical correlation function is obtained for vanishing sources, $J = 0$. In order to avoid cumbersome minus signs due to the exchange of anticommuting Grassmann-valued

quantities, we use left and right derivatives, i.e.,

$$\frac{\delta}{\delta J_i} \equiv \begin{cases} \dfrac{\overrightarrow{\delta}}{\delta J_i} & \text{if } J_i \in \{\overline{\eta}_\alpha, j_\nu^a, \widetilde{\sigma}^a\}\,, \\ \dfrac{\overleftarrow{\delta}}{\delta J_i} & \text{if } J_i \in \{\eta_\alpha, \sigma^a\}\,, \end{cases} \tag{2.25}$$

and analogously for derivatives $\delta/\delta\phi_i$ with respect to the fields. The correlation functions (2.24) contain a redundancy in the sense that they can be decomposed into connected and disconnected parts. The latter do not contribute to the scattering matrix. Thus, one is usually only interested in the former and we define

$$W[J] = \log \mathcal{Z}[J] \tag{2.26}$$

that is the generating functional for connected correlation functions. The simplest case are the macroscopic fields Φ_i that are one-point correlation functions, i.e., expectation values of single fields in the presence of sources:

$$\Phi_i(x) = \langle \phi_i(x) \rangle^{(J)} = \frac{1}{\mathcal{Z}[J]} \frac{\delta \mathcal{Z}[J]}{\delta J_i(x)} = \frac{\delta W[J]}{\delta J_i(x)}\,. \tag{2.27}$$

For example, $\Psi_\alpha(x) = \langle \psi_\alpha(x) \rangle^{(J)}$ and $\mathcal{A}_\nu^a(x) = \langle A_\nu^a(x) \rangle^{(J)}$ are the macroscopic quark and gluon fields, respectively.

The connected correlations functions are free of disconnected contributions but still contain parts that are disconnected upon cutting one internal line. It turns out that the connected correlation functions can be build solely from contributions that are not disconnected after cutting one internal line. This is called one-particle irreducible (1PI), and the corresponding generating functional is the 1PI effective action, Γ_{1PI}, which allows, loosely speaking, for an even more efficient way to store information than using W. Note that one can also define functionals that generate correlation functions that are not disconnected if more than one internal line is cut. This leads to the framework of nPI techniques, see, e.g., Refs. [207–213]. The 1PI effective action is the Legendre transform of W with the macroscopic fields (2.27) as the new variables:[17]

$$\Gamma_{\text{1PI}}[\Phi] = -W[J] + \int_x J_i(x)\,\Phi_i(x)\,. \tag{2.28}$$

[17] The summation $J_i\,\Phi_i$ is understood to yield a well-defined scalar expression in the sense that the ordering of sources and fields is correct, i.e., $J_i\,\Phi_i = \overline{\eta}_\alpha \Psi_\alpha + \overline{\Psi}_\alpha \eta_\alpha + \ldots$ in Eq. (2.28).

The sources are obtained by the inversion of Eq. (2.27), $J = J[\Phi]$, for a given macroscopic field Φ. Furthermore, $\delta\Gamma_{1\mathrm{PI}}/\delta\Phi_i = J_i$, which are the quantum equations of motions that govern the dynamics of the macroscopic fields. Moreover, in the limit of vanishing sources, their solutions describe the stable ground state of the theory.

The central quantities in this work are the propagators, i.e., the physical connected two-point functions. In particular, the quark and gluon propagators

$$S_{\alpha\beta}(x,y) = \left\langle \psi_\alpha(x)\,\bar{\psi}_\beta(y)\right\rangle_{\mathrm{conn}}^{(J=0)}, \tag{2.29}$$

$$D^{ab}_{\nu\sigma}(x,y) = \left\langle A^a_\nu(x)\,A^b_\sigma(y)\right\rangle_{\mathrm{conn}}^{(J=0)}. \tag{2.30}$$

Since the expectation values are calculated based on Eq. (2.24), these propagators are fully dressed—they contain all possible quantum fluctuations of QCD and are consequently nonperturbative objects. Both can be obtained either from W or $\Gamma_{1\mathrm{PI}}$ according to

$$S_{\alpha\beta}(x,y) = \frac{\delta^2 W[J]}{\delta\eta_\beta(y)\,\delta\bar{\eta}_\alpha(x)}\bigg|_{J=0} = \left(\frac{\delta^2\Gamma_{1\mathrm{PI}}[\Phi]}{\delta\Psi_\beta(y)\,\delta\bar{\Psi}_\alpha(x)}\right)^{-1}, \tag{2.31}$$

$$D^{ab}_{\nu\sigma}(x,y) = \frac{\delta^2 W[J]}{\delta j^b_\sigma(y)\,\delta j^a_\nu(x)}\bigg|_{J=0} = \left(\frac{\delta^2\Gamma_{1\mathrm{PI}}[\Phi]}{\delta\mathcal{A}^b_\sigma(y)\,\delta\mathcal{A}^a_\nu(x)}\right)^{-1}, \tag{2.32}$$

where the derivatives of the 1PI effective action have to be evaluated at the stationary point $\delta\Gamma_{1\mathrm{PI}}/\delta\Phi_i = 0$. The corresponding (inverse) bare propagators, known from perturbation theory, are obtained with $\Gamma_{1\mathrm{PI}} = I^{\mathrm{gf}}_{\mathrm{QCD}}$ for vanishing macroscopic fields, $\Phi = 0$. The inverse bare quark propagator reads

$$S^{-1}_{0,\alpha\beta}(x,y) = (\not{\partial} + m)_{\alpha\beta}\,\delta^{(4)}(x-y), \tag{2.33}$$

while the inverse bare gluon propagator is given by

$$\left[D^{ab}_{0,\nu\sigma}(x,y)\right]^{-1} = \delta_{ab}\left[-\delta_{\nu\sigma}\partial^2 + \left(1-\frac{1}{\xi}\right)\partial_\nu\partial_\sigma\right]\delta^{(4)}(x-y). \tag{2.34}$$

The higher-order n-point correlation functions, $n \geq 3$, are analogously obtained by n derivatives of a generating functional. However, by vertices we always mean 1PI correlation functions. For example, the quark-gluon vertex $\Gamma^a_{\nu,\alpha\beta}$ is the 1PI two-quark-one-gluon correlation function and defined by

$$g\Gamma^a_{\nu,\alpha\beta}(x,y,z) = \frac{\delta^3\Gamma_{1\mathrm{PI}}[\Phi]}{\delta\Psi_\beta(z)\,\delta\bar{\Psi}_\alpha(y)\,\delta\mathcal{A}^a_\nu(x)}. \tag{2.35}$$

It is related to the connected two-quark-one-gluon correlation function via

$$\begin{aligned}\left\langle A^a_\nu(x)\,\psi_\alpha(y)\,\bar{\psi}_\beta(z)\right\rangle^{(J=0)}_{\text{conn}} &= \left.\frac{\delta^3 W[J]}{\delta\eta_\beta(z)\,\delta\bar{\eta}_\alpha(y)\,\delta j^b_\nu(x)}\right|_{J=0} \\ &= \left.\frac{\delta}{\delta j^b_\nu(x)}\left(\frac{\delta^2\Gamma_{1\text{PI}}[\Phi]}{\delta\Psi_\beta(z)\,\delta\bar{\Psi}_\alpha(y)}\right)^{-1}\right|_{J=0} \\ &= -\int_{u,v,w} D^{ab}_{\nu\sigma}(x,u)\,S_{\alpha\delta}(y,v)\,g\Gamma^b_{\sigma,\delta\varepsilon}(u,v,w)\,S_{\varepsilon\beta}(w,z)\,.\end{aligned} \tag{2.36}$$

All connected correlation functions admit a similar decomposition into 1PI ones, but the resulting expressions become quickly quite involved [214–216]. These decompositions are frequently used in the derivation of DSEs, which we discuss soon. In terms of Feynman diagrams, Eq. (2.36) means that the connected two-quark-one-gluon correlation function is obtained from the quark-gluon vertex, i.e., the 1PI two-quark-one-gluon correlator, by attaching propagators to the external legs of the latter.

Now, we turn to the DSEs [76–79, 217–220]. They are the equations of motion for the correlations functions and based on the identity (see Appendix B)

$$0 = \int \mathcal{D}\phi\,\frac{\delta}{\delta\phi_i}\,\mathrm{e}^{-I^{\text{gf}}_{\text{QCD}}+I_J} \tag{2.37}$$

that can be rewritten to yield the master DSE

$$\frac{\delta\Gamma_{1\text{PI}}[\Phi]}{\delta\Phi_i} = \left.\frac{\delta I^{\text{gf}}_{\text{QCD}}}{\delta\phi_i}\right|_{\phi_k\to\Phi_k+\delta/\delta J_k} 1\,. \tag{2.38}$$

The DSE for every n-point correlation function can be derived from this equation without any approximation by means of the following procedure:[18]

(i) choose appropriate fields Φ_i and ϕ_i, and compute the first functional derivative of $I^{\text{gf}}_{\text{QCD}}$ explicitly. In the resulting expression, replace any remaining fields according to $\phi_k \to \Phi_k + \delta/\delta J_k$;

(ii) apply $n-1$ additional field derivatives to both sides of Eq. (2.38);

(iii) decompose higher connected n-point functions ($n \geq 3$) into vertices [see Eq. (2.36)];

(iv) set the sources to zero, which is equivalent to evaluate the macroscopic fields at their physical vacuum expectation value, and identify propagators and vertices.

[18] This procedure is well suited for an automated, algorithmic derivation of DSEs for any given action [221].

The resulting equation, the DSE for the n-point correlation function in question, is a self-consistent integral equation that depends on other and higher n-point functions. This is a salient feature all DSEs have in common. They thus form an infinite tower of coupled integral equations, which needs to be truncated to allow for a numerical treatment. Note that truncations, however, are not arbitrary but guided by preserving symmetries and keeping STIs and multiplicative renormalizability intact. We would like to emphasize that the infinite tower of DSEs describes QCD exactly. Thus, DSEs—even (reasonably) truncated ones—constitute a fully nonperturbative approach that is able to describe phenomena, like DCSB, that are beyond the reach of perturbation theory.

The quark DSE

Most important for this work is the DSE which solution is the renormalized dressed quark propagator.[19] Using the recipe given above and resolving the index structure, the DSE for the dressed quark propagator S_f for a flavor f in homogeneous space-time and Fourier transformed to momentum space reads (see Appendix C for details)

$$S_f^{-1}(p) = Z_2^f \left(\mathrm{i}\not{p} + Z_{m_f} m_f \right) + \Sigma_f(p) \tag{2.39}$$

with the self-energy

$$\Sigma_f(p) = g^2 C_2^{\mathrm{fund}} \frac{Z_2^f}{\tilde{Z}_3} \int\!\!\!\!\!\!\diagup_q D_{\nu\sigma}(k) \gamma_\nu S_f(q) \Gamma_\sigma^f(q,p) \,, \tag{2.40}$$

where $k = p - q$. There is a separate DSE each quark flavor f, and color degrees of freedom are removed by means of a color trace from which the second-order Casimir factor $C_2^{\mathrm{fund}} = (N_c^2 - 1)/2N_c$ in the fundamental representation of $\mathrm{SU}(N_c)_{\mathrm{color}}$ originates. For the sake of brevity, the Dirac structure is not resolved explicitly via indices.

The quark DSE (2.39), shown graphically in Fig. 2.2, is one of the central equations in this work. Again, we would like to emphasize that this equation is exact but depends on two other (unknown) correlation functions: the dressed gluon propagator $D_{\nu\sigma}$ and the dressed quark-gluon vertex Γ_σ^f (in its reduced form; see Eq. (A.23)), which obey their own DSEs. They are either known a priori or have to be determined in a self-consistent calculation of the coupled set of DSEs for the quark propagator, the gluon propagator, and the quark-gluon vertex. This again illustrates the infinite-tower nature of the DSEs, and our

[19] From now on, all quantities are understood to be renormalized ones. Thus, they carry an additional dependence on the renormalization point ζ, which we suppress for the sake of brevity, and are independent of the regularization scale Λ_{reg} that regularizes the divergent loop-momentum integrals.

Figure 2.2 Graphical representation of the quark DSE. Solid and curly lines denote quark and gluon propagators, respectively, and a large black dot indicates that the propagator is fully dressed. Dots at joints with more than two lines are vertices. A small black dot denotes a bare vertex, while a large gray dot is a fully dressed one (i.e., a 1PI correlation function). The Feynman diagrams in this work are created using JaxoDraw [222].

truncation to obtain a finite set of equations, which can be solved numerically, is detailed in the upcoming Section 3.1 of the next chapter.

The inverse dressed quark propagator is of the form

$$S_f^{-1}(p) = \mathrm{i}\not{p}\, A_f(p^2) + B_f(p^2)\,, \tag{2.41}$$

where the vector dressing function A_f and the scalar dressing function B_f contain all the nonperturbative information. Thus, they have a nontrivial momentum dependence, and the bare quark propagator is recovered for $A_f(p^2) = Z_2^f$ and $B_f(p^2) = Z_2^f Z_{m_f} m_f$. Inverting Eq. (2.41) in Dirac space yields

$$\begin{aligned} S_f(p) &= \frac{-\mathrm{i}\not{p}\, A_f(p^2) + B_f(p^2)}{p^2 A_f^2(p^2) + B_f^2(p^2)} \\ &= Z_f(p^2)\,\frac{-\mathrm{i}\not{p} + M_f(p^2)}{p^2 + M_f^2(p^2)}\,. \end{aligned} \tag{2.42}$$

Here, we introduced the quark wave function $Z_f(p^2) = 1/A_f(p^2)$ and mass function $M_f(p^2) = B_f(p^2)/A_f(p^2)$. The latter is renormalization-point independent[20] and its infrared value at $p^2 = 0$ can be interpreted as a constituent quark mass. Since the two Dirac tensor structures $\not{p}$ and $\mathbb{1}_{\mathrm{Dirac}}$ behave differently under chiral transformations—the former is invariant, while the latter is not—a nonzero scalar dressing function (or equivalently mass function) signals the breaking of chiral symmetry. With the parametrization of the dressed quark propagator in terms of dressing functions, the quark DSE translates into to a coupled set of self-consistent equations for the dressing functions. They are obtained by suitable projections in Dirac space and given by

$$A_f(p^2) = Z_2^f + \frac{1}{4\mathrm{i}p^2}\,\mathrm{Tr}\big[\not{p}\,\Sigma_f(p)\big] \tag{2.43}$$

[20] Provided the employed truncation preserves multiplicative renormalizability.

and

$$B_f(p^2) = Z_2^f Z_{m_f} m_f + \frac{1}{4}\,\mathrm{Tr}\big[\Sigma_f(p)\big]\,, \tag{2.44}$$

where the trace is taken in Dirac space. We refer the reader to Appendix D for details how we solve these equations in practice.

The gluon DSE

In Landau gauge, the (color-stripped) dressed gluon propagator is described by one dressing function $Z(k^2)$ and is of the form

$$D_{\nu\sigma}(k) = \mathcal{P}^{\mathrm{T}}_{\nu\sigma}(k)\,\frac{Z(k^2)}{k^2} \tag{2.45}$$

with the four-dimensional transverse projector

$$\mathcal{P}^{\mathrm{T}}_{\nu\sigma}(k) = \delta_{\nu\sigma} - \frac{k_\nu\,k_\sigma}{k^2}\,. \tag{2.46}$$

The corresponding DSE is shown diagrammatically in Fig. 2.3 and given by

$$D^{-1}_{\nu\sigma}(k) = Z_3\,D^{-1}_{0,\nu\sigma}(k) + \Pi^{\mathrm{YM}}_{\nu\sigma}(k) + \Pi_{\nu\sigma}(k)\,. \tag{2.47}$$

It contains the bare gluon propagator, obtained from the dressed propagator by setting $Z(k^2) = 1$, and two self-energies: the pure YM self-energy $\Pi^{\mathrm{YM}}_{\nu\sigma}$ contains all diagrams without explicit quark content, while $\Pi_{\nu\sigma}$ denotes the quark-loop contribution that couples the gluon dynamics to the matter sector.

Already in quenched QCD, i.e., pure YM theory without quarks, solving the gluon DSE numerically poses a nontrivial task due to the appearance of one- and two-loop diagrams and the additional dependence on three- and four-point functions; see the comprehensive review [90] and references therein for details and further reading. Therefore, and as described later, we do not calculate the YM diagrams explicitly but take unquenching effects triggered by the quark loop into account. We thus refrain from showing explicit expressions for $\Pi^{\mathrm{YM}}_{\nu\sigma}$, which can be found, e.g., in Ref. [78], while the quark-loop reads

$$\Pi_{\nu\sigma}(k) = -\frac{g^2}{2}\sum_f \frac{Z_2^f}{\widetilde{Z}_3}\int_q \mathrm{Tr}\big[\gamma_\nu\,S_f(p)\,\Gamma^f_\sigma(p,q)\,S_f(q)\big]\,, \tag{2.48}$$

where $p = q - k$, which defines the momentum routing of the loop, and the trace has to be evaluated in Dirac space. Analogously to the quark DSE, the gluon DSE boils down

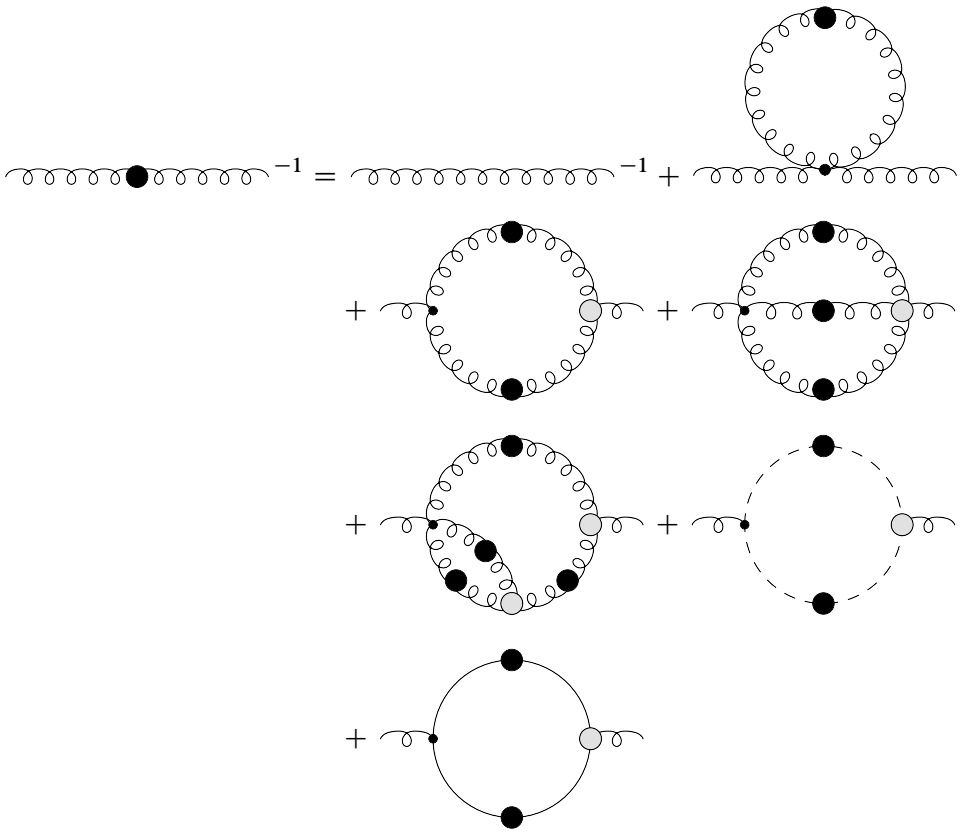

Figure 2.3 Graphical representation of the gluon DSE. Dashed lines denote ghosts, and the quark-loop diagram contains an implicit flavor sum. Signs and symmetry factors are implicit, too.

to a self-consistent equation for the dressing function: contracting Eq. (2.47) with the transverse projector yields

$$\frac{1}{Z(k^2)} = Z_3 + \frac{1}{3k^2}\,\mathcal{P}^{\mathrm{T}}_{\nu\sigma}(k)\left(\Pi^{\mathrm{YM}}_{\nu\sigma}(k) + \Pi_{\nu\sigma}(k)\right). \tag{2.49}$$

Finally, we would like to note that this equation needs further treatment before one can attempt solving it numerically because it is plagued by technical issues, see, e.g., Refs. [223, 224]. First, it turns out that the quark loop has a nonvanishing longitudinal component, $\mathcal{P}^{\mathrm{L}}_{\nu\sigma}(k)\,\Pi_{\nu\sigma}(k) \neq 0$ with the four-dimensional longitudinal projector $\mathcal{P}^{\mathrm{L}}_{\nu\sigma}(k) = k_\nu k_\sigma / k^2$, which seems to be at odds with the transversality of the gluon propagator in Landau gauge; see Ref. [225] for a recent study. Second, spurious quadratic divergences appear. Both issues need to be addressed properly, and details how this is accomplished in this work are given in Appendix D.

Detour: a short FRG overview

Since we later compare with results obtained from it, in the following we take a short detour and discuss another important functional method: the FRG [80–83]. It is based on Wilson's renormalization-group concept [226–229], where quantum fluctuations are integrated out step by step instead of all at once. One starts with the bare action at an ultraviolet cutoff scale Λ_{UV} and integrates out momentum shells starting from high-momentum (short-ranged) down to low-momentum (long-ranged) fluctuations. Technically, this is realized by introducing a momentum scale k that works as an effective infrared cutoff above which all fluctuations are integrated out, and the exponential in the generating functional is supplemented with a regulator term, $\mathrm{e}^{-I^{\mathrm{gf}}_{\mathrm{QCD}}+I_J} \to \mathrm{e}^{-I^{\mathrm{gf}}_{\mathrm{QCD}}-I^{\mathrm{reg}}_k+I_J}$, which makes the generating functional scale dependent. In momentum space, the regulator term is of the form $I^{\mathrm{reg}}_k[\phi] = \frac{1}{2}\int_q \phi_i(-q)R^{ij}_k(q)\phi_j(q)$ and can be seen as a momentum-dependent mass term for the fields. As a consequence, all quantities derived from the now scale-dependent generating functional inherit this dependence. In particular, the 1PI effective action becomes the so-called effective average action Γ_k. The regulator R_k implements the successive integration over momentum shells as explained above. It has to obey $\lim_{q^2/k^2\to 0} R_k(q) > 0$, $\lim_{k^2/q^2\to 0} R_k(q) = 0$, and $\lim_{k\to\Lambda_{\mathrm{UV}}} R_k(q) \to \infty$. Thus, in the momentum-scale region $0 < k < \Lambda_{\mathrm{UV}}$, R_k suppresses all fluctuations below k while the ones above are left unchanged. This guarantees that $\lim_{k\to\Lambda_{\mathrm{UV}}}\Gamma_k = I^{\mathrm{gf}}_{\mathrm{QCD}}$ and $\lim_{k\to 0}\Gamma_k = \Gamma_{1\mathrm{PI}}$, i.e., the effective average action interpolates between the bare action in the ultraviolet and the full quantum effective action in the infrared. The evolution of the effective average action is governed by the nonperturbative flow equation [230–232] (in compact matrix notation)

$$\frac{\partial\Gamma_k[\Phi]}{\partial k} = \frac{1}{2}\,\mathrm{Tr}\left[\left(\Gamma''_k[\Phi] + R_k\right)^{-1}\frac{\partial R_k}{\partial k}\right], \tag{2.50}$$

where $\Gamma''_k[\Phi]_{ij} = \delta^2\Gamma_k / \delta\Phi_i\delta\Phi_j$, and the trace has to be taken in momentum, color, flavor, Dirac, and field space, where minus signs are included for the fermionic subspace of the latter. The functional integro-differential equation (2.50) is the central pillar of the FRG approach and solving it is the eventual aim of every FRG study. A more detailed discussion is beyond the scope of this work, and we refer the reader to the cited literature and references therein.

From Eq. (2.50) follows that the flow equation for Γ_k itself and all derived ones are of one-loop structure, which is technically convenient. However, the flow for an n-point function contains dressed vertices up to order $n+2$. For example, the flow equation for the quark propagator contains diagrams involving the quark-quark, quark-gluon, and quark-ghost scattering kernels, which are four-point functions. In contrast to that, the self-energy

of the quark DSE is one single one-loop diagram. On the other hand, renormalization comes along automatically in the FRG approach thanks to the regulator term, i.e., all appearing integrals are by default ultraviolet finite. Finally, solving an FRG flow equation necessitates the calculation of scale-dependent loop integrals at different scales k and subsequently solving the differential equation with respect to k. This further increases the numerical complexity compared to DSEs, which are integral equations only.

2.4 Nonzero temperature and density

Up to this point, we discussed QCD in vacuum. Since we started in Euclidean space-time right from the beginning, the transition to QCD at nonzero temperature $T > 0$ and in thermal equilibrium is rather straightforward by means of the Matsubara (imaginary-time) formalism [108, 233, 234]. The integration in Euclidean-time direction is restricted to the compact interval $[0, 1/T]$, and with appropriate boundary conditions for the fields, the partition function (2.5) is simply the path-integral representation of the (canonical) partition function $\mathcal{Z} = \operatorname{Tr} \mathrm{e}^{-H/T}$ known from statistical mechanics, where H is the Hamiltonian of the system. Being fermions, quarks obey antiperiodic boundary conditions, i.e., $\psi(0, \boldsymbol{x}) = -\psi(1/T, \boldsymbol{x})$, while periodic boundary conditions hold for gluons and ghosts, $A^a_\mu(0, \boldsymbol{x}) = A^a_\mu(1/T, \boldsymbol{x})$ and $c^a(0, \boldsymbol{x}) = c^a(1/T, \boldsymbol{x})$. As a consequence of the compactification of the time-integration interval, the continuous integration with respect to the energy component in momentum space is replaced by a sum over discrete frequencies,

$$\fint_p h(p) \to T \sum_{\ell_p \in \mathbb{Z}} \int_{\boldsymbol{p}} h(p = (\omega_p, \boldsymbol{p})) \,. \tag{2.51}$$

Depending on the boundary condition, these so-called Matsubara frequencies are odd or even multiples of πT: we have $\omega_p = (2\ell_p + 1)\pi T$ if h obeys antiperiodic boundary conditions and $\omega_p = 2\ell_p \pi T$ if h obeys periodic boundary conditions, where $\ell_p \in \mathbb{Z}$.[21]

From (2.51) follows that the energy and vector components of the momentum are not treated on equal footing anymore—in contrast to the vacuum. Thus, the Euclidean O(4) symmetry in vacuum is explicitly broken to O(3) in the medium, i.e., the Matsubara formalism is noncovariant. Phrased differently, with the introduction of nonzero temperature via the Matsubara formalism, one chooses a specific reference frame: to wit, the rest frame of the heat bath that is constituted by all particles of the system. In that frame, the heat bath is static and equilibrated. The reduced symmetry alters the tensor structure of all propagators and vertices. In a general frame characterized by its normalized four-velocity

[21] Ghosts are Grassmann-valued quantities, but their propagator is bosonic. They thus obey periodic boundary conditions, and their Matsubara frequencies are even, like those for the gluons.

u, these quantities do not depend on external momenta alone but in addition on the four-velocity of the heat bath. For example, the inverse quark propagator is given by

$$\begin{aligned} S_f^{-1}(p;u) = {} & \mathrm{i}\not{u}\, u\cdot p\, C_f(w,\not{p}) + \mathrm{i}\left(\not{p} - \not{u}\, u\cdot p\right) A_f(w,\not{p}) \\ & + B_f(w,\not{p}) + \mathrm{i}\not{u}\, u\cdot p\left(\not{p} - \not{u}\, u\cdot p\right) D_f(w,\not{p})\,, \end{aligned} \tag{2.52}$$

where the dressing functions depend on the scalars $w = u\cdot p$ and $\not{p} = p^2 - w^2$. The latter can be interpreted as a generalized squared three-momentum. In vacuum, $w = 0$ and the quark propagator reduces to its vacuum form, Eq. (2.41), while in the rest frame of the heat bath, i.e., $u = (1,\mathbf{0})$, we get the familiar expression

$$S_f^{-1}(p) = \mathrm{i}\omega_p\gamma_4 C_f(p) + \mathrm{i}\boldsymbol{\gamma}\cdot\boldsymbol{p}\, A_f(p) + B_f(p) + \mathrm{i}\omega_p\gamma_4\boldsymbol{\gamma}\cdot\boldsymbol{p}\, D_f(p) \tag{2.53}$$

with momentum $p = (\omega_p, \boldsymbol{p})$ and $\omega_p = (2\ell_p + 1)\pi T$, $\ell_p \in \mathbb{Z}$. The dressing functions depend separately on ω_p and $\boldsymbol{p}^2$. However, for the sake of brevity, we simply write this as a dependence on p that has to be understood as $F(p) = F(\omega_p, \boldsymbol{p}^2)$, where $F \in \{C_f, A_f, B_f, D_f\}$. The symmetry breaking from O(4) to O(3) becomes apparent through that dependence, different dressing functions for the temporal and spatial tensor structures, $C_f \neq A_f$, and the appearance of a contribution corresponding to $\gamma_4\boldsymbol{\gamma}\cdot\boldsymbol{p}$. The dressing function associated with the latter vanishes in vacuum, chirally-symmetric phases, rainbow-ladder truncations, and perturbation theory. When nonzero, D_f is small in magnitude and its influence on the other dressing functions is quantitatively negligible [235, 236]. We thus set $D_f = 0$ throughout this work.

Since we aim to investigate QCD not only at nonzero temperature but also at nonzero density, we have to describe the system grand canonically. To this end, the quark chemical potential μ_f is added to the action as a Lagrange multiplier for the net quark density n_f,

$$I_{\mathrm{QCD}}^{\mathrm{gf}} \to I_{\mathrm{QCD}}^{\mathrm{gf}} - \sum_f \mu_f\, n_f\,, \tag{2.54}$$

where the net quark density is given by

$$n_f = \int_0^{1/T} \mathrm{d}x_4 \int_{\boldsymbol{x}} \psi_f^\dagger \psi_f\,. \tag{2.55}$$

The quark chemical potential can be absorbed into the quark's kinetic part of the Lagrangian. With $\psi^\dagger\psi = \bar{\psi}\gamma_4\psi$, we can write

$$I_{\mathrm{QCD}}^{\mathrm{gf}} - \sum_f \mu_f\, n_f = \int_0^{1/T} \mathrm{d}x_4 \int_{\boldsymbol{x}} \bar{\psi}_\alpha(\not{\partial} + \hat{m} - \hat{\mu}\,\gamma_4)_{\alpha\beta}\psi_\beta + \ldots\,, \tag{2.56}$$

where $\widehat{\mu} = \mathrm{diag}_{\mathrm{flavor}}(\mu_\mathrm{u}, \mu_\mathrm{d}, \mu_\mathrm{s}, \dots)$ contains the chemical potentials for the different quark flavors. It thus follows that the Matsubara frequencies of the quark are modified according to $\omega_p \to \omega_p + \mathrm{i}\mu_f$, and the dressing functions become chemical-potential dependent.[22] Furthermore, they are complex valued at $\mu_f \neq 0$ and real valued only at vanishing quark chemical potential.

In summary, we use the inverse dressed in-medium quark propagator

$$S_f^{-1}(p) = \mathrm{i}(\omega_p + \mathrm{i}\mu_f)\gamma_4 C_f(p) + \mathrm{i}\boldsymbol{\gamma}\cdot\boldsymbol{p}\, A_f(p) + B_f(p) \tag{2.57}$$

that is the solution of the DSE

$$S_f^{-1}(p) = Z_2^f\left(\mathrm{i}(\omega_p + \mathrm{i}\mu_f)\gamma_4 + \mathrm{i}\boldsymbol{\gamma}\cdot\boldsymbol{p} + Z_{m_f} m_f\right) + \Sigma_f(p)\,. \tag{2.58}$$

The in-medium self-energy looks not much different than in vacuum. With the changes induced by nonzero temperature and quark chemical potential, it is given by

$$\Sigma_f(p) = g^2 C_2^{\mathrm{fund}} \frac{Z_2^f}{\widetilde{Z}_3} T \sum_{\ell_q\in\mathbb{Z}} \!\!\!\!\!\!\int_{\boldsymbol{q}} D_{\nu\sigma}(k)\gamma_\nu S_f(q)\Gamma_\sigma^f(q,p)\,, \tag{2.59}$$

where $q = (\omega_q, \boldsymbol{q})$ with $\omega_q = (2\ell_q + 1)\pi T$ is the internal quark momentum. We use the same momentum routing as in the vacuum, $k = p - q = (\omega_p - \omega_q, \boldsymbol{p} - \boldsymbol{q})$. In writing down the in-medium quark DSE (2.58), we chose to take the renormalization constants from the vacuum since neither nonzero temperature nor quark chemical potential introduce new divergences. All occurring divergences are already present in the vacuum [108]. Finally, the self-consistent equations for the three dressing functions read

$$C_f(p) = Z_2^f + \frac{1}{4\mathrm{i}(\omega_p + \mathrm{i}\mu_f)}\mathrm{Tr}\big[\gamma_4\Sigma_f(p)\big]\,, \tag{2.60}$$

$$A_f(p) = Z_2^f + \frac{1}{4\mathrm{i}\boldsymbol{p}^2}\mathrm{Tr}\big[\boldsymbol{\gamma}\cdot\boldsymbol{p}\,\Sigma_f(p)\big]\,, \tag{2.61}$$

$$B_f(p) = Z_2^f Z_{m_f} m_f + \frac{1}{4}\mathrm{Tr}\big[\Sigma_f(p)\big]\,. \tag{2.62}$$

The medium alters the structure of the Landau gauge gluon propagator, too. It splits into two parts: the magnetic contribution that is transversal ($\perp$) and the electric contribution

[22] In full glory: $S_f^{-1} = S_f^{-1}(\omega_p, \boldsymbol{p}, \mu_f; \{\mu_{f'} : f' \neq f\})$ and $F = F(\omega_p, \boldsymbol{p}^2, \mu_f; \{\mu_{f'} : f' \neq f\})$ with $F \in \{C_f, A_f, B_f\}$. The implicit dependence on all other quark chemical potentials stems from the quark-loop diagrams in the gluon DSE, see Fig. 2.3. However, for the sake of brevity, we suppress all chemical-potential dependencies of propagators and vertices.

that is longitudinal ($\parallel$) with respect to the direction of the heat-bath vector $u = (1, \mathbf{0})$. With $k = (\omega_k, \boldsymbol{k})$, $\omega_k = 2\ell_k \pi T$, the dressed in-medium gluon propagator is therefore of the form

$$D_{\nu\sigma}(k) = \mathcal{P}^{\perp}_{\nu\sigma}(k)\,\frac{Z_{\perp}(k)}{k^2} + \mathcal{P}^{\parallel}_{\nu\sigma}(k)\,\frac{Z_{\parallel}(k)}{k^2} \tag{2.63}$$

with the two projectors

$$\mathcal{P}^{\perp}_{\nu\sigma}(k) = (1-\delta_{\nu 4})(1-\delta_{\sigma 4})\left(\delta_{\nu\sigma} - \frac{k_\nu k_\sigma}{\boldsymbol{k}^2}\right), \tag{2.64}$$

$$\mathcal{P}^{\parallel}_{\nu\sigma}(k) = \mathcal{P}^{\mathrm{T}}_{\nu\sigma}(k) - \mathcal{P}^{\perp}_{\nu\sigma}(k)\,, \tag{2.65}$$

where $\mathcal{P}^{\mathrm{T}}_{\nu\sigma}(k)$ is the four-dimensional transverse projector, see Eq. (2.46). The magnetic and electric dressing functions $Z_{\perp}$ and $Z_{\parallel}$, respectively, are unequal due to the effects of nonzero temperature and/or quark chemical potential. They become degenerate in the vacuum limit so that we recover the vacuum gluon propagator, Eq. (2.45). Analogous to the quark dressing functions, $Z_{\perp,\parallel}(k) = Z_{\perp,\parallel}(\omega_k, \boldsymbol{k}^2)$. Note that the in-medium gluon propagator is still transverse with respect to its four-momentum—as it should be in Landau gauge—because the magnetic and electric projectors are four-dimensionally transverse, i.e., $k_\nu\,\mathcal{P}^{\perp}_{\nu\sigma}(k) = k_\nu\,\mathcal{P}^{\parallel}_{\nu\sigma}(k) = 0$. The self-consistent equations for the magnetic and electric dressing functions read

$$\frac{1}{Z_{\perp}(k)} = Z_3 + \frac{1}{2k^2}\,\mathcal{P}^{\perp}_{\nu\sigma}(k)\left(\Pi^{\mathrm{YM}}_{\nu\sigma}(k) + \Pi_{\nu\sigma}(k)\right), \tag{2.66}$$

$$\frac{1}{Z_{\parallel}(k)} = Z_3 + \frac{1}{k^2}\,\mathcal{P}^{\parallel}_{\nu\sigma}(k)\left(\Pi^{\mathrm{YM}}_{\nu\sigma}(k) + \Pi_{\nu\sigma}(k)\right), \tag{2.67}$$

and are obtained by contracting the in-medium gluon DSE, which takes the same form as in vacuum, Eq. (2.47), but with the necessary changes due to nonzero temperature and/or quark chemical potential, with the corresponding magnetic and electric projectors.

2.5 Phases of QCD

Even though we already touched upon the phase diagram of QCD in the introduction, we now come back to it in this last section of our chapter on the theoretical framework of this work and recapitulate some of its aspects. In general, different phases of matter are categorized by their physical properties under certain thermodynamical circumstances described by, e.g., temperature and density. In this work, we are interested in the chiral phase diagram of QCD, i.e., the phase structure of strong-interaction matter determined by

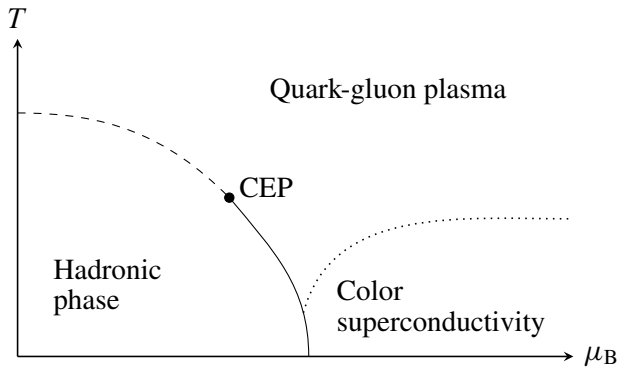

Figure 2.4 Sketch of the QCD phase diagram as obtained from numerous studies within the functional methods of DSEs and the FRG.

whether chiral symmetry is dynamically broken or restored.[23] A contemporary sketch of the QCD phase diagram in terms of temperature and baryon chemical potential obtained from the functional frameworks of DSEs and the FRG—see Refs. [98, 101, 236–249] for selected works—is shown in Fig. 2.4. At low temperatures and densities, chiral symmetry is dynamically broken. Quarks acquire a huge amount of dynamical mass and are confined into hadrons, which are the relevant degrees of freedom in this region of the phase diagram. Staying at low chemical potential, the hadronic phase is connected via an analytic crossover (dashed line) to the deconfined high-temperature phase of the quark-gluon plasma with (partially) restored chiral symmetry. These findings are in perfect agreement with results from first-principles lattice-QCD calculations [52–56] and by now well-established and, without dispute, a solid cornerstone of our understanding of the phase diagram of QCD. At low to moderate temperatures but high chemical potentials, a first-order transition takes place (solid line) that consequently meets the crossover line at a second-order CEP (black circle). For even higher chemical potentials and temperatures (well) below the CEP, color-superconducting phases are present. Their phase boundary with the quark-gluon plasma (dotted line) is either of first or second order, which depends on the details how color superconductivity is realized [242, 246]. Not shown is the possible emergence of inhomogeneous phases in the first-order region of the phase diagram [243].

In this work, we are concerned with the crossover region up to the CEP. In order to distinguish the different phases and locate the crossover line and CEP, we need an order parameter that measures to which extent chiral symmetry is dynamically broken or restored. For example, suitable chiral order parameters are the scalar quark dressing function (e.g., for the zeroth Matsubara frequency and at vanishing three-momentum) or

[23] From now on, the term “phase diagram” always refers to the chiral phase diagram of QCD.

the quark condensate. Usually, the latter is the chiral order parameter of choice and we employ it, too. For a quark flavor f, the quark condensate $\langle\bar{\psi}\psi\rangle_f$ is obtained from the corresponding propagator according to

$$\langle\bar{\psi}\psi\rangle_f = -N_\mathrm{c}\, Z_2^f Z_{m_f} T \sum_{\ell_q\in\mathbb{Z}} \fint_{\boldsymbol{q}} \mathrm{Tr}\big[S_f(q)\big]\,, \tag{2.68}$$

where the factor of N_c stems from the color trace, and the remaining trace is evaluated in Dirac space. The respective vacuum expression of Eq. (2.68) is obvious. Unfortunately, the quark condensate is only well defined in the chiral limit and plagued by a quadratic divergence for all flavors with a nonvanishing quark mass. Therefore, it needs to be regularized in order to get a finite expression. Since the quadratic divergence contained in the condensate is of the form $m_f\Lambda_\mathrm{reg}^2$ with the regularization scale (cutoff) Λ_reg of the summation and integration in Eq. (2.68), $q^2 = \omega_q^2 + \boldsymbol{q}^2 \leq \Lambda_\mathrm{reg}^2$, a well-defined, finite expression is given by the difference

$$\Delta_{f,f'} = \langle\bar{\psi}\psi\rangle_f - \frac{Z_{m_f}}{Z_{m_{f'}}}\frac{m_f}{m_{f'}}\langle\bar{\psi}\psi\rangle_{f'}\,, \tag{2.69}$$

which is known as the subtracted f-f' quark condensate. The divergent part of the f' condensate cancels the corresponding one of the f condensate when the former is multiplied by the corresponding mass ratio. Since the idea behind Eq. (2.69) is to remove only the quadratically-divergent component in $\langle\bar{\psi}\psi\rangle_f$, the subtraction should be carried out with $m_{f'} \gg m_f$.

As detailed in the next chapter, we work with $2+1$ quark flavors, i.e., with two degenerate light up/down quarks and a heavier strange quark. The latter is sufficiently heavier than the former such that the subtracted up-strange quark condensate delivers a clean, distinct signal of the chiral transition. We define the chiral transition temperature T_c by the inflection point of $\Delta_\mathrm{u,s}$ with respect to temperature through

$$T_\mathrm{c}(\{\mu_f\}) = \underset{T}{\mathrm{argmax}}\left|\frac{\partial\Delta_\mathrm{u,s}(T,\{\mu_f\})}{\partial T}\right|. \tag{2.70}$$

Note that T_c is only a pseudocritical temperature in the crossover region of the phase diagram because the crossover is not a true phase transition but connects the hadronic phase continuously and analytically with the quark-gluon plasma. Thus, no unique definition of T_c exists in case of a crossover and its definition varies in the literature. Another widely used definition is the maximum of the chiral susceptibility $\partial\langle\bar{\psi}\psi\rangle_\mathrm{u}/\partial m_\mathrm{u}$. All of these definitions, however, yield the same result at the CEP and beyond in the first-order region, i.e., for "true" phase transitions.

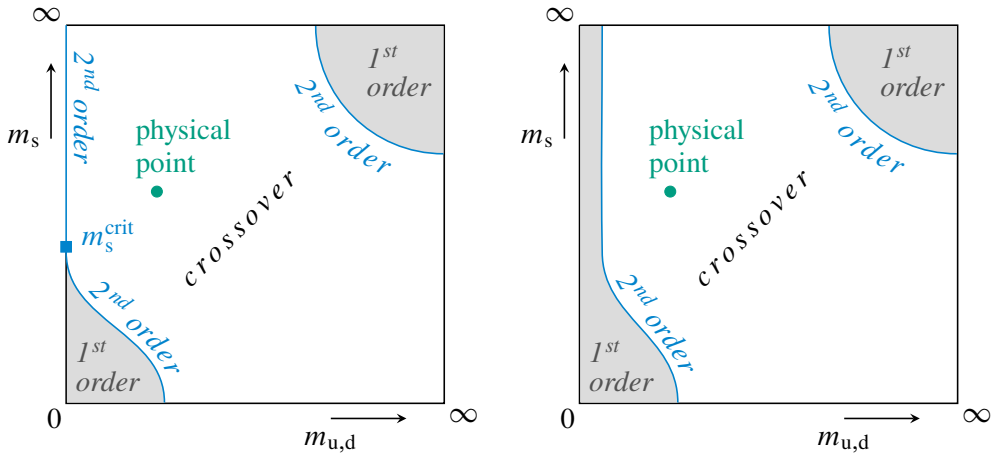

Figure 2.5 Left: Columbia plot at zero chemical potential with $U(1)_A$ broken at all temperatures. Right: Same as the left diagram but with restored $U(1)_A$ symmetry.

Strictly speaking, the phase diagram shown in Fig. 2.4 is only valid for physical quark masses, i.e., for masses which result in a hadron spectrum that is in agreement with the experimentally determined one. From a theoretical point of view, however, it is highly interesting to investigate nonphysical quark masses because then one probes both chiral and deconfinement aspects of QCD. For three flavors (with mass-degenerate up and down quarks, $m_u = m_d \equiv m_{u,d}$) and at vanishing chemical potential, the nature of the QCD transition at nonzero temperature as a function of the quark masses is depicted in the so-called Columbia plot [250], which is sketched in Fig. 2.5. In the limit of infinitely heavy quarks (upper right corner in both diagrams), we are dealing in fact with pure YM theory, and the observed transition is the first-order deconfinement transition of an $SU(N_c = 3)_{color}$ gauge theory [251].[24] Since the chiral transition is an analytic crossover for physical masses, it follows that, as the quark masses decrease from infinity, there is a second-order line that separates the first-order region from the crossover.

The transition of the chiral three-flavor theory (lower left corner in both diagrams) is expected to be of first order [253]. However, the fate of the anomalously broken $U(1)_A$ symmetry is expected to affect the chiral $SU(3)_A$ transition, resulting in two versions of the Columbia plot. If $U(1)_A$ gets restored with temperature, the transition in the chiral two-flavor theory (upper left corner in both diagrams) is conjectured to be of first order,

[24] The underlying symmetry, called center symmetry, is the invariance of YM theory under transformations associated with the center $\mathfrak{C} = \{\mathbb{1} \times e^{2\pi i n/N_c} : n = 0, \ldots, N_c - 1\}$ of $SU(N_c)_{color}$ [252]. A center transformation is a usual gauge transformation $A_\nu \to U[A_\nu - (i/g)\partial_\nu]U^{-1}$, $U \in SU(N_c)_{color}$, where $U(1/T, \boldsymbol{x}) = zU(0, \boldsymbol{x})$ with $z \in \mathfrak{C}$. Center symmetry is realized (broken) at low (high) temperatures, and the transition is of first order only for $N_c = 3$ and $3 + 1$ space-time dimensions.

too [253], and both corners are connected as shown of the right diagram of Fig. 2.5. On the other hand, if $U(1)_A$ is broken at all temperatures, the transition of the chiral two-flavor theory is conjectured to be of second order. This implies the existence of a tricritical strange-quark mass m_s^{crit}, yielding the situation as displayed in the left diagram of Fig. 2.5.

Finally, we would like to note that it is currently not clear which situation is realized in QCD. Furthermore, the relative size of the regions and the location of m_s^{crit} with respect to the physical point are still open questions. Since we do not investigate the structure of the Columbia plot in this work, we refer the reader to Ref. [79] for a more detailed discussion and further references. However, in Chapter 5 we exploit the fact that one arrives at pure YM theory for large enough quark masses.

3 QCD's phase diagram from quarks and gluons

With the theoretical basis provided by the preceding chapter, we now detail how the quark and gluon DSEs are truncated, discuss their solutions, and finally compute the QCD phase diagram using order parameters that are extracted from the propagators. Parts of these results are published in Ref. [98].

To reiterate once more, the quark and gluon DSEs are a coupled set of nonlinear integral equations that further depends on fully dressed vertices. For example, in order to solve the quark DSE for the dressed quark propagator, one needs the dressed gluon propagator and the dressed quark-gluon vertex; the gluon DSE is even more complex, see Fig. 2.3. Thus, truncations are inevitable to get a closed system of equations that can be solved numerically. We employ a well-studied truncation scheme that is detailed below. In short: input from lattice calculations for the pure YM part of the gluon DSE is used, unquenching effects are accounted for by explicit calculations of the quark-loop diagrams, and both is accompanied by an ansatz for the quark-gluon vertex that is motivated by an STI combined with perturbative considerations at large momenta. As a result, we have access to the dressed quark and unquenched gluon propagators at arbitrary temperature and chemical potential. This framework evolved from quenched calculations to $N_\mathrm{f} = 2$, $N_\mathrm{f} = 2 + 1$, and $N_\mathrm{f} = 2 + 1 + 1$ quark flavors [241, 244, 254–261], including forays into color-superconductive and inhomogeneous phases [242, 243, 246], bound-state calculations [101, 262, 263], and other gauge groups [236, 264]. A comprehensive review can be found in Ref. [79]. Even though our truncation and versions thereof are used in several theses [102, 235, 265–270], we shall explain it in some detail to keep this work self-contained to a reasonable degree. Thus, some overlap with these studies cannot be avoided.

3.1 Truncation scheme

The quark-gluon vertex

First, we specify our expression for the quark-gluon vertex, which appears both in the quark DSE and in the quark loop of the gluon DSE. The quark-gluon vertex DSE as shown in Fig. 3.1 depends on the quark and gluon propagators and on other vertices, too. Solving

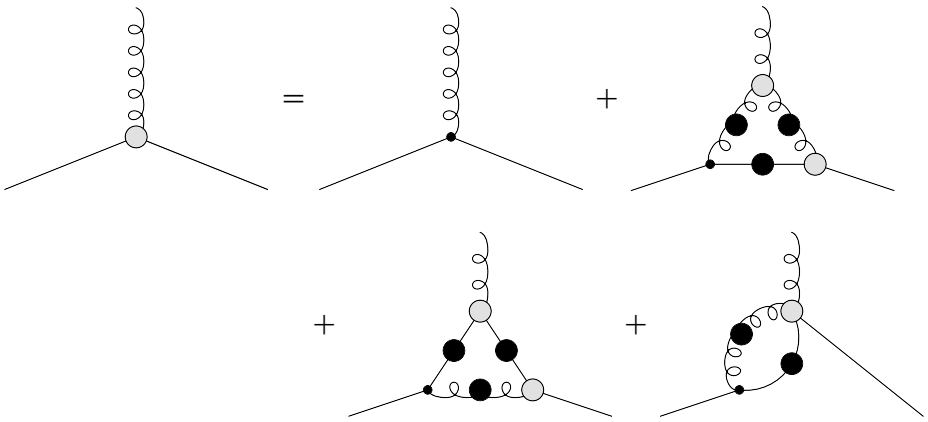

Figure 3.1 DSE for the quark-gluon vertex. In this version, it is always an external quark leg that is attached to the internal bare vertex. This stems from beginning with quark derivatives of the master DSE (2.38) followed by the gluon derivative. A different equation is obtained for the reverse order, which can be found, e.g., in Ref. [271].

it poses a rather challenging task because one has to keep in mind that changes of the quark-gluon vertex feed back into the quark and gluon DSEs and vice versa. Thus, in principle, the coupled system of the DSEs for the quark propagator, gluon propagator, and quark-gluon vertex must be solved self-consistently.

The complexity of the quark-gluon vertex becomes evident by considering its structure in Dirac space. In vacuum, we have one Lorentz index and the two independent quark momenta q (incoming) and p (outgoing). The incoming gluon momentum k is constrained by momentum conservation, $k = p - q$, and is thus a linear combination of the quark momenta. Therefore, the basis decomposition is in general given by

$$\left\{q_\nu, p_\nu, \gamma_\nu\right\} \times \left\{\mathbb{1}_{\text{Dirac}}, \not{q}, \not{p}, \not{q}\not{p}\right\}, \tag{3.1}$$

which results in twelve different tensor structures for the quark-gluon vertex, each accompanied with a dressing function that depends on q^2, p^2, and $p \cdot q$. Note that the basis (3.1) is not unique. For example, desired properties such as transversality with respect to the gluon momentum or invariance under charge conjugation would yield a different basis decomposition [272]. Vacuum results for (parts of) the vertex DSE can be found, e.g., in Refs. [271–278]; for corresponding FRG results, see Refs. [279, 280].[25] At nonzero temperature and density, the situation is even more complex due to the presence of the heat-bath vector u, and the number of tensor structures increases to thirty-two because the

[25] Lattice results for the quark-gluon vertex are rather scarce, and to our knowledge, continuum-extrapolated results at physical pion masses are not available yet. For a recent study, see Ref. [281].

basis now reads

$$\{q_\nu, p_\nu, \gamma_\nu, u_\nu\} \times \{\mathbb{1}_{\text{Dirac}}, \not{q}, \not{p}, \not{q}\not{p}, \not{u}, \not{q}\not{u}, \not{p}\not{u}, \not{q}\not{p}\not{u}\} \,. \tag{3.2}$$

Solving (parts of) the in-medium quark-gluon vertex DSE is thus even more challenging than in vacuum, and the available studies are still exploratory [268, 282]. A different yet complementary approach that allows to compute parts of the in-medium quark-gluon vertex is the recently proposed FRG-assisted difference-DSE method [248, 249], where medium effects are introduced by means of an expansion around FRG vacuum results.

Instead of taking the vertex DSE explicitly into account, we follow a simpler approach and employ an educated guess for the quark-gluon vertex. Our ansatz is based on an STI combined with perturbative considerations in the ultraviolet. The STI in question that is satisfied by the quark-gluon vertex is given by [103, 214]

$$\mathrm{i}k_\nu \Gamma^f_\nu(q,p) = G(k^2)\left[H_f(q,p)\, S_f^{-1}(p) - S_f^{-1}(q)\, \tilde{H}_f(q,p)\right], \tag{3.3}$$

where G is the ghost dressing function, and H_f, $\tilde{H}_f$ are related to the quark-ghost scattering kernel, i.e., they contain a four-point correlation function. While the nonperturbative behavior of the ghost is rather well-known both from functional methods and the lattice, see, e.g., Refs. [90, 158, 160, 283–285], a comprehensive nonperturbative study of H_f and $\tilde{H}_f$ is not available yet.[26] We thus resort to the Abelian version of Eq. (3.3), where $G = H_f = \tilde{H}_f = 1$,

$$\mathrm{i}k_\nu \Gamma^f_\nu(q,p) = S_f^{-1}(p) - S_f^{-1}(q) \,. \tag{3.4}$$

In vacuum, a "solution" of that Abelian STI, which is regular in the limit $k \to 0$, is provided by the Ball–Chiu vertex. It reads [287]

$$\begin{aligned}
\Gamma^{\text{BC}}_{\nu,f}(q,p) = {} & \frac{A_f(p^2) + A_f(q^2)}{2}\,\gamma_\nu \\
& + \frac{A_f(p^2) - A_f(q^2)}{2\,(p^2 - q^2)}\,(p_\nu + q_\nu)(\not{p} + \not{q}) \\
& + \frac{B_f(p^2) - B_f(q^2)}{\mathrm{i}\,(p^2 - q^2)}\,(p_\nu + q_\nu) \\
& + \text{transverse terms}\,,
\end{aligned} \tag{3.5}$$

where the transverse terms are transversal with respect to the gluon momentum, i.e., they vanish upon contraction with $k = p - q$, and are therefore not constrained by the STI.

[26] Recent results in that direction can be found, e.g., in Refs. [276, 286].

From Eq. (3.3), we can draw further information for our ansatz for the quark-gluon vertex. The ghost dressing function is almost temperature independent on a large temperature interval [256, 288–290], and the results of Refs. [276, 286] suggest that H_f and $\widetilde{H}_f$ are infrared enhanced. Furthermore, the ultraviolet behavior is fixed by perturbation theory. With this information in mind, we use the following model: the leading tensor structure of the Ball–Chiu vertex construction (3.5) is supplemented with a phenomenological, infrared-enhanced function $\Gamma(x)$ that accounts for missing non-Abelian contributions and effects of all other tensor structures of the full vertex. Here, x is a squared momentum, and its value depends on the location where the vertex is used. In terms of formulae, our ansatz for the quark-gluon vertex in vacuum reads

$$\frac{1}{\widetilde{Z}_3}\Gamma_\nu^f(q,p) = \Gamma(x)\,\frac{A_f(p^2)+A_f(q^2)}{2}\,\gamma_\nu\,, \tag{3.6}$$

and its in-medium generalization is given by

$$\begin{aligned}\frac{1}{\widetilde{Z}_3}\Gamma_\nu^f(q,p) = \Gamma(x)\Bigg(&\delta_{4\nu}\,\frac{C_f(p)+C_f(q)}{2}\\ &+(1-\delta_{4\nu})\,\frac{A_f(p)+A_f(q)}{2}\Bigg)\gamma_\nu\,.\end{aligned} \tag{3.7}$$

The phenomenological dressing function is the same in both cases and given by the expression

$$\Gamma(x) = \frac{d_1}{d_2+x} + \frac{1}{1+\Lambda^2/x}\left(\frac{\alpha_\mathrm{s}\beta_0}{4\pi}\log\left(1+x/\Lambda^2\right)\right)^{2\delta}\,, \tag{3.8}$$

which is a sum of an infrared-dominant and an ultraviolet-dominant term. The scales $d_2 = 0.5\,\mathrm{GeV}^2$, $\Lambda^2 = 1.96\,\mathrm{GeV}^2$ and the coupling $\alpha_\mathrm{s} = g^2/4\pi = 0.3$ are fixed to match the corresponding scales emerging from the lattice input that is used in our truncation of the gluon DSE, which we discuss soon. This guarantees that the combination $\Gamma^2 Z/A_f^2$ behaves like the running coupling in the ultraviolet, which is an important constraint for any truncation of the quark DSE [271]. Furthermore, $\delta = -9N_\mathrm{c}/(44N_\mathrm{c}-8N_\mathrm{f})$ is the anomalous dimension of the vertex and $\beta_0 = (11N_\mathrm{c}-2N_\mathrm{f})/3$. The only free parameter is thus the infrared strength d_1 that controls the amount of DCSB, and its determination is discussed later.

The squared-momentum argument of Γ is identified with the gluon momentum in the quark self-energy, $x = k^2$, while it is given by the sum of the two squared loop momenta of the quarks in the quark loop of the gluon DSE, $x = p^2 + q^2$. This is necessary to maintain multiplicative renormalizability of the gluon DSE [291].

This vertex ansatz was first introduced in Ref. [254] and successfully used in several other studies; cf. the literature cited in the preamble of this chapter. From a systematic point of view, however, our model is still a rather simple approximation of the full quark-gluon vertex. Nevertheless, it has some important properties. First, it provides the correct logarithmic running of the propagators with the correct anomalous dimension in agreement with resummed perturbation theory in the ultraviolet. Second, it is sufficiently enhanced in the infrared to trigger DCSB, where the amount is controlled by the phenomenological parameter d_1. Third, it is temperature and chemical-potential dependent through the leading-order term of the Ball–Chiu vertex, i.e., it contains at least some of these dependencies the full vertex certainly has. Last, and most importantly, together with our truncation of the gluon DSE that is further detailed below, it reproduces lattice result for the unquenched gluon propagator and a chiral order parameter; see Ref. [79] for details.

On the other hand, our vertex suffers from two main insufficiencies. First, only the leading tensor structure γ_ν is taken into account—only one (two) out of twelve (thirty-two) tensor structures in vacuum (medium). Especially the scalar tensor structure ($\propto \mathbb{1}_{\text{Dirac}}$) is expected to play an important role for the correct pattern of chiral symmetry restoration at high temperatures and/or chemical potentials. Second, related to that is the temperature and chemical potential independence of the infrared strength d_1. It should become smaller at high temperatures and/or chemical potentials. This insufficiency is clearly visible in the thermodynamic quantities computed in Chapters 4 and 5. A systematic improvement of the vertex, however, is not the scope of this work and thus postponed to future studies.

The gluon DSE

An efficient truncation to deal with the complexity of the gluon DSE is to replace all contributions without explicit quark content, i.e., all pure YM diagrams, by a fit to lattice results for the quenched gluon propagator. The three-momentum dependence of the latter for the zeroth Matsubara frequency, $\omega_k = 0$, as obtained from the lattice calculations of Refs. [256, 292] can be accurately described by [256]

$$Z^{\text{que}}_{\perp,\parallel}(\omega_k = 0, \boldsymbol{k}^2) = \frac{\boldsymbol{k}^2\Lambda^2}{(\boldsymbol{k}^2+\Lambda^2)^2}\left[\left(\frac{c}{\boldsymbol{k}^2+\Lambda^2\, a_{\perp,\parallel}(T)}\right)^{b_{\perp,\parallel}(T)} + \frac{\boldsymbol{k}^2}{\Lambda^2}\left(\frac{\alpha_{\text{s}}\beta_0}{4\pi}\log\left(1+\boldsymbol{k}^2/\Lambda^2\right)\right)^{\gamma}\right] \tag{3.9}$$

with temperature-independent scales $\Lambda^2 = 1.96\,\text{GeV}^2$ and $c = 11.5\,\text{GeV}^2$, the coupling $\alpha_{\text{s}} = 0.3$, and the temperature-dependent fit parameters $a_{\perp,\parallel}(T)$ and $b_{\perp,\parallel}(T)$. Since

Eq. (3.9) represents the dressing functions of the quenched gluon, $\beta_0 = 11\,N_c/3$ and the anomalous dimension is given by $\gamma = -13/22$, i.e., $N_f = 0$ in both quantities. The fit of the parameters $a_{\perp,\parallel}(T)$ and $b_{\perp,\parallel}(T)$ to the lattice results of Ref. [292] was performed in Ref. [235]. They were further fitted in temperature direction, including the vacuum $T = 0$, using polynomials in order to have Eq. (3.9) available at arbitrary temperatures. The results are (see Refs. [235, 256] for more details)

$$a_\perp(T) = \begin{cases} 0.5950 + 1.1010\,\tau^2 & \text{if } \tau < 1\,, \\ -0.2965 + 0.8505\,\tau & \text{if } \tau > 1\,, \end{cases} \tag{3.10}$$

$$a_\parallel(T) = \begin{cases} 0.5950 - 0.9025\,\tau + 0.4005\,\tau^2 & \text{if } \tau < 1\,, \\ -3.4835 + 3.6199\,\tau & \text{if } \tau > 1\,, \end{cases} \tag{3.11}$$

$$b_\perp(T) = \begin{cases} 1.3550 + 0.5548\,\tau^2 & \text{if } \tau < 1\,, \\ 0.7103 + 0.4296\,\tau & \text{if } \tau > 1\,, \end{cases} \tag{3.12}$$

$$b_\parallel(T) = \begin{cases} 1.3550 - 0.5741\,\tau + 0.3287\,\tau^2 & \text{if } \tau < 1\,, \\ 0.9319 + 0.1131\,\tau & \text{if } \tau > 1\,, \end{cases} \tag{3.13}$$

where $\tau = T/T_c^{\mathrm{YM}}$ with the transition temperature $T_c^{\mathrm{YM}} = 277\,\mathrm{MeV}$ of $\mathrm{SU}(N_c = 3)_{\mathrm{color}}$ YM theory. The dressing functions for higher Matsubara frequencies are accessed via $Z^{\mathrm{que}}_{\perp,\parallel}(\omega_k, \boldsymbol{k}^2) = Z^{\mathrm{que}}_{\perp,\parallel}(0, \omega_k^2 + \boldsymbol{k}^2)$, which is a good approximation because the gluon fulfills O(4) invariance already for the zeroth Matsubara frequency rather well [256]. We use the same approximation for the quark loop.

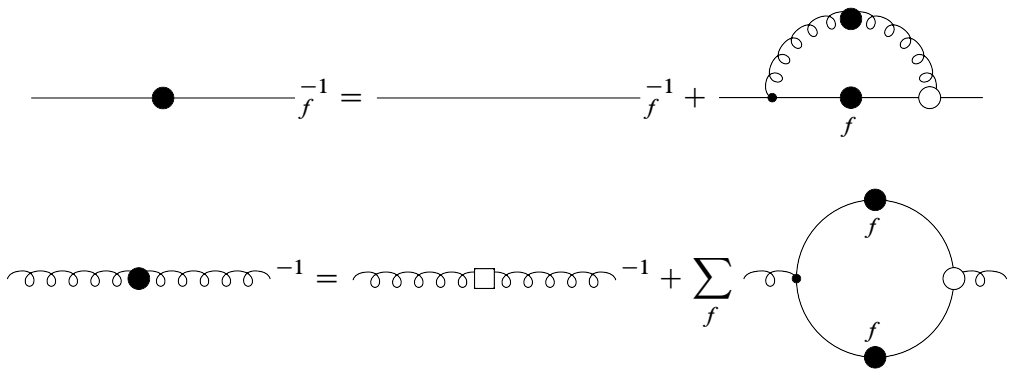

Figure 3.2 Coupled set of truncated DSEs for the quark and gluon propagators that is used in this work. The white circle denotes our vertex ansatz, the white square is the quenched gluon propagator from the lattice, and the flavor index f is made explicit. We use $N_f = 2 + 1$ quark flavors.

With the quenched gluon propagator $D^{\mathrm{que}}_{\nu\sigma}(k)$ from the lattice in terms of the above description, the DSE for the unquenched gluon propagator (2.47) takes the form

$$D^{-1}_{\nu\sigma}(k) = \left[D^{\mathrm{que}}_{\nu\sigma}(k)\right]^{-1} + \Pi_{\nu\sigma}(k)\,. \tag{3.14}$$

We keep the quenched lattice propagator fixed and add the quark loop: for a given quark, the quark loop $\Pi_{\nu\sigma}(k)$ is calculated explicitly, and the result is added to the quenched gluon propagator to yield the unquenched gluon propagator. This approximation misses implicit quark-loop effects in the pure YM self-energies. However, these are subleading in a skeleton expansion compared to the quark-loop diagram. In vacuum, the impact of this approximation on the gluon can be estimated within the framework of Ref. [291] and is found to be below the five-percent level [293]. In other words, obtaining the unquenched gluon by means of Eq. (3.14) is a rather good and well-justified approximation.

Final set of equations

Now, with our ansatz for the quark-gluon vertex and the description of the unquenched gluon as detailed in the previous subsections, we finally arrive at a closed system of truncated DSEs for the quark and gluon propagators, which allows us to calculate them at (in principle) arbitrary temperature and chemical potential. To summarize, our final set of equations reads

$$S_f^{-1}(p) = S_{0,f}^{-1}(p) + \Sigma_f(p)\,, \tag{3.15}$$

$$D^{-1}_{\nu\sigma}(k) = \left[D^{\mathrm{que}}_{\nu\sigma}(k)\right]^{-1} + \Pi_{\nu\sigma}(k)\,, \tag{3.16}$$

where the quark-gluon vertices appearing in the quark self-energy and in the quark loop are given by our ansatz. The equations are shown diagrammatically in Fig. 3.2. The quark and gluon DSEs are nontrivially coupled through the quark-loop diagram, i.e., the back reaction of the quarks onto the YM section is explicitly taken into account. This establishes a temperature and chemical-potential dependence of the gluon controlled by QCD dynamics rather than modeling. Moreover, it allows for a consistent flavor dependence of all results, and the gluon becomes sensitive to the chiral dynamics of the involved quarks.

Note that Eqs. (3.15) and (3.16) still have to undergo the process of regularization and renormalization. In particular, we have to remove the spurious quadratic divergence that appears during the numerical evaluation of the quark loop. However, in order to keep this chapter concise, we relegate these technical processes to Appendix D. There, we collect the actual explicit expressions that are used in our calculations, detail the regularization and renormalization procedure, and discuss numerical aspects how our set of truncated DSEs is solved in practice.

Parameter fixing

Last, we have to fix our parameters, which are the infrared strength of the vertex d_1 and the quark masses. We use $N_\mathrm{f} = 2 + 1$ quark flavors: the light up and down quarks are mass degenerate, $m_\mathrm{u} = m_\mathrm{d} \equiv m_\mathrm{u,d}$, i.e., we work in the isospin-symmetric limit, and the strange quark is heavier, $m_\mathrm{s} \gg m_\mathrm{u,d}$.[27] The mass of the strange quark, however, is not independent but obtained via the mass ratio $m_\mathrm{s}/m_\mathrm{u,d} = 25.7$, which is a result of demanding physical pion and kaon masses in the course of a bound-state calculation using a bound-state-optimized version of our truncation scheme [102] as well as using our truncation scheme within the framework of Ref. [294]. In order to fix d_1 and $m_\mathrm{u,d}$, we compute the subtracted (up-strange) quark condensate $\Delta_\mathrm{u,s}$ [Eq. (2.69)] at vanishing chemical potential as a function of temperature. We observe that

(i) varying the infrared strength of our vertex ansatz results mainly in a change of the inflection point of the subtracted condensate—smaller (larger) values of d_1 yield a smaller (larger) inflection point;

(ii) $m_\mathrm{u,d}$ dominantly controls the high-temperature behavior of $\Delta_\mathrm{u,s}$, while it only mildly affects the location of the inflection point.

Since we define the pseudocritical chiral transition temperature T_c by the inflection point of the subtracted quark condensate with respect to the temperature, see Eq. (2.70), we adapt d_1 and $m_\mathrm{u,d}$ such that T_c as found on the lattice is reproduced [54, 55, 295] while at the same time $\Delta_\mathrm{u,s}$ matches corresponding lattice data at high temperatures. The best result is obtained for $d_1 = 8.49\,\mathrm{GeV}^2$ together with $m_\mathrm{u,d}(\zeta) = 0.8\,\mathrm{MeV}$ (thus, $m_\mathrm{s}(\zeta) = 20.56\,\mathrm{MeV}$) at our renormalization point $\zeta = 80\,\mathrm{GeV}$. These seemingly rather small quark masses are a result of our choice of a large renormalization point deep in the perturbative ultraviolet. Note that our value of d_1 differs from the one reported in Ref. [244] because we employ a Pauli–Villars regulator rather than a hard ultraviolet cutoff for the regularization of the quark self-energy (see Appendix D for details). Phrased differently, d_1 carries an implicit dependence on the employed regularization scheme. We emphasize that these modifications are purely technical in nature, and all previous results, in particular those presented in Refs. [241, 244, 261], remain fully valid.

In Fig. 3.3, we show the vacuum-normalized subtracted quark condensate as a function of temperature at vanishing chemical potential with these parameters (black, solid line) together with continuum-extrapolated lattice data from Ref. [54] (red squares). First, the crossover nature of the chiral transition is clearly visible. The confined, chirally-broken hadronic phase at low temperatures is connected to the deconfined, (partially) chirally-symmetric quark-gluon plasma phase at high temperatures via an analytic crossover rather

[27] Charm-quark effects ($N_\mathrm{f} = 2 + 1 + 1$) are qualitatively negligible [244] and thus not considered here.

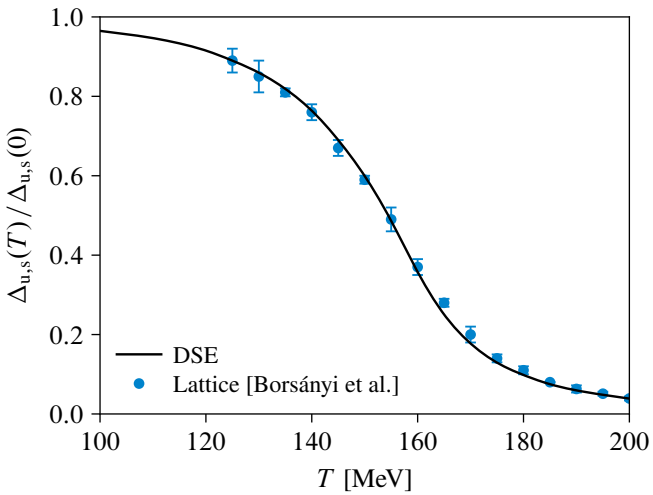

Figure 3.3 Vacuum-normalized subtracted quark condensate as a function of temperature at vanishing chemical potential compared to the continuum-extrapolated lattice results of Ref. [54].

than a true phase transition. Second, we find a pseudocritical chiral transition temperature at vanishing chemical potential of

$$T_c = (156 \pm 1)\,\mathrm{MeV} \tag{3.17}$$

that agrees, by construction, with the lattice result. The given error is purely numerical. A nontrivial result, however, is the almost perfect match of the steepness of the transition, which is an outcome of our calculation. Another nontrivial result is the agreement of the unquenched two-flavor gluon propagator at nonzero temperature [241] with lattice results [296] as discussed and summarized in Ref. [79]. In combination with the nontrivial quantitative agreement with lattice results for the subtracted quark condensate, we conclude that our truncation is well-suited to describe QCD at nonzero temperature. The same is true, albeit within some limitations, for nonzero chemical potential, too.

Finally, we comment on our choice of the chemical potentials. Even though we use mass-degenerate light quarks, we have in principle three different quark chemical potentials: μ_u, μ_d, and μ_s. Usually, it is more customary to use the phenomenologically-motivated chemical potentials for baryon number, electric charge, and strangeness μ_B, μ_Q, and μ_S, respectively. The connection between these two sets of chemical potentials is given by

$$\begin{aligned} \mu_u &= \frac{1}{3}\mu_B + \frac{2}{3}\mu_Q\,, \qquad \mu_d = \frac{1}{3}\mu_B - \frac{1}{3}\mu_Q\,, \\ \mu_s &= \frac{1}{3}\mu_B - \frac{1}{3}\mu_Q - \mu_S\,. \end{aligned} \tag{3.18}$$

From these relations, we find $\mu_B = \mu_u + 2\mu_d$, $\mu_Q = \mu_u - \mu_d$, and $\mu_S = \mu_d - \mu_s$. In principle, the chemical potentials should be adjusted to match the conditions met in a heavy-ion collision. First, from strangeness conservation follows that the strangeness density n_S has to vanish. Second, in Au-Au and Pb-Pb collisions, the baryon number and charge densities n_Q and n_B, respectively, are related by $n_Q \approx 0.4 n_B$ [97]. In practice, μ_B is treated as a free parameter, while μ_Q and μ_S depend appropriately on μ_B such that these conditions are satisfied. For temperatures around 150 MeV, the leading-order result from lattice QCD is $\mu_Q \approx -0.02\mu_B$ while $\mu_S \approx 0.2\mu_B$ [297, 298]. Thus, to a good approximation we choose $\mu_u = \mu_d \equiv \mu_{u,d}$. Furthermore, it was checked within our DSE framework that values for the strange-quark chemical potential $\mu_s \in [0, \mu_{u,d}]$ hardly affects the location of the CEP [268]. Therefore, we choose $\mu_s = 0$, which is the naive way to enforce strangeness neutrality. If not stated otherwise, by referring generically to "chemical potential" we always mean baryon chemical potential, which is given by $\mu_B = 3\mu_{u,d}$.[28]

3.2 Quark and gluon propagators in medium

Before we discuss our result for the QCD phase diagram, we present exemplary results for the quark and gluon propagators. In the upper left and upper right diagram of Fig. 3.4, we show the momentum dependence of the up-quark dressing functions C_u and A_u, in the lower left diagram the renormalization-point independent mass function $M_u = B_u / A_u$, and in the lower right diagram the relative difference between C_u and A_u at vanishing chemical potential for different temperatures. In order to include the vacuum results (dark gray, solid lines), we plot against the squared four-momentum $p^2 = \omega_p^2 + \boldsymbol{p}^2$, which results in a different starting point for each curve. Furthermore, we show only the zeroth Matsubara frequency of the nonzero-temperature results. First of all, the functions show no temperature dependence for $p^2 \gtrsim 40\,\mathrm{GeV}^2$, which illustrates that the medium affects only the infrared because the relevant scale at low momenta is set by the temperature (and, if nonzero, by the chemical potential). This changes as soon as the momentum is (much) larger than the scales set by medium effects, resulting in a degeneracy with the vacuum solution in the ultraviolet. There, the dressing functions tend to their perturbative expressions. Furthermore, the wave function $Z_u = 1/A_u$ is close to one, indicating that the quark is noncomposite in the sense that nonperturbative effects are minute and it behaves like a current quark. This is also reflected in the mass function, which is of the order of the current quark mass. On the other hand in the infrared, the dressing functions differ significantly from their perturbative values. Looking first at the vacuum results, the dressing functions C_u and A_u are degenerate, and the wave function deviates (strongly) from one at

[28] We use this terminology already since the beginning of this chapter.

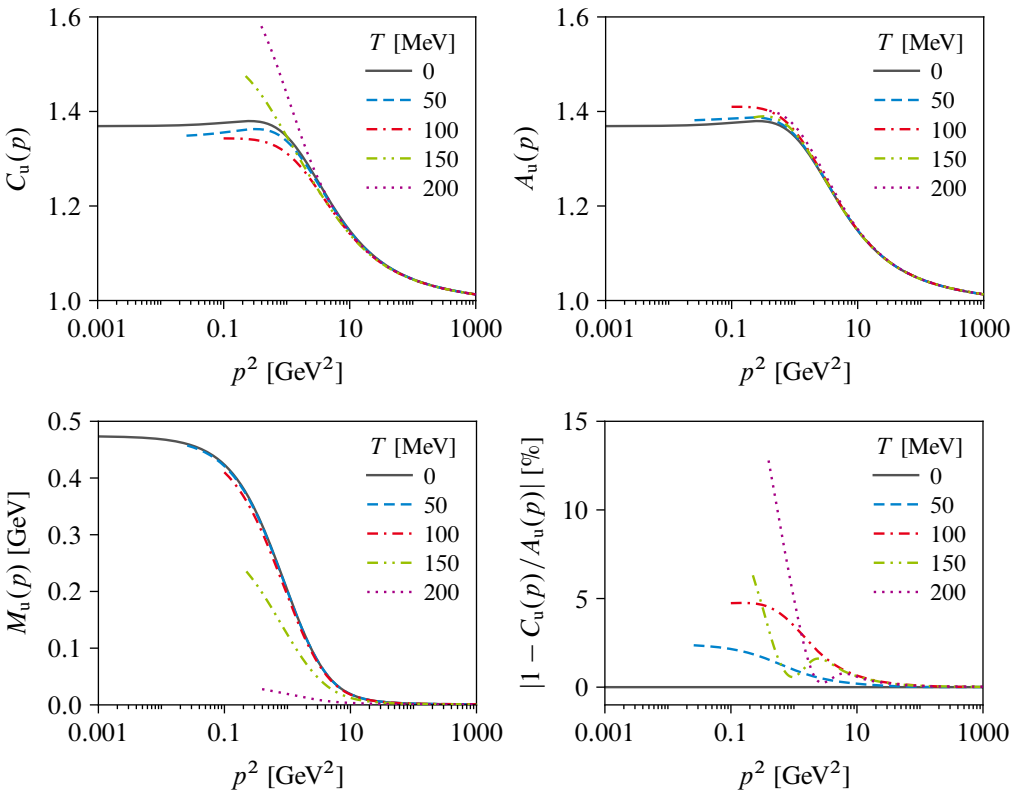

Figure 3.4 Up-quark dressing functions C_u and A_u (upper left and upper right, respectively), mass function $M_u = B_u/A_u$ (lower left), and relative difference between C_u and A_u (lower right) at vanishing chemical potential for different temperatures. We show only the zeroth Matsubara frequency of the $T > 0$ results and plot against the squared four-momentum.

infrared momenta, e.g., $Z_u(p^2 \to 0) \approx 0.73$. Physically, this can be interpreted as the current quark being surrounded by a cloud of gluons and therefore behaving effectively like a constituent quark. This manifests in the mass function, too. The quark rapidly acquires a huge amount of mass that is of the order of a typical constituent quark mass—we see DCSB at work, one of the most prominent nonperturbative features of QCD, which is responsible for the bulk of the mass of visible matter. At nonzero temperature, C_u and A_u are different, but for low temperatures (blue, dashed and red, dashed-dotted lines), we observe a convergence toward the vacuum solution. The mass function tends toward its vacuum version, too, as the temperature decreases, and we note that its temperature dependence is very mild for $T \lesssim 100\,\mathrm{MeV}$ and becomes increasingly noticeable for larger temperatures. The larger the temperature, the smaller the overall magnitude of M_u in the infrared with the most rapid change in the region $0.8\,T_c \lesssim T \lesssim 1.2\,T_c$, i.e, around the pseudocritical chiral transition temperature. This is nothing but the continuous (partial)

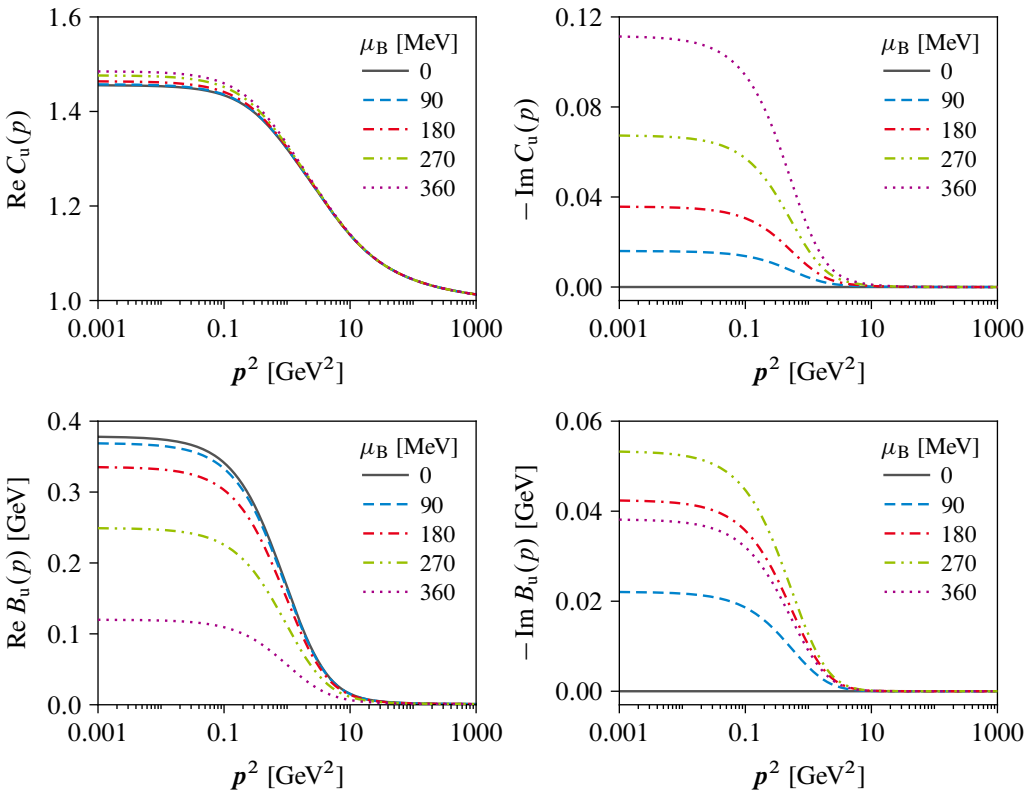

Figure 3.5 Real and imaginary parts of the up-quark dressing functions C_u (upper row) and B_u (lower row) at $T = 145\,\text{MeV}$ for different chemical potentials. We show only the zeroth Matsubara frequency and plot against the squared three-momentum.

restoration of chiral symmetry at high temperatures as already seen in Fig. 3.3. Regarding C_u and A_u, the former first decreases and then experiences a steep rise across the crossover transition, while the latter is generally less temperature dependent than the former. From the relative difference between the two functions, we first see again that the medium only affects the infrared behavior of the quark, and second that C_u and A_u differ even at low temperatures already on a five-percent level at infrared momenta. At high temperatures, i.e., above T_c, the difference grows to around ten percent.

In Fig. 3.5, we show the momentum dependence of the real and (negative) imaginary parts of the temporal dressing function C_u (upper row) and the scalar dressing function B_u (lower row) at $T = 145\,\text{MeV}$ for different chemical potentials. The real part of C_u increases with increasing chemical potential, though rather mildly, while its imaginary part reacts more strongly as μ_B increases but on a smaller magnitude compared to the real part. A_u, which is not shown, behaves similarly but with the difference that the real

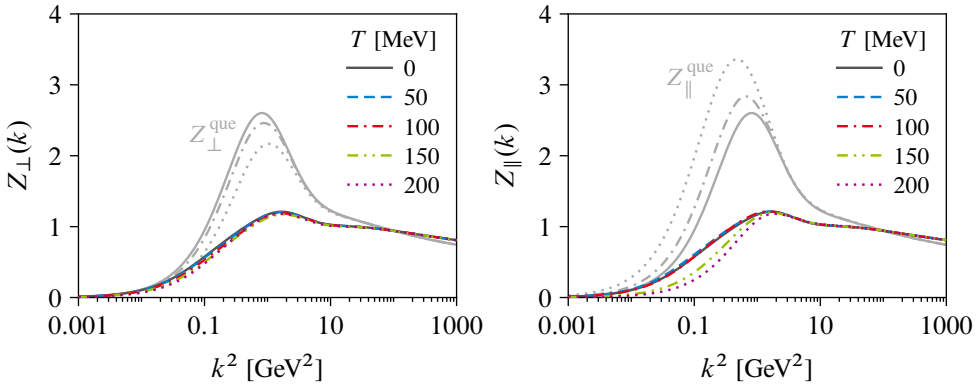

Figure 3.6 Unquenched gluon dressing functions $Z_\perp$ and $Z_\parallel$ (left and right diagram, respectively) at vanishing chemical potential for different temperatures In addition, we show our quenched fits to lattice data [Eq. (3.9)] in light gray. We show only the zeroth Matsubara frequency of the $T > 0$ results and plot against the squared four-momentum.

part decreases with increasing chemical potential. From the real part of B_u follows that increasing chemical potential leads, just as increasing temperature, to a (partial) restoration of chiral symmetry. Since the medium affects only the infrared, the imaginary parts of the dressing functions have to vanish in the ultraviolet. This is indeed true for A_u and B_u and in particular for C_u. The latter is known for developing a bump in the ultraviolet, which is caused if a regularization scheme is used that violates translational invariance, e.g., a sharp ultraviolet cutoff [268, 269]. Particularly, the correct ultraviolet-vanishing behavior of the imaginary part of C_u is vital for the calculation of quark and baryon number fluctuations—the topic we are concerned with in the upcoming chapter. Thus, we use a Pauli–Villars regulator (see Appendix D for details) that is well-suited to get the correct ultraviolet behavior of the imaginary part of C_u, which is apparent from the upper right diagram of Fig. 3.5.

Last, we discuss the unquenched in-medium gluon propagator. In Fig. 3.6, we display the magnetic and electric gluon dressing functions at vanishing chemical potential for different temperatures. Again, we show only the zeroth Matsubara frequency of the $T > 0$ results and plot against the squared four-momentum. In addition, we show the fits to quenched lattice data [Eq. (3.9)] in light gray for comparison at three temperatures. First, we observe large unquenching effects both in the magnetic and electric part of the gluon. Unquenching the gluon, i.e., taking the quark loop explicitly into account, leads to a significant reduction of the bump in the nonperturbative momentum region as well as to a shift of the maximum to slightly larger momenta. Furthermore, the quark-loop effects invert the temperature dependence of the electric dressing function: $Z_\parallel^{\text{que}}$ generally increases with increasing temperature, whereas the unquenched dressing function $Z_\parallel$ decreases as T decreases.

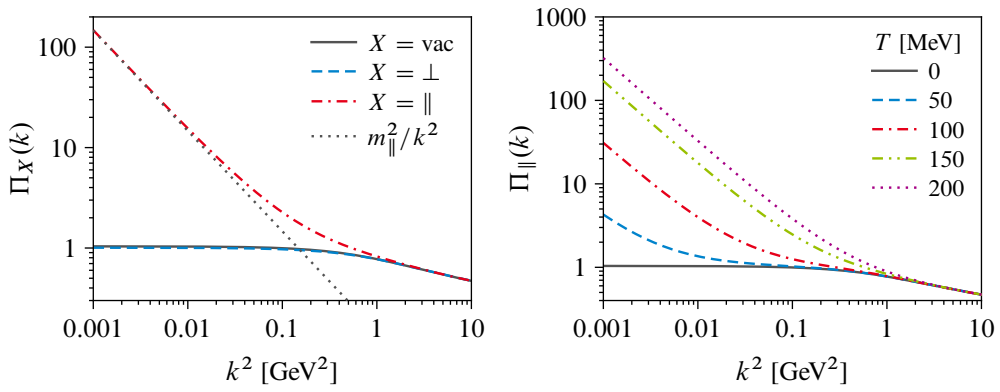

Figure 3.7 Left: projected vacuum quark loop together with the in-medium ($T = 145\,\text{MeV}$, $\mu_\text{B} = 0$) magnetic ($\perp$) and electric ($\parallel$) quark loops. Right: electric quark loop at vanishing chemical potential for different temperatures. The vacuum quark loop is shown for reference.

Second, the magnetic dressing function shows a much weaker temperature dependence than the electric one. In particular, the electric gluon dressing function reacts much more to the chiral dynamics of the quark compared to the magnetic dressing function, which manifests in a significant reduction of $Z_\parallel$ at infrared momenta $k^2 \lesssim 1\,\text{GeV}^2$ for temperatures around and above T_c. This suggests that the often employed approximation of an O(4)-symmetric in-medium gluon, i.e., $Z_\parallel = Z_\perp$, should be avoided if possible.

One reason for the different behavior of the magnetic and electric gluon dressing functions is that the latter develops a thermal screening mass that stems from the quark loop and is the dominant thermal effect induced by the unquenching. The projected in-medium quark loops $\Pi_{\perp,\parallel}$ (again, see Appendix D for explicit expressions) behave like $\Pi_{\perp,\parallel}(k) = (m_{\perp,\parallel})^2/k^2$ as $k^2 \to 0$, where $m_\perp$ and $m_\parallel$ are the magnetic and electric thermal screening masses, respectively. Both appear only at nonzero temperature and/or chemical potential and are dynamically generated, i.e., they do not spoil gauge invariance. Naturally, $m_{\perp,\parallel} = m_{\perp,\parallel}(T, \mu_\text{B})$, and they react strongly as temperature and/or chemical potential is increased. The appearance of such a thermal screening mass is illustrated in the left diagram of Fig. 3.7, where we display the projected vacuum quark loop (dark gray, solid line) together with the magnetic and electric in-medium quark loops at $T = 145\,\text{MeV}$ and vanishing chemical potential. On the one hand, the magnetic quark loop (blue, dashed line) does not develop a thermal mass because $m_\perp$ is only nonzero if the global gauge symmetry is broken like in color-superconducting phases. In the region of the μ_B-T plane that is covered in this work, $m_\perp = 0$ for all T and μ_B. As a result, the magnetic quark loop is similar to the vacuum one and deviates from the vacuum quark loop even at high temperatures and/or chemical potentials only by a few percent. On the other hand, the electric quark loop (red, dashed-dotted line) indeed develops a thermal screening mass,

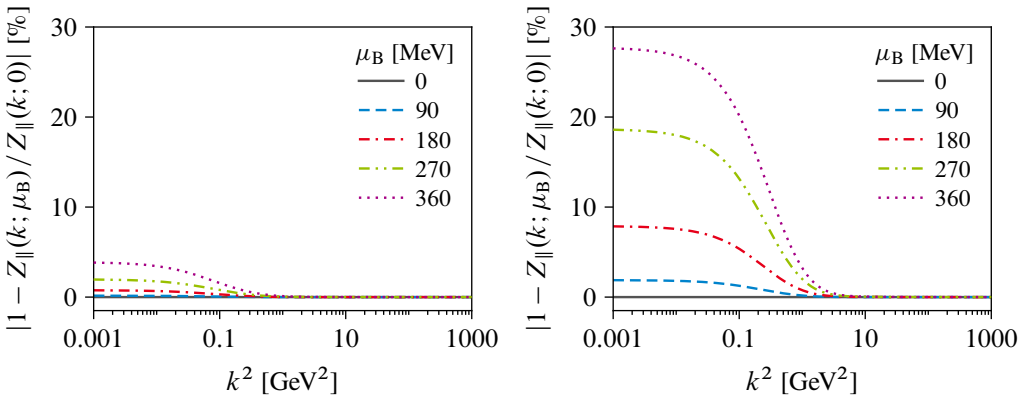

Figure 3.8 Relative difference between the electric gluon dressing function at nonzero and zero chemical potential at $T = 25\,\text{MeV}$ (left) and $T = 145\,\text{MeV}$ (right).

and the behavior $\Pi_\parallel(k) = (m_\parallel)^2/k^2$ with $m_\parallel \neq 0$ as $k^2 \to 0$ is clearly visible (dark gray, dotted line). Here, at $T = 145\,\text{MeV}$ and vanishing chemical potential, we find $m_\parallel \approx 383\,\text{MeV}$. In general, the higher the temperature and/or chemical potential the higher the electric screening mass, which is shown in the right diagram of Fig. 3.7. Again, as for the quark propagator, the medium affects only the infrared behavior of the gluon.

Regarding the chemical-potential dependence of the gluon, which is induced by the chemical-potential dependent quark loops, in Fig. 3.8 we display the relative difference between the electric gluon dressing function at nonzero and zero chemical potential at $T = 25\,\text{MeV}$ (left diagram) and $T = 145\,\text{MeV}$ (right diagram). As expected, increasing chemical potential affects only the infrared dynamics. At $T = 25\,\text{MeV}$, which is rather small and close to the vacuum, the deviation of $Z_\parallel$ from its $\mu_B = 0$ counterpart stays below five percent for $\mu_B \lesssim 400\,\text{MeV}$. At higher temperatures, however, this approximation becomes quickly a poor one, which is apparent from the right diagram of Fig. 3.8. At $T = 145\,\text{MeV}$ and $\mu_B = 360\,\text{MeV}$ (purple, dotted line), i.e., in the midst of the QCD phase diagram, the gluon differs by almost 30% from its vanishing-chemical-potential version. The same holds for low temperatures but very large chemical potentials $\mu_B = \mathcal{O}(1\,\text{GeV})$, i.e., around the nuclear liquid-gas transition.

3.3 Phase structure of QCD

After having spent some time with the propagators, we now discuss our results for the phase structure of QCD. As already mentioned, we use $N_f = 2 + 1$ dynamical quark flavors. In Fig. 3.9, we show the vacuum-normalized subtracted quark condensate as a function of temperature for different chemical potentials. In the left diagram, starting from vanishing

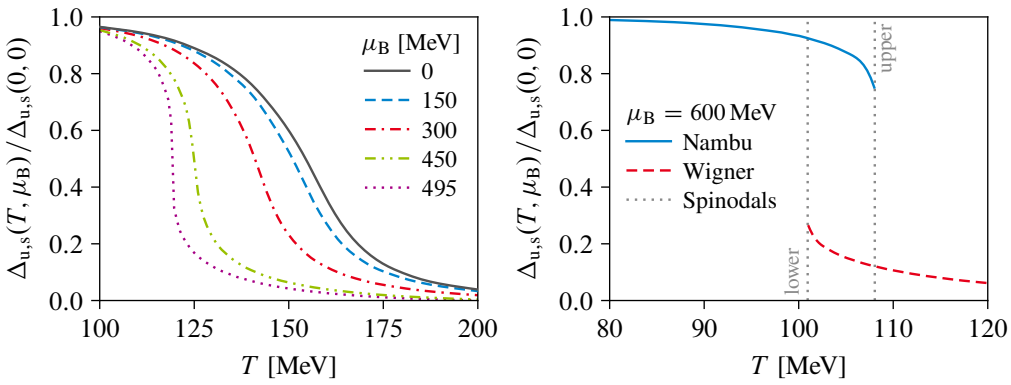

Figure 3.9 Vacuum-normalized subtracted quark condensate as a function of temperature for different chemical potentials in the crossover (left) and first-order region (right).

chemical potential (dark gray, solid line), the inflection point of the condensate and thus T_c shifts to lower temperatures as μ_B increases. At intermediate values of the chemical potential, the crossover remains rather broad (blue, dashed and red, dashed-dotted lines). If we increase μ_B further, the transition becomes steeper (green, dashed-double-dotted line) and culminates at $\mu_B = 495\,\text{MeV}$ in a condensate with an infinite slope at a specific temperature (purple, dotted line), which signals that the transition is not a crossover anymore but of second order. This is precisely the location of the CEP.

At chemical potentials $\mu_B > 495\,\text{MeV}$, the temperature dependence of the subtracted quark condensate is discontinuous. In particular, by tracking the chirally-broken Nambu solution from low to high temperatures and the chirally-symmetric Wigner solutions down from high to low temperatures until they do not exist anymore, i.e., until they are not an attractive fixed point of the quark DSE anymore, we find a region where both solutions coexist. This coexistence region is typical for a first-order phase transition and bounded by spinodals. The upper (lower) spinodal is the one above (below) which the Nambu (Wigner) solution disappears. This is displayed in the right diagram of Fig. 3.9 for a chemical potential of $\mu_B = 600\,\text{MeV}$. The actual (physical) first-order transition lies within the coexistence region and has to be determined based on thermodynamics: the physically realized solution maximizes the pressure, and the transition line is thus given by the line of equal pressure of the Nambu and Wigner phase. We come back to this issue in Chapter 5.

By monitoring the behavior of the subtracted quark condensate across the μ_B-T plane, we can draw the phase diagram of QCD, and our result is shown in Fig. 3.10. The chiral crossover line (black dashed) becomes steeper with increasing chemical potential and terminates in a second-order CEP (black dot) at

$$\left(\mu_B^{\text{CEP}}, T_{\text{CEP}}\right) = (495 \pm 2, 119 \pm 2)\,\text{MeV} \tag{3.19}$$

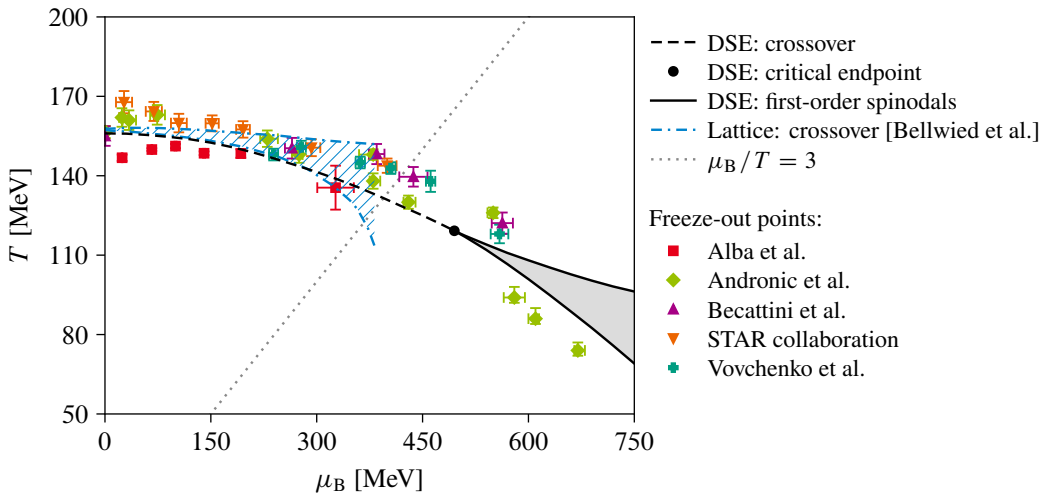

Figure 3.10 Our result for the QCD phase diagram with $N_f = 2 + 1$ quark flavors compared to freeze-out points from heavy-ion collisions extracted by different groups/methods [303–308]. In addition, we show the crossover from the lattice [299] (blue band); see also Refs. [300, 301].

followed by the coexistence region (shaded gray area) of a first-order phase transition bounded by spinodals (black, solid lines). Furthermore, we show the line of chemical potential to temperature ratio $\mu_B / T = 3$ (gray, dotted line), which emphasizes that our CEP is located at rather large chemical potential, $\mu_B^{CEP} / T_{CEP} \approx 4.2$. Again, the error in Eq. (3.19) is purely numerical. We also show results for the crossover line obtained from lattice-QCD calculations (blue band) [299]; see also Refs. [300, 301]. This band features a very small error at small chemical potential that rapidly increases as μ_B increases. At $\mu_B / T \approx 3$, the error becomes so large that further extrapolation becomes meaningless. However, combined evidence of different methods on the lattice suggest that no CEP exists for $\mu_B / T \leq 2$–2.5 [299, 302] in agreement with our result.

In addition, we show results for freeze-out points extracted from heavy-ion collisions by different groups/methods [303–308]. In the crossover region at small chemical potential, the different freeze-out results spread by almost twenty MeV in temperature direction around the pseudocritical chiral transition temperature. While in the presence of a proper (first-order) phase transition one would expect the freeze-out to occur at temperatures below the critical one, this notion is hard to formulate in the crossover region of the phase diagram, where no unique definition of T_c exists. At large chemical potential, however, where we find a first-order phase transition and a mismatch of the temperature ordering of some freeze-out points, we have to expect either corrections to some of the experimental freeze-out data or to the DSE result in order to get a proper ordering of the freeze-out points with respect to our first-order region at large μ_B.

Another characteristic of the crossover line is its curvature. At small chemical potential, the crossover line $T_c(\mu_B)$ normalized to its $\mu_B = 0$ value $T_c = T_c(0)$ can be parameterized by an expansion in the dimensionless ratio of chemical potential to the pseudocritical chiral transition temperature at vanishing chemical potential, i.e.,

$$\frac{T_c(\mu_B)}{T_c} = 1 - \kappa_2 \left(\frac{\mu_B}{T_c}\right)^2 - \kappa_4 \left(\frac{\mu_B}{T_c}\right)^4 + \dots , \tag{3.20}$$

where κ_2 is the curvature. We fit this expression to our crossover line shown in Fig. 3.10 (black, dashed line) for $0 \leq \mu_B \leq 240\,\text{MeV}$ and find

$$\begin{aligned} \kappa_2 &= 0.0238 \pm 0.0010\,, \\ \kappa_4 &= 0.0008 \pm 0.0005\,. \end{aligned} \tag{3.21}$$

The error contains the numerical error from the fit and a conservative estimate from varying the upper bound of the fit interval. Recent lattice calculations, however, yield a curvature in the range $0.0120 \leq \kappa_2 \leq 0.0153$ [299–301, 309]. Thus, our result is approximately a factor of two too large compared to the lattice results.

Intimately related to the mismatch of freeze-out points in the first-order region and a too large curvature of the crossover line is the important question of the systematic error that is accompanied with our truncation. The systematic error of the CEP location is particularly important. To this end, we need to compare systematically with other/different truncations such as the recent FRG calculation of Ref. [247] and the FRG-assisted difference-DSE framework put forward in Refs. [248, 249]. This comprehensive comparison—which is necessary to arrive, in the long term, at a common quantitative statement from functional methods regarding the location of the CEP—is currently ongoing and results will be discussed elsewhere in the future. Nevertheless, in Fig. 3.11 we show our result for the crossover line and CEP (black, dashed line and black circle) in comparison with recent results from other functional studies: the FRG-assisted difference-DSE method, where parts of the quark-gluon vertex are calculated explicitly (blue, dashed-dotted line and blue square) [249]; the same approach but with a quark-gluon vertex constructed based on its STI (red, dashed-double-dotted line and red square) [248]; the FRG approach to QCD as presented in Ref. [247] (green, dotted line and green triangle). First, we notice that the CEPs cluster in the region $490\,\text{MeV} \lesssim \mu_B \lesssim 680\,\text{MeV}$ and $90\,\text{MeV} \lesssim T \lesssim 120\,\text{MeV}$, which hints that sufficiently sophisticated truncations within the functional frameworks of DSEs and the FRG seem to favor this region regarding the location of the CEP.[29] Second,

[29] Simpler DSE truncations without backcoupling to the YM sector and with a model gluon propagator, see, e.g., Refs. [240, 245, 310], typically find a CEP in a region that is excluded by the lattice. Thus, these truncations should be used nowadays for phase-diagram calculations only for exemplary purposes.

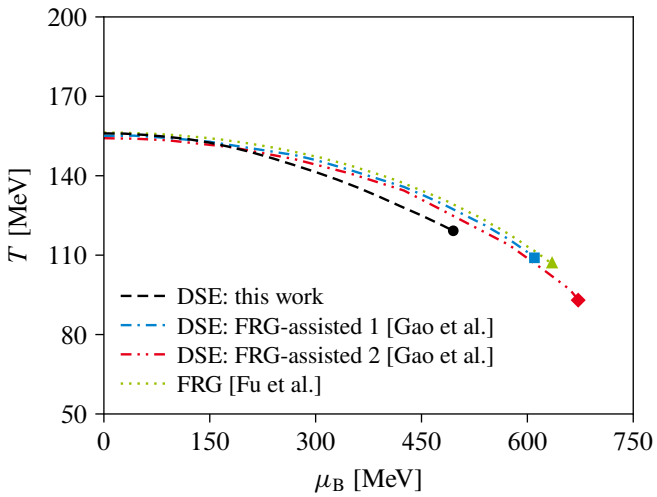

Figure 3.11 QCD phase diagram from functional methods: this work, FRG-assisted difference-DSEs with parts of the quark-gluon vertex calculated explicitly (FRG-assisted 1) [249], same but with an STI-based construction of the vertex (FRG-assisted 2) [248], and the FRG approach to QCD [247]. The crossover transitions and CEPs are indicated by lines and symbols, respectively.

compared to our result, the other studies feature a CEP at higher chemical potentials and slightly lower temperatures together with a smaller curvature of the crossover line. As already mentioned and discussed elsewhere [79], our unquenched gluon propagator agrees satisfactorily with lattice results. The same is true for the FRG calculation and the FRG-assisted difference-DSE method (at least in vacuum). One major difference between these studies and this work is that they use a different quark-gluon vertex: they take more tensor structures into account, which is undoubtedly an advantage compared to our truncation. However, both Ref. [247] and Refs. [248, 249] use an O(4) symmetric gluon, $Z_{\parallel} = Z_{\perp}$. Furthermore, Refs. [248, 249] use the O(4) approximation $C_{\mathrm{u}} = A_{\mathrm{u}}$ in the vertex. Both are, based on our results, rather severe approximations; see Section 3.2. Other approximations of the FRG study and the FRG-assisted DSE approach are, for example, that only vacuum tensor structures are used for the quark-gluon vertex, strange-quark dynamics are not fully taken into account and approximated by light quarks, and imaginary parts of FRG flows due to nonzero chemical potential are discarded. The effect of these and other approximations on the location of the obtained CEPs are not yet clear. Generally speaking, there are approximations that are used in Refs. [247–249] but not in this work and vice versa. The extensive and nontrivial investigation of their impact is currently ongoing and subject to future work.

In the following closing remarks of this chapter, we briefly discuss how our truncation of the quark-gluon vertex can be improved. First, the most obvious extension of our

current setup is to take more tensor structures of the quark-gluon vertex into account. Especially the scalar tensor structure is expected to be important for a correct pattern of chiral symmetry restoration as temperature and/or chemical potential increases. Second, meson contributions to the quark-gluon vertex—made explicit via a skeleton expansion of the diagrams in the vertex DSE—might be important. The exploratory results of Ref. [263] (see also Ref. [102]) indicate that meson contributions decrease the curvature but have no significant impact on the location of the CEP. Taking these results at face value, pion and sigma-meson contributions affect the location of the CEP on the 5–10% level. Third, baryon effects might play a vital role, especially at high chemical potential. The exploratory study of Ref. [261] indicates that baryon contributions have the potential to shift the CEP to larger temperatures and/or chemical potential. These points should be kept in mind if one aims at a systematic improvement of our truncation of the quark-gluon vertex.

3.4 Summary

In this first nonintroductory chapter, we presented our truncation scheme for the quark and gluon propagators of $(2+1)$-flavor QCD in Landau gauge, which parameters have been fixed to yield $T_\mathrm{c}(\mu_\mathrm{B}=0)$ as obtained on the lattice. In agreement with previous works, we found quantitative agreement with lattice results for the temperature dependence of the subtracted quark condensate, which is a nontrivial outcome of our calculation because we fixed only $T_\mathrm{c}(\mu_\mathrm{B}=0)$ but not the steepness of the chiral crossover. Furthermore, we showed the behavior of the quark and gluon dressing functions for various T and μ_B. In particular, the use of a Pauli–Villars regulator cured the erroneous large-momentum behavior of the imaginary part of the temporal quark dressing function C_f, which was found in earlier studies. The obtained phase diagram features a second-order CEP at $\left(\mu_\mathrm{B}^\mathrm{CEP}, T_\mathrm{CEP}\right) \approx (495, 119)\,\mathrm{MeV}$, and the overall changes compared to previous works due to the modified regularization scheme and a slightly lighter strange quark are very small and purely technical in nature. Finally, we compared our result with the recent phase-diagram calculations of Refs. [247–249]. However, an in-depth comparison of the employed approximations is necessary in order to make reliable statements of the systematic error of the CEP locations. This is a topic for work that will be presented elsewhere in the future.

4 Quark and baryon number fluctuations

In the previous chapter, we presented our result for the QCD phase diagram: we found a crossover transition at small chemical potential that terminates in a second-order CEP at large chemical potential, $\mu_{\mathrm{B}}^{\mathrm{CEP}}/T_{\mathrm{CEP}} \approx 4.2$. The currently operating Beam Energy Scan program at RHIC as well as the future Compressed Baryonic Matter experiment at FAIR together with NICA at the Joint Institute for Nuclear Research are dedicated to the experimental exploration of the QCD phase diagram [45–49]. The emphasis is on proving the very existence and subsequently locating the (putative) CEP. Therefore, in order to put the theoretical results to the test, observables were identified that are able to deliver signals of the CEP in experiments. Provided the freeze-out in heavy-ion collisions is sufficiently close to the phase boundary and CEP, fluctuations of the conserved charges baryon number, strangeness, and electric charge are promising candidates and expected to provide this information [311–318]. Various ratios of cumulants of these conserved charges can be extracted from heavy-ion collision experiments in event-by-event analyses and compared to corresponding ratios obtained in theoretical calculations; see Refs. [47, 97, 319, 320] for extensive review articles.

Results for fluctuations from lattice QCD are available at vanishing and small chemical potential [298, 321–324] but need to be extended toward higher chemical potential. Unfortunately, the notorious sign problem poses a severe obstacle. Within the hadron resonance gas approach and refined effective models, a plethora of results on fluctuations of conserved charges have been obtained, see, e.g., Refs. [325–335] for selected works. Studies of fluctuations using DSEs, however, are rather scarce and available only within simple truncations with a model gluon propagator and thus no backcoupling effects [336–339].

In this chapter, we outline how the quark number density—our starting point for the fluctuations—is obtained from the dressed quark propagator and furthermore regularized because it develops a spurious divergence in the course of its numerical evaluation. Then, we compute quark and baryon number fluctuations and ratios thereof, improving thereby the previous results of Refs. [336–339], where no backcoupling of quarks onto the gluon was taken into account. In particular, we discuss the skewness and kurtosis ratios and compare with recent experimental data from the STAR collaboration [95, 96] taken during the first RHIC Beam Energy Scan. The results of this chapter are published in Ref. [98].

4.1 General formulae

In three-flavor QCD (not in the isospin-symmetric limit), there is a conserved charge for each quark flavor controlled by the three quark chemical potentials μ_u, μ_d, and μ_s. The quantities we aim to study are fluctuations of these conserved charges, i.e., higher-order derivatives of the thermodynamic potential

$$\Omega = -\frac{T}{V}\log \mathcal{Z}(T,\mu_\mathrm{u},\mu_\mathrm{d},\mu_\mathrm{s}) \tag{4.1}$$

with respect to the quark chemical potentials,

$$\chi^{\mathrm{uds}}_{ijk} = -\frac{1}{T^{4-(i+j+k)}}\frac{\partial^{i+j+k}\Omega}{\partial\mu_\mathrm{u}^i\,\partial\mu_\mathrm{d}^j\,\partial\mu_\mathrm{s}^k} \tag{4.2}$$

with $i,j,k \in \mathbb{N}_0$. Here, V is the volume of the system and $\mathcal{Z}$ the grand-canonical partition function, i.e., the generating functional (2.14) for vanishing sources with the in-medium action (2.56). The prefactor serves as a normalization in order to render the fluctuations dimensionless. As mentioned in the previous chapter, the quark chemical potentials are related to the ones for baryon number (B), strangeness (S), and electric charge (Q) via

$$\begin{gathered}\mu_\mathrm{u} = \frac{1}{3}\mu_\mathrm{B} + \frac{2}{3}\mu_\mathrm{Q}\,, \qquad \mu_\mathrm{d} = \frac{1}{3}\mu_\mathrm{B} - \frac{1}{3}\mu_\mathrm{Q}\,,\\ \mu_\mathrm{s} = \frac{1}{3}\mu_\mathrm{B} - \frac{1}{3}\mu_\mathrm{Q} - \mu_\mathrm{S}\,.\end{gathered} \tag{4.3}$$

With these relations and using the chain rule of differentiation, we find for example the second-order baryon number fluctuation

$$\begin{aligned}\chi_2^\mathrm{B} &= -\frac{1}{T^2}\frac{\partial^2\Omega}{\partial\mu_\mathrm{B}^2}\\ &= \frac{1}{9}\left[\chi_2^\mathrm{u} + \chi_2^\mathrm{d} + \chi_2^\mathrm{s} + 2\left(\chi_{11}^\mathrm{us} + \chi_{11}^\mathrm{ds} + \chi_{11}^\mathrm{ud}\right)\right]\end{aligned} \tag{4.4}$$

in terms of quark number fluctuations. Other fluctuations can be determined analogously. In general, fluctuations and ratios thereof are sensitive to phase transitions [311–318] and are therefore well-suited to explore the phase structure of QCD. At the CEP, the correlation length of the system diverges (at least in infinite volume), $\xi_\mathrm{cor} \to \infty$, and $\chi_2^\mathrm{B} \propto \xi_\mathrm{cor}^\varepsilon$ with an exponent $\varepsilon > 0$. Thus, the proximity of the CEP is expected to leave clear imprints on the qualitative behavior of the fluctuations. In this work, we consider baryon number fluctuations up to fourth order and leave other fluctuations to future work.

In heavy-ion-collision experiments, the fluctuations manifest themselves as event-by-event fluctuations of the net-baryon number, the net-charge, or the net-strangeness. The cumulants C_n^X of the corresponding probability distribution of the conserved charge $X \in \{\mathrm{B}, \mathrm{Q}, \mathrm{S}\}$ are related to statistical quantities through [97]

$$M_X = C_1^X\,, \qquad \sigma_X^2 = C_2^X\,, \tag{4.5}$$

$$S_X = C_3^X \left(C_2^X\right)^{-3/2}, \qquad \kappa_X = C_4^X \left(C_2^X\right)^{-2}, \tag{4.6}$$

where M_X, σ_X^2, S_X, and κ_X denote the mean, variance, skewness, and kurtosis of the distribution, respectively. On the other hand, the cumulants are related to the fluctuations via $C_n^X = VT^3\chi_n^X$. Thus, the explicit volume dependence cancels in ratios, and prominent ratios related to the baryon number are

$$\frac{\chi_1^{\mathrm{B}}}{\chi_2^{\mathrm{B}}} = \frac{M_{\mathrm{B}}}{\sigma_{\mathrm{B}}^2}\,, \qquad \frac{\chi_3^{\mathrm{B}}}{\chi_2^{\mathrm{B}}} = S_{\mathrm{B}}\sigma_{\mathrm{B}}\,, \qquad \frac{\chi_4^{\mathrm{B}}}{\chi_2^{\mathrm{B}}} = \kappa_{\mathrm{B}}\sigma_{\mathrm{B}}^2\,, \tag{4.7}$$

and analogous expressions hold for charge and strangeness. These relations bridge the gap between theoretical results on the left-hand sides and experimentally accessible quantities on the right-hand sides. Again, see Refs. [47, 97, 320] for more details. Note that in experiment, fluctuations of the net-proton and net-kaon number are measured that serve as proxies for the theoretically calculated baryon number and strangeness fluctuations.

After having discussed some general aspects of fluctuations, we are now left with finding a formula that is suitable for our functional approach to compute quark and subsequently baryon number fluctuations, see Eq. (4.4). To this end, we resort to the 2PI formalism. The thermodynamic potential can be written as a functional of the propagators of the theory and is given by [207] (see also Ref. [340] for an overview)[30]

$$\begin{aligned} -\frac{V}{T}\,\Omega[S,D] = {}& \operatorname{Tr}\log S^{-1} - \operatorname{Tr}\left[\mathbb{1} - S_0^{-1}S\right] \\ & - \frac{1}{2}\operatorname{Tr}\log D^{-1} + \frac{1}{2}\operatorname{Tr}\left[\mathbb{1} - D_0^{-1}D\right] \\ & + \Xi_{\mathrm{int}}[S,D]\,, \end{aligned} \tag{4.8}$$

where S and D denote the dressed quark and gluon propagators, respectively, with all degrees of freedom[31], S_0^{-1} and D_0^{-1} are their bare counterparts, and the interaction functional Ξ_{int} contains all 2PI diagrams with respect to S and D, where all internal lines

[30] The ghost, which we omit for brevity, would appear as another fermionic contribution in Eq. (4.8).

[31] Flavor, color, Dirac, and momentum degrees of freedom for S; color, Lorentz, and momentum ones for D. Thus, the traces in Eq. (4.8) have to be understood in the functional sense over all these spaces.

are given by dressed propagators. The right-hand side of Eq. (4.8) is the exact expression for the 2PI effective action Γ_{2PI} [207] but evaluated at the stationary point. This is vital for the equality of the 2PI effective action with the thermodynamic potential (up to a sign and a four-dimensional volume factor) that holds only at the stationary point. Inserting the explicit expression for Γ_{2PI} into the stationary conditions

$$\frac{\delta\Gamma_{\mathrm{2PI}}}{\delta S} = 0\,, \qquad \frac{\delta\Gamma_{\mathrm{2PI}}}{\delta D} = 0 \tag{4.9}$$

yields the equations of motions for the propagators. These are—not unexpected—the DSEs but this time derived from the 2PI effective action:[32]

$$\begin{aligned} S^{-1} &= S_0^{-1} + \Sigma\,, \\ D^{-1} &= D_0^{-1} + \Pi\,, \end{aligned} \tag{4.10}$$

where the quark and gluon self-energies Σ and Π, respectively, are given by

$$\Sigma = \frac{\delta\Xi_{\mathrm{int}}}{\delta S}\,, \qquad \Pi = -2\,\frac{\delta\Xi_{\mathrm{int}}}{\delta D}\,. \tag{4.11}$$

Diagrammatically, the self-energies are thus obtained from the 2PI diagrams that constitute Ξ_{int} by cutting one internal line.

Therefore, evaluating Eq. (4.8) at the stationary point means nothing but that the propagators have to obey their equations of motion, i.e., are solutions of the corresponding DSEs. Note that the relations given above allow for an alternative way of deriving DSEs. Furthermore, even a theory itself can, in principle, be defined solely by a given 2PI effective action, i.e., without referring to a path integral or Lagrangian in the first place. In general, there are also contributions from one-point functions, i.e., from the macroscopic fields Φ_i [Eq. (2.27)], to the 2PI effective action, which, however, vanish at the stationary point. The corresponding stationary conditions $\delta\Gamma_{\mathrm{2PI}}/\delta\Phi_i = 0$ imply vanishing external sources, $J = 0$. In this case, the macroscopic quark fields vanish, $\langle\psi\rangle^{(J=0)} = \langle\bar{\psi}\rangle^{(J=0)} = 0$, due to their Grassmann nature. Furthermore, $\langle A_\mu\rangle^{(J=0)} = 0$, too, because otherwise Euclidean invariance would be broken.

With an explicit expression of the thermodynamic potential in terms of the propagators, Eq. (4.8), i.e., well-suited for our DSE framework, we can now find a formula for the quark number density. For a flavor f, it is generally given by

$$n_f = -\frac{\partial\Omega}{\partial\mu_f}\,. \tag{4.12}$$

[32] In the derivation of Eqs. (4.10) and (4.11), we used $\delta(\mathrm{Tr}\log A)/\delta A = A^{-1}$ and $\delta(\mathrm{Tr}\,AB)/\delta A = B$.

The μ_f derivative splits into an explicit and an implicit part, where the latter accounts for the chemical-potential dependence of the propagators because $\Omega = \Omega[S, D]$, viz.,

$$\frac{\partial \Omega}{\partial \mu_f} = \frac{\partial \Omega}{\partial \mu_f}\bigg|_{S,\,D=\text{const.}} + \frac{\delta \Omega}{\delta S}\frac{\partial S}{\partial \mu_f} + \frac{\delta \Omega}{\delta D}\frac{\partial D}{\partial \mu_f}\,. \tag{4.13}$$

Now, the stationary conditions come in handy: the last two terms in Eq. (4.13) do not contribute to the quark number density because $\delta\Omega/\delta S = \delta\Omega/\delta D = 0$. The same holds, of course, for the ghost contribution, too, which we do not write explicitly. We thus find

$$\begin{aligned} n_f &= \frac{\partial \Omega}{\partial \mu_f}\bigg|_{S,\,D=\text{const.}} \\ &= \frac{T}{V}\left(\operatorname{Tr}\left[\frac{\partial S_0^{-1}}{\partial \mu_f} S\right] + \frac{\partial \Xi_{\text{int}}}{\partial \mu_f}\bigg|_{S,\,D=\text{const.}}\right). \end{aligned} \tag{4.14}$$

At this point, one might think that we are stuck because to our knowledge there is no closed, explicit expression of Ξ_{int} available for our truncation scheme. However, the only chemical potential-dependent quantities in the interaction functional are the propagators because there are—by definition—no dressed vertices involved in the 2PI formalism. All vertices appearing in the diagrams of Ξ_{int}, in particular the quark-gluon vertex that would be (strongly) chemical-potential dependent in its dressed form, are bare. Thus, with all propagators held fixed, the chemical-potential derivative of the interaction functional vanishes, $\partial \Xi_{\text{int}}/\partial \mu_f\big|_{S,\,D=\text{const.}} = 0$.

Therefore, with $\partial S_0^{-1}/\partial \mu_f = -Z_2^f \gamma_4$ and after carrying out the traces in flavor, color, and momentum space, we eventually find

$$n_f = -N_\text{c}\, Z_2^f\, T \sum_{\ell_q \in \mathbb{Z}} \fint_{\boldsymbol{q}} \operatorname{Tr}\big[\gamma_4 S_f(q)\big]\,, \tag{4.15}$$

where the remaining trace has to be evaluated in Dirac space. This last trace is straightforward to compute and yields the final formula

$$n_f = 4\mathrm{i} N_\text{c}\, Z_2^f\, T \sum_{\ell_q \in \mathbb{Z}} \fint_{\boldsymbol{q}} \frac{(\omega_q + \mathrm{i}\mu_f) C_f(q)}{(\omega_q + \mathrm{i}\mu_f)^2 C_f^2(q) + \boldsymbol{q}^2 A_f^2(q) + B_f^2(q)}\,. \tag{4.16}$$

As a side remark, the quark number density can also be written as an expectation value, $n_f = \langle \bar{\psi}_f \gamma_4 \psi_f \rangle^{(J=0)}$, and its gauge invariance is guaranteed by the Landau–Khalatnikov–Fradkin transformations [341, 342]. Finally, we emphasize that Eq. (4.16) is obtained without any approximation and is therefore exact—in particular, truncation independent.

4.2 Regularization of the quark number density

With the quark number density given in Eq. (4.15), in principle, we simply have to carry out the Dirac trace and subsequently evaluate the three-momentum integration and Matsubara sum. However, it is not that easy, and we observe that

(i) it is necessary to perform the Matsubara sum first, followed by the three-momentum integration;[33]

(ii) a very large number of Matsubara frequencies is necessary—the sum has to cover frequencies up to $|\omega_q| = \mathcal{O}(1\,\mathrm{TeV})$—in order to obtain stable results;

(iii) even with the previous findings taken into account, n_f develops a spurious divergence, which is caused by the necessity of cutoffs in course of the numerical evaluation of the Matsubara sum and three-momentum integration.

The latter is particularly severe because the "naive" expression (4.15) for the quark number density is thus not well-defined and needs to be regularized. It can be argued that the divergence is rooted in the Matsubara sum. To this end, we employ the subtraction scheme used in Refs. [245, 343], which is a Euclidean version of the contour-integration technique for Matsubara sums [37, 108], and discuss it in the following.

Let $h(q_4, \boldsymbol{q}; \{\mu_f\})$ be a function that depends separately on the energy component and spatial components of the four-vector $q = (q_4, \boldsymbol{q})$ as well as on chemical potential. Furthermore, thinking of q_4 as a complex-valued quantity, h is assumed to be analytic in an infinitesimal neighborhood of the real q_4 axis, which includes in particular the Matsubara frequencies at $q_4 = \omega_q = (2\ell_q + 1)\pi T$ with $\ell_q \in \mathbb{Z}$. Now, our aim is to compute the Matsubara sum $T\sum_{\ell_q\in\mathbb{Z}} h(\omega_q, \boldsymbol{q}; \{\mu_f\})$. Keeping the chemical-potential dependence general[34], the Matsubara frequencies lie on the real q_4 axis, and the sum can be written as a contour integral by virtue of the residue theorem:

$$\begin{aligned} T\sum_{\ell_q\in\mathbb{Z}} h(\omega_q, \boldsymbol{q}; \{\mu_f\}) &= \sum_{\ell_q\in\mathbb{Z}} h(\omega_q, \boldsymbol{q}; \{\mu_f\})\,\mathrm{res}(\varphi, \omega_q) \\ &= \oint_{\mathcal{C}} \frac{\mathrm{d}q_4}{2\pi\mathrm{i}}\, h(q_4, \boldsymbol{q}; \{\mu_f\})\,\varphi(q_4) \end{aligned} \tag{4.17}$$

with $\varphi(q_4) = -\mathrm{i}/\left(1 + \mathrm{e}^{\mathrm{i}q_4/T}\right)$, which is analytic and bounded on $\mathbb{C} \setminus \{\omega_q : \ell_q \in \mathbb{Z}\}$ with residue $\mathrm{res}(\varphi, \omega_q) = T$ at the Matsubara frequencies. The contour $\mathcal{C}$, shown in the

[33] Consequently, the summation and integration is not performed in an O(4)-invariant way. Numerically, we thus have independent (and different) cutoffs for the Matsubara sum and the three-momentum integration.

[34] That is, not of the particular form $\omega_q + \mathrm{i}\mu_f$ since h is, apart from the analyticity assumption, arbitrary.

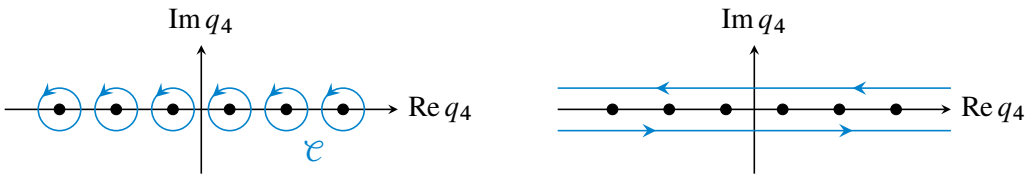

Figure 4.1 Contours (blue, solid lines) for the frequency summation: original contour $\mathcal{C}$ (left) and the deformed one (right). The Matsubara frequencies are indicated by black dots.

left diagram of Fig. 4.1, consists of counterclockwise-oriented circles with infinitesimal radius $\eta > 0$ that enclose each Matsubara frequency. It can be deformed into line integrals in the upper and lower half plane, displayed in the right diagram of Fig. 4.1. Incorporating the minus sign contained in φ, which inverts the direction of the line integrals, and using $\left(1 + \mathrm{e}^{\mathrm{i}q_4/T}\right)^{-1} = 1 - \left(1 + \mathrm{e}^{-\mathrm{i}q_4/T}\right)^{-1}$, we find

$$\begin{aligned} T \sum_{\ell_q \in \mathbb{Z}} h(\omega_q, \boldsymbol{q}; \{\mu_f\}) = &\int_{\infty - \mathrm{i}\eta}^{-\infty - \mathrm{i}\eta} \frac{\mathrm{d}q_4}{2\pi} \frac{h(q_4, \boldsymbol{q}; \{\mu_f\})}{1 + \mathrm{e}^{\mathrm{i}q_4/T}} \\ &- \int_{-\infty + \mathrm{i}\eta}^{\infty + \mathrm{i}\eta} \frac{\mathrm{d}q_4}{2\pi} \frac{h(q_4, \boldsymbol{q}; \{\mu_f\})}{1 + \mathrm{e}^{-\mathrm{i}q_4/T}} \\ &+ \int_{-\infty}^{\infty} \frac{\mathrm{d}q_4}{2\pi} h(q_4, \boldsymbol{q}; \{\mu_f\}) \,, \end{aligned} \tag{4.18}$$

which holds for every function h that is analytic in an infinitesimal neighborhood of the real q_4 axis.

The first two contributions on the right-hand side of Eq. (4.18) involve the Fermi–Dirac distribution functions and are thus ultraviolet finite due to the exponential damping, while the third term does not depend explicitly on temperature or chemical potential and is known as a "vacuum contribution" in the literature [108]. Indeed, the continuous integration $\int_{-\infty}^{\infty} \mathrm{d}q_4 / 2\pi$ is the zero-temperature limit of the Matsubara sum $T \sum_{\ell_q \in \mathbb{Z}}$. Thus, we conclude that this term contains the divergence, and a finite, divergence-free expression can be obtained by subtracting it from the Matsubara sum on the left-hand side.[35] Therefore, the regularized quark number density is given by

$$n_f^{\mathrm{reg}} = -N_\mathrm{c} Z_2^f \oint_{\boldsymbol{q}} \left(T \sum_{\ell_q \in \mathbb{Z}} \mathrm{Tr}\left[\gamma_4 S_f(\omega_q, \boldsymbol{q})\right] - \int_{-\infty}^{\infty} \frac{\mathrm{d}q_4}{2\pi} \mathrm{Tr}\left[\gamma_4 S_f(q_4, \boldsymbol{q})\right] \right). \tag{4.19}$$

[35] A divergence in the quark number density (and derived quantities) occurs on the lattice, too, and it can be further shown that the divergence is already present in the free, noninteracting continuum theory [344].

In order to illustrate the subtraction scheme for the quark number density, in Fig. 4.2 we display the real part of the Matsubara sum (blue, solid line) and the real part of the q_4 integration (red, dashed line) of $\mathrm{Tr}[\gamma_4 S_\mathrm{u}]$ together with their difference (green, dashed-dotted line) as a function of the three-momentum at $T = 100\,\mathrm{MeV}$ and $\mu_\mathrm{B} = 150\,\mathrm{MeV}$. The regularized up-quark number density is then, apart from various prefactors, obtained by integrating the difference with respect to the three-momentum. First, the imaginary part of both the ω_q sum and the q_4 integration of $\mathrm{Tr}[\gamma_4 S_\mathrm{u}]$ vanishes, i.e., the density is real as it should be. Recall that the quark dressing functions are complex valued for nonvanishing chemical potential, and generally $\mathrm{Tr}[\gamma_4 S_\mathrm{u}] \in \mathbb{C}$, too. Second, the integration of the Matsubara sum alone is positive and would result in combination with the global minus sign in Eq. (4.15) in a negative density. The q_4 integration, however, is larger than the sum and their difference yields a negative value upon integration and eventually a positive density. Furthermore, though hardly visible in the figure, the sum does not tend (sufficiently close) to zero for large $|\boldsymbol{q}|$. Consequently, the result of the numerical three-momentum integration depends on the employed cutoff. Finally, the q_4 integration has the same asymptotic behavior than the sum, and the difference of both therefore admits an unambiguous three-momentum integration.

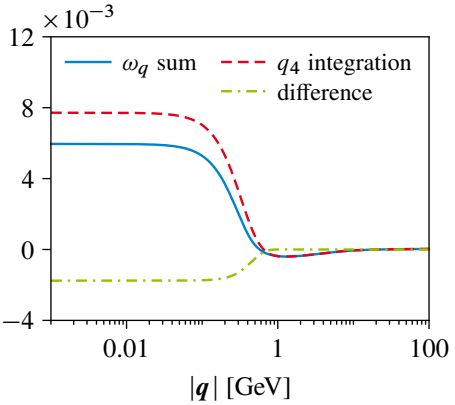

Figure 4.2 $\mathrm{Re}\big(T\sum_{\ell_q\in\mathbb{Z}}\mathrm{Tr}[\gamma_4 S_\mathrm{u}]\big)$ and $\mathrm{Re}\big(\int_{-\infty}^{\infty}\mathrm{d}q_4\,\mathrm{Tr}[\gamma_4 S_\mathrm{u}]/2\pi\big)$, labeled "$\omega_q$ sum" and "q_4 integration," respectively, and their difference.

With a regularized expression for the quark number density at hand, the fluctuations are obtained by additional chemical-potential derivatives of it. For example, the second-order up-quark number fluctuation (also known as the quark number susceptibility) is given by

$$\chi_2^\mathrm{u} = \frac{1}{T^2}\frac{\partial n_\mathrm{u}^\mathrm{reg}}{\partial \mu_\mathrm{u}}\,, \tag{4.20}$$

and other quantities are obtained analogously.

4.3 Fluctuations in the phase diagram

Now, we proceed with our results for the fluctuations. In this work, we discuss quark and baryon number fluctuations, which are obtained within our DSE framework from the quark number density along the lines of the previous section. Before we continue,

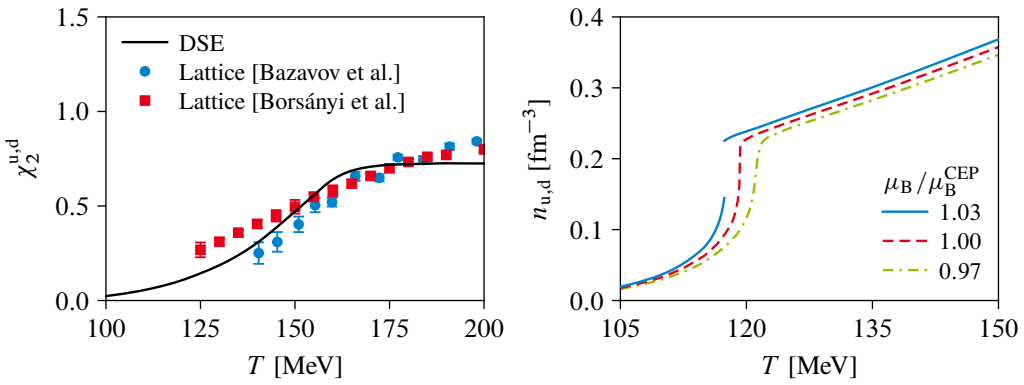

Figure 4.3 Left: second-order up/down-quark number fluctuation at vanishing chemical potential. The lattice results are taken from Refs. [55, 322]. Right: up/down-quark number density in the vicinity of the CEP for three different chemical potentials.

however, we briefly comment on the notation for the remainder of this chapter. Since we work in the isospin-symmetric limit of mass- and chemical-potential-wise degenerated light quarks, the up- and down-quark number fluctuations are consequently degenerate, too, and simply called the up/down-quark number fluctuation $\chi_n^{u,d}$. It does not contain a degeneracy factor of two so that the "true" light-quark number fluctuation, if needed, would be given by $\chi_n^{light} = 2\,\chi_n^{u,d}$. The same applies to the quark number density of the up and down quarks.

Quark number fluctuations

In the left diagram of Fig. 4.3, we show the second-order up/down-quark number fluctuation at vanishing chemical potential as a function of temperature (black, solid line) in comparison to lattice-QCD results (colored symbols) [55, 322]. The agreement with the lattice is not as good as for the subtracted quark condensate, see Fig. 3.3, but still very reasonably. Our result increases up to $T \approx 165\,\text{MeV}$ and reaches an asymptotic value of approximately 0.72 in the high-temperature region above T_c. Clearly, this saturation is well below the Stefan–Boltzmann limit, $\chi_2^{u,d} \to 1$ as $T \to \infty$, and happens at much too low temperatures. This is the first place where the deficiencies of our vertex ansatz as discussed in Chapter 3 become noticeable. The correct high-temperature behavior of the fluctuations is caused by the continuous weakening of the quark-gluon interaction above T_c, which drives the system eventually toward the Stefan–Boltzmann limit. Necessary for that are tensor structures of the quark-gluon vertex which react strongly to the restoration of chiral symmetry. In Landau gauge, the full in-medium quark-gluon vertex contains twenty-four different tensor structures, and half of them are only present when chiral symmetry is broken. This is clearly

not captured by our ansatz, Eq. (3.7). Phrased differently, we overestimate the remnant effects of DCSB at temperatures above T_c, which leads to the high-temperature artifacts seen in $\chi_2^{u,d}$. In this work, however, we are not interested in the high-temperature limit, and our vertex ansatz delivers satisfying results in the temperature region 120–160 MeV, i.e., below and around the pseudocritical chiral transition temperature.

Since $\chi_2^{u,d}$ experiences the most rapid growth in the region of the crossover, its inflection point with respect to temperature can also be used to define the pseudocritical chiral transition temperature, for which no unique definition exists because of the crossover nature of the transition. We find $T_c^{(\chi_2)} = 153\,\text{MeV}$, which is in good agreement with our result from the subtracted quark condensate, Eq. (3.17).

Now, we turn to nonzero chemical potential. The right diagram of Fig. 4.3 displays the up/down-quark number density $n_{u,d} = T^3 \chi_1^{u,d}$ at three different chemical potentials around our CEP as a function of temperature. At $\mu_B = \mu_B^{CEP}$ (red, dotted line), the slope of the density tends to infinity at $T = T_{CEP}$, which will yield a diverging second-order fluctuation. For chemical potentials above the critical one, the system undergoes a first-order phase transition, and the density is therefore discontinuous across the phase boundary and shows a finite jump (blue, solid line). This behavior is consistent with results from effective models, see, e.g., Refs. [63, 345]. The location of the first-order transition lies within the (at this chemical potential very small) region between the upper and lower spinodal lines shown in the phase diagram in Fig. 3.10. Below the chemical potential of the CEP, where the transition is an analytic crossover, the slope of the density around the pseudocritical chiral transition temperature is finite (green, dashed-dotted line). Generally, the density changes continuously as a function of temperature for all $\mu_B < \mu_B^{CEP}$. At large temperatures, the density is an almost linear function of the temperature regardless of the value of the chemical potential.

The fluctuations can also be used to draw conclusions about the scaling behavior at the CEP. Thus, next we discuss the scaling behavior of the second-order up/down-quark number fluctuation in the vicinity of the CEP. At this point, the fluctuation diverges with a characteristic critical exponent ε. For a fixed temperature, the behavior of $\chi_2^{u,d}$ close to the CEP as a function of the chemical potential is described by

$$\chi_2^{u,d} = |\bar{\mu}|^{-\varepsilon}\,, \tag{4.21}$$

where $\bar{\mu} = 1 - \mu_B/\mu_B^{CEP}$. For our scaling analysis, we use the path parallel to the chemical-potential axis at the fixed temperature $T = T_{CEP}$ from lower μ_B up to the critical value μ_B^{CEP}, i.e., we approach the CEP from the crossover side, $\bar{\mu} > 0$. In general, the value of the critical exponent depends on the path that is chosen in the μ_B-T plane [328, 346]. Since the CEP is expected to be in the same universality class as the three-dimensional

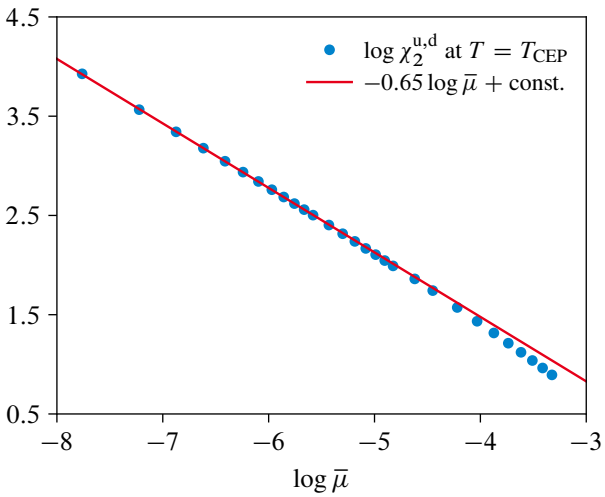

Figure 4.4 Logarithm of the second-order up/down-quark number fluctuation as a function of $\log \bar{\mu}$, where $\bar{\mu} = 1 - \mu_{\mathrm{B}}/\mu_{\mathrm{B}}^{\mathrm{CEP}} > 0$, at $T = T_{\mathrm{CEP}}$. The red, solid line is a linear fit.

Ising model [311, 347–349], here (with a path not asymptotically parallel to the first-order line) one expects a critical exponent of $\varepsilon \approx 0.79$ [350–352]. Mean-field scaling according to Landau theory would entail $\varepsilon = 2/3$ [353]. We extract ε from

$$\log \chi_2^{\mathrm{u,d}} = -\varepsilon \log \bar{\mu} + \text{const.} \tag{4.22}$$

using a linear fit, where the offset is $\bar{\mu}$ independent, and find the critical exponent

$$\varepsilon = 0.65 \pm 0.05\,, \tag{4.23}$$

which is in agreement with the mean-field value. The given error contains the numerical one that stems from the fit but it is dominated by the uncertainty that is accompanied with the precise location of the CEP. The fit together with the scaling behavior is shown in Fig. 4.4. It becomes apparent that scaling sets in rather late, namely not until $\mu_{\mathrm{B}}^{\mathrm{CEP}} - \mu_{\mathrm{B}} \lesssim 3\,\mathrm{MeV}$, indicating that the critical region in chemical-potential direction is quite small. This is consistent with results obtained within effective models, see, e.g., Refs. [328, 345].

It is not surprising, however, that the critical exponents of our CEP are mean field because the effects that trigger the CEP are purely gluonic in nature. In Ref. [258], it was shown that the inclusion of explicit pion and sigma-meson contributions generates the correct critical O(4) scaling at the chiral transition of the chiral two-flavor theory at nonzero temperature but vanishing chemical potential. We thus expect that the extension of these contributions to nonzero chemical potential holds the potential to put our CEP in the correct $\mathbb{Z}_2$ universality class. Building upon the works [101, 262], taking pion and sigma-meson

effects at nonzero temperature and chemical potential within our truncation into account has been accomplished recently [263], though under approximations in an exploratory fashion. A detailed discussion can be found in Ref. [102]. Thus, in principle, we have the framework at hand to compute the critical exponent ε with pion and sigma-meson contributions explicitly taken into account. However, a tremendous computational effort (in terms of CPU hours) is required, and this study is postponed to future work.

Before we continue with the baryon number fluctuations, we would like to comment on strangeness neutrality. Our choice of a vanishing strange-quark chemical potential, $\mu_\mathrm{s} = 0$, combined with the isospin-symmetric limit we are working in (i.e., $\mu_\mathrm{Q} = 0$) corresponds to a fixed strangeness chemical potential of $\mu_\mathrm{S} = \mu_\mathrm{B}/3$; see relations (4.3). As discussed earlier, the strangeness chemical potential is in general a nontrivial function of μ_B and T such that strangeness neutrality is fulfilled, i.e., such that the strangeness density vanishes. However, since this work is the first that is concerned with obtaining thermodynamic quantities from DSEs with the truncation detailed in the previous chapter, we postpone the consistent implementation of strangeness neutrality to future work and keep $\mu_\mathrm{s} = 0$ throughout this work.[36] While we do not expect $\chi_2^{\mathrm{u,d}}$ to be strongly affected by that choice, this is certainly different for χ_2^{s}. Thus, we refrain from comparing this quantity with lattice results. Nevertheless, we use it to compute baryon number fluctuations.

Baryon number fluctuations

With the quark number fluctuations at hand, we are now able to compute the baryon number fluctuations. In particular, we are interested in the changes induced by increasing chemical potential in the fluctuations and ratios thereof as we approach the CEP. In the course of this work, we limit ourselves to fluctuations diagonal with respect to the quark flavor and neglect off-diagonal fluctuations. This is, at least to some extent, justified by lattice-QCD results indicating that off-diagonal fluctuations are subleading as compared to diagonal ones [322, 324]. Then, the n^{th}-order baryon number fluctuation, $n \geq 1$, in the isospin-symmetric limit of degenerate up and down quarks is given by

$$\chi_n^{\mathrm{B}} = \frac{1}{3^n}\left(2\chi_n^{\mathrm{u,d}} + \chi_n^{\mathrm{s}}\right). \tag{4.24}$$

We choose a selection of fixed chemical potentials and evaluate the baryon number fluctuations as functions of temperature. The result is shown in the left diagram of Fig. 4.5,

[36] The impact of strangeness neutrality on thermodynamic quantities was studied in Ref. [354] within the Polyakov-loop enhanced quark-meson model using the FRG. At large chemical potentials, quantitative corrections up to the order of twenty percent for some thermodynamic quantities were found. Therefore, the proper implementation of strangeness neutrality should be aimed at in the long term.

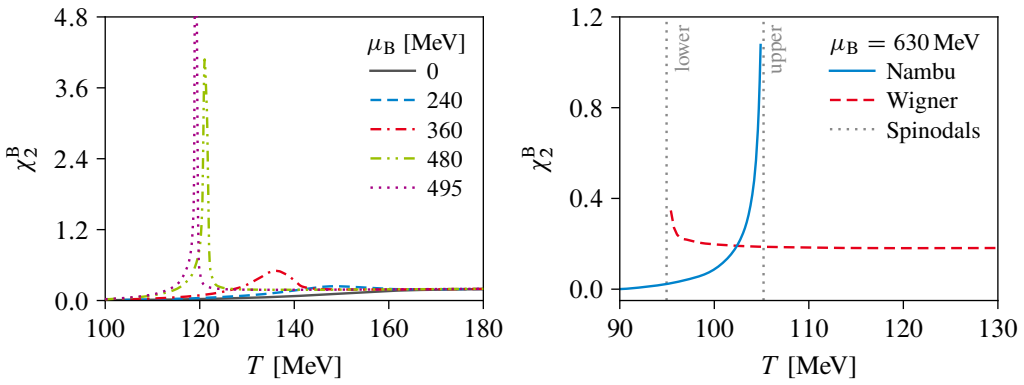

Figure 4.5 Second-order baryon number fluctuation approaching the CEP (left) and beyond in the first-order region of the phase diagram (right).

where we display the second-order baryon number fluctuation approaching the CEP. At vanishing chemical potential (gray, solid line), the behavior is similar to the up/down quark number fluctuation, see Fig. 4.3, i.e., we find a monotonous increase below and around the pseudocritical chiral transition temperature. At nonzero chemical potential about halfway toward the CEP, a bulge begins to develop at and around T_c (blue, dashed line). The bulge becomes larger and more pronounced with increasing chemical potential (red, dashed-dotted line). Close to the location of the CEP, the bulge grows considerably and becomes a sharp peak (green, dashed-double-dotted line) that finally diverges at the CEP (purple, dotted line), as expected from the behavior of the quark number density as discussed above.[37] The behavior of χ_2^B in the first-order region is shown in the right diagram of Fig. 4.5. Similar to the quark condensate, the second-order baryon number fluctuation splits into two branches corresponding to the chirally-broken Nambu solution (blue, solid line) and the (partially) chirally-symmetric Wigner solution (red, dashed line) of the DSE for the quark propagator. The overlap of the two branches defines the coexistence region of a first-order transition that is bounded by spinodals, which are indicated by vertical gray, dotted lines. For temperatures above and below the coexistence region, χ_2^B is only very slowly varying with temperature and almost constant.

Next, we discuss ratios of fluctuations that are directly related to experimental quantities in heavy-ion collisions through event-by-event analyses [see Eq. (4.7)]. In Fig. 4.6, we show the skewness ratio χ_3^B/χ_2^B (left diagram) and the kurtosis ratio χ_4^B/χ_2^B (right diagram), transformed by the inverse hyperbolic sine for better visibility, again as a function of temperature for different chemical potentials up to the CEP. The ratios show distinctive

[37] In principle, one could fine-tune the chemical potential to come arbitrarily close to the actual divergence. In practice, however, limited numerical accuracy together with finite computational resources always lead to a very sharp peak of χ_2^B with a very large but still finite magnitude.

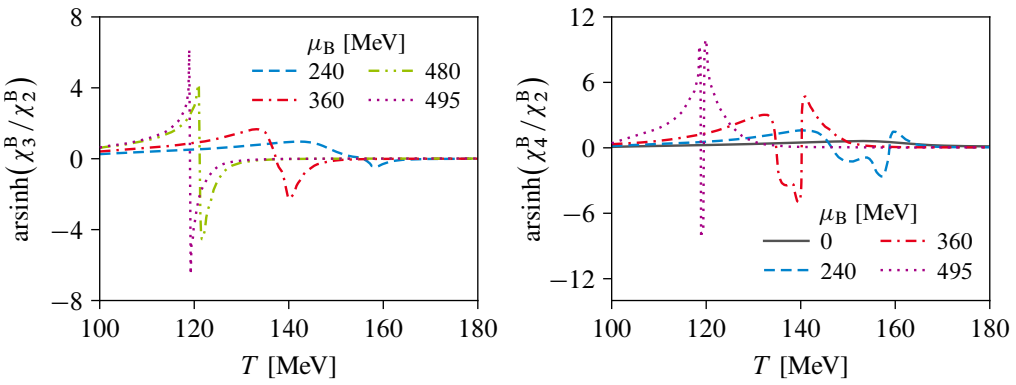

Figure 4.6 Skewness ratio χ_3^B/χ_2^B (left) and kurtosis ratio χ_4^B/χ_2^B (right) approaching the CEP. We show the inverse hyperbolic sine of the ratios for better visibility. Since $\operatorname{arsinh}(x) \sim x$ as $x \to 0$ and $\operatorname{arsinh}(x) \sim \pm\log(2|x|)$ as $x \to \pm\infty$, we get in principle a logarithmic plot in both positive and negative direction.

features. Whereas for small chemical potentials up to halfway toward the CEP all structures are small in size, these grow rapidly as the CEP is approached. The skewness develops a characteristic rise with temperature when the crossover is approached accompanied by a zero crossing and subsequently an equally drastic decrease when the temperature is increased further. This structure becomes extremely pronounced close to the CEP. Note that we do not show the $\mu_B = 0$ result since all odd fluctuations vanish at zero chemical potential. Correspondingly, the kurtosis ratio χ_4^B/χ_2^B develops an asymmetric double-peak structure across the phase boundary. In general, both ratios react strongly across the crossover line and particularly to the presence of the CEP, which emphasizes that (ratios of) fluctuations are well-suited quantities to explore the phase diagram of QCD.

In Fig. 4.7, we display our result for the ratio χ_1^B/χ_2^B computed along our crossover transition line $T_c(\mu_B)$. For small chemical potential up to $\mu_B/T \lesssim 1.5$, it is expected from the hadron resonance gas model that the ratio is approximately given by $\tanh(\mu_B/T)$ [355, 356]. This was found in the Polyakov-loop enhanced quark-meson model as well [357], and also shows up in our calculation. Sizable deviations only occur for larger chemical potential. After its maximum at $\mu_B/T \approx 1.6$, the ratio goes down again and signals the approach to the CEP in the course of which χ_2^B increases significantly as already seen in Fig. 4.5.

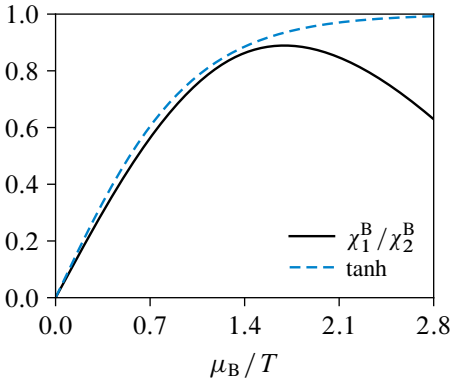

Figure 4.7 Ratio χ_1^B/χ_2^B as a function of μ_B/T compared to the hyperbolic tangent along the crossover line $T_c(\mu_B)$.

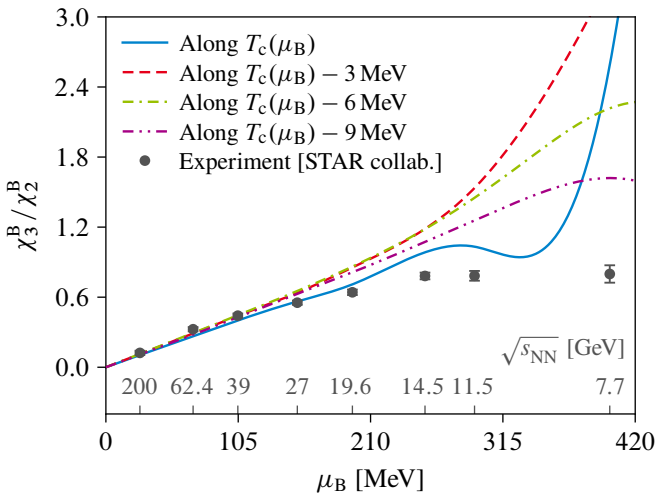

Figure 4.8 Skewness ratio χ_3^B / χ_2^B along the crossover line and along lines with a fixed temperature distance from the crossover. Furthermore, we show experimental data from the STAR collaboration at most central collisions at RHIC [95, 96]. We adopt the μ_B-$\sqrt{s_{NN}}$ translation from Ref. [307].

Even though one has to be cautious when comparing theoretical results (for fluctuations) with experimental data, there is considerable interest to do so. The caveats involved are related to the experimental situation in heavy-ion collisions such as the finite volume and the finite temporal extent of the fireball and the question whether/when the system is in thermal equilibrium. Furthermore, these are related to details of the experimental analysis such as centrality cuts, the question whether proton number fluctuations are a proxy for baryon number fluctuations, and potential other issues. More details can be found in the reviews [47, 97] and references therein.

Nevertheless, we attempt such a comparison in the following. In Figs. 4.8 and 4.9, we present our results for the skewness ratio χ_3^B / χ_2^B and the kurtosis ratio χ_4^B / χ_2^B, respectively (solid, blue lines), along the crossover line. Remember that we determine the latter from the inflection point of the subtracted quark condensate [Eq. (2.70)], and several definitions are employed in the literature because T_c is not uniquely defined. For the skewness, this criterion leaves us on the left and positive branch of the oscillations shown in Fig. 4.6. For the kurtosis, however, we probe the small negative region around the phase boundary once the chemical potential becomes large. At small chemical potential, there is a good agreement between our results and recent experimental data for net-proton fluctuations from the STAR collaboration at most central collisions [95, 96], which was collected during the first phase of the Beam Energy Scan program at RHIC. From a collision energy (center of mass energy per nucleon pair) of $\sqrt{s_{NN}} = 14.5\,\text{GeV}$ on, about halfway toward our CEP, this agreement becomes worse and disappears completely for $\sqrt{s_{NN}} \leq 11.5\,\text{GeV}$.

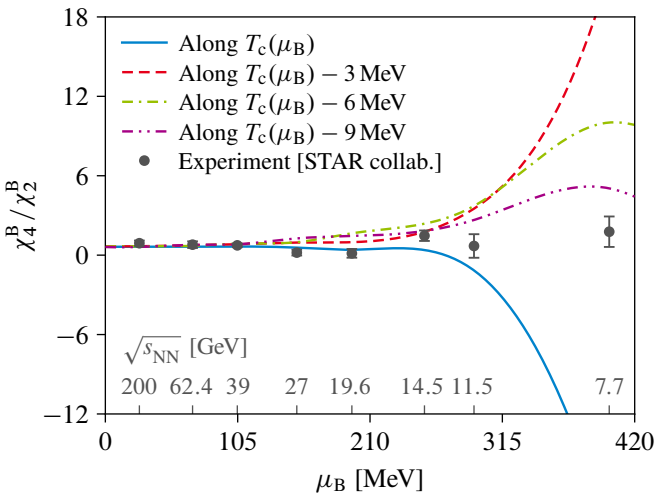

Figure 4.9 Same as Fig. 4.8 but for the kurtosis ratio χ_4^B / χ_2^B.

In order to discuss this aspect further, we also evaluate the skewness and kurtosis ratios on lines with a fixed temperature distance of three, six, and nine MeV below the crossover line. The idea of this comparison is to study the impact of two different effects. First, as already mentioned several times, there is no unique definition of the critical temperature in the crossover region, and it is therefore by no means clear whether a given definition should coincide with the experimental freeze-out line or not. Second, as the chemical potential becomes larger and a potential CEP is approached, it is also not clear whether the freeze-out line and the crossover line have the same curvature. In other words, it may very well be that the freeze-out line bends stronger than the crossover line and the distance between the two lines grows with chemical potential. Taken at face value, our results shown in Figs. 4.8 and 4.9 seem to support this notion at least on a qualitative level. At small chemical potential, variations in both ratios with temperature are very small and cannot be discriminated by the data. The two data points at $\sqrt{s_{NN}} = 19.6\,\mathrm{GeV}$ and $\sqrt{s_{NN}} = 14.5\,\mathrm{GeV}$, however, favor a scenario with a freeze-out line very close to the crossover line, and we conclude that this is generally the case for $\sqrt{s_{NN}} > 14.5\,\mathrm{GeV}$. The results for the kurtosis ratio at $\sqrt{s_{NN}} = 11.5\,\mathrm{GeV}$ and $\sqrt{s_{NN}} = 7.7\,\mathrm{GeV}$, however, suggest that the freeze-out line in this region of the phase diagram is separated from the crossover line by at least nine MeV in temperature direction. The corresponding results for the skewness ratio show the same general trend, although on a less quantitative level than the ones for the kurtosis.

Finally, we would like to note that several caveats are involved in the comparison of our results with the experimental data. On the one hand, we already mentioned the caveats on the experimental side, which are discussed and reviewed in Refs. [47, 97]. On the other

hand, our theoretical calculation in its present state suffers from several limitations. First, the influence of off-diagonal fluctuations is not taken into account yet. Second, as already discussed in Chapter 3, there is a probably substantial error associated with the precise location of the CEP. This error is expected to be reduced in the future by the systematic in-depth comparison with other truncations within DSEs and with FRG studies. Third, one has to keep in mind that the critical exponents of the CEP found in this work are mean field. The transition from mean-field scaling to the correct $\mathbb{Z}_2$ universality class of the three-dimensional Ising model is expected to result in a decrease of the size of the critical region around the CEP [328], which in turn will drive our results closer to the STAR data even if the location of the CEP remains unchanged.

4.4 Summary

Within the truncation scheme presented in the previous chapter, here we investigated for the first time quark and baryon number fluctuations. The starting point has been the quark number density, which has been extracted from the quark propagator by means of an exact formula derived from the thermodynamic potential in propagator representation. With a nonperturbative quark propagator and numerically necessary cutoffs, we found that the expression for the quark number density needed to be regularized. To this end, we employed a subtraction scheme based on a Euclidean version of the contour-integration technique for Matsubara sums. With a regularized quark number density at hand, we computed quark and baryon number fluctuations and ratios thereof across the QCD phase diagram. In particular, we determined the critical scaling behavior of the second-order up/down-quark number fluctuation at our CEP. Given our truncation of the quark-gluon vertex, we found not surprisingly mean-field scaling. We also found that the high-temperature behavior of the fluctuations is quite sensitive to the details of the quark-gluon vertex, which allowed us to identify possible improvements of our truncation scheme. Furthermore, in order to make contact with recent data from the Beam Energy Scan program at RHIC, we determined the skewness and kurtosis ratios along our crossover line. In addition, we also scanned lines with a fixed temperature distance below the transition line. While our results agreed with the STAR data for $\mu_{\mathrm{B}} < 250\,\mathrm{MeV}$ along the crossover, qualitative agreement at larger chemical potential had been obtained (at least to some extent) assuming the freeze-out and crossover lines separate at larger chemical potential.

5 Thermodynamics from the quark condensate

The quark and baryon number fluctuations, which we calculated in the last chapter, are the first foray into QCD thermodynamics within the DSE truncation used in this work. However, our starting point has been the quark number density but not the pressure itself. Generally speaking, in order to understand and explain the various phases and thermodynamic properties of QCD, the quantities of choice are the pressure, entropy density, and energy density—in short, the equation of state (EoS)—as functions of temperature and chemical potential. Moreover, the knowledge of the EoS of matter under a given physical environment is important for numerous reasons ranging from hydrodynamic simulations in the context of heavy-ion collisions to astrophysical issues like supernovae or neutron stars; see, e.g., Refs. [358, 359] for reviews.

At vanishing chemical potential, QCD's EoS is well-known from first-principle lattice QCD, where the full continuum-extrapolated EoS is available [360, 361]. However, the situation is different at nonzero, real-valued chemical potential. There, lattice QCD is hampered by the notorious sign problem [58]. Results for the EoS are limited to rather small chemical potential and usually obtained via extrapolation from imaginary chemical potential or using the Taylor expansion technique [299, 300, 302, 362].

Within functional methods, which do not suffer from the sign problem and are thus well-suited to complement lattice calculations, the computation of the EoS boils down to the calculation of the thermodynamic potential Ω, Eq. (4.1), that contains all thermodynamic information of the system. In contrast to the FRG where solving its flow equation yields directly the thermodynamic potential, see, e.g., Refs. [74, 354, 363–366], accessing this quantity with DSEs is extremely difficult and has been accomplished so far only within simple models [245, 367, 368]. This is due to the fact that at the very beginning of the DSE framework stands a derivative of the effective action. The master DSE reads [Eq. (2.38)]

$$\frac{\delta\Gamma_{1\mathrm{PI}}[\Phi]}{\delta\Phi_i} = \frac{\delta I^{\mathrm{gf}}_{\mathrm{QCD}}}{\delta\phi_i}\bigg|_{\phi_k\to\Phi_k+\delta/\delta J_k} 1\,, \tag{5.1}$$

and at the stationary point, the effective action is, up to a sign and volume factor, equivalent to the thermodynamic potential. Thus, a (functional) integration is necessary to get hold of

the potential itself. This obstacle manifests more directly in the 2PI formalism. Recalling the explicit form of Ω as a functional of the propagators [Eq. (4.8)],

$$\begin{aligned} -\frac{V}{T}\,\Omega[S,D] = \operatorname{Tr}\log S^{-1} - \operatorname{Tr}\left[\mathbb{1} - S_0^{-1}S\right] - \frac{1}{2}\operatorname{Tr}\log D^{-1} \\ + \frac{1}{2}\operatorname{Tr}\left[\mathbb{1} - D_0^{-1}D\right] + \Xi_{\text{int}}[S,D]\,, \end{aligned} \tag{5.2}$$

we readily see that an explicit expression for the interaction functional Ξ_{int} is needed to compute the potential. Unfortunately, such a closed, explicit expression is only available for certain truncations where the quark-gluon vertex does not depend on the quark dressing functions—which, in principle, should be the case; see Eq. (3.5). For example, in rainbow-ladder truncations with a gluon model where the quark-gluon vertex is simply the bare one, the interaction functional is given by $\Xi_{\text{int}}^{\text{rainbow-ladder}}[S] = \frac{1}{2}\operatorname{Tr}\left[\mathbb{1} - S_0^{-1}S\right]$. In particular, to our knowledge there is no closed, explicit expression of Ξ_{int} available for our quark-gluon vertex ansatz.

Therefore, it is highly desirable to develop a truncation-independent way to calculate the thermodynamic potential, and with that the EoS, from DSEs. In this chapter, we present such a method that is based on a general relation between the quark condensate and the entropy density. The method, which is detailed in the following, was initially proposed in Ref. [369]. It is together with first results—the ones presented in the upcoming Section 5.3—published in Ref. [99].

5.1 Connecting the quark condensate and thermodynamics

In this section, we mainly consider only one light flavor with quark chemical potential μ for the sake of brevity. As already mentioned earlier, the fundamental quantity for thermodynamics is the thermodynamic potential

$$\Omega(T,\mu) = -\frac{T}{V}\log\mathcal{Z}(T,\mu)\,, \tag{5.3}$$

where T is the temperature, V the volume of the system, and $\mathcal{Z}$ the grand-canonical partition function. The thermodynamic quantities pressure (P), entropy density (s), and quark number density (n) follow from the standard relations [108]

$$\begin{aligned} P(T,\mu) &= -\big(\Omega(T,\mu) - \Omega(0,0)\big)\,, \\ s(T,\mu) = -\frac{\partial\,\Omega(T,\mu)}{\partial T}\,, &\qquad n(T,\mu) = -\frac{\partial\,\Omega(T,\mu)}{\partial\mu}\,. \end{aligned} \tag{5.4}$$

A subsequent Legendre transform of the pressure yields the energy density

$$\mathcal{E}(T,\mu) = Ts(T,\mu) + \mu n(T,\mu) - P(T,\mu)\,, \tag{5.5}$$

and with that, one defines the interaction measure

$$\mathcal{I}(T,\mu) = \mathcal{E}(T,\mu) - 3P(T,\mu)\,. \tag{5.6}$$

It is related to the trace of QCD's energy-momentum tensor, hence also referred to as the trace anomaly, and measures the deviation of the EoS from the one of an ideal gas, which is given by $\mathcal{E} = 3P$.

In addition to temperature and chemical potential, the current quark mass m can also be seen as an additional variable the thermodynamic potential depends on. It enters the action as an external source for the field bilinear $\bar{\psi}\psi$, and the quark condensate is thus obtained via

$$\langle\bar{\psi}\psi\rangle(T,\mu;m) = \frac{\partial\Omega(T,\mu;m)}{\partial m}\,. \tag{5.7}$$

In principle, this relation can be inverted to yield the thermodynamic potential, at some given temperature and chemical potential, as an integral over the quark condensate with respect to the current quark mass,

$$\Omega(T,\mu;m_2) - \Omega(T,\mu;m_1) = \int_{m_1}^{m_2} \mathrm{d}m'\,\langle\bar{\psi}\psi\rangle(T,\mu;m')\,. \tag{5.8}$$

Unfortunately, this relation is not suitable for an actual calculation because the thermodynamic potential and the quark condensate are both divergent. The divergence is contained in the vacuum contribution of Ω and even present in the noninteracting theory [108]; see also the discussion in Section 4.2 and particularly Eq. (4.18). Since the divergence is independent of temperature and chemical potential—the introduction of a medium does not introduce new, additional divergences—we expect that suitable derivatives of the thermodynamic potential and quark condensate are finite. Therefore, differentiating Eq. (5.8) with respect to temperature and using the relations (5.4) yields the well-defined, i.e., divergence-free equation

$$s(T,\mu;m_2) - s(T,\mu;m_1) = -\int_{m_1}^{m_2} \mathrm{d}m'\,\frac{\partial\langle\bar{\psi}\psi\rangle(T,\mu;m')}{\partial T}\,, \tag{5.9}$$

which, in principle, allows us to extract the entropy density from the quark condensate. What is left to use this relation in practical calculations is to specify the integral limits. We set the lower one to the physical current quark mass, $m_1 = m$, and send the upper one to

infinity, $m_2 \to \infty$. The advantage of the latter is that an infinitely heavy quark freezes out of the system since it is too heavy to get thermally excited and does not contribute to thermodynamics. The corresponding entropy density is then simply the one of pure YM theory: $\lim_{m_2\to\infty} s(T,\mu;m_2) = s_{\mathrm{YM}}(T)$. Thus, our final expression for the entropy density reads

$$s(T,\mu;m) = s_{\mathrm{YM}}(T) + \int_m^\infty \mathrm{d}m' \, \frac{\partial \langle \bar{\psi}\psi \rangle(T,\mu;m')}{\partial T} \,. \tag{5.10}$$

If gluons are no active degrees of freedom, the YM contribution is set to zero. For QCD, lattice calculations conveniently provide s_{YM} over a large temperature range [370, 371]. Note that Eq. (5.10) implies

$$\frac{\partial s(T,\mu;m)}{\partial m} = -\frac{\partial \langle \bar{\psi}\psi \rangle(T,\mu;m)}{\partial T} \,, \tag{5.11}$$

which is nothing but the Maxwell-like relation

$$\frac{\partial^2 \Omega(T,\mu;m)}{\partial m \, \partial T} = \frac{\partial^2 \Omega(T,\mu;m)}{\partial T \, \partial m} \tag{5.12}$$

that can alternatively be used as a starting point to derive Eq. (5.10).

Having the entropy density at hand, the pressure at vanishing chemical potential follows thermodynamically consistent from

$$P(T,0) = P(T_0,0) + \int_{T_0}^{T} \mathrm{d}T' \, s(T',0) \,, \tag{5.13}$$

and an additional integration over the quark number density $n(T,\mu)$ yields the pressure at nonvanishing chemical potential,

$$P(T,\mu) = P(T_0,0) + \int_{T_0}^{T} \mathrm{d}T' \, s(T',0) + \int_0^\mu \mathrm{d}\mu' \, n(T,\mu') \,. \tag{5.14}$$

Analogously to s_{YM}, the pressure offset $P(T_0,0)$ at some reference temperature T_0 and vanishing chemical potential is an input parameter and taken from the lattice [360, 361].

In the case of $2+1$ flavors, which we use in our DSE framework, we have to consider two degenerate light quarks with mass $m_{\mathrm{u,d}}$ and additionally a heavier strange quark with mass $m_{\mathrm{s}} \gg m_{\mathrm{u,d}}$. In order to calculate the entropy density, we integrate within the Columbia plot along the following path in the $m_{\mathrm{u,d}}$-m_{s} plane: first, at fixed strange quark mass, the up/down quark mass from the physical point to the physical strange quark mass and then both masses to infinity; see Fig. 5.1 for a graphical depiction. The generalization of

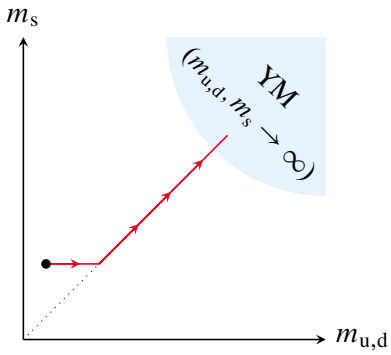

Figure 5.1 Integration path (red) within the Columbia plot for the entropy density for $2+1$ flavors. The thick dot denotes the physical point.

Eq. (5.10) to the $(2+1)$-flavor case reads

$$\begin{aligned} s(T,\{\mu_f\}) = s_{\mathrm{YM}}(T) &+ 2\int_{m_{\mathrm{u,d}}}^{m_\mathrm{s}} \mathrm{d}m' \, \frac{\partial \langle\bar{\psi}\psi\rangle_{\mathrm{u,d}}}{\partial T}(T,\{\mu_f\};m',m_\mathrm{s}) \\ &+ 2\int_{m_\mathrm{s}}^{\infty} \mathrm{d}m' \, \frac{\partial \langle\bar{\psi}\psi\rangle_{\mathrm{u,d}}}{\partial T}(T,\{\mu_f\};m',m') \\ &+ \int_{m_\mathrm{s}}^{\infty} \mathrm{d}m' \, \frac{\partial \langle\bar{\psi}\psi\rangle_{\mathrm{s}}}{\partial T}(T,\{\mu_f\};m',m') \,, \end{aligned} \tag{5.15}$$

which is constructed such that the Maxwell relation (5.12) holds. The factor of two that multiplies the first two integrals accounts for the isospin-degeneracy of the light quarks.

Finally, we would like to stress that Eqs. (5.10) and (5.15) are obtained without any approximation and are therefore exact thermodynamic relations, which establish a general relation between the entropy density and the quark condensate. They are applicable as soon as the quark condensate as a function of the current quark mass (at fixed temperature and chemical potential) is available.

5.2 NJL model study

Before we apply the method as described above to our DSE framework, we first show in the following that it works effectively and yields reliable results. For this proof of principle, we use a two-flavor NJL model as a testing ground. It is a low-energy effective model of QCD, which was originally formulated by Nambu and Jona-Lasinio in the pre-QCD era as a field-theoretical description of interacting nucleons [59, 60] but later reinterpreted

as a model for quarks [372–374]. The NJL model shares the global symmetries of QCD and, in particular, has the feature of DCSB. In contrast to our DSE setup, gluons are no active degrees of freedom and quarks interact, in the simplest form of the NJL model, via pointlike four-quark vertices. A detailed discussion of the multiple facets of the NJL model is well beyond the scope of this work, and we refer the reader to the comprehensive, seminal reviews [61–63].

In the following, we use a two-flavor NJL model in mean-field (Hartree) approximation, where the thermodynamic potential Ω_{NJL} can be calculated analytically. We are therefore in a position to compare the entropy density calculated directly from the thermodynamic potential with the one obtained from the quark condensate according to Eq. (5.10). The two-flavor, mean-field NJL Lagrangian is given by [63]

$$\mathcal{L}_{\text{mf-NJL}} = \bar{\psi}\,(\mathrm{i}\partial\!\!\!/ - M)\,\psi - \frac{(M-m)^2}{4G}\,, \tag{5.16}$$

where m denotes the current quark mass, M the constituent quark mass, and G the coupling constant. Since $\mathcal{L}_{\text{mf-NJL}}$ consists of the free Dirac Lagrangian and a constant, i.e., field-independent term, the resulting thermodynamic potential is the noninteracting one of a free quark gas [108] shifted by the constant term. It thus reads

$$\begin{aligned}\Omega_{\text{mf-NJL}} = \frac{(M-m)^2}{4G} - 2N_{\text{f}}N_{\text{c}}\Bigg[\int_{\boldsymbol{q}} E_{\boldsymbol{q}}\,\Theta(\Lambda_{\text{reg}} - |\boldsymbol{q}|) \\ + T\int_{\boldsymbol{q}}\sum_{z=\pm1}\log\Big(1+\mathrm{e}^{-(E_{\boldsymbol{q}}+z\mu)/T}\Big)\Bigg]\end{aligned} \tag{5.17}$$

with $E_{\boldsymbol{q}} = \sqrt{\boldsymbol{q}^2 + M^2}$ and the Heaviside step function Θ. Here, $N_{\text{f}} = 2$, $N_{\text{c}} = 3$, and μ is the chemical potential of the two degenerate (isospin-symmetric) light quarks. We regularize the divergent vacuum part of the thermodynamic potential with a sharp ultraviolet cutoff, $|\boldsymbol{q}| \leq \Lambda_{\text{reg}}$, but leave the convergent medium contribution unaltered. For a given temperature T and light-quark chemical potential μ, the physical constituent quark mass—the NJL counterpart of the quark mass function in the DSE framework—is the global minimum of the thermodynamic potential and found through the stationary condition $\partial\,\Omega_{\text{mf-NJL}}/\partial M = 0$, and the quark condensate is given by

$$\langle\bar{\psi}\psi\rangle_{\text{mf-NJL}} = -(M-m)/2G\,. \tag{5.18}$$

Finally, the model is complete once the parameters are fixed. The NJL model is nonrenormalizable, and the regularization scale Λ_{reg} is therefore part of the model parameters. We use $m = 5.6\,\text{MeV}$, $\Lambda_{\text{reg}} = 587.9\,\text{MeV}$, and $G = 2.44/\Lambda_{\text{reg}}^2$, which were determined in

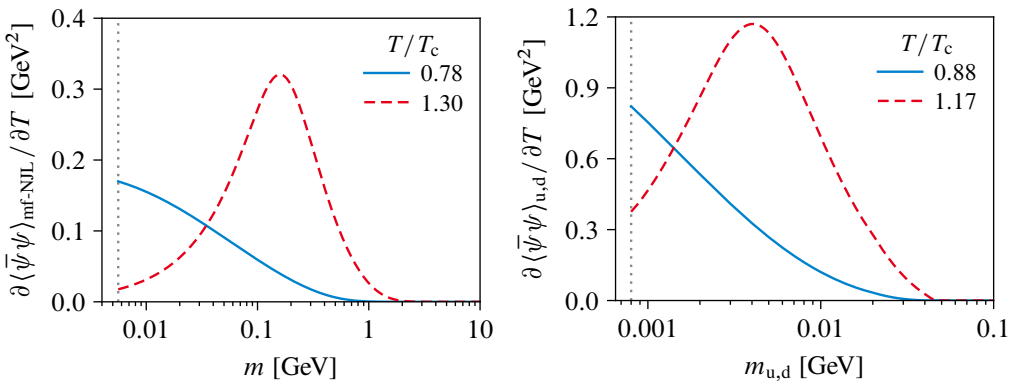

Figure 5.2 Left: integrand of the entropy formula for the NJL model as a function of the bare quark mass at two different temperatures, below and above T_c, and vanishing chemical potential. Right: temperature derivative of the up/down quark condensate from our DSE framework along the mass path shown in Fig. 5.1, again below and above T_c but exemplarily at $\mu_B = 300\,\text{MeV}$. In both diagrams, the vertical gray, dotted line marks the physical quark mass.

Ref. [63] to yield a pion mass and decay constant of $m_\pi = 135\,\text{MeV}$ and $f_\pi = 92.4\,\text{MeV}$, respectively, in vacuum. With these parameters, we find

(i) an in-vacuum constituent quark mass of $M_{\text{vac}} \approx 400\,\text{MeV}$;

(ii) a crossover transition at zero chemical potential with $T_c(\mu = 0) \approx 193\,\text{MeV}$;

(iii) a second-order CEP at $(\mu, T)_{\text{CEP}} \approx (322, 82)\,\text{MeV}$.

We are now in the position to compute the entropy density on the one hand directly from the thermodynamic potential (5.17) using the relations (5.4) and one the other hand via the method described in the previous section, i.e., by means of Eq. (5.10). Note that $s_{\text{YM}} = 0$ because gluons are no active degrees of freedom in the NJL model.

In the left diagram of Fig. 5.2, we show the integrand of the entropy formula, viz., $\partial\langle\bar{\psi}\psi\rangle_{\text{mf-NJL}}/\partial T$ as a function of the bare quark mass at vanishing chemical potential and at two fixed temperatures, one below (blue, solid line) and one above (red, dashed line) T_c. We find that the temperature derivative of the quark condensate is indeed finite, i.e., divergence free, a smooth function of the bare quark mass, and drops independent of temperature to zero for large masses. The reason for the latter is that sufficiently heavy quarks freeze out: their condensate is basically temperature independent. In other words, at one point they are simply too heavy to get thermally excited and do not contribute to the thermodynamics of the system. Therefore, the behavior of $\partial\langle\bar{\psi}\psi\rangle_{\text{mf-NJL}}/\partial T$ as a function of the bare quark mass is such that its integration with respect to m is well-defined, and we conclude that the method described in the previous section should yield reliable results. The overall behavior displayed in Fig. 5.2 can be explained as follows. First, note that the

freeze-out of heavy quarks implies that the heavier the quark mass, the higher T_c, i.e., the transition from dynamically broken chiral symmetry to partially restored chiral symmetry takes place later (in the sense of higher temperatures). Second, the pure, unsubtracted quark condensate [Eq. (2.68)] generally has a large negative value in the chirally broken phase and goes to zero from below during the crossover to the (partially) chirally restored phase. Thus, below T_c (blue, solid line), $\partial \langle \bar{\psi}\psi \rangle_{\text{mf-NJL}} / \partial T$ has a nonzero value and tends monotonously to zero with increasing mass because the quark gets less and less affected by this (small) temperature $T < T_c$ the heavier it becomes. Consequently, at a temperature $T > T_c$ (red, dashed line), for small quark masses we are already (well) beyond the crossover and $\partial \langle \bar{\psi}\psi \rangle_{\text{mf-NJL}} / \partial T$ is small. As the mass increases, the fixed temperature, which is originally above T_c for the physical quark, becomes the critical one for some heavier quark. Thus, $\partial \langle \bar{\psi}\psi \rangle_{\text{mf-NJL}} / \partial T$ increases significantly, develops a peak, and finally drops to zero if the mass is increased further. We find the very same qualitative behavior in our DSE setup, see the right diagram of Fig. 5.2, though on a different mass scale. This is most likely due to the explicit inclusion of the YM sector since the gluon—more precisely, the quark loop—is sensitive to the masses of the quarks.

Finally, in Fig. 5.3, we show the relative error between the NJL entropy density obtained from the quark condensate by means of Eq. (5.10) and directly from the thermodynamic potential through $s = -\partial \Omega_{\text{mf-NJL}} / \partial T$. We find that both results cannot be distinguished by the eye, and the relative error is smaller than 0.05% across the whole covered temperature range. In summary, our method to compute the entropy density from its relation to the quark condensate as described in Section 5.1 works very well and produces reliable results. We are therefore confident that this is the case within our DSE framework, too.

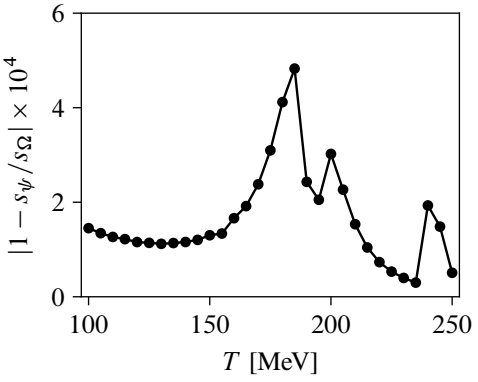

Figure 5.3 Relative error between the NJL entropy density obtained from the quark condensate (s_ψ) and directly from $\Omega_{\text{mf-NJL}}$ (s_Ω).

5.3 Equation of state from DSEs

Now, we proceed with the thermodynamic results obtained with the method described in Section 5.1 using condensate data obtained from our $(2+1)$-flavor DSE framework. The starting point is the entropy density that is obtained via Eq. (5.15). Lattice simulations of pure YM theory show that there is no sizable contribution to s_{YM} / T^3 for $T \lesssim 250\,\text{MeV}$,

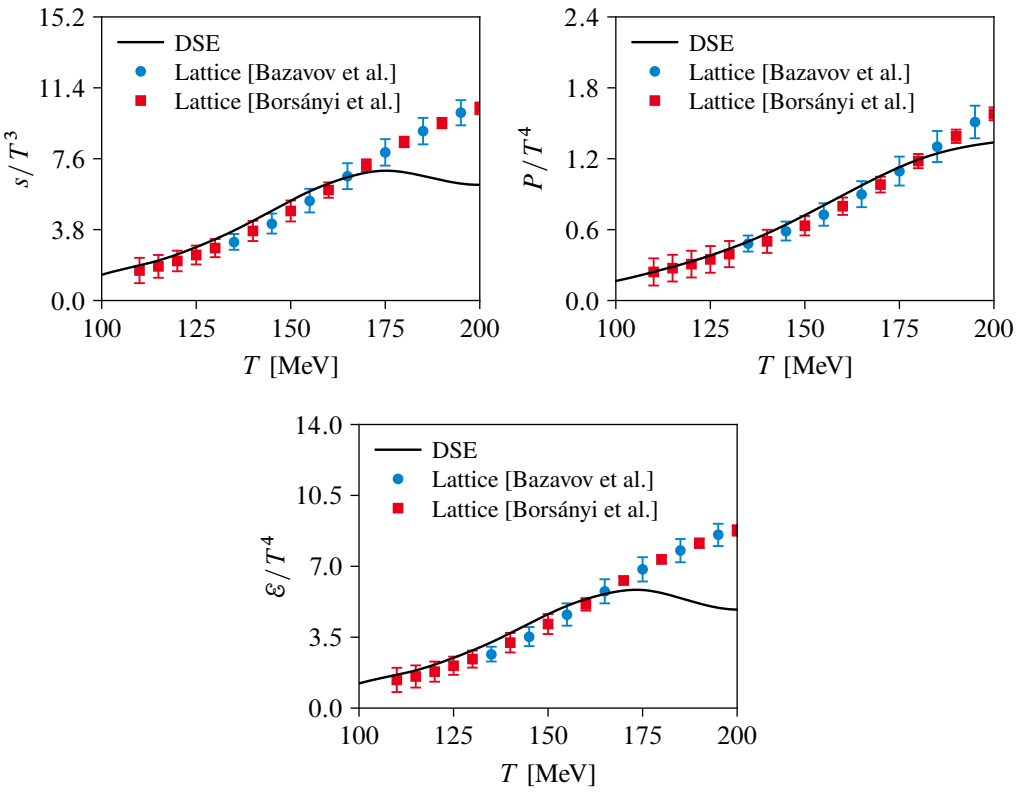

Figure 5.4 EoS at vanishing chemical potential: dimensionless entropy density (upper left), pressure (upper right), and energy density (lower center). For comparison, we also show continuum-extrapolated lattice results [360, 361].

see Refs. [370, 371], which can be safely neglected. Thus, in view of the temperature range covered in this work, we set, to a very good approximation, $s_{\mathrm{YM}} = 0$ in the following. We begin with the EoS at vanishing chemical potential, followed by results at nonvanishing μ_{B}, and close with a discussion regarding the first-order phase boundary.

Vanishing chemical potential

Our result for the dimensionless entropy density, i.e., scaled to T^3, at vanishing chemical potential is shown in the upper left diagram of Fig. 5.4 (black, solid line) compared to continuum-extrapolated lattice-QCD results [360, 361] (symbols). Up to $T \approx 175\,\mathrm{MeV}$, it is a monotonically increasing function of temperature, and the agreement with the lattice data is satisfying, though with a slight overshoot. Beyond that temperature, the entropy density shows an unphysical decrease. This is the second place where the weakness

of our ansatz for the quark-gluon vertex surfaces—the first place was Chapter 4 where we computed quark and baryon number fluctuations. The reason for the unphysical high-temperature behavior of the entropy density is the same as for the saturation of $\chi_2^{\mathrm{u,d}}$ well below the Stefan–Boltzmann limit: our vertex ansatz does not contain tensor structures that react strongly to the restoration of chiral symmetry. Their inclusion would cause a continuous weakening of the quark-gluon interaction at temperatures $T \gtrsim T_\mathrm{c}$, thereby resolving the issue of a decreasing entropy density at high temperatures.[38] We note, however, that our DSE setup yields satisfying results in the range $T = 100$–$160\,\mathrm{MeV}$ below and around the pseudocritical chiral transition temperature.

From the entropy density, we obtain the pressure by integration according to Eq. (5.13) and use $P(T_0)/T_0^4 = 0.242$ at $T_0 = 110\,\mathrm{MeV}$ [360]. The result depicted in the upper right diagram of Fig. 5.4 is in good agreement with the lattice but starts to deviate for $T \gtrsim 185\,\mathrm{MeV}$. This deviation is inherited from the erroneous high-temperature behavior of the entropy density, which is used to compute P. At high temperatures, the pressure saturates at $P/P_\mathrm{SB} \approx 0.3$, where

$$\frac{P_\mathrm{SB}}{T^4} = \frac{19\pi^2}{36} + \frac{1}{9}\left(\frac{\mu_\mathrm{B}}{T}\right)^2 + \frac{1}{162\pi^2}\left(\frac{\mu_\mathrm{B}}{T}\right)^4 \tag{5.19}$$

is the Stefan–Boltzmann pressure of an ideal gas of massless quarks and gluons (for $N_\mathrm{f} = 2 + 1$). Finally, combining the entropy density and pressure we obtain the energy density by means of a Legendre transform, Eq. (5.5), which is shown in the lower central diagram of Fig. 5.4. Since it is a combination of s and P, the agreement with lattice results is reasonable below and around T_c while a decreasing behavior stemming from the entropy density is found at high temperatures.

Nonvanishing chemical potential

Now, we turn to nonzero chemical potential and show our result for the EoS in Fig. 5.5. The entropy density is displayed in the upper left diagram as a function of temperature for different chemical potentials starting from zero up to the CEP value $\mu_\mathrm{B}^\mathrm{CEP} = 495\,\mathrm{MeV}$. A bulge develops around the pseudocritical chiral transition temperature, which becomes more pronounced with increasing chemical potential. Close to and across the CEP, we observe a strong increase of the entropy density, and the slope becomes maximal at $T = T_\mathrm{CEP}$. The erroneous high-temperature behavior found at vanishing chemical potential persists and

[38] This effect could be mimicked by making the infrared strength d_1 of our vertex ansatz (3.8) temperature dependent. An analogous modification is needed in rainbow-ladder truncations with a gluon model, too, in order to obtain proper results for fluctuations and thermodynamics at high temperatures [245, 338].

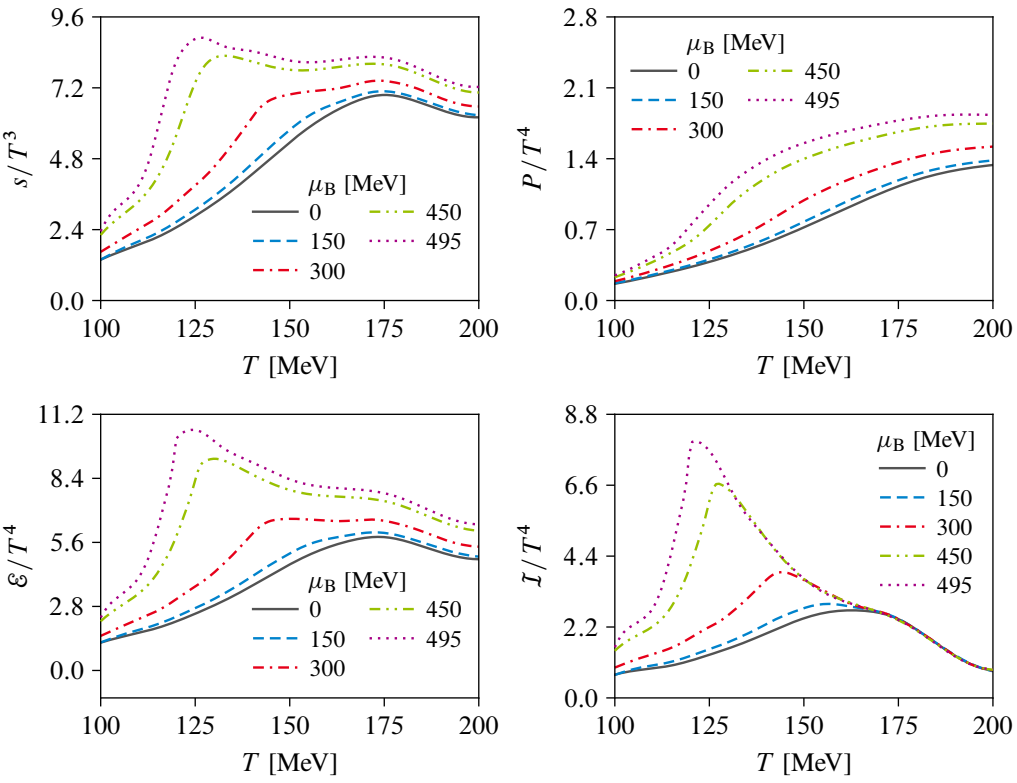

Figure 5.5 EoS at nonvanishing chemical potential: dimensionless entropy density (upper left), pressure (upper right), energy density (lower left), and interaction measure (lower right) as functions of temperature for selected chemical potentials up to the CEP.

becomes nonmonotonic. Again, as discussed earlier in the course of our results for the EoS at vanishing chemical potential, we expect that these artifacts disappear with an improved quark-gluon vertex that provides the correct weakening of the quark-gluon interaction at high temperatures and/or chemical potential.

The pressure follows again from the entropy density via integration according to Eq. (5.14) while the quark number density is obtained as explained in the previous chapter. As seen in the upper right diagram of Fig. 5.5, the pressure gets larger with increasing chemical potential across the whole temperature range, though the changes are less noticeable at low temperatures. For chemical potentials close to the CEP, a kink starts to form at the corresponding transition temperature T_c. Beyond that point, the pressure rises stronger with a steeper slope as a function of temperature, which is most prominent and noticeable at the CEP. The pressure is, however, a smooth function of temperature for all μ_B up to μ_B^{CEP}. These results are consistent with corresponding ones obtained from an FRG study of the Polyakov-loop enhanced quark-meson model [74].

The effect of a nonzero and increasing chemical potential is most prominent in the energy density, lower left diagram of Fig. 5.5, caused by the additional quark number-density term that stems from the Legendre transform [Eq. (5.5)]. Its steep rise close to and at the CEP signals a rapid increase of degrees of freedom from hadrons to quarks and gluons. This behavior carries over to the interaction measure, lower right diagram, which reacts strongly to increasing chemical potential. At vanishing chemical potential, $\mathcal{I}/T^4$ is shape consistent with lattice-QCD results and experiences a strong increase from intermediate chemical potentials onward to the CEP. There, at $\mu_\mathrm{B} = \mu_\mathrm{B}^\mathrm{CEP}$, the slope with temperature becomes infinite at the corresponding critical temperature $T = T_\mathrm{CEP}$. Finally, the peaklike structure of the interaction measure with a large magnitude close and at the CEP indicates that nonperturbative effects are manifest in this region of the QCD phase diagram.

The first-order phase boundary

We conclude this chapter with a discussion about locating the phase boundary in the first-order region of the phase diagram. This would be the next obvious step since we have the pressure as a function of temperature and chemical potential at hand. Unfortunately, as detailed in the following, at this point we hit a limitation of our method.

In order to locate the first-order phase boundary, one usually considers the pressure difference

$$\mathcal{B}(T,\mu) = P_\mathrm{N}(T,\mu) - P_\mathrm{W}(T,\mu) \tag{5.20}$$

between the chirally broken Nambu phase (N) and the chirally symmetric Wigner phase (W) as a function of the chemical potential for a fixed temperature $T < T_\mathrm{CEP}$. Clearly, $\mathcal{B}(T,\mu)$ is only defined up to the critical chemical potential $\mu_\mathrm{c}^\mathrm{N} = \mu_\mathrm{c}^\mathrm{N}(T)$, above which the Nambu solution does not exist anymore (i.e., is no solution of the quark DSE anymore) and only the Wigner solution can be found. Phrased differently, $\mu_\mathrm{c}^\mathrm{N}$ as a function of temperature defines the location of the upper spinodal in the phase diagram [see Figs. 3.9 and 3.10]. The physically realized phase/solution corresponds to the global minimum of the thermodynamic potential, i.e., it maximizes the pressure: $\mathcal{B}(T,\mu) > 0$ indicates that the system is in the Nambu phase, i.e., the Nambu phase is more stable than the Wigner phase, and vice versa. Therefore, $\mathcal{B}(T,\mu) = 0$ defines the phase boundary, and by finding the root of $\mathcal{B}(T,\mu)$ with respect to the chemical potential for various $T \in [0, T_\mathrm{CEP})$, one can draw the first-order phase boundary.

In our approach, the pressure difference (5.20) is explicitly given by

$$\mathcal{B}(T,\mu) = f_{\mu=0}(T) - f_{\mu\neq 0}(T,\mu) \tag{5.21}$$

with the functions

$$f_{\mu=0}(T) = P_{\mathrm{N}}(T_0, 0) - P_{\mathrm{W}}(T_0, 0) + \int_{T_0}^{T} \mathrm{d}T' \left[s_{\mathrm{N}}(T', 0) - s_{\mathrm{W}}(T', 0) \right] \tag{5.22}$$

and

$$f_{\mu\neq 0}(T, \mu) = \int_0^{\mu} \mathrm{d}\mu' \left[n_{\mathrm{W}}(T, \mu') - n_{\mathrm{N}}(T, \mu') \right], \tag{5.23}$$

where n_{W} and n_{N} denote the quark number densities of the Wigner and Nambu phase, respectively. The first term of the pressure difference, Eq. (5.22) is evaluated at vanishing chemical potential only, i.e., it does not depend on chemical potential. Moreover, we note that $f_{\mu=0}(T)$ is positive for all $T \in [0, T_{\mathrm{CEP}})$ because this region of the phase diagram is well below $T_{\mathrm{c}}(\mu = 0)$ where the Nambu phase is realized. Next, we find both in the NJL model and in our DSE setup that the quark number density as a function of the chemical potential (at fixed $T < T_{\mathrm{CEP}}$) of the Wigner phase is generally larger than the corresponding number density of the Nambu phase: $n_{\mathrm{W}}(T, \mu) - n_{\mathrm{N}}(T, \mu) > 0$, and therefore $f_{\mu\neq 0}(T, \mu) > 0$ for all $\mu \in [0, \mu_{\mathrm{c}}^{\mathrm{N}}]$. It thus follows that there exists $\mu_{\mathrm{c}}^{1\mathrm{st}} \in [0, \mu_{\mathrm{c}}^{\mathrm{N}}]$—the location of the first-order line—where $f_{\mu\neq 0}(T, \mu_{\mathrm{c}}^{1\mathrm{st}}) = f_{\mu=0}(T)$, and consequently, $\mathcal{B}(T, \mu_{\mathrm{c}}^{1\mathrm{st}}) = 0$.

From these considerations, it becomes apparent that the correct location of the first-order phase boundary depends crucially on the value of $f_{\mu=0}(T)$. In particular, we need the pressure difference $P_{\mathrm{N}}(T_0, 0) - P_{\mathrm{W}}(T_0, 0)$ at a reference temperature T_0 and vanishing chemical potential as input while all other quantities in Eqs. (5.22) and (5.23) are computed from DSEs. Alas, lattice QCD provides to our knowledge only the physical Nambu pressure $P_{\mathrm{N}}(T_0, 0)$ but not the unphysical Wigner pressure $P_{\mathrm{W}}(T_0, 0)$. Thus, we are unfortunately not able to obtain a reliable location of the phase boundary in the first-order region of the phase diagram. We emphasize, however, that this is not an inherent flaw of our method but more that we hinge on the availability of an external input parameter.

5.4 Summary

In this chapter, we have studied thermodynamic quantities obtained from our DSE setup. To this end, we discussed a novel method that allows to compute the entropy density solely from the quark condensate. The method is exact and independent of the employed truncation. Furthermore, it is applicable as soon as the quark condensate is available and not limited to the DSE approach, though most useful for the latter because accessing

thermodynamic quantities using DSEs is extremely difficult and was achieved so far only within simple models of the rainbow-ladder type. After having demonstrated its effectiveness using a NJL model in mean-field approximation, we used the method with condensate data obtained from our DSE framework and computed the pressure, entropy density, energy density, and interaction measure across the QCD phase diagram. These result are, to our knowledge, the first ones obtained within a DSE truncation beyond rainbow ladder. On the other hand, we were unfortunately not able to determine the first-order phase boundary below the CEP. Again, we stress that this is not an inherent deficiency of our method—we suffer from the lack of availability of an external input parameter. Finally, it became clear, in agreement with the results for fluctuations, that our tensor basis for the quark-gluon vertex needs to be enlarged in order to achieve proper thermodynamics at high temperatures and/or chemical potentials.

6 Finite-volume effects on the phase diagram

In this last chapter before the epilogue, we study finite-volume effects on the phase structure of QCD with an emphasis on the location of our CEP. Generally, there are various reasons for such a study. First, the initial fireball created in a heavy-ion collision is of finite spatial extent, which depends on the collision energy, centrality, and the size of the colliding nuclei. For example, the pion freeze-out volume in Pb-Au collisions can be estimated to about 1000–3000 fm^3 over a large collision-energy range [375], and from transport models [376, 377], one can infer freeze-out volumes in Au-Au and Pb-Pb collision of about 40–300 fm^3 [378]. Volume effects on fluctuations of conserved charges, which are auspicious candidates for locating the (putative) CEP experimentally, may be considerable and thus need to be thoroughly understood [97, 379, 380]. Second, the whole structure of the QCD phase diagram becomes volume dependent for small enough volumes. At zero and small chemical potential, lattice calculations provide ab-initio insights into QCD. The corresponding simulations, however, are necessarily carried out in a finite volume with (anti)periodic boundary conditions, and a thorough understanding of the volume dependence of the results is mandatory. Finally, effects due to volume changes are interesting for their own sake because they reflect the reaction of a system on one of its external parameters.

In the following, we use the same DSE setup to determine the nonperturbative quark and gluon propagators as in the preceding chapters, but we change the structure of the underlying three-dimensional space: the up to now infinite three-dimensional volume is made finite.[39] In particular, we confine the system to a cubic volume and employ periodic as well as antiperiodic boundary conditions. Even though there are no (anti)periodic boundary conditions in a heavy-ion collision and the geometry is not cubic but rather spheric (large centrality) or almond shaped (small centrality), we are confident to cover the relevant physics resulting from a finite volume. Using DSEs for finite-volume studies has two main advantages. First, one is able to study volume effects continuous from very small to very large volumes, and at the same time, infinite-volume results are available without the need of extrapolations. Second, the implementation of different boundary conditions

[39] As we do not discuss vacuum results in this chapter, the term “finite volume” is always understood as three-dimensional finite volume.

is possible without great effort. The first DSE results in a finite volume were presented in Refs. [216, 381] and led to several other works [254, 255, 382–387]. By investigating the truncation described in Section 3.1 in a finite volume, we continue previous studies where the quenched version of our truncation scheme was employed [254, 255]. Other DSE studies, albeit using simpler truncations, can be found in Refs. [339, 388–391], while Refs. [392–399] discuss finite volume from an FRG point of view. The results presented here are published in Ref. [100] and will also be discussed elsewhere in the future [270].

6.1 DSEs in a finite volume

The introduction of a finite, uniform, three-dimensional volume is analogous to the transition from a theory formulated in vacuum to the corresponding one at nonzero temperature. As discussed in Section 2.4, starting with the QCD action in vacuum, nonzero temperature T is introduced by compactifying the imaginary-time integration to the interval $[0, 1/T]$,

$$\int_x \mathcal{L}_{\mathrm{QCD}} \to \int_0^{1/T} \mathrm{d}x_4 \int_{\boldsymbol{x}} \mathcal{L}_{\mathrm{QCD}} \,. \tag{6.1}$$

Finite volume is introduced by constraining the spatial integration to a proper subset of $\mathbb{R}^3$. We use a cube of edge length L, which amounts to the replacement

$$\int_{\boldsymbol{x}} \mathcal{L}_{\mathrm{QCD}} \to \int_{\boldsymbol{x}\in[0,L]^3} \mathcal{L}_{\mathrm{QCD}} \,. \tag{6.2}$$

A more general formulation can be obtained by choosing different lengths in each direction, i.e., the integration volume is the cuboid $[0, L_x] \times [0, L_y] \times [0, L_z]$.[40] However, our truncation has not been studied before in a finite volume, and we thus choose the cube, $L_x = L_y = L_z \equiv L$, for the sake of simplicity. Since the integration domain is compact, the three-momentum becomes discrete, too, in addition to the already discrete temporal Matsubara frequencies in imaginary-time direction. Therefore, a generic momentum integral with kernel K is replaced by sums over spatial modes:

$$\int\!\!\!\!\!\!\int_{\boldsymbol{q}} K(\boldsymbol{q}) \to \frac{1}{L^3} \sum_{\boldsymbol{z}\in\mathbb{Z}^3} K(\boldsymbol{q}_{\boldsymbol{z}}) \tag{6.3}$$

with $\boldsymbol{q}_{\boldsymbol{z}} = \sum_{i=1}^3 \omega_{z_i}^L \boldsymbol{e}_i$, where the integer vector $\boldsymbol{z} \in \mathbb{Z}^3$ labels the spatial modes, and the Cartesian basis $\{\boldsymbol{e}_1, \boldsymbol{e}_2, \boldsymbol{e}_3\}$ spans the three-dimensional Euclidean momentum space. At this point, a simple yet crude approximation is to keep the continuous integration but

[40] Other geometries are possible as well: see, e.g., Refs. [391, 400], where a spherical volume is used.

endowed with an infrared cutoff, $|\boldsymbol{q}| \geq \pi/L$; see, e.g., Refs. [388, 390, 401–403]. We, however, strictly implement (6.3) and sum explicitly over all discrete momenta. While the temporal Matsubara frequencies are fixed by the spin-statistics theorem—odd (even) multiples of πT for quarks (gluons)—there are no similar constraints for the spatial directions. Although the kinematics of the quark self-energy implies periodic spatial boundary conditions for the gluon, quarks are completely unconstrained. We choose either periodic spatial boundary conditions (PBC) or antiperiodic spatial boundary conditions (ABC). The corresponding spatial Matsubara modes read

$$\omega_{z_i}^L = \frac{2\pi}{L} \times \begin{cases} z_i & \text{for PBC}\,, \\ z_i + 1/2 & \text{for ABC}\,. \end{cases} \tag{6.4}$$

Using the replacement (6.3) and discrete three-momenta throughout, it is in principle straightforward to rewrite our DSEs for the quark and gluon propagators to account for finite volume. However, before doing so, it is numerically beneficial to rearrange the three summations in Eq. (6.3) such that they resemble a spherical coordinate system [381]. This is motivated by the fact that the quark and gluon dressing functions depend only on the O(3)-invariant squared three-momentum, i.e., they are independent of directions in momentum space. We thus write

$$\frac{1}{L^3} \sum_{\boldsymbol{z} \in \mathbb{Z}^3} K(\boldsymbol{q}_{\boldsymbol{z}}) = \frac{1}{L^3} \sum_{j,m} K(\boldsymbol{q}_{jm})\,, \tag{6.5}$$

where j labels the spheres with constant radius $|\boldsymbol{q}_{\boldsymbol{z}}|$, and $m = m(j)$ denotes the multiplicity of the individual momentum vectors on a given sphere j. The corresponding vectors are denoted by $\boldsymbol{q}_{jm}$. A two-dimensional sketch for ABC is shown in Fig. 6.1, where spheres correspond to circles and the vectors are indicated by black dots.

Analogous to the continuum, we have to introduce an ultraviolet cutoff Λ_{UV} to arrive at a momentum grid of finite extent. Naively, one imposes the same cutoff in each Cartesian momentum direction and sums over all spheres that are obtained after the rearrangement according to Eq. (6.5). However, it turns out that this leads to so-called cubic artifacts that affect the ultraviolet behavior of the dressing functions. These are caused by the mismatch between the cubic geometry of the regularized (i.e., finite) momentum grid and the O(3)-symmetric continuum at large momenta. We account for that by taking only complete spheres in our summations into account and discard incomplete ones. A sphere is complete if it does not receive additional vectors if the Cartesian cutoff is increased. Thus, it follows that on each (sufficiently large) grid we have a large number of complete spheres in the innermost region, while a rather large number of the outermost spheres

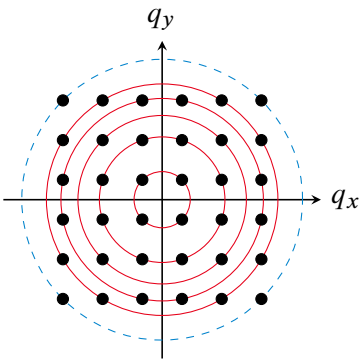

Figure 6.1 Two-dimensional ABC momentum grid. Red, solid circles represent complete spheres that are fully taken into account, while the blue, dashed one is incomplete and discarded in our summations (see text for details). Figure adapted from Ref. [386].

are necessarily incomplete. As apparent from Fig. 6.1, taking only complete spheres into account corresponds to "cutting the edges" of our momentum grid. This procedure was used in earlier studies, too, and reduces the effect of cubic artifacts. Unsurprisingly, (hyper)cubic artifacts are an issue on the lattice as well and several methods were developed to eliminate them [404–407], where our edge cutting is similar to one of them.

Having the above considerations in mind, it is straightforward to present the quark and gluon DSEs in a finite volume. Since the latter affects only the structure of the momentum space, the structure of the propagators in the other spaces (Dirac, Lorentz, color, and flavor) remains unchanged and is given as discussed in Section 2.3. With the external quark and gluon momenta $p = (\omega_p, \boldsymbol{p}_{il})$ and $k = (\omega_k, \boldsymbol{k}_{il})$, respectively, the DSEs for the quark and gluon propagators in a finite volume read

$$S_f^{-1}(p) = S_{0,f}^{-1}(p) + \Sigma_f(p)\,, \tag{6.6}$$

$$D_{\nu\sigma}^{-1}(k) = Z_3\, D_{0,\nu\sigma}^{-1}(k) + \Pi_{\nu\sigma}^{\mathrm{YM}}(k) + \Pi_{\nu\sigma}(k)\,, \tag{6.7}$$

in complete analogy to infinite volume. The quark self-energy is given by

$$\Sigma_f(p) = g^2\, C_2^{\mathrm{fund}}\, \frac{Z_2^f}{\tilde{Z}_3}\, \frac{T}{L^3} \sum_{\ell_q \in \mathbb{Z}} \sum_{j,m} D_{\nu\sigma}(p-q)\, \gamma_\nu\, S_f(q)\, \Gamma_\sigma^f(q,p)\,, \tag{6.8}$$

where $q = (\omega_q, \boldsymbol{q}_{jm})$, while the quark loop reads

$$\Pi_{\nu\sigma}(k) = -\frac{g^2}{2}\, \frac{T}{L^3} \sum_f \frac{Z_2^f}{\tilde{Z}_3} \sum_{\ell_q \in \mathbb{Z}} \sum_{j,m} \mathrm{Tr}\big[\gamma_\nu\, S_f(q)\, \Gamma_\sigma^f(q,p)\, S_f(q-k)\big]\,. \tag{6.9}$$

The next steps to arrive at a closed system of equations are the very same as in infinite volume, see Chapter 3, i.e., we do not change our truncation scheme and parameters for the finite-volume calculations.

The changes due to finite volume naturally carry over to quantities that are obtained from the propagators. For example, the quark condensate is given by

$$\langle\bar{\psi}\psi\rangle_f = -N_\mathrm{c}\, Z_2\, Z_{m_f} \frac{T}{L^3} \sum_{\ell_q \in \mathbb{Z}} \sum_{j,m} \mathrm{Tr}\big[S_f(q)\big]\,. \tag{6.10}$$

As in infinite volume, we use the inflection point of the subtracted quark condensate $\Delta_{\mathrm{u,s}}$ [Eq. (2.69)] with respect to the temperature to define the pseudocritical chiral transition temperature $T_\mathrm{c}(\mu_\mathrm{B})$. Some details about our finite-volume calculations are collected in Appendix D.

Before we present our results for the propagators the phase diagram of QCD in a finite volume, we discuss the finite-volume renormalization procedure because it is different than in infinite volume. Since we take all discrete momentum vectors up to the ultraviolet cutoff explicitly into account, large cutoff values like in the infinite-volume calculations are numerically unfeasible, and we choose $\Lambda_\mathrm{UV} = 10\,\mathrm{GeV}$ in a finite volume. As a consequence of this necessarily rather small cutoff, we have to renormalize in a region that is much closer to the nonperturbative infrared than to the perturbative ultraviolet. Since box sizes of about 8 fm and larger have only a negligible effect on our results, $L \gtrsim 8\,\mathrm{fm}$ can be regarded as infinite volume, and we proceed as follows. We renormalize our dressed propagators at $L = 8\,\mathrm{fm}$ and at the renormalization point $\zeta = (\omega_0, \boldsymbol{\zeta})\big|_{T=50\,\mathrm{MeV}}$, $|\boldsymbol{\zeta}| = 8\,\mathrm{GeV}$, to the corresponding dressed infinite-volume propagators:

$$F(\zeta; L = 8\,\mathrm{fm}) \stackrel{!}{=} F(\zeta; L \to \infty)\,, \tag{6.11}$$

where $F \in \{Z_\perp, Z_\parallel, C_\mathrm{u}, A_\mathrm{u}, \dots\}$. In other words, we fix the renormalization constants in a large volume and keep them unchanged in order to study variations in L consistently.

Last, we would like to comment briefly on a technical detail. The momentum grid corresponding to PBC contains the zero mode $\boldsymbol{q} = \mathbf{0}$. Because its inclusion leads to obstacles in the self-energies and its proper implementation is a nontrivial task, we omit the zero mode in this work, i.e., all PBC results are understood without the zero mode. However, we have preliminary evidence that (the omission of) the zero-mode contribution affects our results for $L \gtrsim 4\,\mathrm{fm}$ below the ten-percent level, and it seems that PBC results with the zero mode closely resemble the ones for ABC [408]. The corresponding supportive (but preliminary) results for $T_\mathrm{c}(L)$ can be found in Appendix D, and more details will be discussed elsewhere in the future [270].

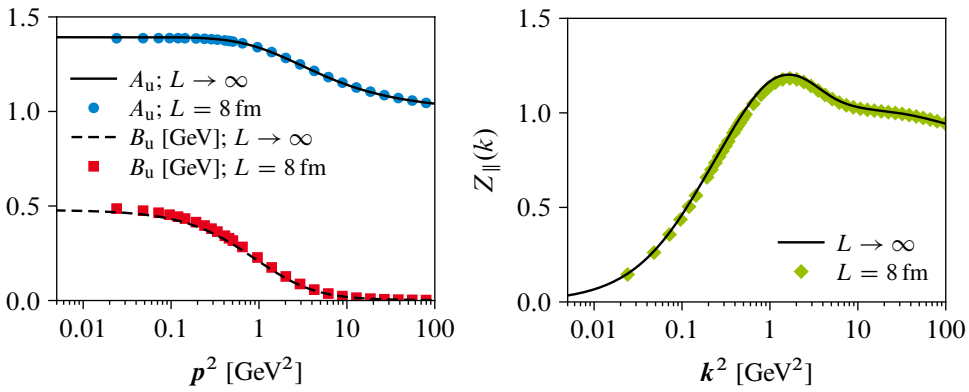

Figure 6.2 Up-quark dressing functions A_u and B_u with PBC (left) and the electric gluon dressing function $Z_\parallel$ (right), all at $L = 8$ fm, compared to the infinite-volume results at $T = 130$ MeV and vanishing chemical potential. We show only the zeroth Matsubara frequency.

6.2 Quark and gluon propagators

In the following, we present our results for the quark and gluon propagators in a finite volume and begin with their large-volume behavior.[41] As already mentioned above, we find that a box size of about 8 fm and larger leaves our results qualitatively unchanged. Thus, we regard $L = 8$ fm as infinite volume, and this size is the largest considered here. In Fig. 6.2, we show the up-quark dressing functions A_u and B_u (left diagram; blue circles and red squares) with PBC together with the electric gluon dressing function $Z_\parallel$ (right diagram; green diamonds) at $L = 8$ fm, $T = 130$ MeV, and $\mu_B = 0$ as functions of the three-momentum for the zeroth Matsubara frequency. Additionally, the corresponding infinite-volume results are shown for comparison. We find that the infinite-volume limit, which should be reached for a sufficiently large L, is satisfactorily fulfilled. However, if one takes a closer look, the infinite-volume limit of our finite-volume calculation is not reached perfectly. While the vector dressing function A_u agrees well with the infinite-volume result (the same holds for C_u, which is not shown), the scalar dressing function B_u does not: it overshoots its infinite-volume counterpart in the infrared. A similar issue can be observed with the electric gluon dressing function, where the infinite-volume counterpart is underestimated in the mid-momentum region. The same holds for the magnetic gluon

[41] Recall that we use a Pauli–Villars regulator in the infinite-volume quark DSE. However, in a finite volume without any improvement, the small ultraviolet cutoff prevents the use of such a regulator. Thus, the results presented in Section 6.2 are obtained with a quark DSE that is regularized with a sharp O(4) regularization scale, $q^2 \leq (\Lambda_{\text{reg}})^2$, which is simply given by the ultraviolet cutoff, $\Lambda_{\text{reg}} = \Lambda_{\text{UV}}$. Since d_1 is regularization dependent, see Section 3.1, we use an adapted value of $d_1 = 8.26\,\text{GeV}^2$ for all calculations with a hard O(4) regularization scale.

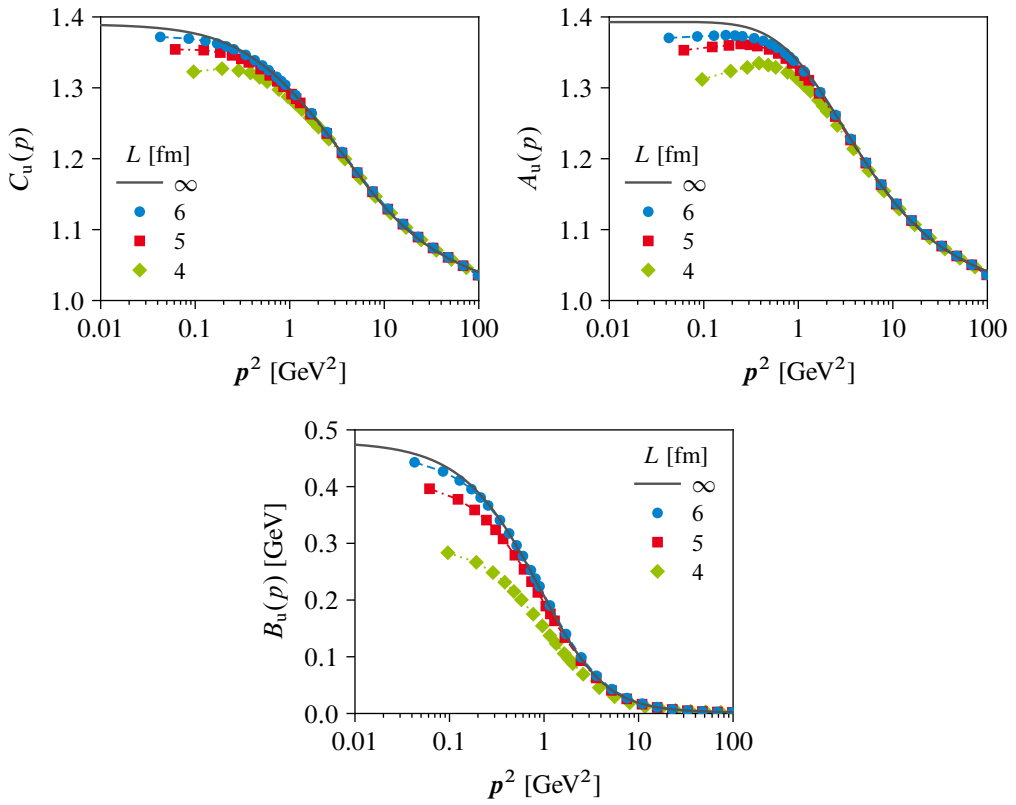

Figure 6.3 Up-quark dressing functions C_u, A_u, and B_u (upper left, upper right, and lower center, respectively) with PBC for different box sizes at $T = 130\,\text{MeV}$ and $\mu_B = 0$. We show only the zeroth Matsubara frequency, and data points are connected by lines to guide the eye.

dressing function $Z_\perp$. We find that these behaviors are caused by the rather small ultraviolet cutoff, i.e., they are finite-size artifacts. Besides that these spoil a clean infinite-volume limit, finite-size effects are particularly noticeable in the quark condensate, resulting in pronounced numerical noise; see Fig. D.1 and the corresponding discussion on how we determine T_c in a finite volume. Similar cutoff effects were already noted in calculations with the quenched version of our truncation scheme [255]. However, since their influence seems not overly severe at first sight, we keep our setup unchanged for now but discuss a proper treatment soon in the upcoming Section 6.3. All these observations are qualitatively similar at other temperatures and chemical potentials, too.

After the large-volume results, we proceed with the impact of a varying box size on the dressing functions. In Fig. 6.3, we display the up-quark dressing functions C_u, A_u, and B_u (upper left, upper right, and lower center, respectively) for different box sizes at $T = 130\,\text{MeV}$ and vanishing chemical potential. Generally, we observe large volume

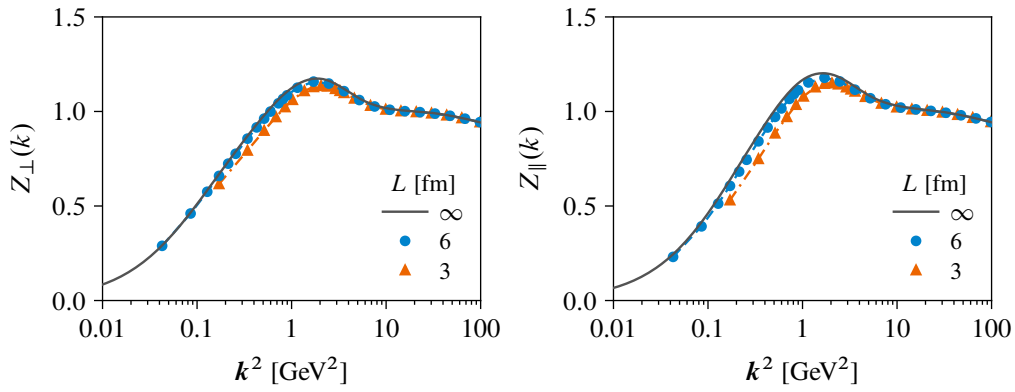

Figure 6.4 Gluon dressing functions $Z_\perp$ and $Z_\parallel$ (left and right, respectively) for different box sizes at $T = 130\,\mathrm{MeV}$ and $\mu_\mathrm{B} = 0$. We show only the zeroth Matsubara frequency, and data points are connected by lines to guide the eye.

effects in the infrared, while the finite-volume results agree with the infinite-volume ones at large momenta $\boldsymbol{p}^2 \gtrsim 10\,\mathrm{GeV}^2$ for all considered box sizes. This is no surprise because the momentum spheres of our spherical momentum summation [Eq. (6.5)] become (extremely) dense as their radii increase, i.e., the discrete momentum vectors are virtually continuous for sufficiently large magnitudes, and the results thus should agree with the infinite-volume calculation. On the other hand in the infrared, at small L the dressing functions are significantly smaller than their $L \to \infty$ counterparts and approach the infinite-volume limit from below as the box size increases. Furthermore, this nicely illustrates the close relationship between nonzero temperature and finite volume: to wit, the former can be seen as an inverse length, and both determine the extent of the four-volume $[0, 1/T] \times [0, L]^3$. From the behavior of the scalar dressing function B_u, we see that the amount of chiral symmetry breaking decreases with decreasing box size. Phrased differently, a decreasing finite volume acts chirally restoring.

This behavior transfers onto the gluon, which is shown for different box sizes at $T = 130\,\mathrm{MeV}$ and vanishing chemical potential in Fig. 6.4. In our truncation scheme, its volume dependence is solely triggered by the quark loop since we have only the continuum-extrapolated quenched gluon from the lattice at our disposal. This is of course an approximation. However, lattice results suggest that it is an acceptable one for the volumes covered in this work [256, 409–411]. We observe that both the magnetic and electric gluon dressing functions are less affected by finite volume as compared to the quark dressing functions. As the box size decreases, the quarks in the quark loop become lighter and lighter, and the resulting effect on the gluon dressing functions is similar as for increasing temperature in infinite volume, i.e., a reduction of both $Z_\perp$ and $Z_\parallel$ at infrared momenta $\boldsymbol{k}^2 \lesssim 5\,\mathrm{GeV}^2$.

6.3 Taming the finite-size effects

As mentioned in the previous section, finite-size artifacts prevent a clean infinite-volume limit of the dressing functions. In order to obtain consistent results for and be able to make reliable statements about the phase structure of QCD in a finite volume, we have to treat (and hence remove) them properly.

In general, the spherical momentum summation according to Eq. (6.5) has two major drawbacks:

(i) the larger the grid the more dense are the complete outer spheres and the more points are on every one of these. Since the dressing functions run logarithmically as functions of large squared momenta in the ultraviolet, they do not change much from outer sphere to outer sphere. Thus, a lot of numerical effort is spent to integrate/sum over an almost constant function;

(ii) the necessarily small ultraviolet cutoff in order to keep the numerical effort feasible results in cubic artifacts, which should not be neglected. Furthermore, the renormalization point, which is even smaller than the already small ultraviolet cutoff, is too close to the nonperturbative infrared where medium and finite-volume effects are important. As a consequence, the renormalization constants are contaminated by medium and finite-volume artifacts.

These drawbacks and the related issues are drastically mitigated by means of the following procedure. We consider discrete momenta with the spherical summation up to some matching cutoff Λ_{vol} and replace the spheres with radii between $\Lambda_{\mathrm{vol}} \leq |\boldsymbol{q}| \leq \Lambda_{\mathrm{UV}}$ with a continuous momentum integral. Consequently, the original replacement, Eq. (6.3), is modified according to

$$\int\!\!\!\!\!\!\diagup_{\boldsymbol{q}} K(\boldsymbol{q}) \to \frac{1}{L^3} \sum_{\boldsymbol{z}\in\mathbb{Z}^3}^{|\boldsymbol{q}_{\boldsymbol{z}}|<\Lambda_{\mathrm{vol}}} K(\boldsymbol{q}_{\boldsymbol{z}}) + \int\!\!\!\!\!\!\diagup_{\boldsymbol{q}} K(\boldsymbol{q})\,\Theta(|\boldsymbol{q}| - \Lambda_{\mathrm{vol}})\,. \tag{6.12}$$

This modification, called “ultraviolet improvement” or simply “improvement” in the following, allows for a much larger ultraviolet cutoff that should alleviate finite-size artifacts caused by a potentially too small cutoff. In addition, the improvement enables us to renormalize exactly as in the continuum, i.e., with a Pauli–Villars regulator in the quark DSE and a renormalization point located deep in the perturbative ultraviolet where medium and finite-volume effects are minute. Our results are independent of Λ_{vol} as long it is larger than any other typical scale of the system like temperature, chemical potential, and quark masses. Recently, a similar treatment has been used in Ref. [391] within a simpler truncation of the DSEs.

With both the unimproved, Eq. (6.3), and the improved finite-volume setup as described above, Eq. (6.12), at hand, we now discuss our results for the QCD phase diagram from both approaches and compare them systematically.

6.4 Results for the phase structure of QCD

T_c at vanishing chemical potential

In Fig. 6.5, we display the pseudocritical chiral transition temperature at vanishing chemical potential for ABC and PBC for the quarks obtained from the unimproved (left) and improved (right) framework. For comparison, the infinite-volume result is indicated by a black, dotted line in both plots. Comparing both diagrams, we clearly see the effect of the ultraviolet improvement at large volumes. In the unimproved case, our results for both ABC and PBC suffer from cubic artifacts and overshoot the infinite-volume line. In contrast, the improved results approach the infinite-volume results smoothly from below, and we infer that volumes $L^3 \gtrsim (8\,\mathrm{fm})^3$ are very close to infinite volume. In order to validate that, we also performed calculations at even larger box sizes. The results are indeed very similar to the infinite-volume ones and agree on the permille level. Thus, we did not include them in the plot. At smaller box sizes, T_c decreases monotonously. While the decrease is rather moderate down to $L \approx 5\,\mathrm{fm}$, volume effects become much more pronounced for even smaller volumes. For example, at $L = 3\,\mathrm{fm}$ and PBC we find that T_c is almost halved as compared to infinite volume. Furthermore, while the relative difference between improved and unimproved results for ABC and PBC is almost the same down to $L = 4\,\mathrm{fm}$, the improved T_c at $L = 3\,\mathrm{fm}$ is more than ten percent smaller than the unimproved one. Therefore, the proper removal of cubic artifacts is important for both small and large volumes. In general, we observe that quarks with PBC are much more sensitive to finite-volume effects across all investigated box sizes. This is most likely caused by the lower infrared cutoff introduced by the discrete momentum grid. From Eq. (6.4), the ratio of the smallest possible magnitude q_{min} of the discretized momentum vectors between ABC and PBC (recall, without the zero mode) is given by $q_{\mathrm{min}}^{\mathrm{ABC}}/q_{\mathrm{min}}^{\mathrm{PBC}} = \sqrt{3/4} \approx 0.87$.

Crossover line and CEP

The impact of a finite volume on the phase structure of QCD is summarized in Fig. 6.6. In the upper (lower) row, we show the phase diagrams for ABC (PBC) for the quarks, and the infinite-volume crossover line including the CEP is added, too. The diagrams on the left hand side correspond to results without ultraviolet improvement while the diagrams on the right hand side are obtained with ultraviolet improvement. Similar to the results for

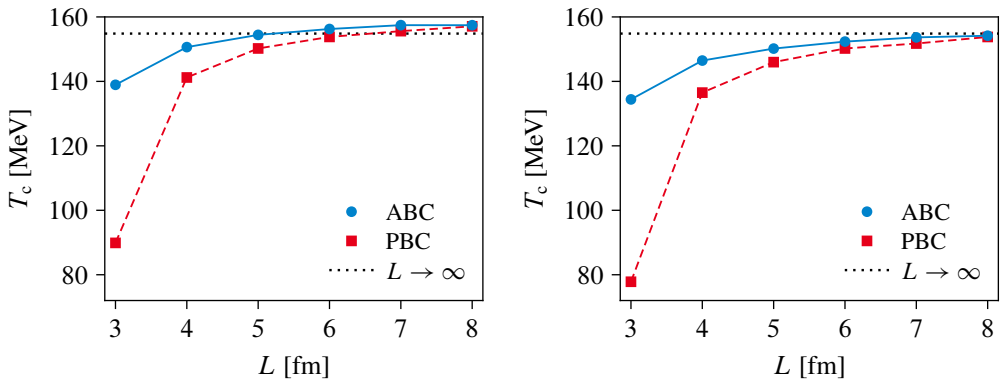

Figure 6.5 Finite-volume effects without (left) and with improvement (right): box-size dependence of the pseudocritical chiral transition temperature for ABC and PBC at $\mu_B = 0$. The black, dotted line is the infinite-volume result. Data points are connected to guide the eye.

T_c at zero chemical potential, we note the drastic effects of the improvement. Whereas the CEPs of the series of larger and larger box sizes do not approach the infinite-volume CEP without improvement, they do so after the improvement is implemented. Both the crossover line and the CEP at $L = 8\,\text{fm}$ using the improved setup are very close to the infinite-volume limit, and the remaining discrepancy is within the numerical error of the $L \to \infty$ calculation. Furthermore, the volume-dependent shift of the crossover line and CEP for increasing box size approach the infinite-volume result uniformly. Thus, while the overall qualitative behavior with and without improvement is the same, quantitative aspects can only be discussed in the improved framework.

For ABC and PBC, both phase diagrams show a similar trend when the box size is decreased: the CEP moves toward smaller temperatures and larger chemical potentials. More precisely, we find that the increase of its location in μ_B direction is larger than the decrease in T direction, leading to a smaller curvature of the crossover line. Overall, the temperature dependence of the crossover line and CEP is analogous to that of the pseudocritical chiral transition temperature at vanishing chemical potential. Results for box sizes $L \gtrsim 5\,\text{fm}$ are quite similar to one another, while those for smaller volumes differ more and more as L becomes smaller. Again, finite-volume effects are significantly more distinct for PBC. In particular, the improved result for $L = 3\,\text{fm}$ shows a very flat crossover line with a CEP at $(\mu_B, T) \approx (1070, 40)\,\text{MeV}$.

The volume dependence of the location of the CEP was investigated also in an FRG treatment within a two-flavor quark-meson model [397]. In that work, the location of the CEP and its shift with L has been calculated for PBC in the range $L = 4$–$10\,\text{fm}$. Compared to our DSE calculation, the infinite-volume CEP of the FRG analysis is generally located at much higher chemical potential and lower temperature. However, a qualitative comparison

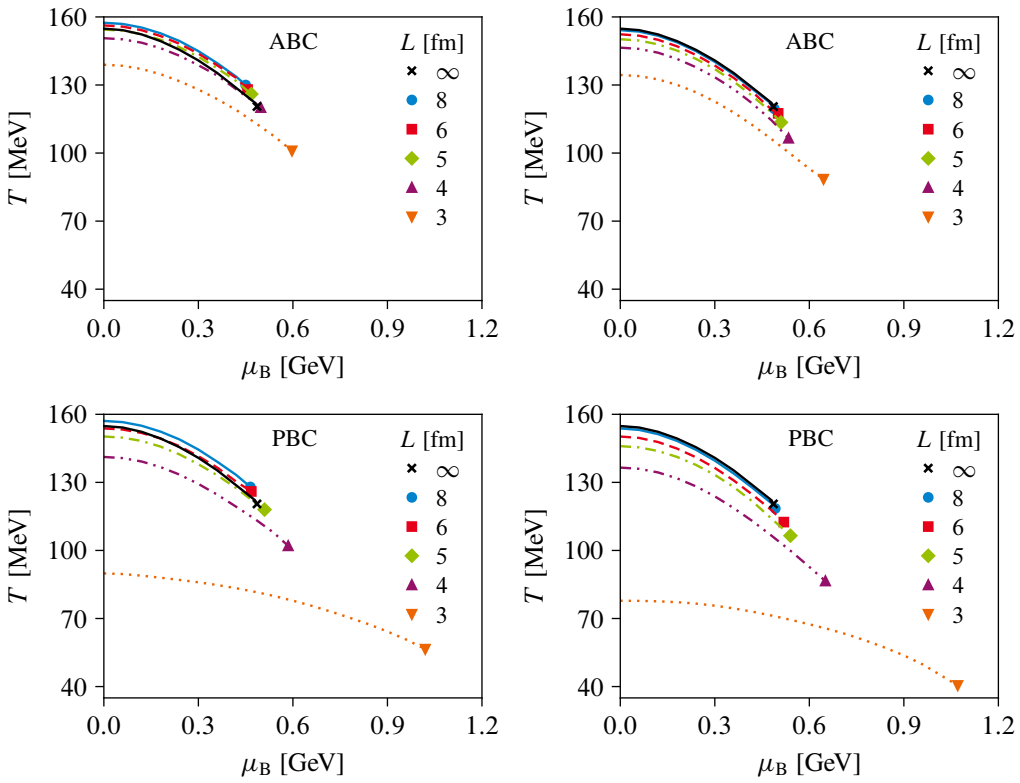

Figure 6.6 Finite-volume effects without (left) and with improvement (right): crossover lines and CEPs (symbols) for different box sizes. The upper (lower) phase diagrams are with ABC (PBC) for the quarks. The improved results for $L \in \{3\,\text{fm}, 4\,\text{fm}, 5\,\text{fm}\}$ were calculated by J. Bernhardt during the final assembling of this work.

of the results of Ref. [397] with the ones presented here yields a satisfying agreement between the present DSE and the FRG findings. Specifically, both the L-dependent relative shift of the CEP and the onset of finite-volume effects below $L = 8\,\text{fm}$ coincide well. However, below $L = 4\,\text{fm}$, the CEP disappeared completely in the FRG framework while we are still able to find one.

Curvature of the crossover line

Finally, we discuss the volume dependence of the curvature κ_2 of the crossover line, which is obtained as in infinite volume [see Eq. (3.20)]. Our results obtained with the improved framework are shown in Fig. 6.7. As already apparent from the phase diagrams, see Fig. 6.6, the curvature is smaller than the infinite-volume result and decreases for smaller box sizes. Overall, this flattening resembles the volume dependence of the pseudocritical

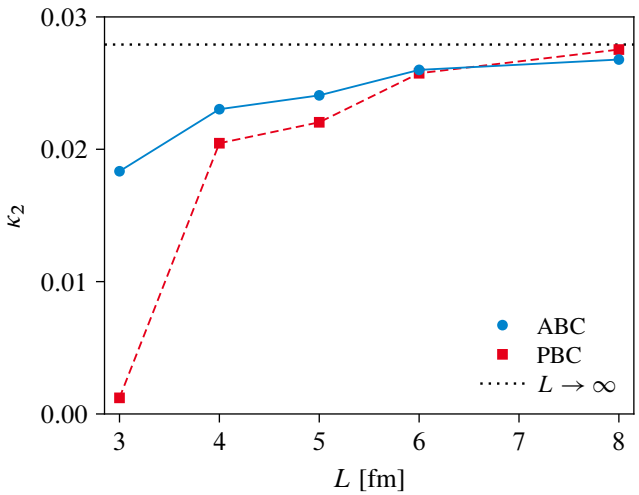

Figure 6.7 Improved finite volume: L dependence of the curvature of the crossover line for ABC and PBC for the quarks. Data points are connected by lines to guide the eye. Again, the results for $L \in \{3\,\text{fm}, 4\,\text{fm}, 5\,\text{fm}\}$ were calculated by J. Bernhardt during the final assembling of this work.

chiral transition temperature: the results for $L = 8\,\text{fm}$ are closest to the infinite-volume value and drop monotonously with decreasing box size for both boundary conditions. Compared to the pseudocritical chiral transition temperatures shown in Fig. 6.5, we find that the curvature displays a somewhat stronger reaction to finite volume. Whereas the T_c's are already quite close to the infinite-volume result for $L \gtrsim 6\,\text{fm}$, the curvature for both ABC and PBC is still off by more than ten percent. Only for very large box sizes of $L \gtrsim 8\,\text{fm}$, we observe agreement with the infinite-volume limit within errors. Here, it is important to note that the fit is quite sensitive to details in the input data and choices of fit intervals, such that κ_2 can only be extracted within a margin of several percent.

The curvature for PBC for the quarks between $L = 2\,\text{fm}$ and $L = 5\,\text{fm}$ was studied with FRG techniques in Ref. [396], again within a two-flavor quark-meson model. Above $L \approx 3\,\text{fm}$, there is qualitative agreement with our results: the curvature increases with L. However, for smaller box sizes an interesting discrepancy occurs. In our case, we find a monotonic decrease for smaller and smaller box sizes, whereas the FRG results at physical pion masses show an increase of the curvature when L gets smaller than $L \approx 3\,\text{fm}$, resulting in a nonmonotonic behavior with L. Even though this increase occurs for box sizes lower than we have investigated here, the sharp drop of κ_2 for $L = 3\,\text{fm}$ appears to contradict such a scenario in our calculations. The reason for this deviation might be rooted in the PBC zero mode that is attributed to be the driving force in the small-volume limit of Ref. [396] but is discarded in our case. However, our preliminary PBC results with the zero mode (see the comment on the bottom of page 91), which seem to closely

resemble ABC results, suggest that even the inclusion of the PBC zero mode would not result in a nonmonotonic behavior of the curvature with decreasing box size. One has to keep in mind, though, that Ref. [396] employs a two-flavor quark-meson model in local potential approximation, and the nonmonotonous behavior of κ_2 for small L might be an approximation artifact. This is subject of further investigations [412], but at present, our results for the small-L behavior of the curvature presumably disagree with the FRG results of Ref. [396].

6.5 Summary

In this last chapter before the epilogue, we investigated the effects of a finite, uniform, three-dimensional cubic volume with edge length L and (anti)periodic boundary conditions on the phase structure of QCD. To this end, we formulated and solved the DSE setup presented in Section 3.1 in that finite cubic volume. This is a major step forward since finite-volume studies of our truncation scheme were so far performed only in its quenched version. We found that finite volume acts chirally restoring as L decreases. Generally, significant volume effects have been observed for box sizes $L \lesssim 5\,\mathrm{fm}$, where sizable shifts of the crossover line and CEP occurred: the smaller the volume the smaller the pseudocritical chiral transition temperature in conjunction with a shift of the CEP toward larger chemical potential. Volumes as large as $L^3 \gtrsim (8\,\mathrm{fm})^3$ are very close to infinite volume. Furthermore, we demonstrated that the naive implementation of finite volume is plagued by finite-size artifacts that spoil a clean infinite-volume limit. Therefore, it is vital to properly remove these artifacts, which we did by means of a continuous-momentum approximation for large momentum magnitudes, in order to make reliable statements about finite-volume effects.

7 Epilogue

In this thesis, we investigated QCD at nonzero temperature and chemical potential using the nonperturbative functional framework of DSEs. We employed a sophisticated combination of lattice results for pure YM theory and a truncated set of DSEs for the quark and gluon propagators of $(2+1)$-flavor QCD, which has been studied extensively in the past [79]. In particular, we used an ansatz for the quark-gluon vertex that is inspired by the STI for the full vertex and provides the correct logarithmic running of the propagators in the ultraviolet momentum region. Furthermore, the gluonic sector and the backcoupling of the quarks onto same has been taken explicitly into account by using fits to temperature-dependent lattice data for the quenched gluon propagator supplemented with an explicit calculation of the quark-loop contribution to the gluon self-energy, thereby unquenching the gluon. As a result, we got access to the fully nonperturbative quark and unquenched gluon propagators at (in principle) arbitrary temperature and chemical potential. The free parameters of our truncation scheme, the infrared strength of the vertex and the quark masses, have been fitted to reproduce the pseudocritical chiral transition temperature at vanishing chemical potential as obtained in recent lattice-QCD calculations.

First, we studied the phase structure of QCD by monitoring the order parameter for chiral symmetry restoration, the subtracted quark condensate, as a function of temperature and chemical potential. Along the temperature axis at vanishing chemical potential, our results for the subtracted condensate as a function of temperature agreed quantitatively with corresponding lattice results, and displayed the typical behavior of an analytic crossover from the hadronic phase to the quark-gluon plasma. This has been a nontrivial output of our calculation because we only fixed the value of the transition temperature but not the steepness of the chiral transition. At nonvanishing chemical potential, the crossover transition became steeper with increasing chemical potential and eventually terminated in a second-order CEP at $(\mu_{\mathrm{B}}, T) \approx (495, 119)\,\mathrm{MeV}$. In light of the current state-of-the-art functional calculations of this work, the FRG-assisted DSE framework of Refs. [248, 249], and the FRG study of Ref. [247], we are inclined to assume a systematic error of (at least) around twenty percent for the CEP results. In order to properly quantify and reduce this error, extended DSE studies and systematic in-depth comparisons with other truncations within DSEs and the FRG are necessary tasks for future works, in particular to pave the

way for a quantitative prediction from functional methods regarding the location of the CEP. Excitingly, heavy-ion collision experiments at RHIC, FAIR, and NICA will be able to probe the corresponding region of the QCD phase diagram—making reliable theoretical predictions vital.

Second, in order to make contact with these experiments, we computed quark and baryon number fluctuations and ratios of the latter across the QCD phase diagram. We found that the nonperturbative evaluation of the quark number density, our starting point for the fluctuations, was initially not well-defined, i.e., divergent, necessitating a subtraction scheme to remove the divergence. With a regularized quark number density at hand, we computed the quark number susceptibility and found satisfying agreement with results from the lattice. In particular, we calculated the skewness and kurtosis ratios, which are a direct link to experiment, along our crossover line up to the CEP. Furthermore, we scanned lines of equal temperature distance below the crossover. For chemical potentials $\mu_\mathrm{B} \lesssim 250\,\mathrm{MeV}$, our results agreed with recent data from the STAR collaboration, which was taken during the first phase of the Beam Energy Scan program at RHIC. For larger values of the chemical potential, we obtained qualitative and quantitative differences when we approached the CEP on our crossover line. However, qualitative agreement (at least to some extent) has been obtained assuming that the crossover transition and the freeze-out line separate at larger chemical potential. A major caveat in this interpretation is the wrong universality class of our CEP—we found mean-field scaling, while the CEP is expected to be in the $\mathbb{Z}_2$ universality class. A task for future work is to validate our expectation that the inclusion of explicit pion and sigma-meson contributions to the quark-gluon vertex, which has been achieved recently in an exploratory fashion [102, 263], put our CEP in the correct universality class of the three-dimensional Ising model. Furthermore, at high temperatures, our fluctuations saturate well below the Stefan–Boltzmann limit. This issue can be traced back to missing tensor structures in our vertex ansatz which react strongly to the restoration of chiral symmetry around and above the pseudocritical chiral transition temperature. In the long term, the inclusion of these are inevitable.

Third, we studied thermodynamics with our DSE framework. We proposed a method to compute the entropy density solely from the quark condensate; a subsequent integration yields the pressure. The key feature of the method is that no approximation is used during its derivation, and only the quark condensate is needed as input. This is particularly useful for DSEs, where accessing the thermodynamic potential is extremely difficult and has been achieved so far only within simple truncations. Even then, the proper removal of the quartic divergence contained in the potential is a nontrivial task. Our proposed method provides a truncation-independent way to compute thermodynamic quantities as soon as one gets hold of the quark condensate. That the method works effectively and yields reliable results was shown using a NJL model. Then, we used condensate

data obtained from our DSE setup and computed the pressure, entropy density, energy density, and interaction measure from zero chemical potential up to the CEP as functions of temperature. These thermodynamic results are, to our knowledge, the first ones obtained from DSEs with a beyond-rainbow-ladder truncation—emphasizing the usefulness of the presented method. At vanishing chemical potential, our thermodynamic results agreed well with lattice QCD for temperatures below and around the pseudocritical chiral transition temperature. However, at high temperatures, we observed an unphysical decrease of the entropy density with temperature. This erroneous behavior is again rooted in the vertex ansatz. Together with the high-temperature artifacts seen in the fluctuations, this emphasizes that an elaborate quark-gluon vertex is needed for proper thermodynamics at high temperatures and/or densities. In particular, tensor structures that react strongly to the restoration of chiral symmetry are of crucial importance. Here, we stress that our proposed method is independent of such details and applicable to any truncation regardless how complicated the vertex may look like. Boldly said, our method significantly extends the boundaries of what the DSE approach is generally capable of in terms of thermodynamics.

Finally, we also studied the impact of a finite, uniform, three-dimensional cubic volume with equal edge lengths L and (anti)periodic boundary conditions for the quarks on the phase diagram of QCD. We extracted the volume dependence of the chiral order parameter and found only moderate effects of the order of ten MeV and smaller for box sizes $L \gtrsim 5\,\mathrm{fm}$. Only for very small volumes sizable shifts of the CEP and the associated crossover line occurred. These shifts were monotonous: smaller volumes corresponded to smaller transition temperatures and the CEP shifted toward larger chemical potential. At least two extensions of the current framework are necessary in the future. First, one needs to adapt the implementation of the finite-volume boundary conditions to the actual physics case—there are no (anti)periodic boundary conditions when two nuclei collide. The situation rather resembles the one of a sphere (large centrality) or an almond-shaped volume (small centrality) with a fuzzy boundary. For example, this situation may be better represented in a calculation in a spherical volume rather than a cube. Second, one needs to address the volume dependence of quantities such as fluctuations of conserved charges. The implicit volume dependence of ratios of fluctuations, which we can study continuously from small to large volumes, and the phenomenological implications are particularly interesting. Work in this direction within our framework is in progress.

A Notation and conventions

A.1 Natural units

Throughout this work, we use natural units:

$$\hbar = c = k_\mathrm{B} = 1\,, \tag{A.1}$$

where $\hbar$, c, and k_B denote Planck's reduced constant, the speed of light, and the Boltzmann constant, respectively. The only remaining unit is energy given in electron volts (eV). For example, the SI units meter (m) and kelvin (K) for length and temperature are related to the energy via $1\,\mathrm{m} \approx 5.1 \times 10^6\,\mathrm{eV}^{-1}$ and $1\,\mathrm{K} \approx 8.6 \times 10^{-5}\,\mathrm{eV}$.

A.2 Euclidean space-time

We work in four-dimensional Euclidean space-time. The metric is given by

$$g_{\nu\sigma} = \delta_{\nu\sigma} \tag{A.2}$$

with the Kronecker delta

$$\delta_{\nu\sigma} = \begin{cases} 0 & \text{if } \nu \neq \sigma\,, \\ 1 & \text{if } \nu = \sigma\,. \end{cases} \tag{A.3}$$

The scalar product of two four-vectors a and b thus reads

$$a \cdot b = \delta_{\nu\sigma}\, a_\nu\, b_\sigma = a_\nu\, b_\nu = a_4\, b_4 + \boldsymbol{a} \cdot \boldsymbol{b}\,. \tag{A.4}$$

A distinction between co- and contravariant indices is not necessary, $a_\nu = a^\nu$. In terms of its components, a four-vector is written as $a = (a_4, \boldsymbol{a})$ emphasizing the Euclidean space-time by using the index 4 for the first component. Boldface letters denote usual three-vectors in $\mathbb{R}^3$. Furthermore, as already employed in (A.4), we use the Einstein summation convention: one has to sum over repeated free indices (with appropriate limits). For example, the expression $\delta_{\nu\sigma}\, a_\nu\, b_\sigma$ is to be understood as $\sum_{\nu,\sigma=1}^{4} \delta_{\nu\sigma}\, a_\nu\, b_\sigma$.

The gamma matrices obey

$$\{\gamma_\nu, \gamma_\sigma\} = \gamma_\nu\gamma_\sigma + \gamma_\sigma\gamma_\nu = 2\delta_{\nu\sigma}\,. \tag{A.5}$$

It follows that $\gamma_\nu^2 = \mathbb{1}$, and we can choose the gamma matrices to be Hermitian, $\gamma_\nu = \gamma_\nu^\dagger$. Furthermore, the Feynman slash notation is used: $\not{p} = \gamma_\nu p_\nu$.

For the sake of brevity, integrals in coordinate and momentum space are written in an abbreviated form, viz.,

$$\int_x = \int \mathrm{d}^4x\,, \qquad \fint_p = \int \frac{\mathrm{d}^4p}{(2\pi)^4}\,, \tag{A.6}$$

and analogously in three dimensions,

$$\int_{\boldsymbol{x}} = \int \mathrm{d}^3x\,, \qquad \fint_{\boldsymbol{p}} = \int \frac{\mathrm{d}^3p}{(2\pi)^3}\,. \tag{A.7}$$

One-dimensional integrations and path integrals, however, are unaffected. Their measure and possible limits are always written explicitly.

From Minkowski to Euclidean space-time

In the following, we briefly sketch how to get from Minkowski to Euclidean space-time. For the former we use the metric $g_{\mathrm{M}}^{\nu\sigma} = \mathrm{diag}(1,-1,-1,-1)$ such that $x_{\mathrm{M}}^2 = x_0^2 - \boldsymbol{x}^2$ for a spatial four-vector $x_{\mathrm{M}}^\nu = (x_0, \boldsymbol{x})$, where the subscript M indicates Minkowski space-time. At heart of the transition to Euclidean space-time lies the imaginary-time formalism, where one analytically continues from real to imaginary times. This is the well-known Wick rotation performed already on the level of the Lagrangian and generating functional rather than for single Feynman diagrams [413–415]. We would like to emphasize that it is not just a simple substitution of integration variables but an actual deformation of the integration contour in the complex x_0 plane.

For the imaginary-time formalism, we consider a function $h(x_0)$ and the contours shown in Fig. A.1. Assuming h can be analytically continued to complex times and is free of singularities in the covered region of the complex x_0-plane,

$$0 = \oint_{\mathcal{C}_1+\ldots+\mathcal{C}_4} h \tag{A.8}$$

holds due to Cauchy's theorem. In the limit $R \to \infty$ and given that h falls off sufficiently

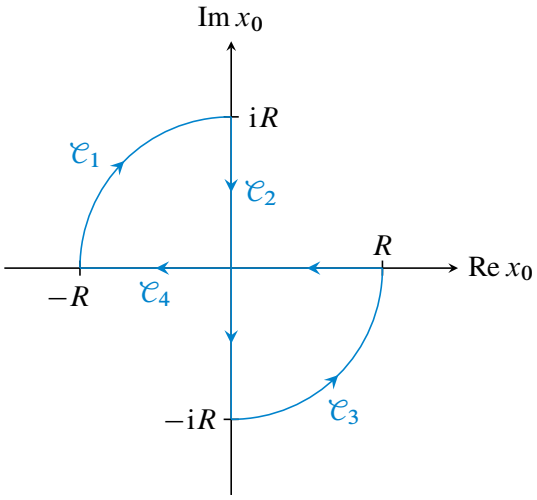

Figure A.1 Integration contours $\mathcal{C}_i$ (blue) for the imaginary-time formalism.

fast for large $|x_0|$, the contributions from the arcs $\mathcal{C}_1$ and $\mathcal{C}_3$ vanish and we arrive at

$$\int_{-\infty}^{\infty} \mathrm{d}x_0\, h(x_0) = -\mathrm{i} \int_{-\infty}^{\infty} \mathrm{d}x_4\, h(-\mathrm{i}x_4)\,, \tag{A.9}$$

where the analytic continuation $x_0 = -\mathrm{i}x_4$ with $x_4 \in \mathbb{R}$ becomes apparent. It follows that

$$x_{\mathrm{M}}^2 = x_0^2 - \boldsymbol{x}^2 = -(x_4^2 + \boldsymbol{x}^2)\,, \tag{A.10}$$

where the right-hand side is the negative norm of the four-vector $x_{\mathrm{E}}^\nu = (x_4, \boldsymbol{x})$ in Euclidean space-time (hence the subscript E) with metric $g_{\mathrm{E}}^{\nu\sigma} = \delta_{\nu\sigma}$. As a consequence, we have to define suitable continuations for general four-vectors a_{M}^ν, gamma matrices γ_{M}^ν, and tensors $T_{\mathrm{M}}^{\nu\sigma}$. We follow Ref. [84] and use[42]

$$\begin{gathered} a_{\mathrm{M}}^0 = -\mathrm{i}a_{\mathrm{E}}^4\,, \qquad a_{\mathrm{M}}^j = a_{\mathrm{E}}^j\,, \qquad \gamma_{\mathrm{M}}^0 = \gamma_{\mathrm{E}}^4\,, \qquad \gamma_{\mathrm{M}}^j = \mathrm{i}\gamma_{\mathrm{E}}^j\,, \\ T_{\mathrm{M}}^{00} = -T_{\mathrm{E}}^{44}\,, \qquad T_{\mathrm{M}}^{0j} = -\mathrm{i}T_{\mathrm{E}}^{4j}\,, \qquad T_{\mathrm{M}}^{j0} = -\mathrm{i}T_{\mathrm{E}}^{j4}\,, \qquad T_{\mathrm{M}}^{jk} = T_{\mathrm{E}}^{jk}\,. \end{gathered} \tag{A.11}$$

The choice for the gamma matrices preserves the meaning of the Feynman slash as an inner product of a vector containing gamma matrices with an ordinary four-vector. These rules imply

$$a_{\mathrm{M}} \cdot b_{\mathrm{M}} = -a_{\mathrm{E}} \cdot b_{\mathrm{E}}\,, \qquad \partial_{\mathrm{M}} \cdot a_{\mathrm{M}} = \partial_{\mathrm{E}} \cdot a_{\mathrm{E}} \tag{A.12}$$

[42] Note that we have some freedom to choose signs here. Therefore, Euclidean conventions tend to differ from author to author and one can find several version in the literature.

and

$$\left\{\gamma_{\mathrm{E}}^{\nu}, \gamma_{\mathrm{E}}^{\sigma}\right\} = 2\delta_{\nu\sigma}\,, \qquad \not{a}_{\mathrm{M}} = -\mathrm{i}\not{a}_{\mathrm{E}}\,, \qquad \not{\partial}_{\mathrm{M}} = \mathrm{i}\not{\partial}_{\mathrm{E}}\,. \tag{A.13}$$

Thus, if we start in Minkowski space with the QCD action

$$I_{\mathrm{QCD,M}} = \int_{x_{\mathrm{M}}} \left(\bar{\psi}_{\mathrm{M}}^{\alpha} (\mathrm{i}\not{D}_{\mathrm{M}} - m)_{\alpha\beta} \psi_{\mathrm{M}}^{\beta} - \frac{1}{4} F^{a}_{\mathrm{M},\nu\sigma} F_{\mathrm{M}}^{a\nu\sigma} \right), \tag{A.14}$$

where $D_{\mathrm{M}}^{\nu} = \partial_{\mathrm{M}}^{\nu} - \mathrm{i}gA_{\mathrm{M}}^{a\nu}\tau^{a}$ and $F_{\mathrm{M}}^{a\nu\sigma} = \partial_{\mathrm{M}}^{\nu} A_{\mathrm{M}}^{a\sigma} - \partial_{\mathrm{M}}^{\sigma} A_{\mathrm{M}}^{a\nu} + g f^{abc} A_{\mathrm{M}}^{b\nu} A_{\mathrm{M}}^{c\sigma}$, we find

$$I_{\mathrm{QCD,M}} = \mathrm{i}\, I_{\mathrm{QCD,E}} = \mathrm{i} \int_{x_{\mathrm{E}}} \left(\bar{\psi}_{\mathrm{E}}^{\alpha} (\not{D}_{\mathrm{E}} + m)_{\alpha\beta} \psi_{\mathrm{E}}^{\beta} + \frac{1}{4} F_{\mathrm{E}}^{a\nu\sigma} F_{\mathrm{E}}^{a\nu\sigma} \right) \tag{A.15}$$

with $D_{\mathrm{E}}^{\nu} = \partial_{\mathrm{E}}^{\nu} + \mathrm{i}gA_{\mathrm{E}}^{a\nu}\tau^{a}$ and $F_{\mathrm{E}}^{a\nu\sigma} = \partial_{\mathrm{E}}^{\nu} A_{\mathrm{E}}^{a\sigma} - \partial_{\mathrm{E}}^{\sigma} A_{\mathrm{E}}^{a\nu} - g f^{abc} A_{\mathrm{E}}^{b\nu} A_{\mathrm{E}}^{c\sigma}$. It follows that the exponential in the partition function becomes damping:

$$\mathrm{e}^{\mathrm{i}I_{\mathrm{QCD,M}}} = \mathrm{e}^{-I_{\mathrm{QCD,E}}}\,. \tag{A.16}$$

Since we work exclusively in Euclidean space-time throughout this thesis, the subscript E is only used in this subsection and omitted everywhere else. Finally, we would like to mention that for a rigorous mathematical treatment one has to resort to axiomatic quantum field theory. Starting in Euclidean space, the questions whether (i) the analytic continuation back to real times is well-defined; (ii) the Euclidean formulation is uniquely related to the theory in Minkowski space are both governed by the Osterwalder–Schrader axioms [416]. A detailed discussion about Wick rotation of spinors and its subtleties can be found in Ref. [417] and references therein.

A.3 Fourier transform

The transition from Euclidean coordinate to momentum space is accomplished by the Fourier transform. We use

$$h(p) = \int_{x} \mathrm{e}^{-\mathrm{i}p\cdot x}\, h(x)\,, \qquad h(x) = \fint_{p} \mathrm{e}^{\mathrm{i}p\cdot x}\, h(p)\,. \tag{A.17}$$

From these conventions, it follows that the integral representations of the delta function in coordinate and momentum space are given by

$$\delta^{(4)}(x) = \fint_{p} \mathrm{e}^{\mathrm{i}p\cdot x}\,, \qquad (2\pi)^4 \delta^{(4)}(p) = \int_{x} \mathrm{e}^{-\mathrm{i}p\cdot x}\,. \tag{A.18}$$

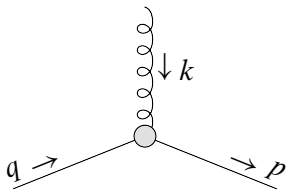

Figure A.2 Momentum routing for the dressed quark-gluon vertex: k and q are incoming, while p is outgoing. Momentum conservation implies that $k = p - q$.

As usual, we distinguish a function from its Fourier transform solely by the appearing argument rather than introducing a special notation. Note that the signs of the exponents in Eq. (A.17) are subject to change, especially for multidimensional Fourier transforms, depending on the choice whether a momentum is incoming or outgoing.

In particular, for propagators we choose one momentum incoming and the other one outgoing. Thus, with p incoming, p' outgoing, and G any of the QCD propagators, the Fourier transform of the latter is given by

$$G(p, p') = \int_{x,x'} \mathrm{e}^{-\mathrm{i}p\cdot x}\, \mathrm{e}^{\mathrm{i}p'\cdot x'}\, G(x, x')\,, \tag{A.19}$$

which implies the Fourier representation

$$G(x, x') = \fint_{p,p'} \mathrm{e}^{\mathrm{i}p\cdot x}\, \mathrm{e}^{-\mathrm{i}p'\cdot x'}\, G(p, p') \tag{A.20}$$

of the coordinate-space propagator. In homogeneous matter, the propagators depend only on relative distances, $G(x, x') = G(x - x')$, and are thus diagonal in momentum space:

$$\begin{aligned} G(p, p') &= \int_{x,x'} \mathrm{e}^{-\mathrm{i}p\cdot x}\, \mathrm{e}^{\mathrm{i}p'\cdot x'}\, G(x - x') \\ &= (2\pi)^4\, \delta^{(4)}(p - p')\, G(p')\,. \end{aligned} \tag{A.21}$$

For the quark-gluon vertex, we choose the gluon momentum k and the quark momentum q incoming, while the other quark momentum p is outgoing (see Fig. A.2), i.e.,

$$g\Gamma^a_{\nu,\alpha\beta}(k, q, p) = \int_{x,y,z} \mathrm{e}^{-\mathrm{i}k\cdot x}\, \mathrm{e}^{-\mathrm{i}q\cdot y}\, \mathrm{e}^{\mathrm{i}p\cdot z}\, g\Gamma^a_{\nu,\alpha\beta}(x, y, z)\,. \tag{A.22}$$

Moreover, momentum conservation allows for a reduced vertex $\Gamma^a_{\nu,\alpha\beta}(q, p)$ defined via

$$g\Gamma^a_{\nu,\alpha\beta}(k, q, p) = \mathrm{i}g\,(2\pi)^4\, \delta^{(4)}(k + q - p)\, \Gamma^a_{\nu,\alpha\beta}(q, p)\,. \tag{A.23}$$

As for the bare propagators, the bare quark-gluon vertex is obtained from Eq. (2.35) for $\Gamma_{\mathrm{1PI}} = I^{\mathrm{gf}}_{\mathrm{QCD}}$ and vanishing macroscopic fields:

$$\begin{aligned} g\Gamma^{(0),a}_{\nu,\alpha\beta}(x,y,z) &= \left.\frac{\delta^3 I^{\mathrm{gf}}_{\mathrm{QCD}}[\Phi]}{\delta\Psi_\beta(z)\delta\bar{\Psi}_\alpha(y)\delta\mathcal{A}^a_\nu(x)}\right|_{\Phi=0} \\ &= \mathrm{i}g\,(\gamma_\nu\tau^a)_{\alpha\beta}\,\delta^{(4)}(x-y)\delta^{(4)}(x-z)\,, \end{aligned} \tag{A.24}$$

and for the reduced bare vertex, we get the expected result

$$\Gamma^{(0),a}_{\nu,\alpha\beta}(q,p) = (\gamma_\nu\tau^a)_{\alpha\beta} \tag{A.25}$$

known from perturbation theory.

B Path integral over a field derivative

Here, we prove Eq. (2.37) on which the DSE formalism is based. For simplicity, we consider an uncharged scalar field φ with action $I[\varphi]$ and partition function

$$\mathcal{Z}[J] = \int \mathcal{D}\varphi \exp\left(-I[\varphi] + \int_x J(x)\varphi(x)\right). \tag{B.1}$$

We have to show that

$$0 = \int \mathcal{D}\varphi \frac{\delta}{\delta\varphi(y)} \exp\left(-I[\varphi] + \int_x J(x)\varphi(x)\right), \tag{B.2}$$

and the necessary assumption to do so is that the path-integral measure is invariant under infinitesimal translations $\varphi \to \varphi + \eta h$, where h is an arbitrary function and $\eta > 0$. We can therefore write

$$\mathcal{Z}[J] = \int \mathcal{D}\varphi \underbrace{\exp\left(-I[\varphi + \eta h] + \int_x J(x)\varphi(x) + \eta \int_x J(x)h(x)\right)}_{(\star)}. \tag{B.3}$$

A Taylor expansion with respect to η yields

$$\begin{aligned}(\star) = {} & \exp\left(-I[\varphi] + \int_x J(x)\varphi(x)\right) \\ & + \eta \int_y h(y)\left(-\frac{\delta I[\varphi]}{\delta\varphi(y)} + J(y)\right)\exp\left(-I[\varphi] + \int_x J(x)\varphi(x)\right) \\ & + \mathcal{O}(\eta^2),\end{aligned} \tag{B.4}$$

and from Eq. (B.3) thus follows

$$\begin{aligned}0 = {} & \int_y h(y) \int \mathcal{D}\varphi \left(-\frac{\delta I[\varphi]}{\delta\varphi(y)} + J(y)\right)\exp\left(-I[\varphi] + \int_x J(x)\varphi(x)\right) \\ & + \mathcal{O}(\eta).\end{aligned} \tag{B.5}$$

Since h is arbitrary and η infinitesimal, we deduce

$$\begin{aligned} 0 &= \int \mathcal{D}\varphi \left(-\frac{\delta I[\varphi]}{\delta \varphi(y)} + J(y) \right) \exp\left(-I[\varphi] + \int_x J(x)\varphi(x) \right) \\ &= \int \mathcal{D}\varphi \, \frac{\delta}{\delta \varphi(y)} \exp\left(-I[\varphi] + \int_x J(x)\varphi(x) \right), \end{aligned} \tag{B.6}$$

which is the desired result.

C Derivation of the quark DSE

Since the quark propagator is the central object in this work, we shall derive its DSE using the recipe given below Eq. (2.38). The quark DSE is obtained by initially choosing $\Phi_i = \bar{\Psi}_\alpha(x)$ and $\phi_i = \bar{\psi}_\alpha(x)$, followed by a derivative with respect to $\Psi_\beta(y)$. Thus, we find

$$\begin{aligned}\frac{\delta^2\Gamma_{1\mathrm{PI}}[\Phi]}{\delta\Psi_\beta(y)\delta\bar{\Psi}_\alpha(x)} = \frac{\delta}{\delta\Psi_\beta(y)}\Bigg[&(\not{\partial} + m)_{\alpha\delta}\Psi_\delta(x) \\ &+ \mathrm{i}g(\gamma_\nu\tau^a)_{\alpha\delta}\left(\mathcal{A}^a_\nu(x)\Psi_\delta(x) + \frac{\delta\Psi_\delta(x)}{\delta j^a_\nu(x)}\right)\Bigg].\end{aligned} \tag{C.1}$$

The derivative $\delta/\delta\Psi_\beta(y)$ on the right-hand side is most conveniently carried out by rewriting all macroscopic fields as derivatives of W [Eq. (2.27)] and using the functional chain rule

$$\frac{\delta}{\delta\Psi_\beta(y)} = \int_z \frac{\delta J_i(z)}{\delta\Psi_\beta(y)}\frac{\delta}{\delta J_i(z)} = \int_z \frac{\delta^2\Gamma_{1\mathrm{PI}}[\Phi]}{\delta\Psi_\beta(y)\delta\Phi_i(z)}\frac{\delta}{\delta J_i(z)}\,, \tag{C.2}$$

which yields the intermediate result

$$\begin{aligned}\frac{\delta^2\Gamma_{1\mathrm{PI}}[\Phi]}{\delta\Psi_\beta(y)\delta\bar{\Psi}_\alpha(x)} = \int_z \frac{\delta^2\Gamma_{1\mathrm{PI}}[\Phi]}{\delta\Psi_\beta(y)\delta\Phi_i(z)}\Bigg[&(\not{\partial} + m)_{\alpha\delta}\frac{\delta^2 W[J]}{\delta J_i(z)\delta\bar{\eta}_\delta(x)} \\ &+ \mathrm{i}g(\gamma_\nu\tau^a)_{\alpha\delta}\left(\frac{\delta^2 W[J]}{\delta J_i(z)\delta j^a_\nu(x)}\frac{\delta W[J]}{\delta\bar{\eta}_\delta(x)}\right. \\ &\left.+ \frac{\delta W[J]}{\delta j^a_\nu(x)}\frac{\delta^2 W[J]}{\delta J_i(z)\delta\bar{\eta}_\delta(x)} + \frac{\delta^3 W[J]}{\delta J_i(z)\delta\bar{\eta}_\delta(x)\delta j^a_\nu(x)}\right)\Bigg].\end{aligned} \tag{C.3}$$

Now, since all necessary derivatives are carried out, we set the sources to zero in order to get the physical correlation functions. The only nonvanishing contribution from the chain rule is $\Phi_i = \bar{\Psi}_\varepsilon$, which entails $J_i = \eta_\varepsilon$. Identifying the dressed and bare quark

propagators [Eqs. (2.31) and (2.33)], we find

$$S^{-1}_{\alpha\beta}(x,y) = S^{-1}_{0,\alpha\beta}(x,y) + \mathrm{i}g\,(\gamma_\nu\tau^a)_{\alpha\delta}\int_z S^{-1}_{\varepsilon\beta}(z,y)\left\langle A^a_\nu(x)\,\psi_\delta(x)\,\bar{\psi}_\varepsilon(z)\right\rangle^{(J=0)}_{\mathrm{conn}}. \tag{C.4}$$

Next, we use the decomposition (2.36) of the connected two-quark-one-gluon correlation function $\left\langle A^a_\nu(x)\,\psi_\delta(x)\,\bar{\psi}_\varepsilon(z)\right\rangle^{(J=0)}_{\mathrm{conn}}$ into propagators and the quark-gluon vertex to arrive at the quark DSE in coordinate space:

$$S^{-1}_{\alpha\beta}(x,y) = S^{-1}_{0,\alpha\beta}(x,y) + \Sigma_{\alpha\beta}(x,y)\,, \tag{C.5}$$

where the self-energy is given by

$$\Sigma_{\alpha\beta}(x,y) = -\mathrm{i}g^2\,(\gamma_\nu\tau^a)_{\alpha\delta}\int_{x',y'} D^{ab}_{\nu\sigma}(x,x')\,S_{\delta\varepsilon}(x,y')\,\Gamma^b_{\sigma,\varepsilon\beta}(x',y',y)\,. \tag{C.6}$$

The remaining tasks are to disentangle the index structure, Fourier transform the quark DSE to get its momentum-space version, and introduce renormalization constants at the appropriate places [see Eqs. (2.17) and (2.18)] to arrive at the DSE for the renormalized quark propagator.

The index structure of Eqs. (C.5) and (C.6) is resolved as follows. First, there is a separate DSE for each quark flavor f. Second, the quark propagator is diagonal in color space, i.e., the color structure of both the bare and dressed quark propagator is, in matrix notation, $\mathbb{1}_{\mathrm{color}}$. With $D^{ab}_{\nu\sigma} = \delta_{ab}D_{\nu\sigma}$ and $\Gamma^a_{\nu,\alpha\beta} = (\tau^a\Gamma_\nu)_{\alpha\beta}$, the color structure of the quark self-energy is given by $\tau^a\tau^a = C_2^{\mathrm{fund}}\mathbb{1}_{\mathrm{color}}$ with $C_2^{\mathrm{fund}} = (N_c^2-1)/2N_c$ being the second-order Casimir factor in the fundamental representation of $\mathrm{SU}(N_c)_{\mathrm{color}}$.[43] Third, the structure in Dirac space is not resolved explicitly to avoid a cluttered notation. After taking the color trace and performing the Fourier transform (see Section A.3 for our conventions), the DSE for the renormalized dressed quark propagator in momentum space is given by

$$S_f^{-1}(p,p') = S^{-1}_{0,f}(p,p') + \Sigma_f(p,p')\,, \tag{C.7}$$

which is now a Dirac-algebra valued equation only. The inverse bare quark propagator reads

$$S^{-1}_{0,f}(p,p') = (2\pi)^4\delta^{(4)}(p-p')\,S^{-1}_{0,f}(p') \tag{C.8}$$

with

$$S^{-1}_{0,f}(p') = Z_2^f\left(\mathrm{i}\not{p}' + Z_{m_f}m_f\right), \tag{C.9}$$

[43] This simple flavor and color structure is sufficient for most applications, including this work. For example, color-superconducting phases exhibit a nontrivial flavor-color structure [238, 242].

where m_f is the renormalized current quark mass, and the self-energy reads

$$\Sigma_f(p,p') = -\mathrm{i}g^2 C_2^{\mathrm{fund}} Z_{1\mathrm{F}}^f \int\!\!\!\!\!\!\int_{q,r,s} D_{\nu\sigma}(p-q,r)\,\gamma_\nu\, S_f(q,s)\,\Gamma_\sigma^f(r,s,p')\,. \tag{C.10}$$

The quark DSE given in Eq. (C.7) allows for different in- and outgoing momenta, $p \neq p'$, and the momentum arguments of the dressed quark-gluon vertex in the self-energy are unconstrained. In this work, however, we consider homogeneous, i.e., translationally invariant matter where, in coordinate space, all propagators depend only on the relative distance $x - x'$ but not on the two space-time points x and x' independently.[44] As a consequence, the propagators are diagonal in momentum space [Eq. (A.21)] and momentum conservation holds at the vertices. This allows for the definition of a reduced vertex $\Gamma_\sigma^f(s,p')$ according to Eq. (A.23), and we eventually find the homogeneous quark DSE in momentum space:

$$S_f^{-1}(p) = S_{0,f}^{-1}(p) + \Sigma_f(p) \tag{C.11}$$

with the self-energy

$$\Sigma_f(p) = g^2 C_2^{\mathrm{fund}} \frac{Z_2^f}{\widetilde{Z}_3} \int\!\!\!\!\!\!\int_q D_{\nu\sigma}(k)\,\gamma_\nu\, S_f(q)\,\Gamma_\sigma^f(q,p)\,, \tag{C.12}$$

where $k = p - q$ denotes the gluon momentum, which follows from momentum conservation. Furthermore, we used $Z_{1\mathrm{F}}^f = Z_2^f / \widetilde{Z}_3$, which results from the nonrenormalization of the ghost-gluon vertex in Landau gauge [103, 137] that allows us to choose $\widetilde{Z}_1 = 1$.

[44] A study of inhomogeneous phases within the DSE framework can be found in Ref. [243].

D Explicit expressions and technical remarks

D.1 Infinite-volume calculations

Integral conventions

In vacuum, the integrands of the self-energies depend on the squared external momentum p^2, the squared loop momentum q^2, and the cosine of the angle between p and q. Thus, we use hyperspherical coordinates with $z = \cos\measuredangle(p,q) = p\cdot q/\sqrt{p^2q^2}$ for the four-dimensional loop integrations:

$$\fint_q \equiv \int \frac{\mathrm{d}^4q}{(2\pi)^4} = \frac{1}{8\pi^3}\int_0^\infty \mathrm{d}q^2\, q^2 \int_{-1}^1 \mathrm{d}z\, \sqrt{1-z^2}\,, \tag{D.1}$$

where the two trivial angular dependencies are already integrated out. The same is true at nonzero temperature, where we use spherical coordinates with $z = \cos\measuredangle(\boldsymbol{p},\boldsymbol{q}) = \boldsymbol{p}\cdot\boldsymbol{q}/\sqrt{\boldsymbol{p}^2\boldsymbol{q}^2}$ for the three-dimensional loop integrations:

$$\fint_{\boldsymbol{q}} \equiv \int \frac{\mathrm{d}^3q}{(2\pi)^3} = \frac{1}{8\pi^2}\int_0^\infty \mathrm{d}\boldsymbol{q}^2\, \sqrt{\boldsymbol{q}^2} \int_{-1}^1 \mathrm{d}z\,, \tag{D.2}$$

where one trivial angular dependence is again already integrated out. As detailed later, the integrals are evaluated using Gaussian quadrature rules in course of numerically solving the DSEs.

Quark DSE in vacuum

The explicit form of the coupled equations for the vacuum dressing functions A_f and B_f [Eqs. (2.43) and (2.44)] within the truncation scheme outlined in Section 3.1 is given by

$$A_f(p^2) = Z_2^f\left(1+\Sigma_A^f(p^2)\right), \tag{D.3}$$

$$B_f(p^2) = Z_2^f\left(Z_{m_f}m_f+\Sigma_B^f(p^2)\right), \tag{D.4}$$

where the projected self-energies read

$$\Sigma_A^f(p^2) = 4\pi\alpha_s C_2^{\text{fund}} \frac{1}{p^2} \int_q \frac{A_f(q^2)\, H_{\text{BC}}^f(p^2,q^2)}{q^2 A_f^2(q^2) + B_f^2(q^2)} K_A \tag{D.5}$$

$$\Sigma_B^f(p^2) = 12\pi\alpha_s C_2^{\text{fund}} \int_q \frac{B_f(q^2)\, H_{\text{BC}}^f(p^2,q^2)}{q^2 A_f^2(q^2) + B_f^2(q^2)} K_B \,. \tag{D.6}$$

Here, $H_{\text{BC}}^f(p^2,q^2) = [A_f(p^2) + A_f(q^2)]/2$, and the kernels are given by

$$K_A = \Gamma(k^2)\frac{Z(k^2)}{k^2}\left[p\cdot q + 2\,\frac{(k\cdot p)\,(k\cdot q)}{k^2}\right], \tag{D.7}$$

$$K_B = \Gamma(k^2)\frac{Z(k^2)}{k^2}\,, \tag{D.8}$$

where $k = p - q$. Furthermore, Z denotes the gluon dressing function, and Γ is the phenomenological vertex dressing [Eq. (3.8)].

The wave function and mass renormalization constants Z_2^f and Z_{m_f}, respectively, are determined using a momentum-subtraction scheme with the renormalization condition

$$S_f^{-1}(p)\big|_{p^2=\zeta^2} = \left(\mathrm{i}\not{p} + m_f\right)\big|_{p^2=\zeta^2} \tag{D.9}$$

at the renormalization point ζ. In other words, we demand $A_f(\zeta^2) = 1$ and $B_f(\zeta^2) = m_f$. It thus follows that the wave function renormalization constant is given by

$$Z_2^f = \frac{1}{1 + \Sigma_A^f(\zeta^2)} \tag{D.10}$$

while the mass renormalization constant is obtained according to

$$Z_{m_f} = \frac{1}{Z_2^f} - \frac{\Sigma_B^f(\zeta^2)}{m_f}\,. \tag{D.11}$$

In practice, we use $\zeta^2 = (80\,\text{GeV})^2$. Furthermore, we employ a Pauli–Villars regulator in order to render the divergent loop integrals in the self-energies finite. This amounts to the replacement ($X = A, B$)

$$K_X \to K_X \times \frac{1}{1 + k^2/\Lambda_{\text{reg}}^2} \tag{D.12}$$

in Eqs. (D.5) and (D.6). We use $\Lambda_{\text{reg}} = 200\,\text{GeV}$ for the regularization scale.

Gluon DSE in vacuum

The full gluon DSE is given by [Eq. (2.47)]

$$D^{-1}_{\nu\sigma}(k) = Z_3\, D^{-1}_{0,\nu\sigma}(k) + \Pi^{\mathrm{YM}}_{\nu\sigma}(k) + \Pi_{\nu\sigma}(k)\,, \tag{D.13}$$

where $\Pi^{\mathrm{YM}}_{\nu\sigma}(k)$ is the pure YM self-energy, i.e., all diagrams with no explicit quark content, and $\Pi_{\nu\sigma}(k)$ denotes the quark loop [Eq. (2.48)]. As already mentioned in the main text, the quark loop develops a spurious quadratic divergence that is caused by the numerically necessary introduction of a momentum cutoff. Furthermore, the quark loop contains a nonvanishing longitudinal component, which seems to be at odds with the transversality of the gluon propagator in Landau gauge. In principle, such nonvanishing longitudinal part poses no problem as long as it is compensated by the pure YM self-energies.[45] However, we do not compute $\Pi^{\mathrm{YM}}_{\nu\sigma}(k)$ explicitly, and hence need a method that renders the quark loop purely transversal and free of spurious quadratic divergences.

To this end, we decompose $\Pi_{\nu\sigma}(k)$ into its transversal and longitudinal components:

$$\Pi_{\nu\sigma}(k) = \mathcal{P}^{\mathrm{T}}_{\nu\sigma}(k)\,\Pi_{\mathrm{T}}(k) + \mathcal{P}^{\mathrm{L}}_{\nu\sigma}(k)\,\Pi_{\mathrm{L}}(k)\,, \tag{D.14}$$

where $\mathcal{P}^{\mathrm{T}}_{\nu\sigma}(k) = \delta_{\nu\sigma} - k_\nu k_\sigma / k^2$ and $\mathcal{P}^{\mathrm{L}}_{\nu\sigma}(k) = k_\nu k_\sigma / k^2$ are the transversal and longitudinal projectors, respectively. Since the longitudinal part contains the same quadratic divergence as the transversal one, we define the regularized transversal component by

$$\Pi^{\mathrm{reg}}_{\mathrm{T}}(k) = \Pi_{\mathrm{T}}(k) - \Pi_{\mathrm{L}}(k)\,. \tag{D.15}$$

Using $\delta_{\nu\sigma}\,\mathcal{P}^{\mathrm{T}}_{\nu\sigma}(k) = 3$, this expression can be written as follows:

$$\begin{aligned}
\Pi^{\mathrm{reg}}_{\mathrm{T}}(k) &= \frac{1}{3}\,\mathcal{P}^{\mathrm{T}}_{\nu'\sigma'}(k)\,\Pi_{\nu'\sigma'}(k) - \mathcal{P}^{\mathrm{L}}_{\nu'\sigma'}(k)\,\Pi_{\nu'\sigma'}(k) \\
&= \frac{1}{3}\,\mathcal{P}^{\mathrm{T}}_{\nu\sigma}(k)\left(\delta_{\nu\nu'}\delta_{\sigma\sigma'} - \delta_{\nu\sigma}\,\mathcal{P}^{\mathrm{L}}_{\nu'\sigma'}(k)\right)\Pi_{\nu'\sigma'}(k) \\
&= \frac{1}{3}\,\mathcal{P}^{\mathrm{T}}_{\nu\sigma}(k)\left(\Pi_{\nu\sigma}(k) - \delta_{\nu\sigma}\,\frac{k_{\nu'}k_{\sigma'}}{k^2}\,\Pi_{\nu'\sigma'}(k)\right),
\end{aligned} \tag{D.16}$$

from which the regularized quark loop can be read off, viz.,

$$\Pi^{\mathrm{reg}}_{\nu\sigma}(k) = \Pi_{\nu\sigma}(k) - \delta_{\nu\sigma}\,\frac{k_{\nu'}k_{\sigma'}}{k^2}\,\Pi_{\nu'\sigma'}(k)\,. \tag{D.17}$$

[45] It might also be the case (in the full YM system) that longitudinal components in the gluon self-energies bear a physical meaning. See Ref. [225] for a recent study in that direction.

This form of the regularized quark loop has already been used in previous works, see, e.g., Ref. [241], and is equivalent to contract the original quark loop $\Pi_{\nu\sigma}(k)$ directly with the Brown–Pennington projector $\delta_{\nu\sigma} - 4\,k_\nu k_\sigma / k^2$ [418] to get the regularized transversal component $\Pi_{\mathrm{T}}^{\mathrm{reg}}(k)$. The regularized quark loop is purely transversal and free of quadratic divergences [216, 291]; the remaining logarithmic divergence is removed analogous to the quark by a subtraction.

Now, with the regularized quark loop at hand, we project the gluon DSE (D.13) onto the gluon dressing function to arrive at

$$\frac{1}{Z(k)} = Z_3 + \frac{\Pi_{\mathrm{T}}^{\mathrm{YM}}(k)}{k^2} + \frac{\Pi_{\mathrm{T}}^{\mathrm{reg}}(k)}{k^2}\,, \tag{D.18}$$

where $\Pi_{\mathrm{T}}^{\mathrm{YM}}(k) = \mathcal{P}_{\nu\sigma}^{\mathrm{T}}(k)\,\Pi_{\nu\sigma}^{\mathrm{YM}}(k)/3$. The renormalization constant Z_3 is eliminated by subtracting Eq. (D.18) from itself at the fixed subtraction point ζ', and using the renormalization condition $Z(k)\big|_{k^2=\zeta'^2} = 1$ leads to

$$\frac{1}{Z(k)} = 1 + \frac{\Pi_{\mathrm{T}}^{\mathrm{YM}}(k)}{k^2} - \frac{\Pi_{\mathrm{T}}^{\mathrm{YM}}(\zeta')}{\zeta'^2} + \frac{\Pi_{\mathrm{T}}^{\mathrm{reg}}(k)}{k^2} - \frac{\Pi_{\mathrm{T}}^{\mathrm{reg}}(\zeta')}{\zeta'^2}\,. \tag{D.19}$$

The first three terms on the right hand side represent the pure YM part, which we do not calculate explicitly, and is replaced by fits to results from quenched lattice calculations [256, 292], i.e., $1 + \Pi_{\mathrm{T}}^{\mathrm{YM}}(k)/k^2 - \Pi_{\mathrm{T}}^{\mathrm{YM}}(\zeta')/\zeta'^2$ is replaced by the fit given in Eq. (3.9) at $T = 0$. Thus, our truncated DSE for the unquenched vacuum gluon dressing function reads

$$\frac{1}{Z(k)} = \frac{1}{Z_\perp^{\mathrm{que}}(k; T=0)} + \frac{\Pi_{\mathrm{T}}^{\mathrm{reg}}(k)}{k^2} - \frac{\Pi_{\mathrm{T}}^{\mathrm{reg}}(\zeta')}{\zeta'^2}\,, \tag{D.20}$$

where the regularized quark-loop contribution is explicitly given by

$$\begin{aligned}\Pi_{\mathrm{T}}^{\mathrm{reg}}(k) = \frac{4\pi\alpha_{\mathrm{s}}}{3} \sum_f Z_2^f \int_q \frac{A_f(q^2)}{N_f^{\mathrm{vac}}(q^2)} \frac{A_f(p^2)}{N_f^{\mathrm{vac}}(p^2)}\, H_{\mathrm{BC}}^f(p^2, q^2) \\ \times \Gamma(p^2+q^2) \left[p\cdot q - 4\,\frac{(k\cdot p)\,(k\cdot q)}{k^2} \right],\end{aligned} \tag{D.21}$$

where $p = q - k$ and $N_f^{\mathrm{vac}}(x) = x\,A_f^2(x) + B_f^2(x)$. The subtraction point ζ' is inherited from the quenched lattice input and given by $\zeta'^2 = (10\,\mathrm{GeV})^2$.

Note that the quantity Π_{vac}, called "vacuum quark loop," that we show in Fig. 3.7 is actually $\Pi_{\mathrm{T}}^{\mathrm{reg}}(k)/k^2$, i.e., the unsubtracted quark-loop contribution to the (inverse) unquenched gluon dressing function; see Eq. (D.20).

Quark DSE in medium

The coupled equations for the three in-medium quark dressing functions C_f, A_f, and B_f [Eqs. (2.60)–(2.62)] are given by

$$C_f(p) = Z_2^f \left(1 + \Sigma_C^f(p)\right), \tag{D.22}$$

$$A_f(p) = Z_2^f \left(1 + \Sigma_A^f(p)\right), \tag{D.23}$$

$$B_f(p) = Z_2^f \left(Z_{m_f} m_f + \Sigma_B^f(p)\right), \tag{D.24}$$

where $p = (\omega_p, \boldsymbol{p})$, and the projected self-energies read

$$\Sigma_C^f(p) = 4\pi\alpha_s C_2^{\text{fund}} \frac{1}{\widetilde{\omega}_p^f} T \sum_{\ell_q \in \mathbb{Z}} \!\!\!\!\!\!\int_{\boldsymbol{q}} \Gamma(k^2) \frac{\widetilde{\omega}_q^f C_f(q) K_{CC}^f + A_f(q) K_{CA}^f}{N_f^{\text{med}}(q)}, \tag{D.25}$$

$$\Sigma_A^f(p) = 4\pi\alpha_s C_2^{\text{fund}} \frac{1}{\boldsymbol{p}^2} T \sum_{\ell_q \in \mathbb{Z}} \!\!\!\!\!\!\int_{\boldsymbol{q}} \Gamma(k^2) \frac{\widetilde{\omega}_q^f C_f(q) K_{AC}^f + A_f(q) K_{AA}^f}{N_f^{\text{med}}(q)}, \tag{D.26}$$

$$\Sigma_B^f(p) = 4\pi\alpha_s C_2^{\text{fund}} T \sum_{\ell_q \in \mathbb{Z}} \!\!\!\!\!\!\int_{\boldsymbol{q}} \Gamma(k^2) \frac{B_f(q) K_{BB}^f}{N_f^{\text{med}}(q)}. \tag{D.27}$$

Here, $q = (\omega_q, \boldsymbol{q})$, $\widetilde{\omega}_q^f = \omega_q + \mathrm{i}\mu_f$, $N_f^{\text{med}}(q) = \left(\widetilde{\omega}_q^f\right)^2 C_f^2(q) + \boldsymbol{q}^2 A_f^2(q) + B_f^2(q)$, and

$$K_{CC}^f = -H_4^f(p,q) \frac{Z_\parallel(k)}{k^2} \frac{\boldsymbol{k}^2}{k^2} + H_S^f(p,q) \left[2 \frac{Z_\perp(k)}{k^2} + \frac{Z_\parallel(k)}{k^2} \frac{\omega_k^2}{k^2}\right], \tag{D.28}$$

$$K_{CA}^f = \left[H_4^f(p,q) + H_S^f(p,q)\right] \frac{Z_\parallel(k)}{k^2} \frac{\boldsymbol{k}\cdot\boldsymbol{q}}{k^2} \omega_k, \tag{D.29}$$

$$K_{AC}^f = \left[H_4^f(p,q) + H_S^f(p,q)\right] \frac{Z_\parallel(k)}{k^2} \frac{\boldsymbol{k}\cdot\boldsymbol{p}}{k^2} \omega_k, \tag{D.30}$$

$$\begin{aligned} K_{AA}^f = {} & H_4^f(p,q) \frac{Z_\parallel(k)}{k^2} \frac{\boldsymbol{k}^2}{k^2} \boldsymbol{p}\cdot\boldsymbol{q} + H_S^f(p,q) \left[2 \frac{Z_\perp(k)}{k^2} \frac{(\boldsymbol{k}\cdot\boldsymbol{p})(\boldsymbol{k}\cdot\boldsymbol{q})}{\boldsymbol{k}^2}\right. \\ & \left. + \frac{Z_\parallel(k)}{k^2} \frac{\omega_k^2}{k^2} \left(\boldsymbol{p}\cdot\boldsymbol{q} - 2 \frac{(\boldsymbol{k}\cdot\boldsymbol{p})(\boldsymbol{k}\cdot\boldsymbol{q})}{\boldsymbol{k}^2}\right)\right], \end{aligned} \tag{D.31}$$

$$K_{BB}^f = H_4^f(p,q) \frac{Z_\parallel(k)}{k^2} \frac{\boldsymbol{k}^2}{k^2} + H_S^f(p,q) \left[2 \frac{Z_\perp(k)}{k^2} + \frac{Z_\parallel(k)}{k^2} \frac{\omega_k^2}{k^2}\right], \tag{D.32}$$

where $H_4^f(p,q) = [C_f(p) + C_f(q)]/2$, $H_S^f(p,q) = [A_f(p) + A_f(q)]/2$, and $k = p - q = (\omega_p - \omega_q, \boldsymbol{p} - \boldsymbol{q}) = (\omega_k, \boldsymbol{k})$. Analogous to the vacuum, we use a Pauli–Villars regulator for the in-medium quark DSE, i.e., the integrands of Eqs. (D.25), (D.26), and (D.27) are multiplied by $1/\left(1 + k^2/\Lambda_{\text{reg}}^2\right)$, where again $\Lambda_{\text{reg}} = 200\,\text{GeV}$.

Since the medium does not introduces new, additional divergences, we renormalize in vacuum and use the thereby obtained renormalization constants for the medium DSEs. This is valid since we use the same regularization scheme (with the same regularization scale) in both the vacuum and medium calculations.

Gluon DSE in medium

In medium, the gluon splits into a part transversal and longitudinal with respect to the direction of the heat bath, see Eq. (2.63). The equations for the magnetic and electric dressing functions read

$$\frac{1}{Z_{\perp,\parallel}(k)} = \frac{1}{Z_{\perp,\parallel}^{\text{que}}(k)} + \frac{\Pi_{\perp,\parallel}^{\text{reg}}(k)}{k^2} - \frac{\Pi_{\text{T}}^{\text{reg}}(\zeta')}{\zeta'^2}\,, \tag{D.33}$$

where the last term stems from the fact that we renormalize in vacuum; recall that $\Pi_{\text{T}}^{\text{reg}}$ is the transversal component of the regularized vacuum quark loop. The regularized magnetic and electric quark loops are obtained according to

$$\Pi_{\perp}^{\text{reg}}(k) = \frac{1}{2}\,\mathcal{P}_{\nu\sigma}^{\perp}(k)\,\Pi_{\nu\sigma}^{\text{reg}}(k)\,, \qquad \Pi_{\parallel}^{\text{reg}}(k) = \mathcal{P}_{\nu\sigma}^{\parallel}(k)\,\Pi_{\nu\sigma}^{\text{reg}}(k)\,, \tag{D.34}$$

where $\mathcal{P}_{\nu\sigma}^{\perp}(k)$ and $\mathcal{P}_{\nu\sigma}^{\parallel}(k)$ are the magnetic and electric projectors, respectively [Eqs. (2.64) and (2.65)]. For the special case of a vanishing external Matsubara frequency, i.e., $k = (0, \boldsymbol{k})$, the magnetic quark loop is explicitly given by ($p = q - k$)

$$\begin{aligned}\Pi_{\perp}^{\text{reg}}(k)\big|_{\omega_k=0} = 8\pi\alpha_{\text{s}} \sum_f Z_2^f\, T \sum_{\ell_q\in\mathbb{Z}} \int_{\boldsymbol{q}} \frac{A_f(q)}{N_f^{\text{med}}(q)} \frac{A_f(p)}{N_f^{\text{med}}(p)}\, H_S^f(p,q) \\ \times\, \Gamma(p^2+q^2)\left[\boldsymbol{p}\cdot\boldsymbol{q} - 3\,\frac{(\boldsymbol{k}\cdot\boldsymbol{p})(\boldsymbol{k}\cdot\boldsymbol{q})}{\boldsymbol{k}^2}\right]\end{aligned} \tag{D.35}$$

while the electric quark loop reads

$$\Pi_{\parallel}^{\text{reg}}(k)\big|_{\omega_k=0} = 8\pi\alpha_{\text{s}} \sum_f Z_2^f\, T \sum_{\ell_q\in\mathbb{Z}} \int_{\boldsymbol{q}} \frac{\Gamma(p^2+q^2)}{N_f^{\text{med}}(q)\,N_f^{\text{med}}(p)} \times$$

$$\times \Bigg\{ \left(\tilde{\omega}_q^f\right)^2 C_f(q)\, C_f(p) \left[H_4^f(p,q) + H_S^f(p,q)\right]$$

$$- A_f(q)\, A_f(p) \left[H_S^f(p,q) \left(2\, \frac{(\boldsymbol{k}\cdot\boldsymbol{p})(\boldsymbol{k}\cdot\boldsymbol{q})}{\boldsymbol{k}^2} - \boldsymbol{p}\cdot\boldsymbol{q} \right) + H_4^f(p,q)\, \boldsymbol{p}\cdot\boldsymbol{q} \right]$$

$$- B_f(q)\, B_f(p) \left[H_4^f(p,q) - H_S^f(p,q)\right] \Bigg\} . \tag{D.36}$$

These expressions for $\omega_k = 0$ are sufficient for this work because we access higher Matsubara frequencies $\omega_k \neq 0$ via $Z_{\perp,\parallel}(\omega_k, \boldsymbol{k}^2) = Z_{\perp,\parallel}(0, \omega_k^2 + \boldsymbol{k}^2)$ and consequently $\Pi^{\text{reg}}_{\perp,\parallel}(\omega_k, \boldsymbol{k}^2) = \Pi^{\text{reg}}_{\perp,\parallel}(0, \omega_k^2 + \boldsymbol{k}^2)$.

Note that the quantities $\Pi_{\perp,\parallel}$, which appear in Section 3.2, are actually $\Pi^{\text{reg}}_{\perp,\parallel}(k)/k^2$, i.e., the unsubtracted, regularized quark-loop contributions to the (inverse) magnetic/electric gluon dressing functions; see Eq. (D.33).

Numerical details

Solving the DSEs in vacuum

The coupled, self-consistent equations (D.3), (D.4), and (D.20) are solved iteratively within a macro-micro cycle. Initially, the gluon is evaluated with constant quarks, $A_f(p^2) = 1$ and $B_f(p^2) = 1\,\text{GeV}$, and subsequently used as input for the quark DSEs. These are then solved by means of a fixed-point iteration (micro cycle) until the desired accuracy is reached.[46] At this point, we completed the first macro cycle. The resulting (now nontrivial) quarks are then used to update the gluon, which is again fed into the quark DSEs, and the second micro cycle—solving the quark DSEs with the updated gluon—starts. After that, we completed the second macro cycle, and proceed with the third macro cycle, i.e., updating the gluon again. The macro cycle terminates, and with that the whole process of solving the DSEs, if the micro cycle took only one iteration to finish.

In order to implement the iterative procedure, we discretize the quark dressing functions on an external grid $\{p_i^2 : i = 1, \ldots, N_p\}$ that contains N_p discrete squared-momentum points. These are distributed between an infrared cutoff Λ_{IR}^2 and an ultraviolet cutoff Λ_{UV}^2 such that $\log(p_{i+1}^2/p_i^2) = \text{const}$. Both cutoffs are chosen such that their effects are negligible. In particular, the ultraviolet cutoff has to obey $\Lambda_{\text{UV}} \gg \Lambda_{\text{reg}}$, where $\Lambda_{\text{reg}} = 200\,\text{GeV}$ is the Pauli–Villars regularization scale. Furthermore, we need an

[46] The micro cycle terminates as soon as the relative error between the quark dressing functions of the current and previous iteration step is less than 10^{-6}.

internal grid $\{q_i^2\}$ that represents the loop integration with respect to q^2. It consists of $N_p - 1$ Gauss–Legendre quadrature rules, each with N_q nodes, that are placed between the external grid points. That is, the upper and lower limits of the j^{th} N_q-point rule are p_j^2 and p_{j+1}^2, respectively, with $j = 1, \ldots, N_p - 1$. Thus, we have $N_q \times (N_p - 1)$ loop-integration nodes in total. The angular integrals are carried out using an N_z-point Gauss–Chebyshev quadrature that is tailored for integrals of the form $\int_{-1}^{1} \mathrm{d}z\, \sqrt{1 - z^2}$. We use $N_p = 32$, $N_q = 6$, $N_z = 128$, $\Lambda_{\text{IR}} = 1\,\text{MeV}$, and $\Lambda_{\text{UV}} = 1.2\,\text{TeV}$.

Since the external and internal grids are disjoint, $\{p_i^2\} \cap \{q_i^2\} = \emptyset$, we interpolate the dressing functions using natural cubic splines on $\{\log(p_i^2)\}$ in order to have the quark dressing functions available at arbitrary momenta. If a dressing function is probed at momenta larger than the ultraviolet cutoff, we extrapolate linearly (on a logarithmic abscissa) based on the last two grid points.

Though the description above has been given in terms of the quark dressing functions, we treat the quark loop in the same manner (though without a Pauli–Villars regulator).

Solving the DSEs in medium

The iteration procedure for solving the in-medium DSEs is the same as for the vacuum calculation. However, the separate dependence of the quark dressing functions on ω_n and $\boldsymbol{p}^2$ increases the complexity. For the sake of simplicity, in this subsection we write the fermionic Matsubara frequencies as $\omega_n = (2n + 1)\,\pi T$, $n \in \mathbb{Z}$.

We compute the quark dressing functions for the $2\,N_\omega$ external Matsubara frequencies $\omega_{-N_\omega}, \ldots, \omega_{N_\omega - 1}$ explicitly, and higher Matsubara modes are access by exploiting O(4) restoration in the ultraviolet, i.e.,

$$F(\omega_n, \boldsymbol{p}^2) = \begin{cases} F(\omega_{-N_\omega}, \omega_n^2 - \omega_{-N_\omega}^2 + \boldsymbol{p}^2) & \text{if } n < -N_\omega\,, \\ F(\omega_n, \boldsymbol{p}^2) & \text{if } -N_\omega \leq n \leq N_\omega - 1\,, \\ F(\omega_{N_\omega - 1}, \omega_n^2 - \omega_{N_\omega - 1}^2 + \boldsymbol{p}^2) & \text{if } n > N_\omega - 1\,, \end{cases} \tag{D.37}$$

where $F \in \{C_f, A_f, B_f\}$. This allows to implement the loop Matsubara sum with respect to ω_ℓ according to

$$\begin{aligned} T \sum_{\ell \in \mathbb{Z}}^{|\omega_\ell| \leq \Lambda_{\text{UV}}} h(\omega_\ell) \approx \int_{-\Lambda_{\text{UV}}}^{\omega_{-N_\omega} - \pi T} \frac{\mathrm{d}q_4}{2\pi}\, h(q_4) + T \sum_{\ell = -N_\omega}^{N_\omega - 1} h(\omega_\ell) \\ + \int_{\omega_{N_\omega - 1} + \pi T}^{\Lambda_{\text{UV}}} \frac{\mathrm{d}q_4}{2\pi}\, h(q_4)\,, \end{aligned} \tag{D.38}$$

i.e., we sum explicitly over the external frequencies and approximate the remaining sum up to the cutoff with a continuous momentum integration, which is numerically implemented using a Gauss–Legendre quadrature. This approximation works extremely well because the Matsubara frequencies ω_ℓ become dense as ℓ increases. For the temperature ranges covered in this work, $N_\omega = 8$ and an N_ω^{cont}-point Gauss–Legendre quadrature for the continuous integrals in Eq. (D.38) with $N_\omega^{\text{cont}} = 16$ are more than sufficient.

Furthermore, even though we use a Pauli–Villars regulator, we find it is vital that the Matsubara sum and the three-momentum integration are performed in an O(4)-invariant way, i.e., such that $q^2 = \omega_\ell^2 + \boldsymbol{q}^2 \leq \Lambda_{\text{UV}}^2$. Thus,

$$T \sum_{\ell \in \mathbb{Z}} \int_{\boldsymbol{q}} \to \frac{T}{8\pi^2} \sum_{\ell \in \mathbb{Z}}^{|\omega_\ell| \leq \Lambda_{\text{UV}}} \int_{\Lambda_{\text{IR}}^2}^{\Lambda_{\text{UV}}^2 - \omega_\ell^2} \mathrm{d}\boldsymbol{q}^2 \sqrt{\boldsymbol{q}^2} \int_{-1}^{1} \mathrm{d}z \,, \tag{D.39}$$

where the Matsubara sum is understood with Eq. (D.38) in mind. It follows that the internal integration grid becomes ω_ℓ dependent through the varying upper limit $\Lambda_{\text{UV}}^2 - \omega_\ell^2$, and we have in total $2 \times (N_\omega + N_\omega^{\text{cont}})$ different internal grids, each depending on the external grid analogous to the vacuum. Additionally, the external grid depends on the external Matsubara frequency, too. In detail, for each external Matsubara frequency ω_n, where $n = -N_\omega, \ldots, N_\omega - 1$, the dressing functions are discretized on the external grid $\{\boldsymbol{p}_i^2 : i = 1, \ldots, N_p\}$ which points are distributed between Λ_{IR}^2 and $\Lambda_{\text{UV}}^2 - \omega_n^2$ such that $\log(\boldsymbol{p}_{i+1}^2 / \boldsymbol{p}_i^2) = \text{const}$. Thus, we have N_ω different external grids. The difference, however, is extremely small because $\Lambda_{\text{UV}}^2 \gg \omega_{-N_\omega}^2 = \omega_{N_\omega - 1}^2$ and $N_\omega = \mathcal{O}(1)$. For each ω_n, the quark dressing functions are interpolated using natural cubic splines on $\{\log(\boldsymbol{p}_i^2)\}$. As in vacuum, we use $N_p = 32$ points for the external grid and $N_q = 6$ for the internal grid. Due to the lack of a distinct weight function in the angular integral, we use a simple N_z-point Gauss–Legendre quadrature rule for its numerical evaluation. Since quantities like the quark condensate are rather sensitive to the precision of the angular integration, we employ $N_z = 160$ nodes.

The numerical treatment of the in-medium quark loops is slightly simpler than for the quarks because we consider only one external Matsubara frequency, which is vanishing. Most important, the approximation (D.38) cannot be used because otherwise the gluon dressing functions develop a pole, and it is crucial that the summation and integration is carried out in an O(4)-invariant manner. Thus, for the quark loops we use Eq. (D.39) but without Eq. (D.38), i.e., the Matsubara sum is explicitly carried out all the way up to the ultraviolet cutoff. Moreover, it is numerically convenient to subtract the electric thermal screening mass

$$m_\parallel^2 = \lim_{\boldsymbol{k}^2 \to 0} \Pi_\parallel^{\text{reg}}(k)\big|_{\omega_k = 0} \tag{D.40}$$

from the electric quark loop before interpolating, which is again accomplished by natural cubic splines on a logarithmic scale, and adding it later to recover the full electric quark loop again. The thermal mass is rather sensitive to numerical details. In particular, it is necessary that the ultraviolet limit $C_f(q) \to A_f(q)$ as $\boldsymbol{p}^2 \to \infty$ is fulfilled. While in principle true, for the thermal mass the limit must be reached to a high precision, which is unfortunately not the case. In accordance with previous works, we remedy that by using

$$C_f(q) \to \mathrm{e}^{-q^2/\Lambda_{\mathrm{mix}}^2}\, C_f(q) + \left(1 - \mathrm{e}^{-q^2/\Lambda_{\mathrm{mix}}^2}\right) A_f(q) \tag{D.41}$$

with $\Lambda_{\mathrm{mix}}^2 = 40\,\mathrm{GeV}^2$ in the calculation of $m_{\parallel}^2$ that is later added back to the subtracted electric quark loop.

Last, we note that the two different solutions within the first-order coexistence region are found by means of different initial conditions for the quark loop. An initial value of $B_f(p) = 1\,\mathrm{GeV}$ usually drives the system toward the Nambu solution, while the Wigner solution is found by using $B_f(p) = 1\,\mathrm{MeV}$ for the initial quark-loop evaluation.

D.2 Finite-volume calculations

Determination of T_{c}

As in the infinite-volume case, we define the pseudocritical chiral transition temperature by the inflection point of the subtracted quark condensate with respect to the temperature,

$$T_{\mathrm{c}}(\mu_{\mathrm{B}}) = \operatorname*{argmax}_{T} \left| \frac{\partial \Delta_{\mathrm{u,s}}(T, \mu_{\mathrm{B}})}{\partial T} \right| . \tag{D.42}$$

In infinite volume, the subtracted quark condensate is sufficiently well-behaved in the sense that the numerical noise is minimal, and a cubic spline interpolation of the data points yields a sound location of the inflection point. However, the situation is different in finite volume. We find that the quark condensate is susceptible to finite-size effects, resulting in a shaky behavior, and an interpolation does not yield reliable results for T_{c}. Thus, instead of interpolating, we fit the function

$$h(T) = a + b \tanh \frac{T - c}{d} \tag{D.43}$$

to the finite-volume condensate data. The hyperbolic tangent describes the temperature dependence of the subtracted quark condensate accurately—even for higher chemical potentials up to the CEP—and the transition temperature is readily read-off, $T_{\mathrm{c}} = c$.

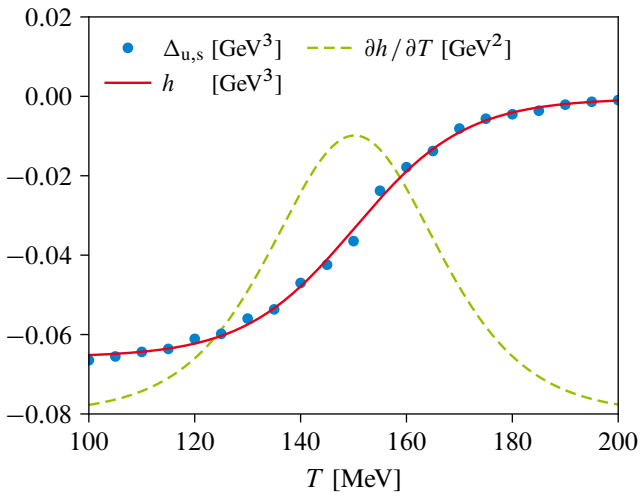

Figure D.1 Subtracted condensate $\Delta_{u,s}$, fit function h as given in Eq. (D.43), and $\partial h/\partial T$ at $L = 5\,\text{fm}$ (unimproved) with PBC at vanishing chemical potential. The derivative is scaled by 0.045 and shifted by $-0.08\,\text{GeV}^2$ in y direction.

The result of this procedure is depicted in Fig. D.1, where we show the subtracted quark condensate (blue dots), fit function h (red, solid line), and its temperature derivative (green, dashed line) at vanishing chemical potential for a system size of $L = 5\,\text{fm}$ with PBC. The shaky behavior of the condensate is clearly visible, and the fit parameters are given by

$$\begin{aligned} a &= (-0.0331 \pm 0.0005)\,\text{GeV}^3\,, \qquad b = (0.0326 \pm 0.0007)\,\text{GeV}^3\,, \\ c &= (0.1502 \pm 0.0005)\,\text{GeV}\,, \qquad d = (0.0209 \pm 0.0011)\,\text{GeV}\,. \end{aligned} \tag{D.44}$$

Thus, we find $T_c(\mu_B = 0) = (150.2 \pm 0.5)\,\text{MeV}$ for the pseudocritical chiral transition temperature at $L = 5\,\text{fm}$ with PBC. The errors are purely numerical.

The condensate obtained with improvement is not shaky and is well-behaved as in infinite volume. However, for the sake of consistency, we apply the hyperbolic tangent fit to the unimproved finite-volume calculations, the improved finite-volume calculations, and infinite-volume results to determine T_c in Section 6.4. For example, in infinite volume this procedure yields $T_c(\mu_B = 0) = 155\,\text{MeV}$ compared to $T_c(\mu_B = 0) = 156\,\text{MeV}$ using splines [Eq. (3.17)]. Thus, the difference is very small and purely technical in its origin.

Comment on the zero-mode contribution

On page 91, we stated that our PBC results with a proper inclusion of the zero mode resemble closely ABC results. Here, we present preliminary evidence for that claim.

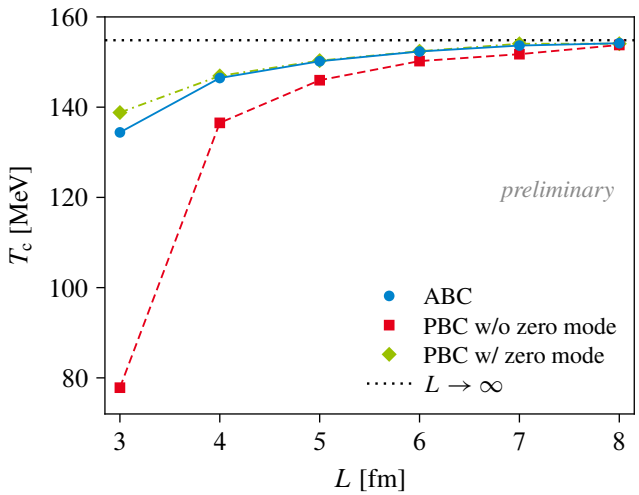

Figure D.2 Improved finite volume: box-size dependence of $T_c(\mu_B = 0)$ for ABC, PBC without zero mode, and PBC with zero mode. The black, dotted line is the infinite-volume result, and data points are connected by lines to guide the eye. The PBC results with zero mode are preliminary and were provided by J. Bernhardt.

In Fig. D.2, we show the box-size dependence of the pseudocritical chiral transition temperature (with improvement) for ABC, PBC without the zero mode, and PBC with the zero mode at vanishing chemical potential. The former are the results displayed in Fig. 6.5. Down to $L = 4\,\mathrm{fm}$, the ABC results lie on top of the PBC results with zero mode, and they differ only by around three percent at our smallest investigated box size of $L = 3\,\mathrm{fm}$. The difference between PBC results with and without the zero mode is below the ten-percent level for $L \gtrsim 4\,\mathrm{fm}$. However, the inclusion/omission of the PBC zero mode yields significantly different results for small volumes $L \lesssim 4\,\mathrm{fm}$. A more detailed discussion will be presented elsewhere in the future [270].

Numerical remarks

The introduction of a finite volume does not change the iterative procedure that we use to solve the DSEs. However, finite volume renders the loop integrations/summations numerically much simpler because there is a fixed prescription how they have to be carried out; see Eqs. (6.3) and (6.5). For the unimproved case, the external grid is necessarily a subset of the internal grid, which consists of all $\boldsymbol{q}_{jm}$. For the external grid on which the dressing functions are discretized (for each external Matsubara frequency), we pick a random representative[47] from the first twenty spheres. After that, we pick random representatives from all spheres which radii are equidistantly distributed on a

logarithmic scale. In terms of numbers of points, this procedure yields a rather small external grid compared to the internal one and thus keeps the numerical effort feasible. For the improved case, see Eq. (6.12), the external grid is enlarged by points that are constructed as in infinite volume. Similar to the latter, it is furthermore necessary in both the unimproved and the improved framework that the Matsubara sum and the spherical momentum summation/continuous integration are carried out such that $\omega_q^2 + \boldsymbol{q}_{jm}^2 \leq \Lambda_{\mathrm{UV}}^2$, i.e., in an O(4)-invariant way.

In the improved framework, we observe that our results are independent of Λ_{vol} as long as it is much larger than any other characteristic scale in our system like temperature, chemical potential, and quark masses. This allows us to choose different matching points for different box sizes L and therefore to work with a fixed number of grid points (usually between fifteen and twenty) in each Cartesian direction for the discrete momenta with magnitudes below the matching point.

Our numerical methods are otherwise nearly identical to the ones employed in the infinite-volume calculations.

[47] This also serves as a numerical check because the dressing functions must depend on squared momenta only, i.e., they are blind to directions in momentum space.

Bibliography

[1] M. Gell-Mann, *A schematic model of baryons and mesons*, Phys. Lett. **8**, 214 (1964).

[2] G. Zweig, *An SU_3 model for strong interaction symmetry and its breaking. I*, CERN preprint 8182/TH.401 (1964).

[3] G. Zweig, *An SU_3 model for strong interaction symmetry and its breaking. II*, CERN preprint 8419/TH.412 (1964).

[4] E. D. Bloom et al., *High-Energy Inelastic e-p Scattering at 6° and 10°*, Phys. Rev. Lett. **23**, 930 (1969).

[5] M. Breidenbach et al., *Observed Behavior of Highly Inelastic Electron-Proton Scattering*, Phys. Rev. Lett. **23**, 935 (1969).

[6] J. D. Bjorken and S. L. Glashow, *Elementary particles and SU(4)*, Phys. Lett. **11**, 255 (1964).

[7] S. L. Glashow, J. Iliopoulos, and L. Maiani, *Weak Interactions with Lepton-Hadron Symmetry*, Phys. Rev. D **2**, 1285 (1970).

[8] M. Kobayashi and T. Maskawa, *CP-Violation in the Renormalizable Theory of Weak Interaction*, Prog. Theor. Phys. **49**, 652 (1973).

[9] H. Harari, *A new quark model for hadrons*, Phys. Lett. B **57**, 265 (1975).

[10] J. E. Augustin et al., *Discovery of a Narrow Resonance in e^+e^- Annihilation*, Phys. Rev. Lett. **33**, 1406 (1974).

[11] J. J. Aubert et al., *Experimental Observation of a Heavy Particle J*, Phys. Rev. Lett. **33**, 1404 (1974).

[12] S. W. Herb et al., *Observation of a Dimuon Resonance at 9.5 GeV in 400-GeV Proton-Nucleus Collisions*, Phys. Rev. Lett. **39**, 252 (1977).

[13] F. Abe et al., *Evidence for Top Quark Production in $\bar{p}p$ Collisions at $\sqrt{s} = 1.8$ TeV*, Phys. Rev. Lett. **73**, 225 (1994), arXiv:hep-ex/9405005.

[14] F. Abe et al., *Observation of Top Quark Production in $\bar{p}p$ Collisions with the Collider Detector at Fermilab*, Phys. Rev. Lett. **74**, 2626 (1995), arXiv:hep-ex/9503002.

[15] S. Abachi et al., *Observation of the Top Quark*, Phys. Rev. Lett. **74**, 2632 (1995), arXiv:hep-ex/9503003.

[16] O. W. Greenberg, *Spin and Unitary-Spin Independence in a Paraquark Model of Baryons and Mesons*, Phys. Rev. Lett. **13**, 598 (1964).

[17] M. Y. Han and Y. Nambu, *Three Triplet Model with Double SU(3) Symmetry*, Phys. Rev. **139**, B1006 (1965).

[18] R. P. Feynman, *QED: The Strange Theory of Light and Matter*, 3rd ed. (Princeton University Press, 2006).

[19] M. Gell-Mann, *Quarks*, Acta Phys. Austr. Supp. **9**, 733 (1972), lecture given at the XI. Internationale Universitätswochen für Kernphysik, 21 February–4 March 1972, Schladming (Austria).

[20] H. Fritzsch and M. Gell-Mann, *Current algebra: Quarks and what else?*, contribution to the 16th International Conference on High-Energy Physics, 6–13 September 1972, Batavia, Illinois (USA), arXiv:hep-ph/0208010.

[21] H. Fritzsch, M. Gell-Mann, and H. Leutwyler, *Advantages of the color octet gluon picture*, Phys. Lett. B **47**, 365 (1973).

[22] D. J. Gross and F. Wilczek, *Asymptotically Free Gauge Theories. I*, Phys. Rev. D **8**, 3633 (1973).

[23] S. Weinberg, *Nonabelian Gauge Theories of the Strong Interactions*, Phys. Rev. Lett. **31**, 494 (1973).

[24] S. Weinberg, *Current Algebra and Gauge Theories. II. Non-Abelian Gluons*, Phys. Rev. D **8**, 4482 (1973).

[25] D. J. Gross and F. Wilczek, *Ultraviolet Behavior of Nonabelian Gauge Theories*, Phys. Rev. Lett. **30**, 1343 (1973).

[26] H. D. Politzer, *Reliable Perturbative Results for Strong Interactions?*, Phys. Rev. Lett. **30**, 1346 (1973).

[27] W. E. Caswell, *Asymptotic Behavior of Non-Abelian Gauge Theories to Two-Loop Order*, Phys. Rev. Lett. **33**, 244 (1974).

[28] A. Deur, S. J. Brodsky, and G. F. de Téramond, *The QCD running coupling*, Prog. Part. Nucl. Phys. **90**, 1 (2016), arXiv:1604.08082 [hep-ph].

[29] S. Bethke, *Experimental tests of asymptotic freedom*, Prog. Part. Nucl. Phys. **58**, 351 (2007), arXiv:hep-ex/0606035.

[30] B. R. Stella and H.-J. Meyer, *Υ(9.46 GeV) and the gluon discovery (a critical recollection of PLUTO results)*, Eur. Phys. J. H **36**, 203 (2011), arXiv:1008.1869 [hep-ex].

[31] A. Ali and G. Kramer, *Jets and QCD: a historical review of the discovery of the quark and gluon jets and its impact on QCD*, Eur. Phys. J. H **36**, 245 (2011), arXiv:1012.2288 [hep-ph].

[32] D. J. Gross, *Nobel Lecture: The discovery of asymptotic freedom and the emergence of QCD*, Rev. Mod. Phys. **77**, 837 (2005).

[33] J. Greensite, *The confinement problem in lattice gauge theory*, Prog. Part. Nucl. Phys. **51**, 1 (2003), arXiv:hep-lat/0301023.

[34] R. Alkofer and J. Greensite, *Quark confinement: the hard problem of hadron physics*, J. Phys. G: Nucl. Part. Phys. **34**, S3 (2007), arXiv:hep-ph/0610365.

[35] R. Alkofer, C. S. Fischer, M. Q. Huber, F. J. Llanes-Estrada, and K. Schwenzer, *Confinement and Green functions in Landau-gauge QCD*, Proc. Sci. **CONFINEMENT8**, 019 (2008), arXiv:0812.2896 [hep-ph].

[36] J. Greensite, *An Introduction to the Confinement Problem*, Lecture Notes in Physics 821 (Springer, 2011).

[37] D. J. Gross, R. D. Pisarski, and L. G. Yaffe, *QCD and instantons at finite temperature*, Rev. Mod. Phys. **53**, 43 (1981).

[38] P. Braun-Munzinger and J. Wambach, *Colloquium: Phase diagram of strongly interacting matter*, Rev. Mod. Phys. **81**, 1031 (2009), arXiv:0801.4256 [hep-ph].

[39] K. Fukushima and T. Hatsuda, *The phase diagram of dense QCD*, Rep. Prog. Phys. **74**, 014001 (2011), arXiv:1005.4814 [hep-ph].

[40] J. C. Collins and M. J. Perry, *Superdense Matter: Neutrons Or Asymptotically Free Quarks?*, Phys. Rev. Lett. **34**, 1353 (1975).

[41] N. Cabibbo and G. Parisi, *Exponential hadronic spectrum and quark liberation*, Phys. Lett. B **59**, 67 (1975).

[42] U. W. Heinz and M. Jacob, *Evidence for a New State of Matter: An Assessment of the Results from the CERN Lead Beam Programme*, arXiv:nucl-th/0002042.

[43] K. Adcox et al., *Formation of dense partonic matter in relativistic nucleus-nucleus collisions at RHIC: Experimental evaluation by the PHENIX collaboration*, Nucl. Phys. A **757**, 184 (2005), arXiv:nucl-ex/0410003.

[44] B. Müller, J. Schukraft, and B. Wysłouch, *First Results from Pb+Pb Collisions at the LHC*, Ann. Rev. Nucl. Part. Sci. **62**, 361 (2012), arXiv:1202.3233 [hep-ex].

[45] M. M. Aggarwal et al., *An Experimental Exploration of the QCD Phase Diagram: The Search for the Critical Point and the Onset of De-confinement*, arXiv:1007.2613 [nucl-ex].

[46] BES-II whitepaper, https://drupal.star.bnl.gov/STAR/starnotes/public/sn0598, 2014.

[47] A. Bzdak, S. Esumi, V. Koch, J. Liao, M. Stephanov, and N. Xu, *Mapping the phases of quantum chromodynamics with beam energy scan*, Phys. Rep. **853**, 1 (2020), arXiv:1906.00936 [nucl-th].

[48] B. Friman et al., eds., *The CBM Physics Book: Compressed Baryonic Matter in Laboratory Experiments*, Lecture Notes in Physics 814 (Springer, 2011).

[49] NICA whitepaper, http://theor0.jinr.ru/twiki-cgi/view/NICA/NICAWhitePaper, 2014.

[50] W. Busza, K. Rajagopal, and W. van der Schee, *Heavy Ion Collisions: The Big Picture, and the Big Questions*, Ann. Rev. Nucl. Part. Sci. **68**, 339 (2018), arXiv:1802.04801 [hep-ph].

[51] C. Gattringer and C. B. Lang, *Quantum Chromodynamics on the Lattice: An Introductory Presentation*, Lecture Notes in Physics 788 (Springer, 2010).

[52] Y. Aoki, G. Endrődi, Z. Fodor, S. D. Katz, and K. K. Szabó, *The order of the quantum chromodynamics transition predicted by the standard model of particle physics*, Nature **443**, 675 (2006), arXiv:hep-lat/0611014.

[53] Y. Aoki et al., *The QCD transition temperature: results with physical masses in the continuum limit II*, J. High Energy Phys. **06**, 088 (2009), arXiv:0903.4155 [hep-lat].

[54] S. Borsányi et al., *Is there still any T_c mystery in lattice QCD? Results with physical masses in the continuum limit III*, J. High Energy Phys. **09**, 073 (2010), arXiv:1005.3508 [hep-lat].

[55] A. Bazavov et al., *The chiral and deconfinement aspects of the QCD transition*, Phys. Rev. D **85**, 054503 (2012), arXiv:1111.1710 [hep-lat].

[56] T. Bhattacharya et al., *QCD Phase Transition with Chiral Quarks and Physical Quark Masses*, Phys. Rev. Lett. **113**, 082001 (2014), arXiv:1402.5175 [hep-lat].

[57] P. de Forcrand, *Simulating QCD at finite density*, Proc. Sci. **LAT2009**, 010 (2009), arXiv:1005.0539 [hep-lat].

[58] G. Aarts, *Introductory lectures on lattice QCD at nonzero baryon number*, J. Phys. Conf. Ser. **706**, 022004 (2016), arXiv:1512.05145 [hep-lat].

[59] Y. Nambu and G. Jona-Lasinio, *Dynamical Model of Elementary Particles Based on an Analogy with Superconductivity. I*, Phys. Rev. **122**, 345 (1961).

[60] Y. Nambu and G. Jona-Lasinio, *Dynamical Model of Elementary Particles Based on an Analogy with Superconductivity. II*, Phys. Rev. **124**, 246 (1961).

[61] S. P. Klevansky, *The Nambu–Jona-Lasinio model of quantum chromodynamics*, Rev. Mod. Phys. **64**, 649 (1992).

[62] T. Hatsuda and T. Kunihiro, *QCD phenomenology based on a chiral effective Lagrangian*, Phys. Rep. **247**, 221 (1994), arXiv:hep-ph/9401310.

[63] M. Buballa, *NJL-model analysis of quark matter at large density*, Phys. Rep. **407**, 205 (2005), arXiv:hep-ph/0402234.

[64] D. U. Jungnickel and C. Wetterich, *Effective action for the chiral quark-meson model*, Phys. Rev. D **53**, 5142 (1996), arXiv:hep-ph/9505267.

[65] D. U. Jungnickel and C. Wetterich, *Effective linear meson model*, Eur. Phys. J. C **1**, 669 (1998), arXiv:hep-ph/9606483.

[66] J. Berges, D. U. Jungnickel, and C. Wetterich, *Two flavor chiral phase transition from nonperturbative flow equations*, Phys. Rev. D **59**, 034010 (1999), arXiv:hep-ph/9705474.

[67] B.-J. Schaefer and J. Wambach, *The phase diagram of the quark meson model*, Nucl. Phys. A **757**, 479 (2005), arXiv:nucl-th/0403039.

[68] S. Carignano, M. Buballa, and B.-J. Schaefer, *Inhomogeneous phases in the quark-meson model with vacuum fluctuations*, Phys. Rev. D **90**, 014033 (2014), arXiv:1404.0057 [hep-ph].

[69] R.-A. Tripolt, B.-J. Schaefer, L. von Smekal, and J. Wambach, *Low-temperature behavior of the quark-meson model*, Phys. Rev. D **97**, 034022 (2018), arXiv:1709.05991 [hep-ph].

[70] K. Fukushima, *Chiral effective model with the Polyakov loop*, Phys. Lett. B **591**, 277 (2004), arXiv:hep-ph/0310121.

[71] C. Ratti, M. A. Thaler, and W. Weise, *Phases of QCD: Lattice thermodynamics and a field theoretical model*, Phys. Rev. D **73**, 014019 (2006), arXiv:hep-ph/0506234.

[72] B.-J. Schaefer, J. M. Pawlowski, and J. Wambach, *Phase structure of the Polyakov-quark-meson model*, Phys. Rev. D **76**, 074023 (2007), arXiv:0704.3234 [hep-ph].

[73] T. K. Herbst, J. M. Pawlowski, and B.-J. Schaefer, *The phase structure of the Polyakov-quark-meson model beyond mean field*, Phys. Lett. B **696**, 58 (2011), arXiv:1008.0081 [hep-ph].

[74] T. K. Herbst, J. M. Pawlowski, and B.-J. Schaefer, *Phase structure and thermodynamics of QCD*, Phys. Rev. D **88**, 014007 (2013), arXiv:1302.1426 [hep-ph].

[75] K. Fukushima and V. Skokov, *Polyakov loop modeling for hot QCD*, Prog. Part. Nucl. Phys. **96**, 154 (2017), arXiv:1705.00718 [hep-ph].

[76] C. D. Roberts and A. G. Williams, *Dyson–Schwinger equations and their application to hadronic physics*, Prog. Part. Nucl. Phys. **33**, 477 (1994), arXiv:hep-ph/9403224.

[77] C. D. Roberts and S. M. Schmidt, *Dyson–Schwinger equations: density, temperature and continuum strong QCD*, Prog. Part. Nucl. Phys. **45**, S1 (2000), arXiv:nucl-th/0005064.

[78] R. Alkofer and L. von Smekal, *The infrared behavior of QCD Green's functions: Confinement, dynamical symmetry breaking, and hadrons as relativistic bound states*, Phys. Rep. **353**, 281 (2001), arXiv:hep-ph/0007355.

[79] C. S. Fischer, *QCD at finite temperature and chemical potential from Dyson–Schwinger equations*, Prog. Part. Nucl. Phys. **105**, 1 (2019), arXiv:1810.12938 [hep-ph].

[80] J. Berges, N. Tetradis, and C. Wetterich, *Nonperturbative renormalization flow in quantum field theory and statistical physics*, Phys. Rep. **363**, 223 (2002), arXiv:hep-ph/0005122.

[81] J. M. Pawlowski, *Aspects of the functional renormalisation group*, Ann. Phys. **322**, 2831 (2007), arXiv:hep-th/0512261.

[82] H. Gies, *Introduction to the Functional RG and Applications to Gauge Theories*, in *Renormalization Group and Effective Field Theory Approaches to Many-Body Systems*, Lecture Notes in Physics 852 (Springer, 2012), arXiv:hep-ph/0611146.

[83] N. Dupuis et al., *The nonperturbative functional renormalization group and its applications*, Phys. Rep. **910**, 1 (2021), arXiv:2006.04853 [cond-mat.stat-mech].

[84] G. Eichmann, H. Sanchis-Alepuz, R. Williams, R. Alkofer, and C. S. Fischer, *Baryons as relativistic three-quark bound states*, Prog. Part. Nucl. Phys. **91**, 1 (2016), arXiv:1606.09602 [hep-ph].

[85] E. Weil, G. Eichmann, C. S. Fischer, and R. Williams, *Electromagnetic decays of the neutral pion*, Phys. Rev. D **96**, 014021 (2017), arXiv:1704.06046 [hep-ph].

[86] H. Sanchis-Alepuz and R. Williams, *Recent developments in bound-state calculations using the Dyson–Schwinger and Bethe–Salpeter equations*, Comput. Phys. Commun. **232**, 1 (2018), arXiv:1710.04903 [hep-ph].

[87] R. Williams, *Vector mesons as dynamical resonances in the Bethe–Salpeter framework*, Phys. Lett. B **798**, 134943 (2019), arXiv:1804.11161 [hep-ph].

[88] G. Eichmann, C. S. Fischer, W. Heupel, N. Santowsky, and P. C. Wallbott, *Four-Quark States from Functional Methods*, Few-Body Syst. **61**, 38 (2020), arXiv:2008.10240 [hep-ph].

[89] M. Q. Huber, C. S. Fischer, and H. Sanchis-Alepuz, *Spectrum of scalar and pseudoscalar glueballs from functional methods*, Eur. Phys. J. C **80**, 1077 (2020), arXiv:2004.00415 [hep-ph].

[90] M. Q. Huber, *Nonperturbative properties of Yang–Mills theories*, Phys. Rep. **879**, 1 (2020), arXiv:1808.05227 [hep-ph].

[91] C. S. Fischer and M. Q. Huber, *Landau gauge Yang–Mills propagators in the complex momentum plane*, Phys. Rev. D **102**, 094005 (2020), arXiv:2007.11505 [hep-ph].

[92] G. Eichmann, C. S. Fischer, W. Heupel, and R. Williams, *The muon $g-2$: Dyson–Schwinger status on hadronic light-by-light scattering*, AIP Conf. Proc. **1701**, 040004 (2016), arXiv:1411.7876 [hep-ph].

[93] G. Eichmann, C. S. Fischer, E. Weil, and R. Williams, *Single pseudoscalar meson pole and pion box contributions to the anomalous magnetic moment of the muon*, Phys. Lett. B **797**, 134855 (2019), arXiv:1903.10844 [hep-ph], Erratum: Phys. Lett. B **799**, 135029 (2019).

[94] G. Eichmann, C. S. Fischer, and R. Williams, *Kaon-box contribution to the anomalous magnetic moment of the muon*, Phys. Rev. D **101**, 054015 (2020), arXiv:1910.06795 [hep-ph].

[95] J. Adam et al., *Nonmonotonic Energy Dependence of Net-Proton Number Fluctuations*, Phys. Rev. Lett. **126**, 092301 (2021), arXiv:2001.02852 [nucl-ex].

[96] M. Abdallah et al., *Cumulants and correlation functions of net-proton, proton, and antiproton multiplicity distributions in Au+Au collisions at energies available at the BNL Relativistic Heavy Ion Collider*, Phys. Rev. C **104**, 024902 (2021), arXiv:2101.12413 [nucl-ex].

[97] X. Luo and N. Xu, *Search for the QCD critical point with fluctuations of conserved quantities in relativistic heavy-ion collisions at RHIC: an overview*, Nucl. Sci. Tech. **28**, 112 (2017), arXiv:1701.02105 [nucl-ex].

[98] P. Isserstedt, M. Buballa, C. S. Fischer, and P. J. Gunkel, *Baryon number fluctuations in the QCD phase diagram from Dyson–Schwinger equations*, Phys. Rev. D **100**, 074011 (2019), arXiv:1906.11644 [hep-ph].

[99] P. Isserstedt, C. S. Fischer, and T. Steinert, *Thermodynamics from the quark condensate*, Phys. Rev. D **103**, 054012 (2021), arXiv:2012.04991 [hep-ph].

[100] J. Bernhardt, C. S. Fischer, P. Isserstedt, and B.-J. Schaefer, *Critical endpoint of QCD in a finite volume*, Phys. Rev. D **104**, 074035 (2021), arXiv:2107.05504 [hep-ph].

[101] P. J. Gunkel, C. S. Fischer, and P. Isserstedt, *Quarks and light (pseudo-)scalar mesons at finite chemical potential*, Eur. Phys. J. A **55**, 169 (2019), arXiv:1907.08110 [hep-ph].

[102] P. J. Gunkel, *Hadronic effects in the QCD phase diagram*, PhD thesis (Justus-Liebig-Universität Gießen, Germany, 2021).

[103] W. J. Marciano and H. Pagels, *Quantum chromodynamics*, Phys. Rep. **36**, 137 (1978).

[104] C. Itzykson and J. B. Zuber, *Quantum Field Theory*, International Series in Pure and Applied Physics (McGraw-Hill, 1980).

[105] P. Pascual and R. Tarrach, *QCD: Renormalization for the Practitioner*, Lecture Notes in Physics 194 (Springer, 1984).

[106] M. E. Peskin and D. V. Schroeder, *An Introduction to Quantum Field Theory*, Advanced Book Program (Addison-Wesley, 1995).

[107] B. L. Ioffe, V. S. Fadin, and L. N. Lipatov, *Quantum Chromodynamics: Perturbative and Nonperturbative Aspects*, Cambridge Monographs on Particle Physics, Nuclear Physics, and Cosmology (Cambridge University Press, 2010).

[108] J. I. Kapusta and C. Gale, *Finite-Temperature Field Theory: Principles and Applications*, 2nd ed., Cambridge Monographs on Mathematical Physics (Cambridge University Press, 2006).

[109] C.-N. Yang and R. L. Mills, *Conservation of Isotopic Spin and Isotopic Gauge Invariance*, Phys. Rev. **96**, 191 (1954).

[110] R. P. Feynman, *Quantum Theory of Gravitation*, Acta Phys. Polon. **24**, 697 (1963).

[111] B. S. DeWitt, *Quantum Theory of Gravity. II. The Manifestly Covariant Theory*, Phys. Rev. **162**, 1195 (1967).

[112] B. S. DeWitt, *Quantum Theory of Gravity. III. Applications of the Covariant Theory*, Phys. Rev. **162**, 1239 (1967).

[113] S. Mandelstam, *Quantum Electrodynamics Without Potentials*, Ann. Phys. **19**, 1 (1962).

[114] S. Mandelstam, *Quantization of the Gravitational Field*, Ann. Phys. **19**, 25 (1962).

[115] S. Mandelstam, *Feynman Rules for Electromagnetic and Yang–Mills Fields from the Gauge-Independent Field-Theoretic Formalism*, Phys. Rev. **175**, 1580 (1968).

[116] L. D. Faddeev and V. N. Popov, *Feynman diagrams for the Yang–Mills field*, Phys. Lett. B **25**, 29 (1967).

[117] L. D. Faddeev, *The Feynman integral for singular Lagrangians*, Theor. Math. Phys. **1**, 1 (1969).

[118] A. Haar, *Der Massbegriff in der Theorie der Kontinuierlichen Gruppen*, Ann. Math. **34**, 147 (1933), in German.

[119] D. L. Cohn, *Measure Theory*, 2nd ed. (Birkhäuser, 2013).

[120] G. 't Hooft, *Renormalization of massless Yang–Mills fields*, Nucl. Phys. B **33**, 173 (1971).

[121] F. A. Berezin, *The Method of Second Quantization*, Pure and Applied Physics 24 (Academic Press, 1966).

[122] M. Fierz, *Über die relativistische Theorie kräftefreier Teilchen mit beliebigem Spin*, Helv. Phys. Acta **12**, 3 (1939), in German.

[123] W. Pauli, *The Connection Between Spin and Statistics*, Phys. Rev. **58**, 716 (1940).

[124] G. Leibbrandt, *Introduction to noncovariant gauges*, Rev. Mod. Phys. **59**, 1067 (1987).

[125] H. S. Chan and M. B. Halpern, *New ghost-free infrared-soft gauges*, Phys. Rev. D **33**, 540 (1986).

[126] N. Nakanishi and I. Ojima, *Covariant Operator Formalism of Gauge Theories and Quantum Gravity*, World Scientific Lecture Notes in Physics Vol. 27 (World Scientific, 1990).

[127] H. Hüffel and D. Markovic, *Perturbative Yang–Mills theory without Faddeev–Popov ghost fields*, Phys. Lett. B **780**, 418 (2018), arXiv:1712.10302 [hep-th].

[128] G. 't Hooft and M. J. G. Veltman, *Regularization and renormalization of gauge fields*, Nucl. Phys. B **44**, 189 (1972).

[129] B. W. Lee and J. Zinn-Justin, *Spontaneously Broken Gauge Symmetries Part 1: Preliminaries*, Phys. Rev. D **5**, 3121 (1972).

[130] B. W. Lee and J. Zinn-Justin, *Spontaneously Broken Gauge Symmetries Part 2: Perturbation Theory and Renormalization*, Phys. Rev. D **5**, 3137 (1972).

[131] B. W. Lee and J. Zinn-Justin, *Spontaneously Broken Gauge Symmetries Part 4: General Gauge Formulation*, Phys. Rev. D **7**, 1049 (1973).

[132] B. W. Lee, *Renormalization of gauge theories—unbroken and broken*, Phys. Rev. D **9**, 933 (1974).

[133] J. Zinn-Justin, *Renormalization of Gauge Theories*, in *Trends in Elementary Particle Theory*, Lecture Notes in Physics 37 (Springer, 1975).

[134] G. 't Hooft, *The glorious days of physics: Renormalization of gauge theories*, arXiv:hep-th/9812203.

[135] J. Zinn-Justin, *Renormalization of gauge theories and master equation*, Mod. Phys. Lett. A **14**, 1227 (1999), arXiv:hep-th/9906115.

[136] A. A. Slavnov, *Ward identities in gauge theories*, Theor. Math. Phys. **10**, 99 (1972).

[137] J. C. Taylor, *Ward identities and charge renormalization of the Yang–Mills field*, Nucl. Phys. B **33**, 436 (1971).

[138] J. C. Ward, *An Identity in Quantum Electrodynamics*, Phys. Rev. **78**, 182 (1950).

[139] Y. Takahashi, *On the Generalized Ward Identity*, Nuovo Cim. **6**, 371 (1957).

[140] W. Pauli and F. Villars, *On the Invariant Regularization in Relativistic Quantum Theory*, Rev. Mod. Phys. **21**, 434 (1949).

[141] V. N. Gribov, *Quantization of non-Abelian gauge theories*, Nucl. Phys. B **139**, 1 (1978).

[142] I. M. Singer, *Some Remarks on the Gribov Ambiguity*, Commun. Math. Phys. **60**, 7 (1978).

[143] A. G. Williams, *QCD, gauge fixing, and the Gribov problem*, Nucl. Phys. B Proc. Supp. **109**, 141 (2002), arXiv:hep-lat/0202010.

[144] R. F. Sobreiro and S. P. Sorella, *Introduction to the Gribov ambiguities in Euclidean Yang–Mills theories*, lectures given by S. P. Sorella at the 13th Jorge Andre Swieca Summer School on Particles and Fields, 19–22 January 2005, Campos de Jordao (Brazil), arXiv:hep-th/0504095.

[145] N. Vandersickel and D. Zwanziger, *The Gribov problem and QCD dynamics*, Phys. Rep. **520**, 175 (2012), arXiv:1202.1491 [hep-th].

[146] G. Parisi and Y. Wu, *Perturbation theory without gauge fixing*, Sci. Sin. **24**, 483 (1981).

[147] D. Zwanziger, *Covariant quantization of gauge fields without Gribov ambiguity*, Nucl. Phys. B **192**, 259 (1981).

[148] J. Zinn-Justin and D. Zwanziger, *Ward identities for the stochastic quantization of gauge fields*, Nucl. Phys. B **295**, 297 (1988).

[149] P. H. Damgaard and H. Hüffel, *Stochastic quantization*, Phys. Rep. **152**, 227 (1987).

[150] L. Baulieu and D. Zwanziger, *QCD(4) from a five-dimensional point of view*, Nucl. Phys. B **581**, 604 (2000), arXiv:hep-th/9909006.

[151] L. Baulieu, P. A. Grassi, and D. Zwanziger, *Gauge and topological symmetries in the bulk quantization of gauge theories*, Nucl. Phys. B **597**, 583 (2001), arXiv:hep-th/0006036.

[152] D. Zwanziger, *Time independent stochastic quantization, DS equations, and infrared critical exponents in QCD*, Phys. Rev. D **67**, 105001 (2003), arXiv:hep-th/0206053.

[153] D. Zwanziger, *Nonperturbative Faddeev–Popov formula and infrared limit of QCD*, Phys. Rev. D **69**, 016002 (2004), arXiv:hep-ph/0303028.

[154] L. Baulieu and M. Schaden, *Gauge group TQFT and improved perturbative Yang–Mills theory*, Int. J. Mod. Phys. A **13**, 985 (1998), arXiv:hep-th/9601039.

[155] M. Schaden, *Quantization in the presence of Gribov ambiguities*, contribution to the 4th Workshop on Quantum Chromodynamics, 1–6 June 1998, Paris (France), arXiv:hep-th/9810162.

[156] A. Cucchieri, *Gribov copies in the minimal Landau gauge: The Influence on gluon and ghost propagators*, Nucl. Phys. B **508**, 353 (1997), arXiv:hep-lat/9705005.

[157] P. J. Silva and O. Oliveira, *Gribov copies, lattice QCD and the gluon propagator*, Nucl. Phys. B **690**, 177 (2004), arXiv:hep-lat/0403026.

[158] I. L. Bogolubsky, E. M. Ilgenfritz, M. Müller-Preussker, and A. Sternbeck, *Lattice gluodynamics computation of Landau gauge Green's functions in the deep infrared*, Phys. Lett. B **676**, 69 (2009), arXiv:0901.0736 [hep-lat].

[159] A. Maas, J. M. Pawlowski, D. Spielmann, A. Sternbeck, and L. von Smekal, *Strong-coupling study of the Gribov ambiguity in lattice Landau gauge*, Eur. Phys. J. C **68**, 183 (2010), arXiv:0912.4203 [hep-lat].

[160] A. Sternbeck and M. Müller-Preussker, *Lattice evidence for the family of decoupling solutions of Landau gauge Yang–Mills theory*, Phys. Lett. B **726**, 396 (2013), arXiv:1211.3057 [hep-lat].

[161] E. Noether, *Invariante Variationsprobleme*, Nachrichten von der Gesellschaft der Wissenschaften zu Göttingen, Mathematisch-Physikalische Klasse **1918**, 235 (1918), in German.

[162] E. Noether, *Invariant variation problems*, Transp. Theory Stat. Phys. **1**, 186 (1971), arXiv:physics/0503066, English translation of the original article by M. A. Tavel.

[163] W. Greiner and J. Reinhardt, *Field Quantization* (Springer, 1996).

[164] J. Goldstone, *Field Theories with «Superconductor» Solutions*, Nuovo Cim. **19**, 154 (1961).

[165] J. Goldstone, A. Salam, and S. Weinberg, *Broken Symmetries*, Phys. Rev. **127**, 965 (1962).

[166] Y. Nambu, *Quasiparticles and Gauge Invariance in the Theory of Superconductivity*, Phys. Rev. **117**, 648 (1960).

[167] A. J. Beekman, L. Rademaker, and J. van Wezel, *An introduction to spontaneous symmetry breaking*, SciPost Phys. Lect. Notes **11**, 1 (2019), arXiv:1909.01820 [hep-th].

[168] S. L. Adler, *Axial-Vector Vertex in Spinor Electrodynamics*, Phys. Rev. **177**, 2426 (1969).

[169] J. S. Bell and R. Jackiw, *A PCAC Puzzle: $\pi^0 \to \gamma\gamma$ in the σ-Model*, Nuovo Cim. A **60**, 47 (1969).

[170] H. Fukada and Y. Miyamoto, *On the γ-Decay of Neutral Meson*, Prog. Theor. Phys. **4**, 347 (1949).

[171] J. Steinberger, *On the Use of Subtraction Fields and the Lifetimes of Some Types of Meson Decay*, Phys. Rev. **76**, 1180 (1949).

[172] J. S. Schwinger, *On Gauge Invariance and Vacuum Polarization*, Phys. Rev. **82**, 664 (1951).

[173] M. A. Shifman, *Anomalies in gauge theories*, Phys. Rep. **209**, 341 (1991).

[174] S. L. Adler, *Anomalies*, arXiv:hep-th/0411038.

[175] B. R. Holstein, *Anomalies for pedestrians*, Am. J. Phys. **61**, 142 (1993).

[176] C. Becchi, A. Rouet, and R. Stora, *The Abelian Higgs–Kibble model, unitarity of the S operator*, Phys. Lett. B **52**, 344 (1974).

[177] C. Becchi, A. Rouet, and R. Stora, *Renormalization of the Abelian Higgs–Kibble Model*, Commun. Math. Phys. **42**, 127 (1975).

[178] C. Becchi, A. Rouet, and R. Stora, *Renormalization of Gauge Theories*, Ann. Phys. **98**, 287 (1976).

[179] I. V. Tyutin, *Gauge Invariance in Field Theory and Statistical Physics in Operator Formalism*, preprint of the Lebedev Physical Institute of the Russian Academy of Sciences, no. 39 (1975), arXiv:0812.0580 [hep-th].

[180] M. Z. Iofa and I. V. Tyutin, *Gauge invariance of spontaneously broken non-Abelian theories in the Bogolyubov–Parasiuk–Hepp–Zimmerman method*, Theor. Math. Phys. **27**, 316 (1976).

[181] N. Nakanishi, *Covariant Quantization of the Electromagnetic Field in the Landau Gauge*, Prog. Theor. Phys. **35**, 1111 (1966).

[182] N. Nakanishi, *Indefinite-Metric Quantum Field Theory*, Prog. Theor. Phys. Suppl. **51**, 1 (1972).

[183] N. Nakanishi, *Indefinite-Metric Quantum Theory of Genuine and Higgs-Type Massive Vector Fields*, Prog. Theor. Phys. **49**, 640 (1973).

[184] B. Lautrup, *Canonical quantum electrodynamics in covariant gauges*, Kong. Dan. Vid. Sel. Mat. Fys. Med. **35**, 11 (1967).

[185] T. Kugo and I. Ojima, *Local Covariant Operator Formalism of Nonabelian Gauge Theories and Quark Confinement Problem*, Prog. Theor. Phys. Suppl. **66**, 1 (1979).

[186] O. Piguet and S. P. Sorella, *Algebraic Renormalization: Perturbative Renormalization, Symmetries and Anomalies*, Lecture Notes in Physics Monographs 28 (Springer, 1995).

[187] T. Kugo and S. Uehara, *General procedure of gauge fixing based on BRS invariance principle*, Nucl. Phys. B **197**, 378 (1982).

[188] L. Baulieu, C. Becchi, S. Lazzarini, H. Saleur, and F. Thuillier (eds.), *Mathematical foundations of quantum field theory: a volume dedicated to the memory of Raymond Stora*, Nucl. Phys. B **912**, 1 (2016).

[189] V. Koch, *Aspects of Chiral Symmetry*, Int. J. Mod. Phys. E **6**, 203 (1997), arXiv:nucl-th/9706075.

[190] Y. Ne'eman, *Derivation of strong interactions from a gauge invariance*, Nucl. Phys. **26**, 222 (1961).

[191] M. Gell-Mann, *Symmetries of Baryons and Mesons*, Phys. Rev. **125**, 1067 (1962).

[192] P. A. Zyla et al. (Particle Data Group), *Review of Particle Physics*, Prog. Theor. Exp. Phys. **2020**, 083C01 (2020).

[193] T.-W. Chiu, T.-H. Hsieh, and P.-K. Tseng, *Topological susceptibility in 2 + 1 flavors lattice QCD with domain-wall fermions*, Phys. Lett. B **671**, 135 (2009), arXiv:0810.3406 [hep-lat].

[194] J. Noaki et al., *Chiral properties of light mesons with $N_f = 2 + 1$ overlap fermions*, Proc. Sci. **LAT2009**, 096 (2009), arXiv:0910.5532 [hep-lat].

[195] H. Fukaya et al., *Determination of the Chiral Condensate from (2 + 1)-Flavor Lattice QCD*, Phys. Rev. Lett. **104**, 122002 (2010), arXiv:0911.5555 [hep-lat], Erratum: Phys. Rev. Lett. **105**, 159901 (2010).

[196] K. Fujikawa, *Path Integral Measure for Gauge Invariant Fermion Theories*, Phys. Rev. Lett. **42**, 1195 (1979).

[197] K. Fujikawa, *Path integral for gauge theories with fermions*, Phys. Rev. D **21**, 2848 (1980), Erratum: Phys. Rev. D **22**, 1499 (1980).

[198] A. A. Belavin, A. M. Polyakov, A. S. Schwartz, and Y. S. Tyupkin, *Pseudoparticle solutions of the Yang–Mills equations*, Phys. Lett. B **59**, 85 (1975).

[199] G. 't Hooft, *Symmetry Breaking Through Bell–Jackiw Anomalies*, Phys. Rev. Lett. **37**, 8 (1976).

[200] G. 't Hooft, *Computation of the quantum effects due to a four-dimensional pseudoparticle*, Phys. Rev. D **14**, 3432 (1976), Erratum: Phys. Rev. D **18**, 2199 (1978).

[201] G. 't Hooft, *How instantons solve the U(1) problem*, Phys. Rep. **142**, 357 (1986).

[202] P. G. Harris et al., *New Experimental Limit on the Electric Dipole Moment of the Neutron*, Phys. Rev. Lett. **82**, 904 (1999).

[203] C. Abel et al., *Measurement of the Permanent Electric Dipole Moment of the Neutron*, Phys. Rev. Lett. **124**, 081803 (2020), arXiv:2001.11966 [hep-ex].

[204] H.-Y. Cheng, *The strong CP problem revisited*, Phys. Rep. **158**, 1 (1988).

[205] R. D. Peccei, *The Strong CP Problem and Axions*, in *Axions*, Lecture Notes in Physics 741 (Springer, 2008), arXiv:hep-ph/0607268.

[206] A. Hook, *TASI Lectures on the Strong CP Problem and Axions*, Proc. Sci. **TASI2018**, 004 (2019), arXiv:1812.02669 [hep-ph].

[207] J. M. Cornwall, R. Jackiw, and E. Tomboulis, *Effective action for composite operators*, Phys. Rev. D **10**, 2428 (1974).

[208] R. E. Norton and J. M. Cornwall, *On the Formalism of Relativistic Many Body Theory*, Ann. Phys. **91**, 106 (1975).

[209] J. Berges, *n-particle irreducible effective action techniques for gauge theories*, Phys. Rev. D **70**, 105010 (2004), arXiv:hep-ph/0401172.

[210] M. E. Carrington and Y. Guo, *Techniques for n-particle irreducible effective theories*, Phys. Rev. D **83**, 016006 (2011), arXiv:1010.2978 [hep-ph].

[211] M. C. A. York, G. D. Moore, and M. Tassler, *3-loop 3PI effective action for 3D SU(3) QCD*, J. High Energy Phys. **06**, 077 (2012), arXiv:1202.4756 [hep-ph].

[212] M. E. Carrington, W.-j. Fu, T. Fugleberg, D. Pickering, and I. Russell, *Bethe–Salpeter equations from the 4PI effective action*, Phys. Rev. D **88**, 085024 (2013), arXiv:1310.3295 [hep-ph].

[213] R. Williams, C. S. Fischer, and W. Heupel, *Light mesons in QCD and unquenching effects from the 3PI effective action*, Phys. Rev. D **93**, 034026 (2016), arXiv:1512.00455 [hep-ph].

[214] E. Eichten and F. Feinberg, *Dynamical symmetry breaking of non-Abelian gauge symmetries*, Phys. Rev. D **10**, 3254 (1974).

[215] M. Baker and C. Lee, *Overlapping-divergence-free skeleton expansion in non-Abelian gauge theories*, Phys. Rev. D **15**, 2201 (1977), Erratum: Phys. Rev. D **17**, 2182 (1978).

[216] C. S. Fischer, *Non-perturbative Propagators, Running Coupling and Dynamical Mass Generation in Ghost-Antighost Symmetric Gauges in QCD*, PhD thesis (Eberhard Karls Universität Tübingen, Germany, 2003), arXiv:hep-ph/0304233.

[217] F. J. Dyson, *The S Matrix in Quantum Electrodynamics*, Phys. Rev. **75**, 1736 (1949).

[218] J. S. Schwinger, *On the Green's functions of quantized fields. I.* Proc. Nat. Acad. Sci. USA **37**, 452 (1951).

[219] J. S. Schwinger, *On the Green's functions of quantized fields. II.* Proc. Nat. Acad. Sci. USA **37**, 455 (1951).

[220] C. S. Fischer, *Infrared properties of QCD from Dyson–Schwinger equations*, J. Phys. G: Nucl. Part. Phys. **32**, R253 (2006), arXiv:hep-ph/0605173.

[221] M. Q. Huber, A. K. Cyrol, and J. M. Pawlowski, *DoFun 3.0: Functional equations in Mathematica*, Comput. Phys. Commun. **248**, 107058 (2020), arXiv:1908.02760 [hep-ph].

[222] D. Binosi, J. Collins, C. Kaufhold, and L. Theussl, *JaxoDraw: A graphical user interface for drawing Feynman diagrams. Version 2.0 release notes*, Comput. Phys. Commun. **180**, 1709 (2009), arXiv:0811.4113 [hep-ph].

[223] C. S. Fischer and L. von Smekal, *Scaling, decoupling and transversality of the gluon propagator*, AIP Conf. Proc. **1343**, 247 (2011), arXiv:1011.6482 [hep-ph].

[224] M. Q. Huber and L. von Smekal, *Spurious divergences in Dyson–Schwinger equations*, J. High Energy Phys. **06**, 015 (2014), arXiv:1404.3642 [hep-ph].

[225] G. Eichmann, J. M. Pawlowski, and J. M. Silva, *On mass generation in Landau-gauge Yang–Mills theory*, arXiv:2107.05352 [hep-ph].

[226] K. G. Wilson, *Renormalization Group and Critical Phenomena. I. Renormalization Group and the Kadanoff Scaling Picture*, Phys. Rev. B **4**, 3174 (1971).

[227] K. G. Wilson, *Renormalization Group and Critical Phenomena. II. Phase-Space Cell Analysis of Critical Behavior*, Phys. Rev. B **4**, 3184 (1971).

[228] K. G. Wilson and J. B. Kogut, *The renormalization group and the ε expansion*, Phys. Rep. **12**, 75 (1974).

[229] K. G. Wilson, *The renormalization group: Critical phenomena and the Kondo problem*, Rev. Mod. Phys. **47**, 773 (1975).

[230] C. Wetterich, *Exact evolution equation for the effective potential*, Phys. Lett. B **301**, 90 (1993), arXiv:1710.05815 [hep-th].

[231] U. Ellwanger, *Flow equations for N point functions and bound states*, Z. Phys. C **62**, 503 (1994), arXiv:hep-ph/9308260.

[232] T. R. Morris, *The exact renormalization group and approximate solutions*, Int. J. Mod. Phys. A **9**, 2411 (1994), arXiv:hep-ph/9308265.

[233] T. Matsubara, *A New Approach to Quantum-Statistical Mechanics*, Prog. Theor. Phys. **14**, 351 (1955).

[234] N. P. Landsman and C. G. van Weert, *Real- and imaginary-time field theory at finite temperature and density*, Phys. Rep. **145**, 141 (1987).

[235] J. Lücker, *Chiral and Deconfinement Phase Transitions in $N_f = 2$ and $N_f = 2 + 1$ Quantum Chromodynamics*, PhD thesis (Justus-Liebig-Universität Gießen, Germany, 2013).

[236] R. Contant and M. Q. Huber, *Phase structure and propagators at nonvanishing temperature for QCD and QCD-like theories*, Phys. Rev. D **96**, 074002 (2017), arXiv:1706.00943 [hep-ph].

[237] D. Nickel, J. Wambach, and R. Alkofer, *Color superconductivity in the strong-coupling regime of Landau gauge QCD*, Phys. Rev. D **73**, 114028 (2006), arXiv:hep-ph/0603163.

[238] D. Nickel, R. Alkofer, and J. Wambach, *Unlocking of color and flavor in color-superconducting quark matter*, Phys. Rev. D **74**, 114015 (2006), arXiv:hep-ph/0609198.

[239] F. Marhauser, D. Nickel, M. Buballa, and J. Wambach, *Color-spin locking in a self-consistent Dyson–Schwinger approach*, Phys. Rev. D **75**, 054022 (2007), arXiv:hep-ph/0612027.

[240] S.-x. Qin, L. Chang, H. Chen, Y.-x. Liu, and C. D. Roberts, *Phase Diagram and Critical End Point for Strongly Interacting Quarks*, Phys. Rev. Lett. **106**, 172301 (2011), arXiv:1011.2876 [nucl-th].

[241] C. S. Fischer and J. Luecker, *Propagators and phase structure of $N_f = 2$ and $N_f = 2 + 1$ QCD*, Phys. Lett. B **718**, 1036 (2013), arXiv:1206.5191 [hep-ph].

[242] D. Müller, M. Buballa, and J. Wambach, *Dyson–Schwinger approach to color superconductivity at finite temperature and density*, Eur. Phys. J. A **49**, 96 (2013), arXiv:1303.2693 [hep-ph].

[243] D. Müller, M. Buballa, and J. Wambach, *Dyson–Schwinger study of chiral density waves in QCD*, Phys. Lett. B **727**, 240 (2013), arXiv:1308.4303 [hep-ph].

[244] C. S. Fischer, J. Luecker, and C. A. Welzbacher, *Phase structure of three and four flavor QCD*, Phys. Rev. D **90**, 034022 (2014), arXiv:1405.4762 [hep-ph].

[245] F. Gao, J. Chen, Y.-x. Liu, S.-x. Qin, C. D. Roberts, and S. M. Schmidt, *Phase diagram and thermal properties of strong-interaction matter*, Phys. Rev. D **93**, 094019 (2016), arXiv:1507.00875 [nucl-th].

[246] D. Müller, M. Buballa, and J. Wambach, *Dyson–Schwinger Approach to Color-Superconductivity: Effects of Selfconsistent Gluon Dressing*, arXiv:1603.02865 [hep-ph].

[247] W.-j. Fu, J. M. Pawlowski, and F. Rennecke, *QCD phase structure at finite temperature and density*, Phys. Rev. D **101**, 054032 (2020), arXiv:1909.02991 [hep-ph].

[248] F. Gao and J. M. Pawlowski, *QCD phase structure from functional methods*, Phys. Rev. D **102**, 034027 (2020), arXiv:2002.07500 [hep-ph].

[249] F. Gao and J. M. Pawlowski, *Chiral phase structure and critical end point in QCD*, Phys. Lett. B **820**, 136584 (2021), arXiv:2010.13705 [hep-ph].

[250] F. R. Brown et al., *On the Existence of a Phase Transition for QCD with Three Light Quarks*, Phys. Rev. Lett. **65**, 2491 (1990).

[251] L. G. Yaffe and B. Svetitsky, *First-order phase transition in the SU(3) gauge theory at finite temperature*, Phys. Rev. D **26**, 963 (1982).

[252] B. Svetitsky and L. G. Yaffe, *Critical behavior at finite-temperature confinement transitions*, Nucl. Phys. B **210**, 423 (1982).

[253] R. D. Pisarski and F. Wilczek, *Remarks on the chiral phase transition in chromodynamics*, Phys. Rev. D **29**, 338 (1984).

[254] C. S. Fischer, *Deconfinement Phase Transition and the Quark Condensate*, Phys. Rev. Lett. **103**, 052003 (2009), arXiv:0904.2700 [hep-ph].

[255] C. S. Fischer and J. A. Mueller, *Chiral and deconfinement transition from Dyson–Schwinger equations*, Phys. Rev. D **80**, 074029 (2009), arXiv:0908.0007 [hep-ph].

[256] C. S. Fischer, A. Maas, and J. A. Müller, *Chiral and deconfinement transition from correlation functions: SU(2) vs. SU(3)*, Eur. Phys. J. C **68**, 165 (2010), arXiv:1003.1960 [hep-ph].

[257] C. S. Fischer, J. Luecker, and J. A. Mueller, *Chiral and deconfinement phase transitions of two-flavour QCD at finite temperature and chemical potential*, Phys. Lett. B **702**, 438 (2011), arXiv:1104.1564 [hep-ph].

[258] C. S. Fischer and J. A. Mueller, *On critical scaling at the QCD $N_f = 2$ chiral phase transition*, Phys. Rev. D **84**, 054013 (2011), arXiv:1106.2700 [hep-ph].

[259] C. S. Fischer, L. Fister, J. Luecker, and J. M. Pawlowski, *Polyakov loop potential at finite density*, Phys. Lett. B **732**, 273 (2014), arXiv:1306.6022 [hep-ph].

[260] C. S. Fischer, J. Luecker, and J. M. Pawlowski, *Phase structure of QCD for heavy quarks*, Phys. Rev. D **91**, 014024 (2015), arXiv:1409.8462 [hep-ph].

[261] G. Eichmann, C. S. Fischer, and C. A. Welzbacher, *Baryon effects on the location of QCD's critical end point*, Phys. Rev. D **93**, 034013 (2016), arXiv:1509.02082 [hep-ph].

[262] P. J. Gunkel and C. S. Fischer, *Masses and decay constants of (axial-)vector mesons at finite chemical potential*, Eur. Phys. J. A **57**, 147 (2021), arXiv:2012.01957 [hep-ph].

[263] P. J. Gunkel and C. S. Fischer, *Locating the critical endpoint of QCD: Mesonic backcoupling effects*, Phys. Rev. D **104**, 054022 (2021), arXiv:2106.08356 [hep-ph].

[264] R. Contant and M. Q. Huber, *Dense two-color QCD from Dyson–Schwinger equations*, Phys. Rev. D **101**, 014016 (2020), arXiv:1909.12796 [hep-ph].

[265] J. A. Müller, *A Dyson–Schwinger Approach to Finite Temperature QCD*, PhD thesis (Technische Universität Darmstadt, Germany, 2011).

[266] D. Müller, *QCD at finite density with Dyson–Schwinger equations*, PhD thesis (Technische Universität Darmstadt, Germany, 2013).

[267] P. Büscher, *Phase Diagram of Two-Color QCD in a Dyson–Schwinger Approach*, PhD thesis (Technische Universität Darmstadt, Germany, 2014).

[268] C. A. Welzbacher, *Quarks and Gluons in the Phase Diagram of Quantum Chromodynamics*, PhD thesis (Justus-Liebig-Universität Gießen, Germany, 2016).

[269] R. Contant, *Phase structure of QCD and QCD-like theories*, PhD thesis (Karl-Franzens-Universität Graz, Austria, 2019).

[270] J. Bernhardt, PhD thesis (Justus-Liebig-Universität Gießen, Germany), in progress.

[271] R. Alkofer, C. S. Fischer, F. J. Llanes-Estrada, and K. Schwenzer, *The quark-gluon vertex in Landau gauge QCD: Its role in dynamical chiral symmetry breaking and quark confinement*, Ann. Phys. **324**, 106 (2009), arXiv:0804.3042 [hep-ph].

[272] R. Williams, *The quark-gluon vertex in Landau gauge bound-state studies*, Eur. Phys. J. A **51**, 57 (2015), arXiv:1404.2545 [hep-ph].

[273] A. Windisch, M. Hopfer, and R. Alkofer, *Towards a Self-consistent Solution of the Landau Gauge Quark-Gluon Vertex Dyson–Schwinger Equation*, Acta Phys. Polon. B Proc. Supp. **6**, 347 (2013), arXiv:1210.8428 [hep-ph].

[274] E. Rojas, J. P. B. C. de Melo, B. El-Bennich, O. Oliveira, and T. Frederico, *On the quark-gluon vertex and quark-ghost kernel: combining lattice simulations with Dyson–Schwinger equations*, J. High. Energy Phys. **10**, 193 (2013), arXiv:1306.3022 [hep-ph].

[275] A. C. Aguilar, D. Binosi, D. Ibañez, and J. Papavassiliou, *New method for determining the quark-gluon vertex*, Phys. Rev. D **90**, 065027 (2014), arXiv:1405.3506 [hep-ph].

[276] A. C. Aguilar, J. C. Cardona, M. N. Ferreira, and J. Papavassiliou, *Non-Abelian Ball–Chiu vertex for arbitrary Euclidean momenta*, Phys. Rev. D **96**, 014029 (2017), arXiv:1610.06158 [hep-ph].

[277] O. Oliveira, W. de Paula, T. Frederico, and J. P. B. C. de Melo, *The quark-gluon vertex and the QCD infrared dynamics*, Eur. Phys. J. C **79**, 116 (2019), arXiv:1807.10348 [hep-ph].

[278] F. Gao, J. Papavassiliou, and J. M. Pawlowski, *Fully coupled functional equations for the quark sector of QCD*, Phys. Rev. D **103**, 094013 (2021), arXiv:2102.13053 [hep-ph].

[279] M. Mitter, J. M. Pawlowski, and N. Strodthoff, *Chiral symmetry breaking in continuum QCD*, Phys. Rev. D **91**, 054035 (2015), arXiv:1411.7978 [hep-ph].

[280] A. K. Cyrol, M. Mitter, J. M. Pawlowski, and N. Strodthoff, *Nonperturbative quark, gluon, and meson correlators of unquenched QCD*, Phys. Rev. D **97**, 054006 (2018), arXiv:1706.06326 [hep-ph].

[281] A. Kızılersü, O. Oliveira, P. J. Silva, J.-I. Skullerud, and A. Sternbeck, *Quark-gluon vertex from $N_f = 2$ lattice QCD*, Phys. Rev. D **103**, 114515 (2021), arXiv:2103.02945 [hep-lat].

[282] R. Contant, M. Q. Huber, C. S. Fischer, C. A. Welzbacher, and R. Williams, *On the Quark-Gluon Vertex at Non-vanishing Temperature*, Acta Phys. Polon. B Proc. Supp. **11**, 483 (2018), arXiv:1805.05885 [hep-ph].

[283] C. S. Fischer, A. Maas, and J. M. Pawlowski, *On the infrared behavior of Landau gauge Yang–Mills theory*, Ann. Phys. **324**, 2408 (2009), arXiv:0810.1987 [hep-ph].

[284] A. K. Cyrol, L. Fister, M. Mitter, J. M. Pawlowski, and N. Strodthoff, *Landau gauge Yang–Mills correlation functions*, Phys. Rev. D **94**, 054005 (2016), arXiv:1605.01856 [hep-ph].

[285] M. Q. Huber, *Correlation functions of Landau gauge Yang–Mills theory*, Phys. Rev. D **101**, 114009 (2020), arXiv:2003.13703 [hep-ph].

[286] O. Oliveira, T. Frederico, and W. de Paula, *The soft-gluon limit and the infrared enhancement of the quark-gluon vertex*, Eur. Phys. J. C **80**, 484 (2020), arXiv:2006.04982 [hep-ph].

[287] J. S. Ball and T.-W. Chiu, *Analytic properties of the vertex function in gauge theories. I*, Phys. Rev. D **22**, 2542 (1980).

[288] L. Fister and J. M. Pawlowski, *Yang–Mills correlation functions at finite temperature*, arXiv:1112.5440 [hep-ph].

[289] M. Q. Huber and L. von Smekal, *On two- and three-point functions of Landau gauge Yang–Mills theory*, Proc. Sci. **LATTICE2013**, 364 (2014), arXiv:1311.0702 [hep-lat].

[290] A. K. Cyrol, M. Mitter, J. M. Pawlowski, and N. Strodthoff, *Nonperturbative finite-temperature Yang–Mills theory*, Phys. Rev. D **97**, 054015 (2018), arXiv:1708.03482 [hep-ph].

[291] C. S. Fischer and R. Alkofer, *Nonperturbative propagators, running coupling, and dynamical quark mass of Landau gauge QCD*, Phys. Rev. D **67**, 094020 (2003), arXiv:hep-ph/0301094.

[292] A. Maas, J. M. Pawlowski, L. von Smekal, and D. Spielmann, *The Gluon propagator close to criticality*, Phys. Rev. D **85**, 034037 (2012), arXiv:1110.6340 [hep-lat].

[293] C. S. Fischer, private communication.

[294] W. Heupel, T. Goecke, and C. S. Fischer, *Beyond rainbow-ladder in bound state equations*, Eur. Phys. J. A **50**, 85 (2014), arXiv:1402.5042 [hep-ph].

[295] J. N. Guenther, *Overview of the QCD phase diagram: Recent progress from the lattice*, Eur. Phys. J. A **57**, 136 (2021), arXiv:2010.15503 [hep-lat].

[296] R. Aouane, F. Burger, E.-M. Ilgenfritz, M. Müller-Preussker, and A. Sternbeck, *Landau gauge gluon and ghost propagators from lattice QCD with $N_f = 2$ twisted mass fermions at finite temperature*, Phys. Rev. D **87**, 114502 (2013), arXiv:1212.1102 [hep-lat].

[297] A. Bazavov et al., *Freeze-out Conditions in Heavy Ion Collisions from QCD Thermodynamics*, Phys. Rev. Lett. **109**, 192302 (2012), arXiv:1208.1220 [hep-lat].

[298] S. Borsányi, Z. Fodor, S. D. Katz, S. Krieg, C. Ratti, and K. K. Szabó, *Freeze-Out Parameters: Lattice Meets Experiment*, Phys. Rev. Lett. **111**, 062005 (2013), arXiv:1305.5161 [hep-lat].

[299] R. Bellwied et al., *The QCD phase diagram from analytic continuation*, Phys. Lett. B **751**, 559 (2015), arXiv:1507.07510 [hep-lat].

[300] A. Bazavov et al., *Chiral crossover in QCD at zero and non-zero chemical potentials*, Phys. Lett. B **795**, 15 (2019), arXiv:1812.08235 [hep-lat].

[301] S. Borsányi et al., *QCD Crossover at Finite Chemical Potential from Lattice Simulations*, Phys. Rev. Lett. **125**, 052001 (2020), arXiv:2002.02821 [hep-lat].

[302] A. Bazavov et al., *The QCD equation of state to $\mathcal{O}(\mu_B^6)$ from lattice QCD*, Phys. Rev. D **95**, 054504 (2017), arXiv:1701.04325 [hep-lat].

[303] P. Alba et al., *Freeze-out conditions from net-proton and net-charge fluctuations at RHIC*, Phys. Lett. B **738**, 305 (2014), arXiv:1403.4903 [hep-ph].

[304] A. Andronic, P. Braun-Munzinger, K. Redlich, and J. Stachel, *Hadron yields, the chemical freeze-out and the QCD phase diagram*, J. Phys. Conf. Ser. **779**, 012012 (2017), arXiv:1611.01347 [nucl-th].

[305] A. Andronic, P. Braun-Munzinger, K. Redlich, and J. Stachel, *Decoding the phase structure of QCD via particle production at high energy*, Nature **561**, 321 (2018), arXiv:1710.09425 [nucl-th].

[306] F. Becattini, J. Steinheimer, R. Stock, and M. Bleicher, *Hadronization conditions in relativistic nuclear collisions and the QCD pseudo-critical line*, Phys. Lett. B **764**, 241 (2017), arXiv:1605.09694 [nucl-th].

[307] L. Adamczyk et al., *Bulk properties of the medium produced in relativistic heavy-ion collisions from the beam energy scan program*, Phys. Rev. C **96**, 044904 (2017), arXiv:1701.07065 [nucl-ex].

[308] V. Vovchenko, V. V. Begun, and M. I. Gorenstein, *Hadron multiplicities and chemical freeze-out conditions in proton-proton and nucleus-nucleus collisions*, Phys. Rev. C **93**, 064906 (2016), arXiv:1512.08025 [nucl-th].

[309] C. Bonati, M. D'Elia, F. Negro, F. Sanfilippo, and K. Zambello, *Curvature of the pseudocritical line in QCD: Taylor expansion matches analytic continuation*, Phys. Rev. D **98**, 054510 (2018), arXiv:1805.02960 [hep-lat].

[310] F. Gao and Y.-x. Liu, *QCD phase transitions via a refined truncation of Dyson–Schwinger equations*, Phys. Rev. D **94**, 076009 (2016), arXiv:1607.01675 [hep-ph].

[311] M. A. Stephanov, K. Rajagopal, and E. V. Shuryak, *Signatures of the Tricritical Point in QCD*, Phys. Rev. Lett. **81**, 4816 (1998), arXiv:hep-ph/9806219.

[312] M. A. Stephanov, K. Rajagopal, and E. V. Shuryak, *Event-by-event fluctuations in heavy ion collisions and the QCD critical point*, Phys. Rev. D **60**, 114028 (1999), arXiv:hep-ph/9903292.

[313] S. Jeon and V. Koch, *Fluctuations of Particle Ratios and the Abundance of Hadronic Resonances*, Phys. Rev. Lett. **83**, 5435 (1999), arXiv:nucl-th/9906074.

[314] S. Jeon and V. Koch, *Charged Particle Ratio Fluctuation as a Signal for Quark-Gluon Plasma*, Phys. Rev. Lett. **85**, 2076 (2000), arXiv:hep-ph/0003168.

[315] M. Asakawa, U. W. Heinz, and B. Müller, *Fluctuation Probes of Quark Deconfinement*, Phys. Rev. Lett. **85**, 2072 (2000), arXiv:hep-ph/0003169.

[316] V. Koch, A. Majumder, and J. Randrup, *Baryon-Strangeness Correlations: A Diagnostic of Strongly Interacting Matter*, Phys. Rev. Lett. **95**, 182301 (2005), arXiv:nucl-th/0505052.

[317] S. Ejiri, F. Karsch, and K. Redlich, *Hadronic fluctuations at the QCD phase transition*, Phys. Lett. B **633**, 275 (2006), arXiv:hep-ph/0509051.

[318] B. Friman, F. Karsch, K. Redlich, and V. Skokov, *Fluctuations as probe of the QCD phase transition and freeze-out in heavy ion collisions at LHC and RHIC*, Eur. Phys. J. C **71**, 1694 (2011), arXiv:1103.3511 [hep-ph].

[319] V. Koch, *Hadronic Fluctuations and Correlations*, in *Relativistic Heavy Ion Physics* (Springer, 2010), arXiv:0810.2520 [nucl-th].

[320] M. Asakawa and M. Kitazawa, *Fluctuations of conserved charges in relativistic heavy ion collisions: An introduction*, Prog. Part. Nucl. Phys. **90**, 299 (2016), arXiv:1512.05038 [nucl-th].

[321] M. Cheng et al., *Baryon number, strangeness, and electric charge fluctuations in QCD at high temperature*, Phys. Rev. D **79**, 074505 (2009), arXiv:0811.1006 [hep-lat].

[322] S. Borsányi, Z. Fodor, S. D. Katz, S. Krieg, C. Ratti, and K. Szabó, *Fluctuations of conserved charges at finite temperature from lattice QCD*, J. High Energy Phys. **01**, 138 (2012), arXiv:1112.4416 [hep-lat].

[323] A. Bazavov et al., *Fluctuations and correlations of net baryon number, electric charge, and strangeness: A comparison of lattice QCD results with the hadron resonance gas model*, Phys. Rev. D **86**, 034509 (2012), arXiv:1203.0784 [hep-lat].

[324] R. Bellwied et al., *Fluctuations and correlations in high temperature QCD*, Phys. Rev. D **92**, 114505 (2015), arXiv:1507.04627 [hep-lat].

[325] V. Skokov, B. Stokić, B. Friman, and K. Redlich, *Meson fluctuations and thermodynamics of the Polyakov-loop-extended quark-meson model*, Phys. Rev. C **82**, 015206 (2010), arXiv:1004.2665 [hep-ph].

[326] V. Skokov, B. Friman, and K. Redlich, *Quark number fluctuations in the Polyakov-loop-extended quark-meson model at finite baryon density*, Phys. Rev. C **83**, 054904 (2011), arXiv:1008.4570 [hep-ph].

[327] F. Karsch, B.-J. Schaefer, M. Wagner, and J. Wambach, *Towards finite density QCD with Taylor expansions*, Phys. Lett. B **698**, 256 (2011), arXiv:1009.5211 [hep-ph].

[328] B.-J. Schaefer and M. Wagner, *QCD critical region and higher moments for three-flavor models*, Phys. Rev. D **85**, 034027 (2012), arXiv:1111.6871 [hep-ph].

[329] K. Morita and K. Redlich, *Momentum scale dependence of the net quark number fluctuations near chiral crossover*, Prog. Theor. Exp. Phys. **2015**, 043D03 (2015), arXiv:1409.8001 [hep-ph].

[330] W.-j. Fu and J. M. Pawlowski, *Relevance of matter and glue dynamics for baryon number fluctuations*, Phys. Rev. D **92**, 116006 (2015), arXiv:1508.06504 [hep-ph].

[331] W.-j. Fu and J. M. Pawlowski, *Correlating the skewness and kurtosis of baryon number distributions*, Phys. Rev. D **93**, 091501 (2016), arXiv:1512.08461 [hep-ph].

[332] W.-j. Fu, J. M. Pawlowski, F. Rennecke, and B.-J. Schaefer, *Baryon number fluctuations at finite temperature and density*, Phys. Rev. D **94**, 116020 (2016), arXiv:1608.04302 [hep-ph].

[333] M. Szymański, M. Bluhm, K. Redlich, and C. Sasaki, *Net-proton number fluctuations in the presence of the QCD critical point*, J. Phys. G: Nucl. Part. Phys. **47**, 045102 (2020), arXiv:1905.00667 [nucl-th].

[334] S. Yin, R. Wen, and W.-j. Fu, *Mesonic dynamics and the QCD phase transition*, Phys. Rev. D **100**, 094029 (2019), arXiv:1907.10262 [hep-ph].

[335] W.-j. Fu, X. Luo, J. M. Pawlowski, F. Rennecke, R. Wen, and S. Yin, *Hyper-order baryon number fluctuations at finite temperature and density*, arXiv:2101.06035 [hep-ph].

[336] M. He, D.-k. He, H.-t. Feng, W.-m. Sun, and H.-s. Zong, *Continuum study of quark-number susceptibility in an effective interaction model*, Phys. Rev. D **76**, 076005 (2007).

[337] M. He, J.-F. Li, W.-M. Sun, and H.-S. Zong, *Quark number susceptibility around the critical end point*, Phys. Rev. D **79**, 036001 (2009), arXiv:0811.1835 [hep-ph].

[338] X.-y. Xin, S.-x. Qin, and Y.-x. Liu, *Quark number fluctuations at finite temperature and finite chemical potential via the Dyson–Schwinger equation approach*, Phys. Rev. D **90**, 076006 (2014).

[339] J. Chen, F. Gao, and Y.-x. Liu, *Chemical Freeze-out Parameters via a Non-perturbative QCD Approach*, arXiv:1510.07543 [hep-ph].

[340] R. W. Haymaker, *Variational methods for composite operators*, Riv. Nuovo Cim. **14**, 1 (1991).

[341] L. D. Landau and I. M. Khalatnikov, *The gauge transformation of the Green function for charged particles*, Sov. Phys. JETP **2**, 69 (1956).

[342] E. S. Fradkin, *Concerning some general relations of quantum electrodynamics*, Sov. Phys. JETP **2**, 361 (1956).

[343] F. Gao and Y.-x. Liu, *Interface effect in QCD phase transitions via Dyson–Schwinger equation approach*, Phys. Rev. D **94**, 094030 (2016), arXiv:1609.08038 [hep-ph].

[344] R. V. Gavai and S. Sharma, *Divergences in the quark number susceptibility: The origin and a cure*, Phys. Lett. B **749**, 8 (2015), arXiv:1406.0474 [hep-lat].

[345] B.-J. Schaefer and J. Wambach, *Susceptibilities near the QCD (tri)critical point*, Phys. Rev. D **75**, 085015 (2007), arXiv:hep-ph/0603256.

[346] R. B. Griffiths and J. C. Wheeler, *Critical Points in Multicomponent Systems*, Phys. Rev. A **2**, 1047 (1970).

[347] S. Gavin, A. Gocksch, and R. D. Pisarski, *QCD and the chiral critical point*, Phys. Rev. D **49**, R3079 (1994), arXiv:hep-ph/9311350.

[348] J. Berges and K. Rajagopal, *Color superconductivity and chiral symmetry restoration at nonzero baryon density and temperature*, Nucl. Phys. B **538**, 215 (1999), arXiv:hep-ph/9804233.

[349] A. M. Halasz, A. D. Jackson, R. E. Shrock, M. A. Stephanov, and J. J. M. Verbaarschot, *Phase diagram of QCD*, Phys. Rev. D **58**, 096007 (1998), arXiv:hep-ph/9804290.

[350] R. Guida and J. Zinn-Justin, *3D Ising model: the scaling equation of state*, Nucl. Phys. B **489**, 626 (1997), arXiv:hep-th/9610223.

[351] M. Campostrini, A. Pelissetto, P. Rossi, and E. Vicari, *25th-order high-temperature expansion results for three-dimensional Ising-like systems on the simple-cubic lattice*, Phys. Rev. E **65**, 066127 (2002), arXiv:cond-mat/0201180.

[352] J. Zinn-Justin, *Quantum Field Theory and Critical Phenomena*, 5th ed., International Series of Monographs on Physics 171 (Oxford University Press, 2021).

[353] W. Gebhardt and U. Krey, *Phasenübergänge und kritische Phänomene* (Vieweg, 1980).

[354] W.-j. Fu, J. M. Pawlowski, and F. Rennecke, *Strangeness Neutrality and QCD Thermodynamics*, SciPost Phys. Core **2**, 002 (2020), arXiv:1808.00410 [hep-ph].

[355] F. Karsch, K. Redlich, and A. Tawfik, *Thermodynamics at non-zero baryon number density: a comparison of lattice and hadron resonance gas model calculations*, Phys. Lett. B **571**, 67 (2003), arXiv:hep-ph/0306208.

[356] F. Karsch and K. Redlich, *Probing freeze-out conditions in heavy ion collisions with moments of charge fluctuations*, Phys. Lett. B **695**, 136 (2011), arXiv:1007.2581 [hep-ph].

[357] G. A. Almási, B. Friman, and K. Redlich, *Baryon number fluctuations in chiral effective models and their phenomenological implications*, Phys. Rev. D **96**, 014027 (2017), arXiv:1703.05947 [hep-ph].

[358] J. M. Lattimer and M. Prakash, *The equation of state of hot, dense matter and neutron stars*, Phys. Rep. **621**, 127 (2016), arXiv:1512.07820 [astro-ph.SR].

[359] M. Oertel, M. Hempel, T. Klähn, and S. Typel, *Equations of state for supernovae and compact stars*, Rev. Mod. Phys. **89**, 015007 (2017), arXiv:1610.03361 [astro-ph.HE].

[360] S. Borsányi, Z. Fodor, C. Hoelbling, S. D. Katz, S. Krieg, and K. K. Szabó, *Full result for the QCD equation of state with 2 + 1 flavors*, Phys. Lett. B **730**, 99 (2014), arXiv:1309.5258 [hep-lat].

[361] A. Bazavov et al., *Equation of state in (2 + 1)-flavor QCD*, Phys. Rev. D **90**, 094503 (2014), arXiv:1407.6387 [hep-lat].

[362] S. Borsányi et al., *QCD equation of state at nonzero chemical potential: continuum results with physical quark masses at order μ^2*, J. High Energy Phys. **08**, 053 (2012), arXiv:1204.6710 [hep-lat].

[363] T. K. Herbst, M. Mitter, J. M. Pawlowski, B.-J. Schaefer, and R. Stiele, *Thermodynamics of QCD at vanishing density*, Phys. Lett. B **731**, 248 (2014), arXiv:1308.3621 [hep-ph].

[364] J. M. Pawlowski, *Equation of state and phase diagram of strongly interacting matter*, Nucl. Phys. A **931**, 113 (2014).

[365] K. Otto, M. Oertel, and B.-J. Schaefer, *Hybrid and quark star matter based on a non-perturbative equation of state*, Phys. Rev. D **101**, 103021 (2020), arXiv:1910.11929 [hep-ph].

[366] K. Otto, M. Oertel, and B.-J. Schaefer, *Nonperturbative quark matter equations of state with vector interactions*, Eur. Phys. J. ST **229**, 3629 (2020), arXiv:2007.07394 [hep-ph].

[367] D. Blaschke, C. D. Roberts, and S. M. Schmidt, *Thermodynamic properties of a simple confining model*, Phys. Lett. B **425**, 232 (1998), arXiv:nucl-th/9706070.

[368] S.-S. Xu, Y. Yan, Z.-F. Cui, and H.-S. Zong, *2 + 1 flavors QCD equation of state at zero temperature within Dyson–Schwinger equations*, Int. J. Mod. Phys. A **30**, 1550217 (2015), arXiv:1506.06846 [hep-ph].

[369] T. Steinert, *The QCD phase diagram within effective models*, PhD thesis (Justus-Liebig-Universität Gießen, Germany, 2018).

[370] G. Boyd et al., *Thermodynamics of SU(3) lattice gauge theory*, Nucl. Phys. B **469**, 419 (1996), arXiv:hep-lat/9602007.

[371] S. Borsányi, G. Endrődi, Z. Fodor, S. D. Katz, and K. K. Szabó, *Precision SU(3) lattice thermodynamics for a large temperature range*, J. High Energy Phys. **07**, 056 (2012), arXiv:1204.6184 [hep-lat].

[372] H. Kleinert, *On the Hadronization of Quark Theories*, contribution to the 14th International School of Subnuclear Physics: Understanding the Fundamental Constitutents of Matter, 23 July–8 August 1976, Erice (Italy).

[373] M. K. Volkov, *Meson Lagrangians in a superconductor quark model*, Ann. Phys. **157**, 282 (1984).

[374] T. Hatsuda and T. Kunihiro, *Possible critical phenomena associated with the chiral symmetry breaking*, Phys. Lett. B **145**, 7 (1984).

[375] D. Adamova et al., *Universal Pion Freeze-Out in Heavy-Ion Collisions*, Phys. Rev. Lett. **90**, 022301 (2003), arXiv:nucl-ex/0207008.

[376] S. A. Bass et al., *Microscopic models for ultrarelativistic heavy ion collisions*, Prog. Part. Nucl. Phys. **41**, 255 (1998), arXiv:nucl-th/9803035.

[377] M. Bleicher et al., *Relativistic hadron-hadron collisions in the ultra-relativistic quantum molecular dynamics model*, J. Phys. G: Nucl. Part. Phys. **25**, 1859 (1999), arXiv:hep-ph/9909407.

[378] G. Graef, M. Bleicher, and Q. Li, *Examination of scaling of Hanbury-Brown–Twiss radii with charged particle multiplicity*, Phys. Rev. C **85**, 044901 (2012), arXiv:1203.4071 [nucl-th].

[379] V. Skokov, B. Friman, and K. Redlich, *Volume fluctuations and higher-order cumulants of the net baryon number*, Phys. Rev. C **88**, 034911 (2013), arXiv:1205.4756 [hep-ph].

[380] G. A. Almási, R. D. Pisarski, and V. Skokov, *Volume dependence of baryon number cumulants and their ratios*, Phys. Rev. D **95**, 056015 (2017), arXiv:1612.04416 [hep-ph].

[381] C. S. Fischer, R. Alkofer, and H. Reinhardt, *The elusiveness of infrared critical exponents in Landau gauge Yang–Mills theories*, Phys. Rev. D **65**, 094008 (2002), arXiv:hep-ph/0202195.

[382] C. S. Fischer, B. Grüter, and R. Alkofer, *Solving coupled Dyson–Schwinger equations on a compact manifold*, Ann. Phys. **321**, 1918 (2006), arXiv:hep-ph/0506053.

[383] C. S. Fischer and M. R. Pennington, *Finite volume effects in a quenched lattice-QCD quark propagator*, Phys. Rev. D **73**, 034029 (2006), arXiv:hep-ph/0512233.

[384] C. S. Fischer, A. Maas, J. M. Pawlowski, and L. von Smekal, *Large volume behaviour of Yang–Mills propagators*, Ann. Phys. **322**, 2916 (2007), arXiv:hep-ph/0701050.

[385] T. Goecke, C. S. Fischer, and R. Williams, *Finite volume effects and dynamical chiral symmetry breaking in QED_3*, Phys. Rev. B **79**, 064513 (2009), arXiv:0811.1887 [hep-ph].

[386] J. Luecker, C. S. Fischer, and R. Williams, *Volume behavior of quark condensate, pion mass, and decay constant from Dyson–Schwinger equations*, Phys. Rev. D **81**, 094005 (2010), arXiv:0912.3686 [hep-ph].

[387] J. A. Bonnet, C. S. Fischer, and R. Williams, *Effects of anisotropy in QED_3 from Dyson–Schwinger equations in a box*, Phys. Rev. B **84**, 024520 (2011), arXiv:1103.1578 [hep-ph].

[388] B.-L. Li, Z.-F. Cui, B.-W. Zhou, S. An, L.-P. Zhang, and H.-S. Zong, *Finite volume effects on the chiral phase transition from Dyson–Schwinger equations of QCD*, Nucl. Phys. B **938**, 298 (2019), arXiv:1711.04914 [hep-ph].

[389] C. Shi, Y.-H. Xia, W.-B. Jia, and H.-S. Zong, *Chiral phase diagram of strongly interacting matter at finite volume*, Sci. Chin. Phys. Mech. Astron. **61**, 082021 (2018).

[390] Y.-P. Zhao, R.-R. Zhang, H. Zhang, and H.-S. Zong, *Chiral phase transition from the Dyson–Schwinger equations in a finite spherical volume*, Chin. Phys. C **43**, 063101 (2019), arXiv:1903.11243 [hep-ph].

[391] Y.-Z. Xu, C. Shi, X.-T. He, and H.-S. Zong, *Chiral crossover transition from the Dyson–Schwinger equations in a sphere*, Phys. Rev. D **102**, 114011 (2020), arXiv:2009.12035 [nucl-th].

[392] J. Braun, B. Klein, and H.-J. Pirner, *Volume dependence of the pion mass in the quark-meson-model*, Phys. Rev. D **71**, 014032 (2005), arXiv:hep-ph/0408116.

[393] J. Braun, B. Klein, and H.-J. Pirner, *Influence of quark boundary conditions on the pion mass in finite volume*, Phys. Rev. D **72**, 034017 (2005), arXiv:hep-ph/0504127.

[394] J. Braun, B. Klein, H.-J. Pirner, and A. H. Rezaeian, *Volume and quark mass dependence of the chiral phase transition*, Phys. Rev. D **73**, 074010 (2006), arXiv:hep-ph/0512274.

[395] J. Braun, B. Klein, and P. Piasecki, *On the scaling behavior of the chiral phase transition in QCD in finite and infinite volume*, Eur. Phys. J. C **71**, 1576 (2011), arXiv:1008.2155 [hep-ph].

[396] J. Braun, B. Klein, and B.-J. Schaefer, *On the phase structure of QCD in a finite volume*, Phys. Lett. B **713**, 216 (2012), arXiv:1110.0849 [hep-ph].

[397] R.-A. Tripolt, J. Braun, B. Klein, and B.-J. Schaefer, *Effect of fluctuations on the QCD critical point in a finite volume*, Phys. Rev. D **90**, 054012 (2014), arXiv:1308.0164 [hep-ph].

[398] L. Fister and J. M. Pawlowski, *Functional renormalization group in a finite volume*, Phys. Rev. D **92**, 076009 (2015), arXiv:1504.05166 [hep-ph].

[399] A. Juričić and B.-J. Schaefer, *Chiral Thermodynamics in a Finite Box*, Acta Phys. Polon. B Proc. Supp. **10**, 609 (2017), arXiv:1611.03653 [hep-ph].

[400] Z. Zhang, C. Shi, and H.-S. Zong, *Nambu–Jona-Lasinio model in a sphere*, Phys. Rev. D **101**, 043006 (2020), arXiv:1908.08671 [hep-ph].

[401] A. Bhattacharyya, P. Deb, S. K. Ghosh, R. Ray, and S. Sur, *Thermodynamic properties of strongly interacting matter in finite volume using the Polyakov–Nambu–Jona-Lasinio model*, Phys. Rev. D **87**, 054009 (2013), arXiv:1212.5893 [hep-ph].

[402] A. Bhattacharyya, R. Ray, and S. Sur, *Fluctuation of strongly interacting matter in the Polyakov–Nambu–Jona-Lasinio model in a finite volume*, Phys. Rev. D **91**, 051501(R) (2015), arXiv:1412.8316 [hep-ph].

[403] R.-L. Liu, M.-Y. Lai, C. Shi, and H.-S. Zong, *Finite volume effects on QCD susceptibilities with a chiral chemical potential*, Phys. Rev. D **102**, 014014 (2020).

[404] D. B. Leinweber, J. I. Skullerud, A. G. Williams, and C. Parrinello, *Gluon propagator in the infrared region*, Phys. Rev. D **58**, 031501 (1998), arXiv:hep-lat/9803015.

[405] P. Boucaud et al., *Quark propagator and vertex: systematic corrections of hypercubic artifacts from lattice simulations*, Phys. Lett. B **575**, 256 (2003), arXiv:hep-lat/0307026.

[406] F. de Soto and C. Roiesnel, *On the reduction of hypercubic lattice artifacts*, J. High Energy Phys. **2007**, 09:007 (2007), arXiv:0705.3523 [hep-lat].

[407] J. Simeth, A. Sternbeck, M. Göckeler, H. Perlt, and A. Schiller, *Using NSPT for the Removal of Hypercubic Lattice Artifacts*, Proc. Sci. **LATTICE2014**, 294 (2015), arXiv:1501.06322 [hep-lat].

[408] J. Bernhardt, private communication.

[409] A. Cucchieri, A. Maas, and T. Mendes, *Infrared properties of propagators in Landau-gauge pure Yang–Mills theory at finite temperature*, Phys. Rev. D **75**, 076003 (2007), arXiv:hep-lat/0702022.

[410] V. G. Bornyakov and V. K. Mitrjushkin, *Lattice QCD gluon propagators near transition temperature*, Int. J. Mod. Phys. A **27**, 1250050 (2012), arXiv:1103.0442 [hep-lat].

[411] R. Aouane, V. G. Bornyakov, E. M. Ilgenfritz, V. K. Mitrjushkin, M. Müller-Preussker, and A. Sternbeck, *Landau gauge gluon and ghost propagators at finite temperature from quenched lattice QCD*, Phys. Rev. D **85**, 034501 (2012), arXiv:1108.1735 [hep-lat].

[412] B.-J. Schaefer, private communication.

[413] G. C. Wick, *Properties of Bethe–Salpeter Wave Functions*, Phys. Rev. **96**, 1124 (1954).

[414] J. S. Schwinger, *On the Euclidean structure of relativistic field theory*, Proc. Nat. Acad. Sci. USA **44**, 956 (1958).

[415] J. S. Schwinger, *Euclidean Quantum Electrodynamics*, Phys. Rev. **115**, 721 (1959).

[416] K. Osterwalder and R. Schrader, *Axioms for Euclidean Green's Functions II*, Commun. Math. Phys. **42**, 281 (1975).

[417] P. van Nieuwenhuizen and A. Waldron, *On Euclidean spinors and Wick rotations*, Phys. Lett. B **389**, 29 (1996), arXiv:hep-th/9608174.

[418] N. Brown and M. R. Pennington, *Studies of confinement: How the gluon propagates*, Phys. Rev. D **39**, 2723 (1989).

Acknowledgments

First of all, I would like to express my deep gratitude to Christian Fischer for giving me the opportunity to work on such a fascinating topic, for his continuous support in all possible ways, for his enthusiasm, and for having always time for "a quick question."

Furthermore, I am very grateful to Michael Buballa for introducing me to DSEs when I was a Master's student in Darmstadt, for stimulating discussions during the PhD Committee meetings, and for being the second referee. It should also not go unmentioned that he read the draft version of this thesis during his summer holidays.

Special thanks go to Richard Williams for sharing his near-infinite knowledge about DSEs, for many inspiring discussions about physics and beyond, and for providing the best coffee and tea. More special thanks go to my "doctoral twin" Pascal Gunkel for countless discussions and sharing the highs and lows of being a PhD student.

Moreover, I am grateful to Christian Fischer, Volker Koch, and the Helmholtz Graduate School for Hadron and Ion Research for FAIR for making a memorable research stay at the Lawrence Berkeley National Laboratory possible. In the course of that, I am thankful for the hospitality of the whole Nuclear Theory Group at the Berkeley Lab. Throughout my time in Berkeley, I would like to thank Judy Kendall for providing a home away from home.

I am indebted to Markus Huber and Julian Bernhardt for proof-reading this thesis and for all the helpful comments and hints.

I would like to thank Bernd-Jochen Schaefer for enlightening discussions and his continuous interest in my work.

Furthermore, I happily enjoy the fruitful collaborations with Thorsten Steinert and Julian Bernhardt on topics that are covered in this work.

I would like to thank Anton Andronic for making his freeze-out data available and Fei Gao and Jan Pawlowski for providing me with their phase-diagram results.

Though quite some time passed since then, I thank Tom Steele for introducing me to the amazing and fascinating world of quarks and gluons in the course of a research project during my time abroad at the University of Saskatchewan.

My thanks must also go to the (from my point of view) “old generation” of the Fischer group—Christian, Esther, Nico, Paul, Pascal, and Richard—for a warm welcome and a pleasant, relaxed yet inspiring atmosphere with many discussions about various topics. The same holds for the “new generation”—Chen, Joshua, Julian, Markus, Najmul, Stephan, and Walaa—and all the other members of the Theory Institute.

Finally, I would like to thank my family for always supporting and believing in me. In particular, I thank Katja for her love, patience, support, and all the other invaluable things with which she enriches my life.

Erklärung

Hiermit erkläre ich:

Ich habe die vorgelegte Dissertation selbstständig und ohne unerlaubte fremde Hilfe und nur mit den Hilfen angefertigt, die ich in der Dissertation angegeben habe. Alle Textstellen, die wörtlich oder sinngemäß aus veröffentlichten Schriften entnommen sind, und alle Angaben, die auf mündlichen Auskünften beruhen, sind als solche kenntlich gemacht. Ich stimme einer eventuellen Überprüfung meiner Dissertation durch eine Antiplagiat-Software zu. Bei den von mir durchgeführten und in der Dissertation erwähnten Untersuchungen habe ich die Grundsätze guter wissenschaftlicher Praxis, wie sie in der *Satzung der Justus-Liebig-Universität Gießen zur Sicherung guter wissenschaftlicher Praxis* niedergelegt sind, eingehalten.

Teile dieser Arbeit sind bereits veröffentlicht:

- Philipp Isserstedt, Michael Buballa, Christian S. Fischer und Pascal J. Gunkel, *Baryon number fluctuations in the QCD phase diagram from Dyson–Schwinger equations*, Phys. Rev. D **100**, 074011 (2019), arXiv:1906.11644 [hep-ph].
- Philipp Isserstedt, Christian S. Fischer und Thorsten Steinert, *Thermodynamics from the quark condensate*, Phys. Rev. D **103**, 054012 (2021), arXiv:2012.04991 [hep-ph].
- Julian Bernhardt, Christian S. Fischer, Philipp Isserstedt und Bernd-Jochen Schaefer, *Critical endpoint of QCD in a finite volume*, Phys. Rev. D **104**, 074035 (2021), arXiv:2107.05504 [hep-ph].

(Philipp Isserstedt)